Label-Free Electrical Sensing of Single Cells Translocating through Micropores at Gigahertz Frequencies

Dissertation
zur Erlangung des Doktorgrades
an der Fakultät für Mathematik, Informatik und Naturwissenschaften
Fachbereich Physik
der Universität Hamburg

vorgelegt von

Paul V. Gwozdz

Hamburg

2019

Gutachter der Dissertation:	Prof. Dr. Robert H. Blick Prof. Dr. Wolfgang Parak Prof. Dr. Petri Kursula
Zusammensetzung der Prüfungskommission:	Prof. Dr. Robert H. Blick Prof. Dr. Wolfgang Parak Prof. Dr. Michael Potthoff Prof. Dr. Alexander Lichtenstein Dr. Robert Zierold
Vorsitzender der Prüfungskommision:	Prof. Dr. Michael Potthoff
Datum der Disputation:	04.11.2019
Vorsitzender Fach-Promotionsausschuss PHYSIK:	Prof. Dr. Michael Potthoff
Leiter des Fachbereichs PHYSIK:	Prof. Dr. Wolgang Hansen
Dekan der Fakultät MIN:	Prof. Dr. Heinrich Graener

You cannot patent a hole

Opinion of attorney to dismiss the first patent application of Wallace H. Coulter

Abstract

The first part of the thesis is dedicated to the resistive pulse method operating with direct currents. Borosilicate glass micropores, used for the experiments, are manufactured by direct laser ablation with an ArF-based excimer laser. The electric current measurements across the micropore are discussed numerically and experimentally. It is shown how time domain direct current measurements across the micropores, which are filled with a conductive electrolyte solution, deliver information about the sizes of individual translocating particles. Noise measurements are performed to illustrate that the resistive pulse method is not capable to perform high speed measurements which are needed for the application of the method for e.g. DNA sequencing.

It is explained in the second part of the thesis how a micropore is embedded between two in-plane metal electrodes. These electrodes are used to bring the electrical field of a radio frequency wave into the vicinity or the pore. The interaction of the electrical field with Jurkat T cells is used to characterize the translocating cells and to extract information about the cells in addition to their size. In detail, it is shown that these measurements enable the experimentalist to probe specific properties of the cell such as its electrical conductivity and dielectric permittivity.

The preparation of the measurement chip is discussed in detail. It is shown how the micropore is aligned between the two electrodes and how this microscopic sensing region is interfaced with the measurement equipment. Coplanar waveguides are introduced which lead the radio frequency wave into the sensing region and reflection measurements are performed to measure the particle of interest. The chip design is tested by time domain measurements with a vector network analyzer, which is capable of directly measuring the chip reflection versus time.

A heterodyne measurement setup is introduced which enables to resolve the reflection using lock-in amplifiers with increased sampling speed compared to the vector network analyzer. The setup is used to observe translocating polystyrene beads and Jurkat T cells in different electrolyte solutions. The findings are discussed using time resolved optical microscopy and patch clamp experiments and it is shown that cells which undergo apoptosis can be identified with this method.

Zusammenfassung

Im ersten Teil dieser Dissertationsschrift wird die Resistive Pulse Methode besprochen, die mit Gleichstrom arbeitet. Für die Experimente werden Glasmikroporen verwendet, die mit Hilfe von Laserablation mit Hilfe eines ArF Excimer Laser direkt in ein Glassubstrat gebohrt werden. Die entsprechenden Gleichstrommessungen an den Mikroporen, welche hierfür mit leitfähiger Elektrolytlösung gefüllt sind, werden sowohl numerisch als auch experimentell diskutiert. Es wird gezeigt, wie zeitaufgelöste Gleichstrommessungen an den Poren die Vermessung der Partikeldurchmesser ermöglichen. Darüber hinaus werden Rauschmessungen durchgeführt, die zeigen, dass die Resistive Pulse Methode nicht in der Lage ist die typische Dynamik auf der Nanoskala aufzulösen, die beispielsweise für Anwendungen bei der DNA-Sequenzierung benötigt wird.

Im zweiten Teil der Arbeit werden die Mikroporen zwischen zwei Metallelektroden eingebettet. Dadurch ist es möglich eine Radiofrequenzwelle in die Nähe der Pore zu bringen. Das so erzeugte Feld zwischen den Elektroden wird verwendet um einzelne Jurkat T-Zellen zu charakterisieren und Informationen jenseits des Durchmessers der Zellen zu generieren. Es wir detailliert erklärt, dass diese Methode in der Lage ist Zelleigenschaften, wie deren elektrische Leitfähigkeit und dielektrische Permittivität zu vermessen.

Die Produktion der Messchips wird beschrieben. Zunächst wird die Positionierung der Mikropore zwischen den beiden Elektroden dargestellt und es wird gezeigt, wie der Chip in die Messapparatur eingebettet werden kann. Hierfür werden koplanare Wellenleiter eingeführt, weil diese in den dargestellten Experimenten verwendet werden, um die Radiofrequenzwelle an die Signalregion zu transportieren. Für die Partikelmessungen werden Reflexionsmessungen durchgeführt. Für einen ersten Test des Chips wird die zeitabhängige Modulation der Reflexion mit Hilfe eines Vektor-Netzwerkanalysators gemessen.

Im letzten Teil der Dissertationsschrift wird ein heterodynes Messverfahren eingeführt. Dieses ermöglicht es ebenfalls eine Reflexionsmessung durchzuführen, allerdings bei erheblich höheren Sampling Raten, als es der Netzwerkanalysator erlaubt. Das Setup wird verwendet um Polystyrolkügelchen und Jurkat T-Zellen, die in verschiedenen Elektrolytlösungen suspendiert sind zu vermessen, wenn diese durch die Mikropore translozieren. Schließlich werden die gemachten Beobachtungen mit Hilfe von mikroskopischen Methoden und Patch Clamp Experimenten diskutiert.

Contents

List of Figures

Chapter 1

Introduction

Counting cells in experimental cell cultures is a standard procedure in every biology laboratory to determine the concentration of a specific cell type. However, it is tedious and slow if it has to be done manually and thus it limits the amount of cell cultures that can be characterized drastically. To determine the concentration of a cell suspension hemocytometers are still routinely used. A pre-defined amount of cell suspension is placed in a fluidic chamber within the transparent hemocytometer. This can be seen in Fig. 1.1. To increase the optical contrast and to distinguish between different cell types the test sample can be labeled using a dye. On the surface of the hemocytometer a grid is engraved such that the number of cells within a specific area can be counted under optical control in a microscope (see zoomed-in view in Fig. 1.1). The number of cells in the grid can be translated into the concentration of the cell sample. This is practical for a small number of cell samples but it is impossible to use this method in clinical and high throughput applications. Beside the extremely limited throughput, only information about the cell concentration is collected.

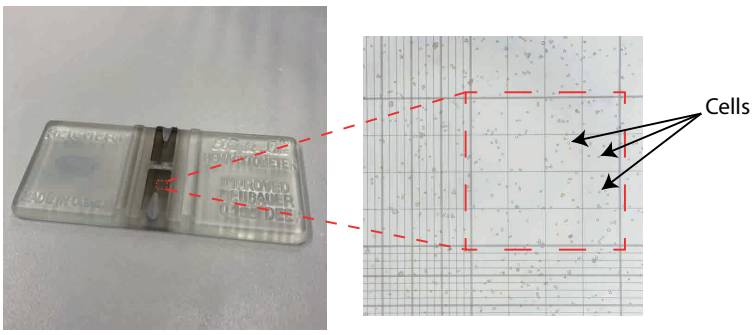

Figure 1.1: Hemocytometer used for manual cell counting. (zoomed-in view) Area in which the cells are counted under optical control. The number of cells within the area can be calculated back to the original cell concentration.

In this respect, the resistive pulse technique was a major breakthrough since its first proposal by Wallace H. Coulter in 1953 [1]. This method allows for a label-free, electrical measurement of the size and concentration of particles which are suspended in electrically conducting electrolyte solution [2] eliminating the need for time consuming, manual determination of these quantities by an experimentalist using a microscope.

The Coulter principle relies on the measurement of small electrical currents that arise from the ion flow through a micrometer sized aperture that is separating two reservoirs filled with the conducting electrolyte solution. If a particle translocates through the aperture, it blocks a fraction of the current, leading to a short current blockage that is monitored by measuring the current along time and thus allowing to count and size individual particles. Remarkably, this simple method was successfully miniaturized and further developed until it became possible to sequence single stranded DNA by using apertures in the low nanometer range [3, 4, 5, 6, 7].

But beside the resistive pulse method that is using DC for the measurement a number of alternative flow cytometric, single particle methods were developed. The methods cover a plethora of frequency ranges using AC signals or optical methods [8]. In the framework of this thesis a novel label-free, single particle measurement setup sensing particles electronically at high AC frequencies is proposed, developed and realized.

The thesis is divided into two parts. In **Part I** the resistive pulse method is presented and it will be shown how glass pores, which are drilled directly into a glass substrate can be used as a sensor for detecting and sizing single particles without the need of a chemical label. Using these glass pores it will be discussed how the noise within the system ultimately limits the temporal resolution of the method. Furthermore, it will be discussed why the amount of information that can be deduced from the measurement of translocating particles is limited to the measurement of particle size and the particle translocation time.

Part II of the thesis is dedicated to the development of a system in which the particles translocate through the micropore while experiencing a high frequency AC field. This method, called dielectric spectroscopy, enables to acquire information about the translocating particles beyond their size. Frequencies above 700 MHz are used, allowing to sense the inside of a biological cell. At DC the inside of a cell is shielded because the cell membrane acts as a capacitor with little to no conductivity. It will be shown that the capacitance can be shorted out at these frequencies thus enabling the measurement of cell properties associated with their biological state. In the context of the thesis it will be shown how cell apoptosis, which is the programmed cell death, is being detected in this way. The method is introduced theoretically, and numerical simulations will be used to determine the expected signal originating from translocating particles. Within

the discussion it will be shown that the noise spectrum of this method is not showing high frequency noise, which is vast contrast to the corresponding DC measurement. It will be outlined how this method is potentially paving the way for being used as a particle detection strategies operating at increased measurement bandwidth and thus allowing in future to detect DNA translocating through small channels or pores at its natural translocation velocity.

Part I

DC

Chapter 2

Resistive Pulse Sensing

Resistive pulse sensing (RPS) is a technique that was invented to count biological cells and colloids, which are suspended in a conductive electrolyte solution. The technique was patented in 1953 by Wallace H. Coulter [1] and the method was evaluated and its functionality was shown three years later [9, 10]. Since then the technique has developed into a versatile tool in a plethora of scientific applications, way beyond counting biological cells. A lot of information can be found in numerous review articles concerning the development of the original patent into a large business model [11], the development of tunable RPS [12], the miniaturization of the method and the consequent challenges [13, 14], the progression of RPS into novel measurement platforms [15] and the application of the method for biological applications as, e.g. virus counting and DNA detection and sequencing [16, 3].

A schematic of a RPS setup is shown in Fig. 2.1 (a). Two reservoirs, which are filled with a conductive electrolyte solution, are electrically connected by a pore or a channel with a lateral size bigger than the geometrical dimension of the particles under investigation. One Ag/AgCl electrode is submerged into each reservoir and the electrodes are connected to a sensitive direct-current (DC) amplifier, which allows for the measurement of the current flowing through the channel and simultaneously allows to apply a voltage across the electrodes. When a voltage is applied, the ions in the electrolyte will flow through the channel thus producing an ionic current. Particles that are suspended in the electrolyte can be dragged through the channel by the applied voltage or by applying a pressure gradient. When a particle is translocating through the channel it displaces the electrolyte due to its presence, thereby increasing the resistance of the channel and thus producing a temporal current drop during the translocation time. Typical translocation times for individual particles are in the millisecond and sub-millisecond range, thus potentially allowing for measuring thousands of individual particles within minutes.

When W. H. Coulter presented the first commercial version of his invention, i.e. the

Coulter Counter, it was exclusively used for counting cells and thus for determining cell concentrations. But very rapidly, it was realized experimentally that the amplitude of the observed current drop is a measure for determining the particle volume [17].

Although there are alternative methods to determine the size distribution of suspended particles, the RPS technology holds some advantages over existing strategies. Two prominent alternative methods which are routinely used to determine the size distribution of particle solutions are dynamic light scattering (DLS) [18] and disc centrifugation [19, 20]. In the case of DLS, a laser is directed on a sample of diluted particles and as the light hits the particles it undergoes Rayleigh scattering. A detector measures the time fluctuations of the intensity of the scattered light that are caused by the random motion of the particles in the fluid. From this information, the size distribution of the sample can be derived. In the case of disc centrifugation, the sedimentation velocity of different sized particles is used to determine the size distribution of a test sample. Variations of these methods and other methods exist but they have a common disadvantage namely the measurement is derived from a macroscopic sample so that the methods rely on intrinsic averaging over the whole sample. As a matter of fact, these methods are only applicable to suspensions of particles with similar size [13].

Beside that, it is possible to measure the size distribution of particles in the micrometer range using optical microscopy, but this is typically very time-consuming as this is a serial process, which cannot be parallelized easily. The same is true for scanning electron microscopy (SEM), transmission electron microscopy (TEM) and other imaging methods. They can be used to investigate particles with diameters in the nanometer range but this is only practical, at reasonable experimental effort, if the particles under investigation can be dried. Here, the serial nature of the imaging process is the limiting factor, too. Additionally, SEM and TEM measurements are experimentally even more challenging, require an experienced user and extremely expensive equipment [13].

In contrast RPS is a fast method, enabling the investigation of the size distribution of polydispersed particle solutions on a single particle level. Furthermore, it is scalable, allowing to measure molecules in the nanometer range up to macroscopic particles like biological cells which have diameters in the micrometer range.

In addition, RPS allows for label-free detection and analysis, which is a huge advantage because the process of labeling can be time-consuming and it potentially alters the behavior of the investigated particles as the interaction of a chemical dye with the particle is not always a priori known.

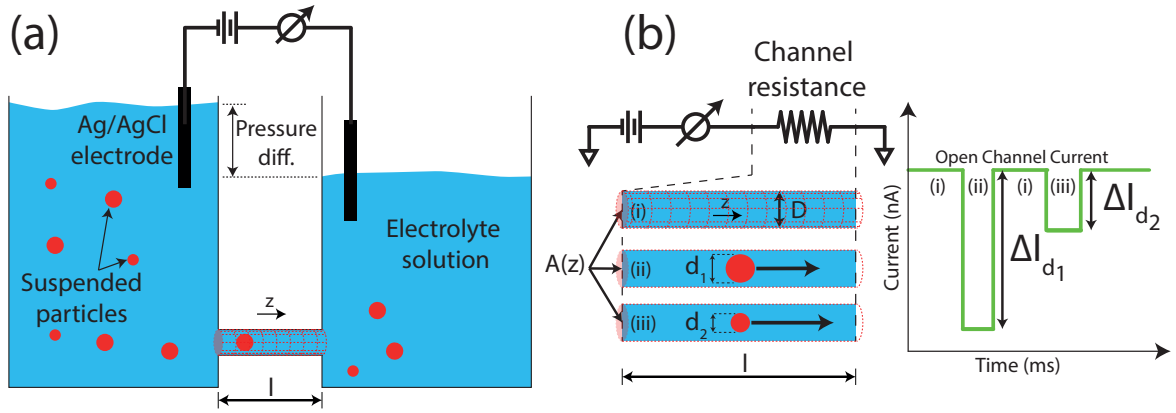

Figure 2.1: (a) Schematic of a RPS setup. Particles that shall be characterized are suspended in a reservoir that is connected via a channel or a pore to a second reservoir. A voltage is applied using two Ag/AgCl electrodes that are immersed in the reservoirs. Particles translocate through the channel due to an applied pressure or voltage. (b) Equivalent circuit model of the channel and a characteristic time domain measurements that the setup is capable of performing.

2.1 Theoretical Considerations

In the present section it will be outlined how DC measurements across micrometer sized channels, filled with electrolyte solution, can be used to measure the volume of a particle when it is translocating through these orifices. Different theoretical models describing this process are introduced. After that, properties of induced fluidic flow, which is responsible for driving particle translocation through the channels or pores are discussed. Finally, some relevant applications presented in the literature are summarized.

2.1.1 Resistive Pulse Sensing, Theoretical Considerations

The general setup of a RPS experiment is shown in Fig. 2.1 (a). In this model a channel is interconnecting two fluidic reservoirs filled with electrolyte solution. Two Ag/AgCl electrodes are located within the reservoirs and they are connected to the measurement electronics, which is also used to apply a voltage across the channel. The channel, which is filled with electrolyte solution having a resistivity of ρ acts as a resistor when a voltage is applied across the electrodes. A simplified equivalent circuit model of the system is given in Fig. 2.1 (b). Assuming a homogeneous current distribution across the area $A(z)$ of the channel (see Fig. 2.1 (b)) the corresponding lower limit estimation for the resistance R can be calculated via

$$R = \rho \int_0^{\mathrm{L}} \frac{dz}{A(z)} \tag{2.1}$$

where L is the length of the channel [21, 2].

For the sake of simplicity, here the discussion is concentrated on a cylindrical channel and if the cylindrical channel has a diameter D and a length L, the electrical resistance according to Eq. 2.1 is

$$R = \rho \frac{L}{\pi \left(\frac{D}{2}\right)^2}. \tag{2.2}$$

For spherical particles with a resistivity of ρ_p and a diameter of d suspended in electrolyte solution having a resistivity ρ, J. C. Maxwell presented an approximation for the effective resistivity ρ_eff of the corresponding solution [21]. From his discussion, based on simple continuity assumptions, the relationship between the resistivity ρ_eff of the electrolyte, which is containing particles, and the resistivity of the particle itself and the medium it is suspended in reads

$$\frac{\rho_\mathrm{eff} - \rho}{2\rho_\mathrm{eff} + \rho} = f \frac{\rho_\mathrm{p} - \rho}{2\rho_\mathrm{p} + \rho} \tag{2.3}$$

where f is the volume fraction of the particles in suspension. The only approximation in Eq. 2.3 is that the particles have to be highly diluted (i.e. $f \ll 1$) so that there is little to none interaction between adjacent particles. Solving this equation for the resistivity of the electrolyte-particle mixture gives

$$\rho_\mathrm{eff} = \rho \frac{1 + fB}{1 - 2fB} \quad \text{with} \quad B = \frac{\rho_\mathrm{p} - \rho}{2\rho_\mathrm{p} + \rho}. \tag{2.4}$$

For $f \ll 1$ Eq. 2.4 can be further expanded in a Taylor series with respect to ρ resulting in

$$\rho_\mathrm{eff} \approx \rho + 3\rho f B. \tag{2.5}$$

This equation can be simplified by taking into account, that in conventional RPS experiments the particles under test have a higher resistivity than the electrolyte solution [22]. For testing the devices polystyrene beads are used, which have a resistivity in the order of $\rho_\mathrm{p} = 10^4\,\Omega\mathrm{m}$ [23] while the electrolyte is highly conducting with resistivity values around $\rho = 1\,\Omega m$ [24]. As a matter of fact, the factor B approximately equals $1/2$ and thus according to Maxwell's approximation the presence of a particle in the channel occupying a volume fraction f increases the resistivity of the channel to

$$\rho_\mathrm{eff} \approx \rho \cdot (1 + \frac{3}{2} f). \tag{2.6}$$

A sphere with diameter d centered within a channel of diameter D and length L occupies a volume fraction of $f = 2d^3/3D^2L$. If this is inserted into Eq. 2.6 the resistance

R' of a channel containing a particle can be calculated using Eq. 2.2. Accordingly, the measured resistance change due to the presence of the particle in the channel can be written as

$$\Delta R = R' - R = \frac{4\rho d^3}{\pi D^4}. \tag{2.7}$$

Although Eq. 2.7 only holds for spheres with $d \ll D$ it already gives a good impression on how such a system can be utilized. The resistive pulse is proportional to the volume of the sphere if the diameter of the channel is constant, thus the resistive pulse height can be used to measure the diameter of the particle translocating the channel as indicated in Fig. 2.1 (b). Often it is useful to divide the resistance change ΔR by the open channel resistance R, thus obtaining the so called Maxwell-Garnet approximation

$$\frac{\Delta R}{R} = \frac{d^3}{D^2 L} = \frac{3}{2}\frac{v}{V} = g \cdot \frac{v}{V} \tag{2.8}$$

where V and v are the volumes of the channel and the particle within the channel, respectively. The factor g is the so called geometry or form factor. In Eq. 2.8 it is assumed, that the electric field is constant over the channel diameter and length, which obviously neglects wall effects as well as access resistances at the entry and exit of the channel. Nevertheless, this lower bond approximation shows that particle sizing is feasible with a RPS setup as the resistance change in a channel with constant diameter D and length L is proportional to the particle volume.

Depending on the ratio between the particle diameter and the diameter of the channel, a better approximation of the resistive pulse can be given by

$$\frac{\Delta R}{R} = \frac{d^3}{D^2 L} \cdot \frac{1}{1 - 0.8\left(\frac{d}{D}\right)^3}. \tag{2.9}$$

This expression is the Maxwell-Garnet approximation (see Eq. 2.8) multiplied by a numerical factor. In contrast to Eq. 2.8 this expression is not an analytical solution but rather a numerical approximation that holds for particles within an intermediate size range. First numerical calculations regarding this problem were presented by W. R. Smythe for spherical and spheroidal particles within a tube, respectively [25, 26]. On the basis of these calculations Eq. 2.9 was then given by DeBlois [27].

Depending on the ratio between the size of the particle and the channel size an even better approximations can be given, which describes the resistivity change adequately even for particle diameters similar to the channel diameter [28, 29]. For such particles the resistance change can be described as

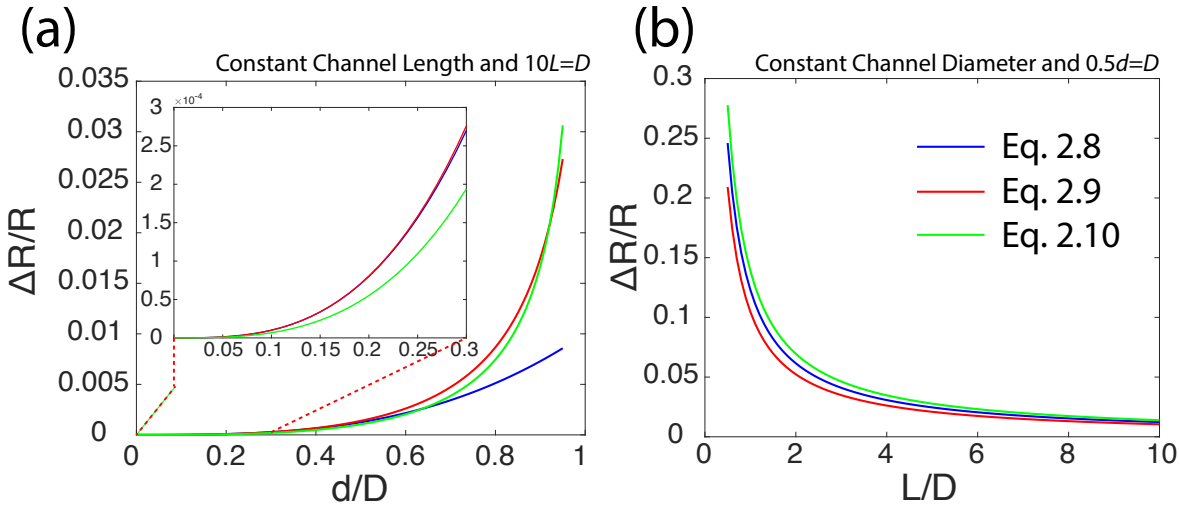

Figure 2.2: (a) Resistive pulse amplitude according to Eq. 2.8 (blue), Eq. 2.9 (red) and 2.10 (green) for a fixed pore length with $10L = D$. (b) Resistive pulse amplitude for the same equations for different pore lengths with $D = 0.5d$ and a constant particle diameter.

$$\frac{\Delta R}{R} = \frac{D}{L}\left(\frac{\arcsin(\frac{d}{D})}{\sqrt{1-\left(\frac{d}{D}\right)^2}} - \frac{d}{D}\right). \tag{2.10}$$

In Fig. 2.2 (a) the resistance changes according to Eq. 2.8, Eq. 2.9 and Eq. 2.10 is plotted in relative units. The plot shows the resistance change for a cylindrical pore with $D/L = 1/10$. For particles that are relatively small (i.e. $d/D < 0.4$) the three models show good agreement. For higher values of d/D the simple model of Eq. 2.8 deviates strongly from the other two models. As this model describes the limit of infinitesimally small particles it is expected that it will underestimate the resistance increase for big particles. For particles that approach the diameter of the pore (i.e. $d \approx D$) Eq. 2.9 tends to underestimate this limit as here an infinitesimal high resistivity change is expected which is modeled by Eq. 2.10, only.

Fig. 2.2 (b) shows how the resistance change behaves if the channel length is changed. In the figure the diameter of the channel is assumed to be $D = 0.5d$. For the three models it is shown that the resistance change is increased for a shorter channel length. Experimentally, this shortening can be realized by decreasing the thickness of the membrane material in which the channel is embedded. The qualitative behavior shown in the figure was experimentally demonstrated with nanometer sized pores embedded in SiN membranes of different thicknesses [30].

Translocating Time of Particles

Apart from the amplitude of the resistance change, in general the translocation time is an important measurement quantity of RPS experiments. The translocation time of a particle, when it is driven through a channel via pressure-driven flow, depends strongly on the radial position of the particle within the channel. According to Berge *et al.* [31] the translocation time of a particle translocating through the central axis of a cylindrical channel can be approximated by

$$\Delta t_0 = \frac{4\eta L^2}{R^2 \Delta P} \tag{2.11}$$

with η being the viscosity of the electrolyte and ΔP the pressure drop across the channel. It will be shown in Sec. 2.1.2 that in the case of pressure-driven flow the velocity profile of the liquid is strongly dependent on the radial position inside the channel (see Fig. 2.4 (a)). As a matter of fact, the translocation time is influenced by the radial position inside the channel, too. Using the parametrization shown in Fig. 2.3 the translocation time of a particle translocating beyond the central axis can be estimated by

$$\Delta t = \frac{\Delta t_0}{(1-x^2)(c_1 - c_2 x^5)} \tag{2.12}$$

with the parameter $x = r/R$, R being the radius of the channel, r the radial position of the particle, $c_1 = 1 - 2/3(b/R)^2$ with b being the particle radius, $c_2 = 23.36(1 - c_1)$ and $(c_1 - c_2 x^5)$ being a numerical correction factor derived from a fit to experimental data [31, 32].

Off-Axis Particle Trajectories

Eq. 2.8, Eq. 2.9 and Eq. 2.10 describe the resistivity change for particles translocating through the center of cylindrical channels. Obviously, this is not always the case. A theoretical description of the resistive pulse caused by particles translocating beyond the central channel axis can be given as

$$\frac{\Delta R}{\Delta R_0} = 1 + \alpha \left(x \frac{d}{D} \right)^3 \tag{2.13}$$

where ΔR is the measured resistivity blockage, ΔR_0 is the corresponding resistivity blockage that would arise when the same particle has had translocated the pore through the axis, α is a correction coefficient which depends on the channel dimensions and has to be extracted form experimental data and the remaining parameters are the same as described previously and as are shown in Fig. 2.3. Obviously, for an on-axis particle, i.e. $x = 0$, it follows that $\Delta R = \Delta R_0$. If the particle translocates off-axis, i.e. $x > 0$, the measured

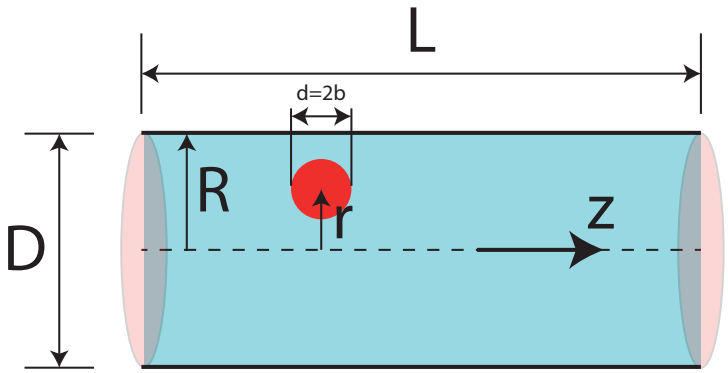

Figure 2.3: Parameter set describing the radial position of a particle translocating through a cylindrical microchannel, with length L and diameter D. The particle, having a radius b, is assumed to move in positive z-direction.

resistive pulse increases. Simultaneously, according to Eq. 2.12 the translocation time increases. This effect will be shown experimentally in Sec. 2.3.3. It was reported that Eq. 2.13 can be used to correct data for the, so called, off-axis effect thus slightly improve the particle size determination capabilities of a RPS device [33].

2.1.2 Flow Properties Liquids in Channels

Transport of particles through a channel is governed by several different physical phenomena. In the scope of this thesis the liquid is set in motion by applying a pressure difference across a micropore (MP), which leads to a liquid motion that is dragging the particles in suspension through the pore. After the discussion of the pressure-driven flow it will also be shown how an electrical voltage drop across the channel leads to liquid motion within it. Both approaches are discussed numerically in the following.

Pressure-Driven Flow

In general, liquid flow within a channel can be described by the Navier-Stokes equation. A review on this equation is presented e.g. in Ref. [34]. This differential equation can be used to describe pressure-driven flow (PDF) in microchannels and pores.

In the first row of Fig. 2.4 (a) the expected parabolic flow profile is illustrated schematically for water in a channel, that is being exposed to a pressure difference.

Generally, the velocity profile $\vec{v}$ of a newtonian fluid of viscosity μ and density ρ under an applied pressure p can be derived using the Navier-Stokes equation

$$\rho\left(\frac{\partial\vec{v}}{\partial t}+(\vec{v}\cdot\nabla)\vec{v}\right)=-\nabla p+\mu\triangle\vec{v}+\vec{f} \tag{2.14}$$

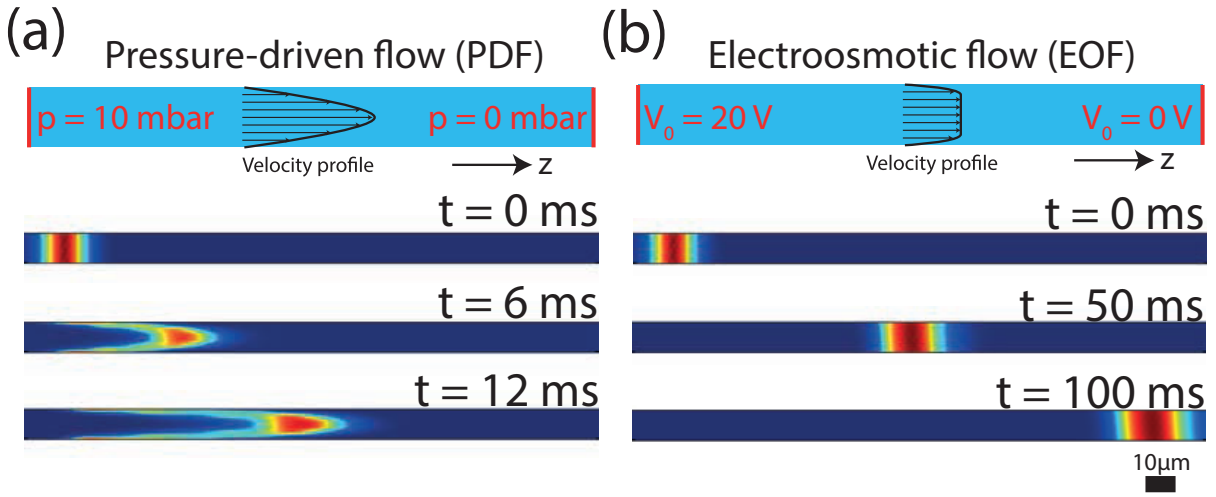

Figure 2.4: (First row in (a) and (b)) Schematic of expected velocity profile for pressure-driven flow (a) and electroosmotic flow (b). (Remaining rows in (a) and (b)) Finite element simulation of the flow profile of a diluted species which has initially a flat concentration profile perpendicular to the channel and a gaussian concentration profile in z-direction. Simulations are carried out in long 2D channels with a constant width of 10 µm. The material parameters used for the simulations are the dielectric constant, dynamic viscosity and density of water ($\epsilon_r = 80$, $\mu = 0.001$Pas and $\rho = 1000\text{kg/m}^3$) and a conductivity of $\sigma = 0.001\,\text{S/m}$. The peak concentration of the initially gaussian distributed species is chosen to be $c_0 = 1\,\text{mol/l}$. In (a) the time dependent evolution of the diluted species is given for three time steps when a pressure gradient is applied across the channel. (b) The same simulation showing the result of the time evolution of the diluted species with an applied voltage across the channel due to electroosmosis. For this simulation the walls of the channel had be given a ζ-potential of $-0.1\,\text{V}$.

were $\vec{f}$ is a place holder for various body forces as e.g. gravity. For problems concerning fluidic systems, mass conservation does hold which can be written as

$$\frac{\partial \rho}{\partial t} + \nabla(\rho \vec{v}) = 0 \tag{2.15}$$

and at the interface between the channel walls and the liquid phase a no-slip boundary condition is typically used which means that the velocity at the channel walls is assumed to be zero.

In Fig. 2.4 (a) a finite element method (FEM) simulation of pressure-driven flow through a two dimensional fluidic channel is shown. The channel has a width of 10 µm and in the simulation a pressure gradient of 10 mbar is applied. If the problem is solved analytically, which is possible for the simple 2D problem, a parabolic velocity field in z-direction is expected. To illustrate this velocity field a concentration gradient of a diluted species is added to the numerical simulation which has a Gaussian shape in z-direction.

The time dependent migration of the diluted species due to the velocity field $\vec{v}$, which is numerically evaluated by solving Eq. 2.14 and Eq. 2.15 under the no-slip boundary condition, is given in Fig. 2.4 (a) for three time steps. At $t = 0\,\mathrm{s}$ the concentration is still in its initial configuration as it has not been exposed to the velocity field, yet. For $t = 6\,\mathrm{ms}$ and $t = 10\,\mathrm{ms}$ it can be observed that the concentration gradient is moving in z-direction in a parabolic manner as expected.

Electroosmotic Flow

Electroosmotic flow is the fluidic flow of liquid through a channel due to an electric field. This effect is caused by the fact that most boundaries in fluidic experiments are build from non conductive materials like glass, quartz or polymers, having intrinsic surface charges. When these materials are exposed to an electrolyte solution, in the static case, polar liquids and dissolved ions in the solution will be attracted by the surface charges which, in turn forms an electrical double layer. Due to Brownian motion the ions in the solution are not tightly bound but they can move more freely the further they are away from the wall. After a couple of nm away from the channel wall there is no excess of one type of ions in solution as the potential drop of the redistributed ions in solution quickly decays. Due to this surface charge effect, liquid can be pumped through the channel by applying a voltage across the channel. The resulting electric field moves the excess ions in the double layer thus redistributing the ions and producing a drag force on the liquid [35, 36].

This behaviour can be described by Navier-Stokes equation (see Eq. 2.14) if an appropriate volume force is taken into account which can be written as

$$\vec{f} = \rho_\mathrm{e} \cdot \nabla(\psi + \phi) \tag{2.16}$$

with ρ_e being the net electric charge density of the liquid and ψ the potential drop across the channel due to the applied voltage across the channel. The potential ϕ origins from the interaction of the surface charge density of the channel and the free ions in the liquid as described above.

Eq. 2.14 together with Eq. 2.16 can be solved analytically for a simple two dimensional case, too. In Fig. 2.4 (b) a numerical solution is given for a channel similar to the one described previously. Here, electroosmosis is initiated by a 20 V voltage drop across the channel and no pressure gradient is applied. The ζ-potential describing the potential drop due to the electric double layer is set to $-0.1\mathrm{V}$.

As can be seen in the simulation the Gaussian concentration gradient is moving through the channel without changing its shape. Diffusion of the diluted species is included in the simulation thus the distribution widens while translocating the channel.

When solving Eq. 2.14 with Eq. 2.16 a no slip boundary condition is used so that the velocity field of the liquid is expected to be zero on the wall with a rapid increase with increasing distance from the wall and finally constant profile in the bulk (see Fig 2.4 (b) top figure). This behavior is not observed in the simulation which is due to the fact that the non constant velocity field is situated mostly in the electrical double layer which thickness is only a couple of nm thick, and thus negligible in a channel with a width of 10 µm.

2.1.3 Application of the Method

After discussing the fundamental theoretical considerations regarding the RPS, here a short overview shall be given on the experimental and industrial status quo of the method. Extensive reviews concerning this field can be found in the Ref. [13, 37, 38]

The first RPS instrument was designed by W. H. Coulter with the aim to electrically count thousands of white blood cells within seconds [38]. After he successfully introduced such a counter, which is often referred to as a Coulter Counter, yet, the second and all following generation of these Coulter Counters were able not only to count biological cells and other test particles but to size the individual particles, too. Nowadays, these counters are available from different companies (e.g. Beckman Counter) enabling the sizing of particles ranging from 400 nm to big particles with diameter of about 1 mm [37].

The sizing capabilities of the instruments are typically determined by the diameter of the channels used in the experiments. In general the bigger the test particles are the bigger the channel has to be and vice versa. On the one hand, if the suspended particles exceed a certain maximal diameter the channel is likely to clogg, which can ultimately end a measurement. On the other hand, particles which are a lot smaller than the channel diameter may not be detected if the induced resistive pulse does not exceed the noise floor of the ionic current.

A method extending the size range of particles that can be measured with one pore is the so called tunable resistive pulse sensing (TRPS) method [12]. The core of these devices is a MP which is embedded within a flexible membrane made of the thermoplastic polyurethane. Already the pioneering work showed that with such a device pores can be produced and tuned so that the detection of individual DNA molecules is possible [39]. The pores are produced by punching the membrane with a tungsten needle [39]. During the experiments the membrane can be stretched laterally thus changing the opening diameter of the pore. To a certain extend this allows to tune every pore in such a way that the measurement can be optimized for a wider size range of test particles [40, 41]. Furthermore, the setup allows to control the particle translocation velocity. A bigger pore leads to an increased velocity and thus to a higher measurement throughput. The method

was commercialized by iZON Science and it is able to measure particle sizes from 40 nm to over 11 µm [12].

It was suggested by Church *et al.* that the RPS method can be used for DNA sequencing. They patented the idea in 1995 [42] and their first results were published shortly after that [43]. The idea was that if a thin pore could be used, which has a precise diameter of 1-3 nm, single stranded DNA could translocate through this pore due to electrophoresis. As it was proposed by J. D. Watson and F. Crick in 1953 the genetic information on the DNA is encoded with four bases, namely adenine, thymidine, guanine and cytosine [44]. The four bases differ slightly in volume and therefore if it were possible to monitor the ionic current through a so called nanopore (NP) during DNA translocation, it should in principle be possible to decipher the sequence of the DNA as it should be measured as a modulation of the resistive pulse current measurement over time.

A couple of prerequisites are necessary to realize this method one of which is a suitable NP. Church *et al.* used a biological transmembrane protein called α-hemolysin [45] which they embedded in a planar lipid membrane. Consequently, an other prerequisite is the possibility to generate pure lipid membranes on an orifice in which the transmembrane pore can be embedded. Such a system was first achieved by P. Mueller *et al.* in 1962 [46]. Here, it is important that the lipid membrane which is spanned over an orifice, which is separating two reservoirs, forms a tight electrical seal between the reservoirs. The expected currents across the pore are in the pA range and thus if the electrical seal is not very high (it should be in the GΩ range) the leakage currents will exceed the current which is flowing through the pore by many orders of magnitude.

Although Church *et al.* have not been successful in decoding DNA sequences from their measurements the proposed method turned out to be promising enough so that a lot of research was done to realize such a system and to bring the vision of label-free, single strand DNA sequencing into reality. Albeit, biologically engineered α-hemolysin being the first biological NP proofing to work for DNA sequencing [47, 5] a second biological NP namely MspA [48] has been established to facilitate DNA sequencing [7, 49, 50]. Today a number of detailed reviews covering the field of DNA sequencing using NPs exist [4, 51, 52, 53].

In summary, there are a plethora of measurement schemes based on RPS. Astonishingly, this simple method even delivered a platform capable of sequencing DNA.

2.2 Pore Preparation and Characterization

Pore based RPS measurements are described in the following which will shed light on how the volume of single translocating particles under test can be conducted using micron-sized

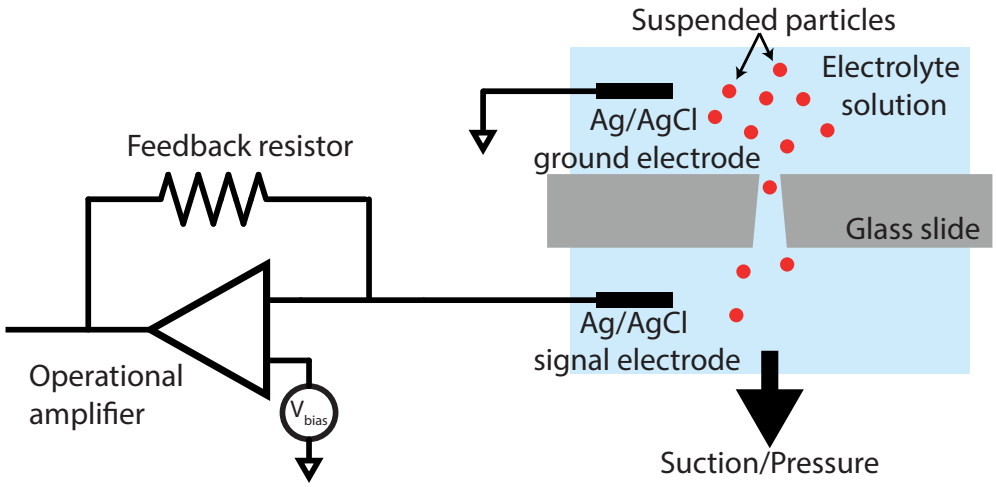

Figure 2.5: Schematic of the pore based RPS measurement setup. The measurement is conducted with an operational amplifier with a feedback resistor. The inverted input to the operational amplifier is connected to one of the fluidic compartment that is separated by a glass slide which contains a micropore. A ground electrode is connected to the other compartment. Suspended particles can be driven through the pore by an applied suction or pressure. Data from the resistive pulse experiments are sampled with a data acquisition system.

glass pores, in the following referred to as micropores (MPs). After an experimental discussion it will be shown what the limitations of such a setup are and how these limitations can be overcome to gain additional insight into the individual particle properties.

2.2.1 Pore Preparation

A schematic of the measurement setup, used for the experiments, is shown in Fig. 2.5. The device consists of a glass slide which embeds a MP. A pump is used to attract particles suspended in electrolyte solution due to an applied suction. The particles translocate from the upper reservoir into the lower reservoir via the MP. Two Ag/AgCl electrodes are immersed into the fluidic reservoirs and are connected to an operational amplifier with variable gain. This amplifier is capable of measuring nano-ampere currents and thus the temporal resistive pulses caused by the translocating particles.

Some approaches exist to prepare such glass MPs. An early approach was published by N. Fertig *et al.* in 2001. Here, glass slides were pre-thinned and then irradiated by a single high energy gold atom from a linear accelerator. After a wet-etching step of the irradiated glass substrate, using concentrated hydrofluoric acid (HF), a MP is formed [54]. A few years later pore drilling with pulses from a femtosecond laser was presented, enabling to produce pores as small as 15 nm [55, 56]. In 2009 M. Yu *et al.* presented a method to

drill pores directly into borosilicate glass with diameters as small as 90 nm. For drilling they were using an ArF-based excimer laser with a wavelength of 193 nm [57, 58]. The method has also proven to work for quartz substrates [59]. With some modifications this method will be used in this thesis to produce MPs as will be discussed in the following.

For the experiments, microscope borosilicate glass slides with a nominal thickness of (170 ± 5) µm are used as the membrane material[1]. A pore is drilled in the glass by direct laser ablation using pulsed UV light with a wavelength of 193 nm from an ArF-based excimer laser system [60]. The schematic of the commercial laser setup[2] used for laser ablation can be seen in Fig. 2.6 (a). Pulsed UV light is coupled out of the laser chamber and is partially coupled into an energy monitor that controls the output energy of the beam. The output beam energy per pulse can be stabilized between 10 mJ and 15 mJ. Furthermore, the repetition rate of the laser pulse can be tuned to values as high as 500 Hz. Using mirrors, the main beam is directed through a variable attenuator, which enables to decrease the energy delivered to the sample in a range of (2-100) %, if necessary. Finally, a projection mask is illuminated with the UV light and the image of the mask is projected on the final substrate with an adjustable lens. This projection mask is build from a thin metal sheet into which geometrical entities are drilled. These individual entities can be chosen for the ablation process.

The laser head, containing the projection lens, is movable in z-direction to focus the mask onto the sample, which is mandatory because material is only ablated efficiently within the focus plane of the projected mask. The focusing can be controlled by a camera which is calibrated to have a similar focus plane as the laser beam. As a matter of fact, if the camera image is in focus, so is the laser beam.

Before the pore drilling can be started the laser beam is focused manually. To do that a cross shaped mask is roughly focused on the surface of the glass substrate which is positioned on a movable x-y-stage. The laser is triggered for about 20 pulses thus locally ablating material in form of the cross mask. If the cross is not transferred sharply into the substrate, the z-position of the lens is adjusted accordingly until the contours of the cross are clearly visible ensuring a correct laser focus. Due to the design of the x-y-stage the substrate cannot be positioned perfectly perpendicular to the laser beam thus the pore is typically drilled only a couple of micrometers away from the cross shaped test structure. If the pore is drilled too far away from this point the tilt of the substrate can be big enough to compromise the adjusted focal plane.

The glass slide is mounted on a through hole inside the sample holder, which in turn is mounted on the x-y stage. An UV diode is positioned underneath the through hole

[1] High Precision Microscope Cover Glasses, Carl Roth GmbH
[2] MMflex by Optec Laser Systems

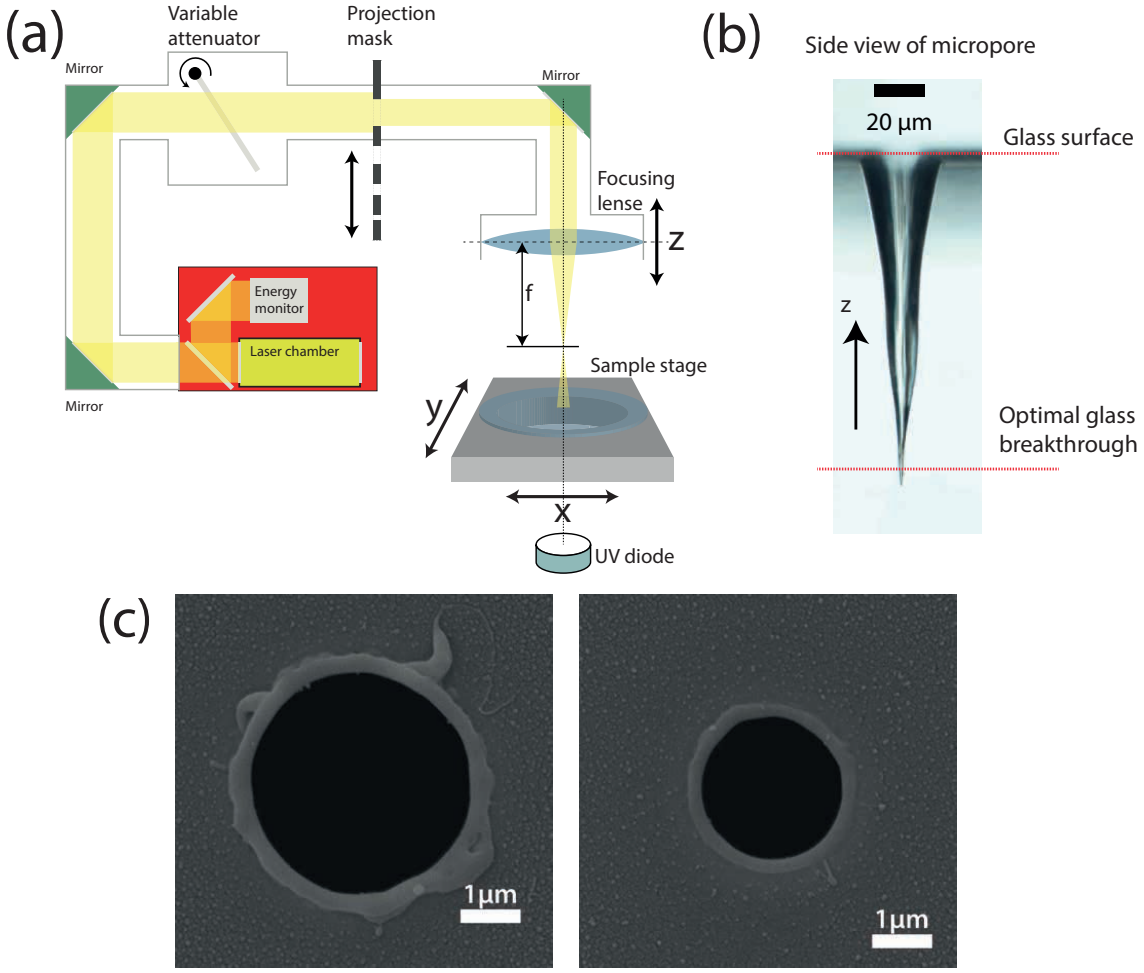

Figure 2.6: (a) Schematic of the pore production setup. It consists of an ArF-based excimer laser chamber producing pulsed UV light that is projected, through a projection mask, onto a sample placed on a moveable sample stage via a focusing lens. (b) Geometry of a micropore, observed from the side, when drilled with a 20 µm projection mask. (c) Two SEM pictures of micropores drilled (left) with a projection mask diameter of 20 µm and a laser energy of 11 mJ/pulse and (right) with a projection mask with 15 µm diameter and a laser energy of 11.5 mJ/pulse.

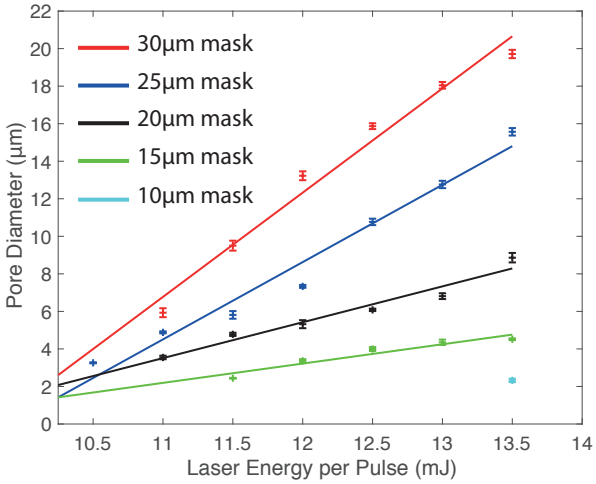

Figure 2.7: Diameters of the micropores versus laser energy and projection mask diameter. Every data point corresponds to 5 pores drilled with the same laser parameter and projection mask. The pore diameters are determined with SEM measurements. Pore drilling with the 10 µm mask was only possible at laser energies of 13.5 mJ/pulse (light blue), with the 15 µm mask at laser energies bigger than 11.5 mJ/pulse (green) and with the 20 µm mask at laser energies bigger than 11 mJ/pulse (black).

facing the laser beam. This diode is constantly measuring if UV light from the laser is reaching the diode via the sample material. In this position the laser ablation process can be started. Once the glass is completely etched through the UV light from the laser is detected and the ablation process is stopped immediately.

In Fig. 2.6 (b) the result of an ablation process with a circular mask having a nominal diameter of 20 µm, is shown. The projected beam is only focused on one side of the substrate. During the drilling process, as the material is ablated deeper within the material, the laser beam walks out of focus thus ablating less material the deeper it penetrates the substrate. As the intensity of the laser is still maximized in the middle of the beam the pore has a conical shape with a micron-sized opening at the side where the laser breaks through the glass. This small opening is in the following referred to as the MP.

Fig. 2.6 (c) shows SEM images of MPs that were produced in this manner. The left figure shows a pore that was drilled with a circular projection mask with a diameter of 20 µm and a laser energy of 11 mJ/pulse and the right figure shows a pore drilled with a projection mask with a 15 µm diameter and a laser energy of 11.5 mJ/pulse. Obviously, the smaller mask results in a smaller pore diameter.

To quantify the influence of the mask size and the laser energy on the resulting pore size, calibration tests were done. The results are shown in Fig. 2.7. For a set of circular projection masks with different nominal diameters, starting from 30 µm to 10 µm, and

different laser energies, starting from 10.5 mJ/pulse to 13.5 mJ/pulse, pores are produced in a microscope glass slide with a thickness of 170 µm. For every projection mask and laser energy a set of 5 identical pores are produced and the diameter of every resulting pore is measured with an SEM. The error bars correspond to the error of the mean value calculated from the measured diameters of the MPs.

A clear trend is visible for the energy dependence of the pore diameters. The data shows a linear correlation between the pore diameter and the laser energy. Furthermore, it is shown in Fig. 2.7 that bigger mask diameters lead to bigger pore diameters.

A couple of aspects shall be pointed out regarding the results shown in Fig. 2.7. For a projection mask with a diameter of 10 µm, MPs with a diameter of (2.43 ± 0.04) µm are produced only if the laser energy is at least set to 13.5 mJ/pulse. If the laser energy is decreased no pore can be produced as the tip of the resulting cone (see Fig. 2.6 (b)) is not penetrating the glass deep enough to produce a pore. The same effect is observed when using the 15 µm and 20 µm mask at energies lower than 11.5 mJ/pulse and 11 mJ/pulse, respectively.

For big masks and high laser energies, the resulting pores show extremely rough edges with sometimes big glass pieces, which are broken off from the surface. Additionally, these pores show an oval opening. In this case the biggest axis was measured and used for the evaluation of the data presented in Fig. 2.7.

In summary, the 30 µm mask did not produce clean and round pores regardless of the energy. For the 25 µm mask clean surfaces and round pores are produced at energies lower than 12.5 mJ/pulse, while the 20 µm mask produces oval pores for energies bigger than 13 mJ/pulse, but the surface of the pore is not damaged due to the ablation process. All other parameter sets produce round pores with an undamaged surface.

2.2.2 Electrical Characterization of Micropores

In this section the electrical properties of the MPs shall be discussed. All measurements discussed here are done with a 0.1 M KCl electrolyte solution. The measurements are conducted on the planar patch clamping system Port-a-Patch from the company Nanion. It comprises of a sample holder for screw caps on which the glass slides are glued. In Fig. 2.8 (a) the screw cap with the glass slide which embeds the MP is shown. The sample holder contains the signal electrode which is connected to the head stage of a patch clamp amplifier[3]. Additionally, it has a port that can be used to apply a pressure or a suction to the bottom of the MP chip. Electrical connection is closed through the body of Port-a-Patch via a ground electrode that is immersed into a electrolyte droplet that is pipetted on top of the chip.

[3]EPC 10 USB Single, Patch Clamp Amplifier, HEKA

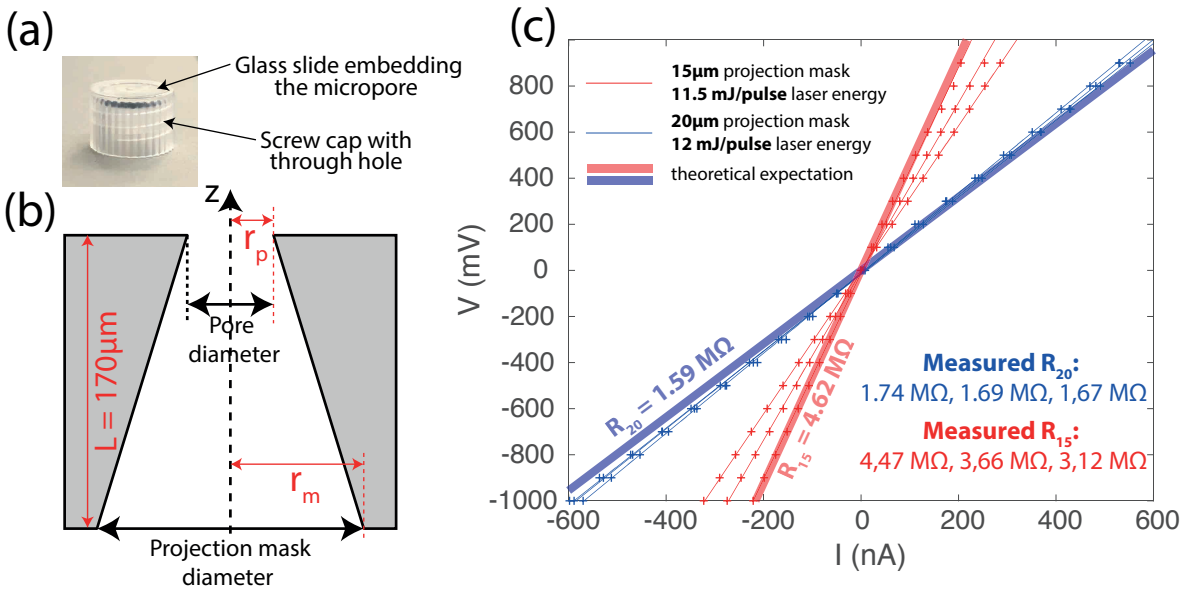

Figure 2.8: (a) Measurement glass chip glued to a screw cap. (b) Idealized pore geometry as a side view. (c) Resistance measurements of MPs. Pores are drilled with (red) a 15 µm projection mask at 11.5 mJ/pulse laser energy and (blue) a 20 µm projection mask at 12 mJ/pulse laser energy. Thick solid lines are the expected IV-curve for the MPs according to Eq. 2.18 and the findings shown in Fig. 2.7.

The amplifier allows to apply a bias voltage across the two electrodes and simultaneously measure the resulting current. It was discussed in Sec. 2.1.1 that the MP acts as an ohmic resistor in the presence of an applied voltage. Consequently, a linear IV characteristic is expected. In the present case the pore is conically shaped as can be seen schematically in Fig. 2.8 (b) which allows to estimate the resistance of the pore according to Eq. 2.1. The area $A(z)$ of the MP is z-dependent and given as

$$A(z) = \pi(r_\mathrm{m} - \frac{r_\mathrm{m} - r_\mathrm{p}}{L} z)^2 \tag{2.17}$$

with r_p and r_m being the radii of the MP and the pore produced by the laser due to the projection mask, respectively. Furthermore, L is the thickness of the glass slide (see Fig. 2.8 (b)). The integral in Eq. 2.1 can now be solved using Eq. 2.17 and the result is

$$R = \frac{\rho L}{\pi r_\mathrm{m} r_\mathrm{p}} \tag{2.18}$$

where ρ is the resistivity of the electrolyte solution.

In Fig. 2.8 (c) the resistance measurement for six MPs and the corresponding theoretical estimations derived from Eq. 2.18 are shown. Two parameter sets for the pore production were chosen to verify the hypothesis given by Eq. 2.18. The pores were pro-

duced with a circular projection mask with 15 µm and 20 µm in diameter and an output energy of the laser was set to 11.5 mJ/pulse and 12 mJ/pulse, respectively. To evaluate Eq. 2.18 the values for r_p from Fig. 2.8 were taken without measuring the actual opening diameters in the SEM prior to or after the resistance measurements. The thickness of the glass slide was set to $L = 170\,\mu m$ and the resistivity of the 0.1 M KCl solution was assumed to be $\rho = 0.781\,\Omega m$ according to Ref. [24]. Consequently, this results in expected resistances of $R_{15} = 4.62\,M\Omega$ and $R_{20} = 1.59\,M\Omega$ for the pores drilled with the 15 µm and 20 µm projection mask, respectively. Both expected IV curves are shown as thick solid lines in Fig. 2.8 (c).

For the measurement, the MPs are filled with 0.1 M KCl solution and the measurements are conducted by consecutively applying a constant voltage across the drilled MPs between −1 V to 900 mV. Simultaneously, the current, which is flowing through the pore is measured and plotted against the applied voltage. The results are shown in Fig. 2.8 (c). As expected a linear correlation for every MP is observed indicating their ohmic behavior.

A linear fit on the data is used to derive the resistance of the MPs. For the three pores drilled with the 20 µm projection masks resistance values of 1.74 MΩ, 1.67 MΩ and 1.69 MΩ are obtained. These values are in good agreement with the theoretical expectation keeping in mind that Eq. 2.18 is giving an lower limit estimation on the resistance. Furthermore, it shall be pointed out that a good reproducibility is achieved for theses pores as the measured resistance values vary by 4% for the three pores tested and the biggest deviation between the measured and expected value is 9%.

For the pores drilled with the 15 µm projection mask the measured resistance is lower than expected. The measured values for the three pores are 4.47 MΩ, 3.66 MΩ and 3.12 MΩ and thus show a variation of 30% from the highest measured resistance to the lowest measured resistance. Apart from one pore, the measured values tend to show lower values than theoretically expected ($R_{15} = 4.62\,M\Omega$) by up to 33%. The reason for that is the uncertainty of the resulting pore radius when drilling the pore with these parameters. It was already shown in Fig. 2.7 that for the 15 µm projection mask and a laser energy of 11.5 mJ/pulse a pore is drilled only if the focus of the laser beam is adjusted carefully. For lower energies no pore can be produced because the ablation process is not deep enough to penetrate the material. The focus of the laser beam has to be adjusted carefully because if the beam is focused slightly above the glass surface no pore can be formed. If the beam is focused slightly inside the glass surface the resulting pore will be bigger than expected. Obviously, the method has its limitation when trying to produce pores with this mask or even smaller masks within the substrate.

In this sense the error bars given in Fig. 2.7 tend to underestimate the uncertainties because they are derived from an average pore diameter for a set of pores drilled adjacent

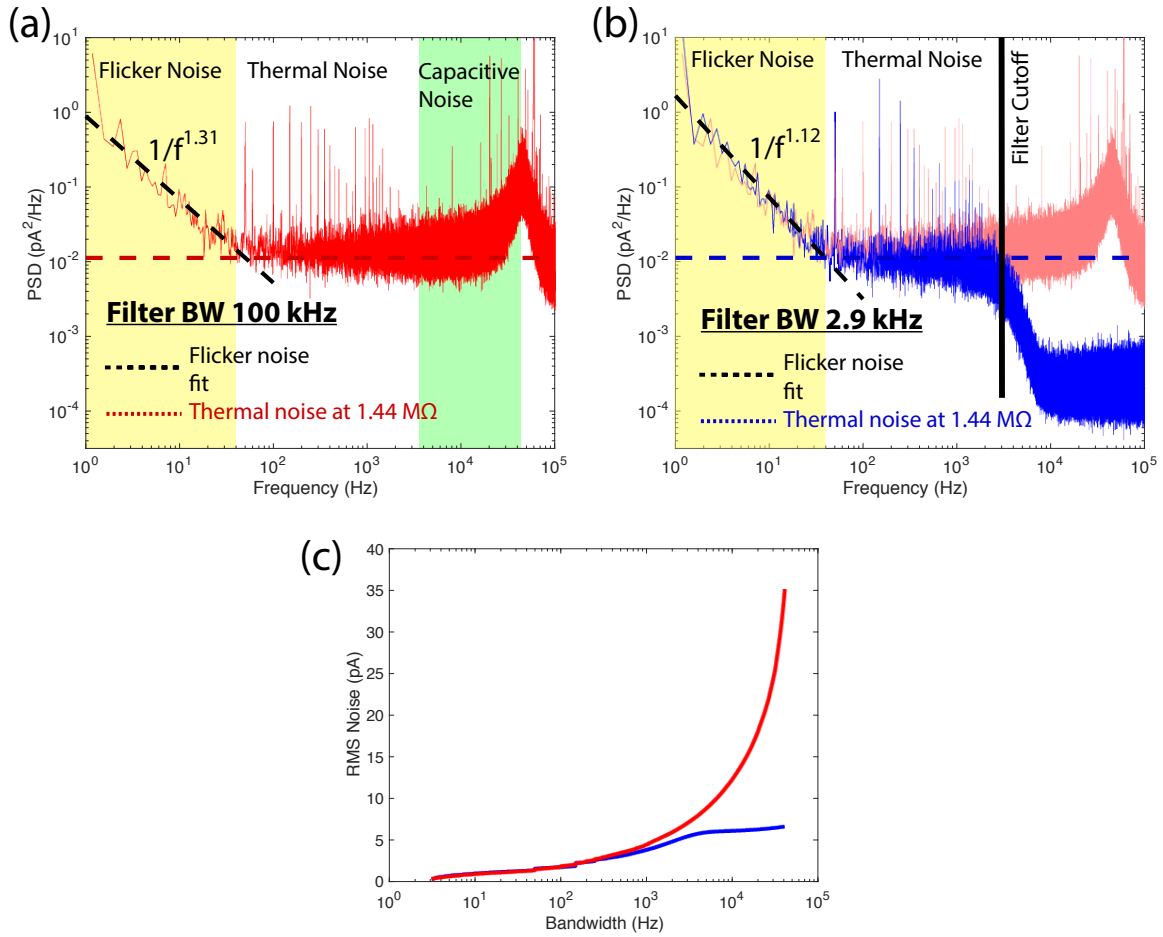

Figure 2.9: PSD of a micropore with a resistance of 1.44 MΩ at a bias voltage of 100 mV. (a) A 100 kHz and a (b) 2.9 kHz lowpass filter is applied during the experiment. (c) RMS noise floor derived from the PSD spectra given in (a) and (b).

to each other with the same focus setting for all pores. The pores shown in Fig. 2.8 (c) are drilled independently so the focus is set manually for every individual pore.

This method shows a high degree of reproducibility for the 20 µm mask but its prediction on pore size is limited for the smaller pore diameters. Nevertheless, the overall expectations regarding the resistance values are fulfilled. It is save to say that MPs with diameters as small as (2.44 ± 0.02) µm can be produced. The only limiting factor in the accuracy of the actual pore diameter is the manual focus of the laser.

2.2.3 Noise Characteristic of Micropores

Electronic noise in micro- and nanopore experiments is a crucial feature in RPS experiments as it governs the signal to noise ratio of the acquired signals. Additionally, it ultimately limits the temporal resolution of these setups as will be discussed here.

The noise spectrum of a time domain signal can be described by a power spectral density (PSD). It gives an estimation on the noise amplitude with respect to the frequency. A typical PSD noise measurement of a MP is shown in Fig. 2.9 (a) and (b). The pore that was used for the measurement had a resistance of 1.44 MΩ which was measured in 0.1 M KCl electrolyte solution at a bias voltage of 100 mV. To determine the PSD the time domain current, sampled by the amplifier, is acquired at a sample rate of 400 kHz with an external data acquisition system for 1 s. A fast Fourier transform (FFT) is used to determine the PSD numerically by a custom processing software. Finally, each PSD is averaged 20 times with consecutive time domain measurements. For the experiments two amplifier filter settings can be processed simultaneously, with the patch clamp amplifier at hand.

In Fig. 2.9 (a) the PSD that is acquired with the highest low pass filter (LPF) which is available for the used amplifier (i.e. 100 kHz) is shown [61]. Different regimes in the frequency spectrum are apparent which contribute to the overall noise in the system.

Low Frequency Regime

In the low frequency regime the so called flicker- or $1/f$ noise dominates the PSD. In the measurement that is presented in Fig. 2.9 (a) it has a significant contribution between DC and 40 Hz. The origin of flicker noise is still a matter of debate but in general it can be modeled as

$$S_n(f) = \frac{\alpha I^2}{N_\mathrm{c} f^\kappa} \tag{2.19}$$

where S is the PSD in units of A^2/Hz, I is the measured current, N_c is the number of charge carriers in the sensing volume, α is the so called Hooge parameter and f is the frequency [62, 63]. The parameter κ can be determined from a fit to the PSD as is shown in Fig. 2.9 (a). For the low frequency regime with frequencies up to 40 Hz an exponent of $\kappa = 1.31$ is determined.

Intermediate Frequency Regime

For increasing frequencies, the flicker noise becomes less dominant until the PSD becomes independent from the frequency which is a characteristic of thermal noise. It can be analytically quantised as

$$S_n(f) = \frac{4k_\mathrm{B}T}{R} \tag{2.20}$$

where k_B is the Boltzmann constant, T is the absolute temperature and R is the resistance over which the noise is generated [64]. For the experiment the horizontal dashed line

indicates the expected thermal noise at room temperature over a resistance of 1.44 MΩ. The line is not fitted but rather illustrates the value that is derived from Eq. 2.20.

These two noise contribution (Eq. 2.19 and Eq. 2.20) cannot be decreased to a high extend. As the flicker noise is inversely proportional to the number of charge carriers in the sensing volume, increasing the molarity of the electrolyte decreases this noise source as was shown in literature [62]. The thermal noise is a function of the resistance, which is governed by the pore dimensions. Since most RPS experiments are conducted at room temperature the temperature cannot be dramatically changed, either.

High Frequency Regime

For higher frequencies, the noise increases primarily due to dielectric noise [64, 65] modeled as

$$S_n(f) = 8\pi k_\mathrm{B} T D C f. \tag{2.21}$$

where D is the dielectric loss factor (also known as dielectric loss tangent) and C is the capacitance of all dielectric materials contributing to the dielectric noise [64]. In the present case the dielectric material is primarily the glass substrate. Energy is absorbed by the material and is dissipated in the lossy dielectric material [66].

Finally, capacitive noise is dominant at even high frequencies. The PSD for this contribution is given as

$$S_n(f) = 4\pi^2 C_\mathrm{i}^2 S_\mathrm{V} f^2 \tag{2.22}$$

where C_i is the collective capacity and S_V is the voltage noise density of the input of the measurement amplifier [67]. The presence of capacitive noise has a plethora of origins. Parasitic capacitances from the wiring as well as input capacitances at the amplifier contribute to the total capacity C_i and thus to the noise characteristic of the measurement. Additionally, the glass substrate itself forms a capacitor because it is locally immersed in electrolyte solution. It shall be pointed out that the pores are drilled directly into the substrate without pre-thinning the material. This is advantageous for the expected noise characteristic. If the glass were locally thinned this would negatively influence the capacitive noise because the capacitance of the system is inversely proportional to the thickness of the dielectric substrate.

In the spectrum shown in Fig. 2.9 (a) there is a drop in PSD for even higher frequencies. This is due to the bandwidth limitations of the amplifier. Noise contributions of the current signals with frequencies higher than 100 kHz are strongly attenuated.

Derived Values from the PSD

The PSD can be used to give an estimation of the root-mean-square (RMS) noise of the measured current $I_{\mathrm{RMS}}(B)$. It can be derived from the PSD as

$$I_{\mathrm{RMS}}(B) = \sqrt{\int_{f_{\min}}^{B} S_n(f)df} \tag{2.23}$$

where B is the measurement bandwidth (BW).

It is apparent that the maximal BW of a measurement is limited as with increasing BW the RMS noise increases. A typical strategy to get a meaningful signal-to-noise-ratio during signal acquisition is the use of a lowpass filter which eliminates the contribution of high frequency noise. To illustrate that, in Fig. 2.9 (b) the same measurement is shown with a low pass filter having a cutoff frequency of 2.9 kHz which is a typical value for the RPS experiments presented in the scope of this thesis. Due to the presence of the filter the noise is highly attenuated at frequencies higher than the cutoff value of the filter.

In Fig 2.9 (c) the expected RMS current $I_{\mathrm{RMS}}(B)$ according to Eq. 2.23 is evaluated versus the measurement BW. The red curve gives the expected $I_{\mathrm{RMS}}(B)$ for the unfiltered signal. Obviously, the RMS amplitude is increasing drastically as the BW is getting bigger than 2.9 kHz. If the signal is filtered at 2.9 kHz as shown in Fig 2.9 (b) the high frequency noise is filtered out and consequently the expected $I_{\mathrm{RMS}}(B)$ is reduced at BWs bigger than the cutoff value of the low pass filter.

For a RPS experiment a typical definition of the signal-to-noise ratio (SNR) can be given as

$$\mathrm{SNR}(B) = \frac{\Delta I}{I_{\mathrm{RMS}}(B)} \tag{2.24}$$

with ΔI being the amplitude of the resistive pulse. The amplitude is a function of the pore geometry and the particle geometry as described in Sec. 2.1.1 and thus it cannot be changed. For small values of ΔI a reduction in BW increases the SNR. However, this happens at the expense of measurement BW and thus at the expense of temporal resolution of the measurement.

2.3 Time Domain Measurement of Particle Size and Concentration

In this section time domain RPS measurements with MPs are discussed. The section starts with a FEM simulation which was used to simulate the electronic response of translocating particles through a MP. After that, experimental data is presented show-

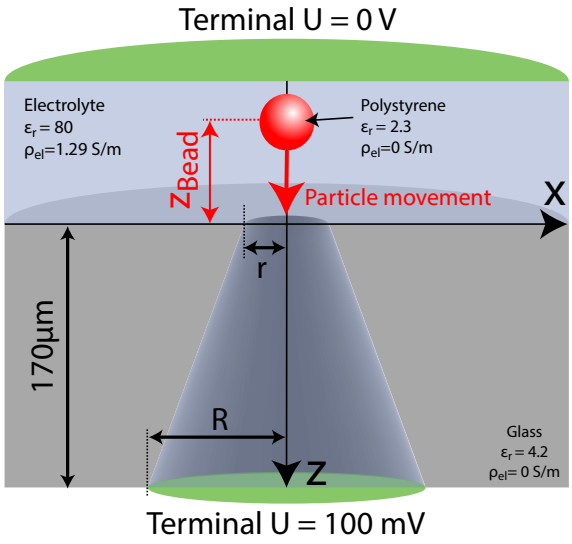

Figure 2.10: Schematic of the simulation geometry used to model the micropore measurements. The pore is conically shaped and at the bottom of the micropore one terminal is located that is used to evaluate the current that is flowing through the pore when a voltage is applied. A second terminal is located at the upper surface of the simulation volume. The material parameters used in the simulation are given in the figure.

ing how RPS experiments can be used to determine the sizes of particles suspended in electrolyte solution.

2.3.1 Simulation of Particle Translocation Through Micropores

Here, a numerical study is given to illustrate the RPS method theoretically. The simulations are carried out using the commercially available FEM software package COMSOL. This software package allows to model the measurement geometry (i.e. the MP) and apply different physics engines to simulate the physical effects in question. For the simulation the model is divided in a finite amount of elements, which are called mesh cells. The underlining differential equations governing the physics are solved on the mesh points thus allowing to give a numerical approximation on the behavior of the system for a given geometry.

A schematic of the simulation geometry is given in Fig. 2.10. It consists of a conical MP within a glass substrate filled with a conducting liquid. The pore is modeled with a narrow diameter of $2r = 2.6\,\mu\text{m}$ on top, an opening diameter of $2R = 25\,\mu\text{m}$ at the bottom and a length of the pore of $170\,\mu\text{m}$. Furthermore, a solid sphere is introduced to mimic a polystyrene bead. Its radius and position will be varied in the simulation to study the influence of both parameters on the expected RPS signal. The mesh of the

model is shown in Fig. 3.14 (b) and (c) in the next part because the model illustrated in Fig. 2.10 is part of a bigger model that is also used for AC simulations that are described in the second part of the thesis.

The model is simulated using the AC/DC physics with the "Electrical Currents" interface, which needs information about the electrical conductivity ρ as well as the electrical permittivity ϵ_r and the relative permeability μ_r of all geometrical domains in the model. The permeability of the materials, in absence of any magnetic field, does not contribute to the result and can be set to $\mu_\mathrm{r} = 1$. The glass and the polystyrene were assumed to behave as an insulator with permittivities of $\epsilon_{\mathrm{r,Glass}} = 4.2$ and $\epsilon_{\mathrm{r,Poly}} = 2.3$, respectively. To mimic the experimental conditions (i.e. 0.1 M KCl) a conductivity for the liquid of 1.29 S/m and a permittivity of $\epsilon_{\mathrm{r,liquid}} = 80$ was assumed.

Two terminal boundary conditions are used to allow to apply a potential difference across the pore. One terminal is set at the bigger radius of the pore and the other terminal is put at the top of the upper fluidic chamber (see Fig. 2.10). A potential difference of 0.1 V is applied between these two terminals. During the post processing of the simulation the current flow is globally evaluated via these terminals.

To simplify the simulation procedure the dynamic of the particle due to an applied pressure gradient is not considered here. The polystyrene sphere is moved through the pore using a parametric sweep along the pore axis giving an impression on the resistive pulse response.

In the simulation the polystyrene particle is translocated through the pore in positive z-direction (see Fig. 2.10). For every position and radius of the particle the model is evaluated numerically and the resulting current is calculated from one of the terminals.

The DC response that is simulated for the translocation of beads with diameter 2 µm, 1.6 µm, 1.2 µm and 0.8 µm is shown in Fig. 2.11. In general it is shown that beads with bigger diameters lead to higher blockage currents as expected from the theoretical discussion shown in Fig. 2.2 (a). The open pore current is altered rapidly when the bead approaches the opening of the pore. When the bead is located inside the pore completely, the blockage current is maximimal. To illustrate this effect a sphere is drawn into Fig. 2.11 at the position of minimal current. This sphere is an in-scale representation of the simulated bead and for every bead diameter the minimal current corresponds to the position where the bead is completely inside the pore. As the bead is moving further inside the pore the blockage current is decreased as the simulated pore is conically shaped. Thus by moving further inside of the pore, as the distance between the pore walls and the bead surface increases, the blockage of the ion current due to the bead decreases accordingly. The smallest bead does only show a very tiny signal. Furthermore, this signal shows numerical noise and thus the position of the peak cannot be resolved here.

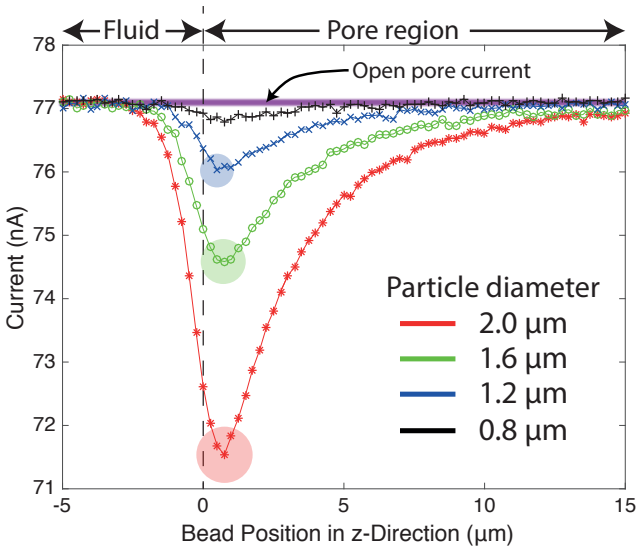

Figure 2.11: Simulated blockage current of translocating polystyrene beads through a micropore. The diameter of the beads is changed from 2 µm to 0.8 µm. The pore opening is located at $z = 0$, the small pore diameter is 2.6 µm and the big pore diameter is 25 µm. Colored spheres give an in-scale representation of the position of the bead inside the pore when the blockade current is maximal.

In the simulation volume the thickness of the glass substrate is assumed to be 170 µm. As can be seen in Fig. 2.11 even for the biggest bead diameter the open pore current is almost reached when the particle is translocating 15 µm into the pore. Beyond this position the presence of the particle is not showing a significant current blockage.

This simulation gives a good impression on the shape of the resistive pulse as will be confirmed by the experimental data in the following. The simulation shows when the resistive pulse reaches its highest amplitude (i.e. when the particle is fully inside the pore) and it shows that the resistance change due to the presence of the particle is only produced by the first 15 µm of the depth of the MP.

2.3.2 Time Domain Measurements

As a next step it shall be tested if a real glass chip with a MP of that kind is a suitable RPS sensor. For this purpose polystyrene beads with defined diameter are translocated through such MPs. Furthermore, it will be discussed how the resistive pulse signals are used to determine the size distributions of the beads.

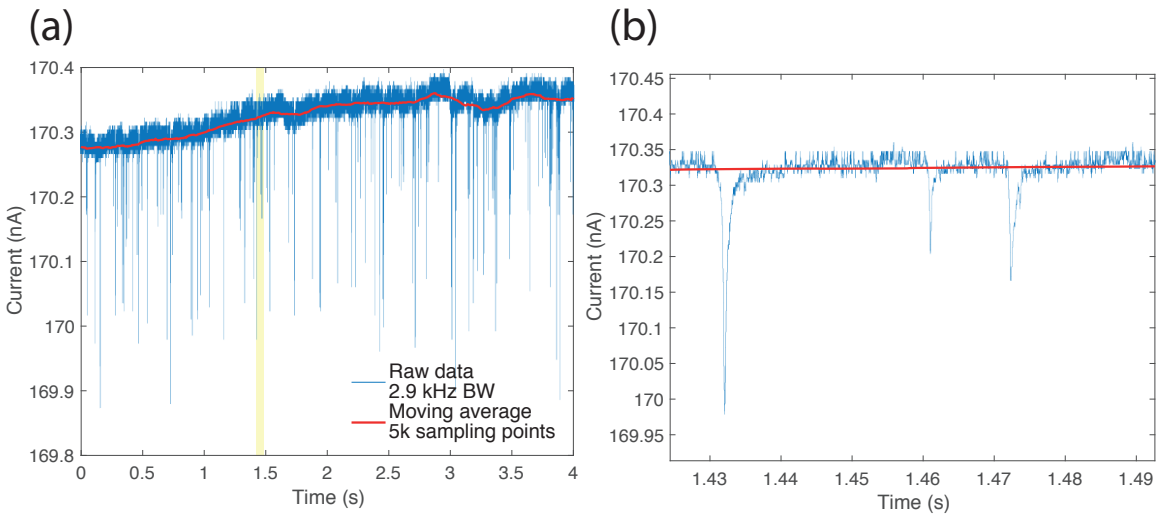

Figure 2.12: (a) Raw DC data acquired with a 5 MΩ micropore and a polydispersed sample of polystyrene beads having diameter of 200 nm and 300 nm, respectively. The open pore current is determined by a moving average shown as a solid red line. (b) The zoomed-in view of the region marked in yellow in (a) which shows three events and the corresponding background estimation.

Measurements

The experiments are carried out with a polydispersed particle sample containing a mix of polystyrene beads with diameter of 200 nm[4] and 300 nm[5]. Additionally, a suspension containing only 200 nm beads is tested. The beads come with a relative size uncertainty of ±2% and for the measurement the beads are transferred into 0.1 M KCl buffer as the electrolyte.

The MP used for the experiments are commercially available NPC-1 chips from the company Nanion. These pores are embedded in borosilicate glass and are conically shaped similar to the pores presented previously but they have a much smaller MP and consequently a very low electrical resistance. The pore diameter is given by the supplier as 1 µm [68] and at a bias voltage of 1 V with the 0.1 M KCl buffer the chips show a resistance of 5.8 MΩ. This is advantageous for the measurement as it allows to test the translocation of beads with diameters down to 200 nm and potentially lower. Polystyrene beads in the micrometer range tend to sediment quickly within the electrolyte due to gravity [69]. The smallest pore diameter that can be produced by laser ablation, as described in Sec. 2.2, has a diameter of 2.44 µm thus it is capable of measuring particles in the micrometer range. In a suspension where the particles sediment quickly the MP is likely to clog rapidly thus

[4]Polybead Polystyrene Yellow Dyed Microspheres 0.20 µm, Polysciences Europe GmbH
[5]Polybead Carboxylate Red Dyed Microspheres 0.30 µm, Polysciences Europe GmbH

preventing to acquire a reasonable statistic. In commercial RPS instruments this problem is sometimes solved by stirring the particle suspension during the experiment but this is not implemented in the setup at hand. As a result it was decided to present the working principle with the NPC-1 chips while the bigger pores that are produced with the method presented in Sec. 2.2 will be used extensively in the following chapter.

An exemplary time trace showing the translocation of pressure-driven polydispersed beads with a 1 V bias voltage is given in Fig. 2.12 (a). Every individual peak in the data is caused by the translocation of an individual particle and even without further analysis it can be seen, that two peak amplitude plateaus are observed. Bigger amplitudes are caused by translocating beads with 300 nm diameter and small amplitudes are caused by the 200 nm beads. The particle suspension is pipetted onto the side of the chip where the MP is located. Particles are attracted by an applied suction and thus translocate as illustrated in Fig. 2.10. A zoomed-in view into the yellow region shown in Fig. 2.12 (a) is given in Fig. 2.12 (b) and it shows a very similar peak structure as obtained from the FEM simulation shown in Fig. 2.11 with a very rapid decrease of the blockage current when the beads approach the MP, a minimal blockage current when they are completely inside the pore and a slower return to the baseline current due to the conical shape of the pore.

Data Analysis

To analyze the raw data, first the background current (i.e. the open pore current) has to be approximated because it slowly varies with time. This is mainly caused by the applied pressure as it can be observed that the open pore current changes when the pressure across the MP is varied. Using a moving average (solid red line in Fig. 2.12) allows to estimate the baseline current. The moving average samples the time domain data over a window containing 5 k samples. As can be seen in the zoomed-in view into the data in Fig. 2.12 (b) this gives a good approximation even at the presence of the resistive pulse signals. If the number of samples in the moving average is chosen too small the moving average is following the resistive pulse signal thus compromising the amplitude determination.

In a second step of the analysis the estimated background is subtracted from the raw data thus giving a time trace centered around zero without the drift. The result of this operation can be seen in Fig. 2.13 (a). To find the individual resistive pulses a moving standard deviation of the subtracted data set is calculated with a window containing 5 k samples and the $1 \times \sigma$ and $2 \times \sigma$ regions are displayed as green and yellow bands in the figure. A simple peak finding algorithm can now be used to identify individual peaks (see red triangles in Fig. 2.13 (a)). Peaks are accepted by the algorithm if they exceed

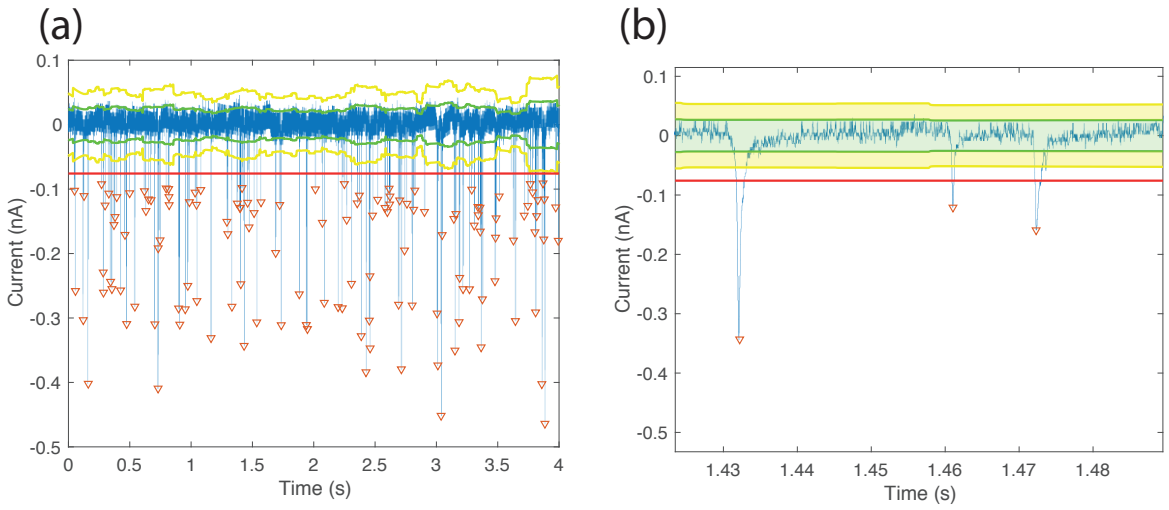

Figure 2.13: Processing of measured RPS experiments shown in Fig. 2.12. (a) The moving average is subtracted from the raw data thus obtaining a resistive pulse trace centered around zero. In green the $1 \times \sigma$ moving standard deviation is shown and correspondingly in yellow the $2 \times \sigma$ moving standard deviation. The red line indicates the averaged $3 \times \sigma$ moving standard deviation that is used as a threshold for the peak finding procedure. Identified peaks are marked with an orange triangle. (b) The zoomed-in view shows the same time trace as shown in Fig. 2.12 (b), after peak identification

an amplitude bigger than $3 \times \sigma$ of a moving standard deviation and the resulting peak amplitude is interpreted as the amplitude of the resistive pulse caused by a translocating particles. The $3 \times \sigma$ threshold is calculated as the average of the moving $3 \times \sigma$ region within data sweeps of 4 s length and thus this threshold is flat over these specific ranges, as shown exemplary as the solid red line in Fig. 2.13 (a).

A particle which is translocating the MP is inducing a resistive pulse. If a second particle is entering the pore before the first particle has left the sensing region one resistive pulse is influenced by both particles, simultaneously. These events are removed from the data set and are not further processed as their occurrence is rare. To filter these events out not only has the resistive pulses to exceed the threshold value but the peaks also have to have certain peak prominence. The peak prominence is a measure on how big the amplitude of a peak is with respect to adjacent peaks. If the peaks are well isolated like shown in Fig. 2.13 (b), the peak prominence is similar to the amplitude. If a second resistive pulse is superimposing a signal this decreases the prominence of the first peak while the overall amplitude is typically unchanged.

The identified and filtered peak amplitudes are stored in a separate file. Additionally, a time domain data in a fixed window around the position of the identified peak is stored in the same file so that each resistive pulse event can be further analyzed to determine

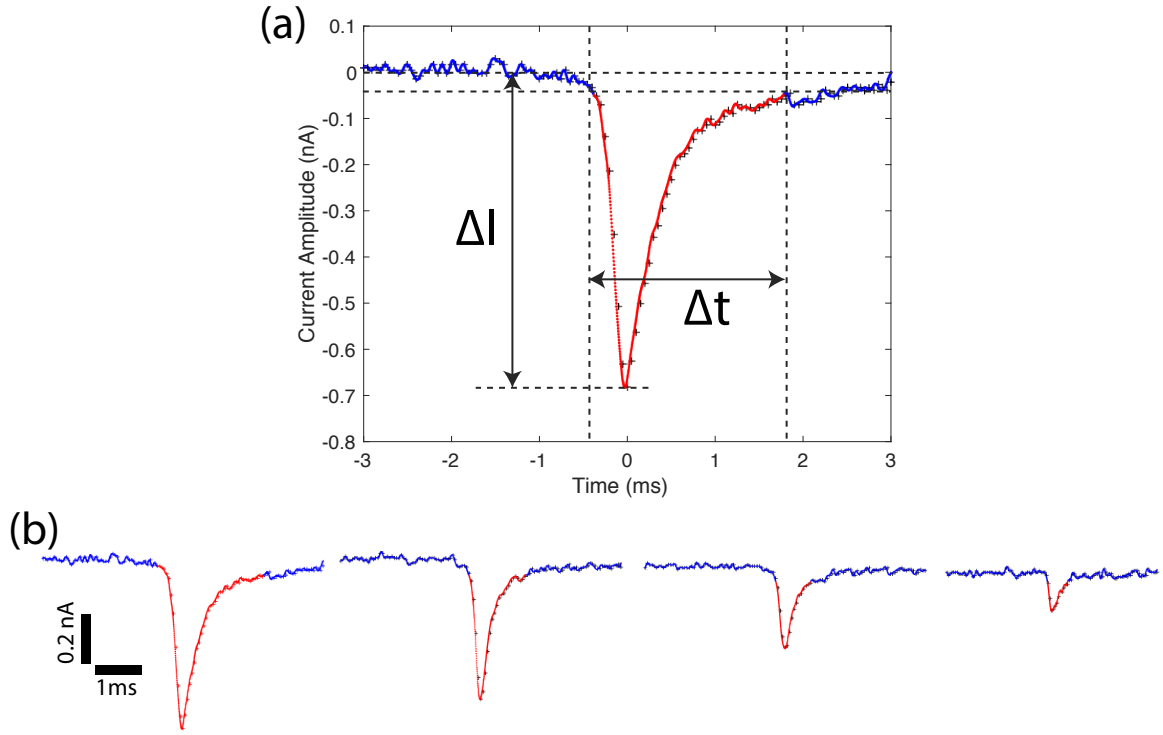

Figure 2.14: (a) Determining the peak width of single translocation events by thresholding. In blue the background current around the event is shown while in red, the region that is recognized as the event is shown. (b) Event width determination for a variety of events with different peak amplitudes.

the translocation time, here referred to as the width of the events.

Identifying the event width is done in the following way. Again a threshold algorithm is applied to the individual peak data sets. The result can be seen in Fig. 2.14 (a). Every event is divided into two parts with $t < 0$ and $t > 0$ while $t = 0$ is the time point where the highest peak amplitude is located. The beginning of the event is defined as the point where the data drops below a threshold of 0.05 nA for the first time for times $t < 0$. Accordingly, the event ends when the current drops rises above 0.05 nA for $t > 0$. The difference of the two times is defined as the duration of the event. To illustrate the functionality of the procedure the events are colored in red while the background is colored in blue in Fig. 2.14 (a). In Fig. 2.14 (b) the corresponding results for high amplitude and low amplitude events is depicted, showing that this method gives acceptable results over all peak amplitudes.

Occasionally, multiple peaks are stored within one event window which generally distorts the measurement of the event width. Those events are identified and withdrawn from further analysis because these events are rare and discarding them does not compromise the statistic of the measurement.

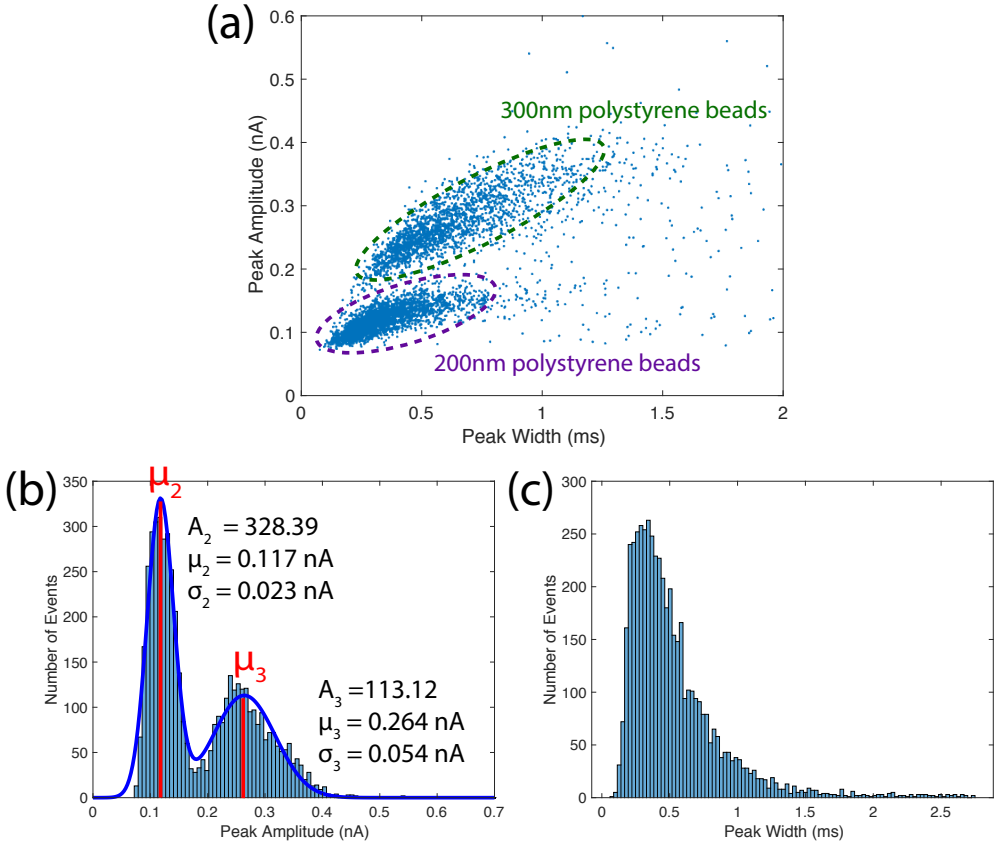

Figure 2.15: (a) Processed, two dimensional representation of the data acquired with a conical glass micropore and a polydispersed suspension of polystyrene beads containing beads with diameter of 200 nm and 300 nm. (b) Histogram of the amplitudes of the resistive pulses clearly showing two populations corresponding to the small an big polystyrene beads. The histogram is fitted with a sum of two gauss functions and the best fit parameter are given adjacent to the peaks. (c) Histogram of the overall peak width.

2.3.3 Discussion of the DC Results

It is most elucidating to show a two dimensional representation of the RPS data, containing the peak amplitude ΔI and peak width Δt. The result for the polydispersed sample containing 200 nm and 300 nm polystyrene beads is shown in Fig. 2.15 (a). It is obvious that two clouds of data points are visible, originating from the two particle sizes. As stated previously, bigger particles lead to higher resistive pulse signals. Furthermore, bigger particles tend to translocate slower through the pore. Both claims are experimentally supported here. According to Eq. 2.8 the resistive pulse amplitude is proportional to the third power of the particle diameter thus a discrimination between particle sizes is expected.

The data shows a positive correlation between resistive pulse amplitude and the width

of the resistive pulse for each particle population. This effect can be explained by particles which do not translocate through the central axis of the pore. It was explained in Sec. 2.1.2 that in the case of a pressure-driven flow, as used here, the velocity of the liquid is slower near the pore walls. As a matter of fact particles translocating at trajectories near the wall will experience a lower drag force due to the reduced liquid velocity. This effect was theoretically described in Eq. 2.12. At the same time it was stated that according to Eq. 2.13 the resistive pulse amplitude is increased for particles translocating beyond the axis. Both effects combined lead to a positive correlation between these two measurement parameters.

In Fig. 2.15 (b) and (c) the projection histograms for the peak amplitude and peak width are shown. The different particle diameter separate well in ΔI. A fit is done on the histogram of the event amplitude to determine the mean amplitudes for the two bead sizes. The fit is the sum of two gaussian function given as

$$f_{\text{fit}}(\Delta I) = A_2 \exp\left(-\frac{(\Delta I - \mu_2)^2}{2\sigma_2^2}\right) + A_3 \exp\left(-\frac{(\Delta I - \mu_3)^2}{2\sigma_3^2}\right) \tag{2.25}$$

where μ_2 and μ_3 is the mean resistive pulse amplitude caused by the 200 nm and 300 nm particles, respectively. Accordingly, σ_2^2 and σ_3^2 are the variances of the distributions and A_2 and A_3 are the corresponding amplitudes. A nonlinear least squares fit procedure is used to determine the parameters in Eq. 2.25. The result as well as the best fit parameters of the fit are shown in Fig 2.15 (b). Eq. 2.25 does fit the distribution satisfactory. The mean amplitude of the two bead sizes differ as $\mu_3/\mu_2 = 2.24$ and the width of the distribution caused by the 300 nm beads is bigger.

In Fig. 2.16 the result from experiments are shown with the same MP but in this case only beads with 200 nm in diameter are translocated through the pore. Red dots in Fig. 2.16 (a) are determined from the amplitude and the width of the individual resistive pulses. As a comparison the results from the previous experiments shown in Fig. 2.15 (a) are displayed as transparent blue dots in the figure, too. A good correlation between the two measurements can be observed. The properties of the correlation between the signal amplitude and the signal width is observed for the mono-dispersed sample, too.

In Fig. 2.16 (b) and (c) the histograms corresponding to the projection of the two measurement quantities are given. As expected in the histogram containing the peak amplitudes only one peak is visible for this experiment. As it was done previously, this distribution was fitted but this time with a gaussian function having only one term, namely the first term in Eq. 2.25. The fit as well as the best fit parameters are given in Fig. 2.16 (b).

As the measurement is done with only one bead diameter the histogram containing the peak width can be used to determine the mean translocation time for the small particles.

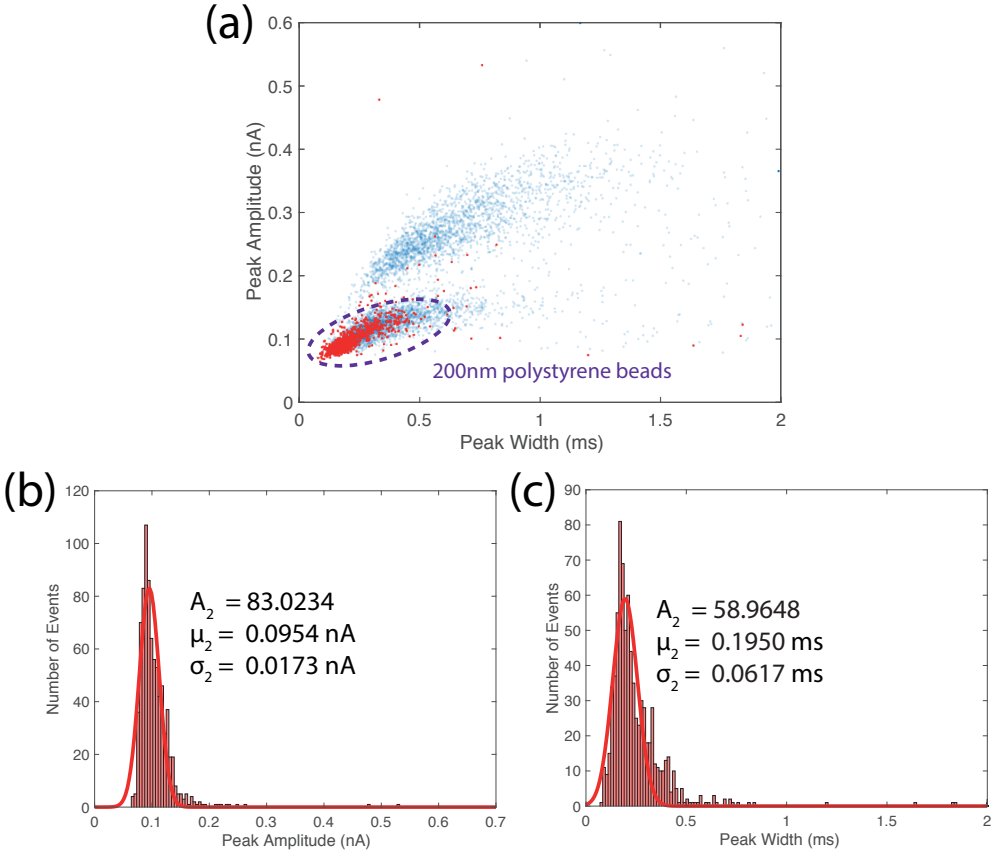

Figure 2.16: (a) Processed data acquired with the same glass micropore as used in Fig. 2.15 and a monodisperse suspension of polystyrene beads containing beads with a diameter of 200 nm. The results from Fig. 2.15 (a) are plotted as transparent blue dots in the scatter plot. (b) Histogram of the amplitudes of the resistive pulses clearly showing one populations. The histogram is fitted with a Gauss functions and the best fit parameter are given adjacent to the peak. (c) Histogram of the overall peak width of the sample. A single Gauss fit is giving the mean translocation time of the beads.

To do that a similar gaussian fit is applied to the data shown in Fig. 2.16 (c). This results in a mean translocation time of 0.1950 ms. The distribution shows an excess of data for translocation times bigger than the mean translocation time. This effect can be easily attributed to the correlation between the signal amplitude and signal width. A similar effect is visible in the peak amplitude fit. Nevertheless, the fit give an acceptable estimation on the mean amplitude and mean event width.

2.4 Limitations of the RPS Method

To this date RPS became more famous than ever [14, 70]. The method is attractive since it allows for a precise analysis of size distribution and concentration of polydispersed particles as was discussed previously. Still the method has some drawbacks that shall be discussed here.

As demonstrated experimentally and theoretically (see Eq. 2.7) the amplitude of the signal is proportional to the particle volume and inversely proportional to the sensing volume and thus to the pore diameter. Therefore, by using a pore with a fixed opening diameter, a high measurement sensitivity can only be expected in a certain particle size range. The particles that are investigated cannot be larger than the pore and they even have to be substantially smaller to prevent clogging of the device. Additionally, the signal amplitude is decreased drastically when the particles become small compared to the pore. Some companies, selling Coulter Counters, claim that they can measure particle sizes with diameter of 2 % of the pore diameter [37]. In our experiments this is not achieved. A clear signal is achieved at 20 % particle size with respect to the pore radius. Probably slightly smaller particles can be measured with the setup at hand but the sensitivity is a function not only on the pore and particle geometry but the molarity of the electrolyte and the bias voltage play an important role, too. Studying all these effects which are limiting the sensitivity of the RPS setup is beyond the scope of this thesis.

Another drawback of the method is caused by the measurement electronics and the membrane material in which the pore is embedded. As shown in Fig. 2.5 the electrical measurement is conducted by an operational amplifier with a high feedback resistor that allows for the measurement of small currents in the nA to pA regime. To interface the electronic with the amplifier, wires are inevitably. The longer these wires are the higher the parasitic capacitance. Another source of parasitic capacitance is the input capacity of the amplifier and the capacitance of the feedback resistors. Additionally, the capacity of the membrane becomes increasingly dominant for thin membranes as used for e.g. nanopore experiments. The sum of all parasitic capacitances become a problem as they pick up high frequency noise thus substantially limiting the sensitivity and dynamic range

of these devices [62, 63, 71].

For particles in the micrometer range with sub-millisecond translocation times high frequency noise is not the biggest limitation because a low pass filter can be used to attenuate high frequency noise effectively. However, if the dynamic of the translocation event takes place at much smaller timescales, a measurement bandwidth of 2.9 kHz is not acceptable. This problem is known for a long time as it prevents the use of the method in nanoscopic applications as e.g. for DNA sequencing with synthetic or biological nanopores. In these experiments, strands of DNA translocate through a nanopore due to electrophoresis and the resistive pulse is measured. Early experiments pioneering this field showed that different individual bases on the DNA strand lead to different blockage currents thus the modulation of the current trace over time should reveal the sequence of the strand [72].

In a typical solid-state nanopore the DNA can flow with a velocity of $10 - 1000\,\mathrm{nt/ns}$ [4, 37]. This high translocation time sets a necessity of providing a measurement BW orders of magnitude higher than conventional RPS methods can achieve. It was shown that by reducing the capacitive contributions to the overall setup it is possible to get a measurement BW of up to 10 MHz [67, 73]. This allowed to measure DNA translocations through their solid-state nanopore with µs temporal resolution. To achieve this a high degree of integration of the amplifier is mandatory. Although these amplifiers are capable of delivering the highest known DC measurement BWs, the BWs are still at least three orders of magnitude too small to measure single DNA bases at their natural translocation time when they translocate through nanopores.

Another drawback of the RPS method is its limitation to DC measurements. It fundamentally limits the application to measurements of particle size and concentration. Some experiments were presented demonstrating the possibility of determining the particles surface charge and ζ-potential by determining the individual electroosmotic mobilities. However, these measurements are based on the translocation time of the particle [74]. As a matter of fact, the information that can be acquired with the RPS is fundamentally limited.

In the next chapter it will be shown how the presented RPS setup can be expanded in terms of measurement BW and measurement frequency. To do that a MP will be equipped with a pair of planar electrodes, which embeds the MP. It will allow to measure translocation events at radio frequencies (RF) thus allowing to derive some insight into particle characteristics beside their size. Furthermore, it will be demonstrated how the PSD of the new design does not show dielectric and capacitive noise up to measurement BWs of 1 MHz thus paving the way to low noise measurements at high speeds.

Part II

AC

Chapter 3

RF-Based Single Particle Detection and Characterization

Pore or channel based DC measurements as discussed in the previous chapter are fundamentally limited as they can mainly be used for counting and sizing particles [13]. In comparison, AC signals acting on particles like biological cells lead to an electronic response which shows a frequency-dependent fingerprint. For cells this is valid in particular because of their complex membrane structure and their manifold intracellular organization [75]. Dielectric spectroscopy is a method widely used to measure these properties in a variety of ways to determine the complex permittivity and conductivity of a collective cell sample or at the single cell level [76]. Roughly speaking, the dielectric constant decreases while the conductivity increases for increasing AC frequencies. Electronic properties of biological cells tend to change (sometimes orders of magnitude) when a cell is changing its biological state, e.g. when cells become malignant [77, 78, 79], which makes dielectric spectroscopy a promising diagnostic tool for clinical applications. In the second part of this thesis a MP based measurement technique is developed and discussed which uses AC signals acting on individual particles thus delivering a label-free, single particle measurement setup capable of analyzing translocating particles with various diameters at radio frequencies (RF).

In this chapter it is described how the MP based measurements presented previously can be expanded in terms of measurement frequency. While the RPS measurements are conducted at DC here it will be shown how AC signals acting on particles translocating through MPs can be used to derive useful insight into the properties of individual particles beside their size and concentration.

The chapter will start with a general introduction to dielectric spectroscopy, especially covering spectroscopy on biological cells. It will be discussed how cells show frequency depending responses when exposed to AC signals, which is giving insight into physiologi-

cally relevant cell properties. This discussion is followed by an overview on how these cell properties can be measured and a short summary on relevant experimental publications regarding this field. Finally, the specific measurement strategy used in the scope of this thesis is described.

In the experiments which will be presented, the AC signals acting on the cells will have a frequency of $> 700\,\mathrm{MHz}$. Transmission lines are routinely used to conduct signals at these frequencies and in the scope of this thesis they are used to create a sensing volume in close proximity to a glass MP thus creating a sensing region were individual particles can be measured. Therefore, an introduction into transmission line theory is given. It will be described how radio frequency (RF) waves are transmitted or absorbed on transmission lines and the critical parameters to describe these properties are introduced. This will lead to the introduction of scattering parameters which rises the question on how these scattering parameters can be measured and finally on how they can be utilized for the intended measurement.

After this introduction the process is described that was used to manufacture the transmission line based measurement chip, followed by the theoretical and experimental description and discussion of the measurements that are conducted on polystyrene beads which provide a first proof of principle.

3.1 Biological Relevance of RF Spectroscopy

In this section the effective models describing the electrical properties of cells as well as the general measurement strategy to derive these frequency dependent properties are discussed. To put the method into perspective, a short review on different dielectric spectroscopy methods presented in the last decade is given. Finally, the measurement device used in the rest of the thesis is introduced at the end of this section.

3.1.1 Electrical Properties of Biological Tissues and Cells

All lossy dielectric materials which are exposed to AC fields either absorb the field energy and transform it into heat (i.e. resistive loss) or they store the energy due to polarization effects [80]. Energy loss and polarization are strongly dependent on the frequency of the AC field. For low frequencies the dipoles in a dielectric material which are permanent or induced, can follow the alternating electrical field without any substantial phase shift with respect to the electrical field. In this case the field energy is stored predominantly within the medium due to polarization. When the frequency increases the dipoles are forced to oscillate faster to follow the electrical field accordingly. During this process, they can interact with one another and thus loose energy, which leads to heating of

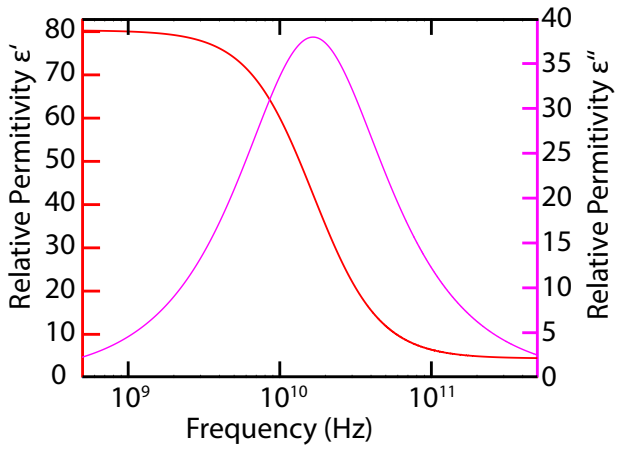

Figure 3.1: (a) Dielectric dispersion in ϵ' and ϵ'' for pure water.

the material. Furthermore, for increasing frequencies the phase difference between the electrical field and the dipole oscillation continuously increases until finally, for extremely high frequencies the dipoles cannot follow anymore because of their inertia.

This behavior is described by the complex dielectric permittivity of a material which can be given as

$$\epsilon(\omega) = \epsilon'(\omega) - i\epsilon''(\omega) = \epsilon'(\omega) - i\frac{\sigma(\omega)}{\epsilon_0 \omega} \tag{3.1}$$

where $i = \sqrt{-1}$, $\omega = 2\pi f$ is the angular frequency and $\epsilon'(\omega)$ and $\epsilon''(\omega)$ are the frequency dependent real and imaginary parts of the complex permittivity $\epsilon(\omega)$, respectively. The second term in Eq. 3.1 is the general dielectric permittivity for a lossy medium where σ is the conductivity of the material and ϵ_0 is the dielectric constant of vacuum. It follows that $\epsilon'(\omega)$ is the frequency dependent dielectric permittivity while $\epsilon''(\omega)$ is the loss factor [81].

Obviously, the dielectric behavior is a process which is frequency dependent and thus it changes on different time scales. Such processes can be best described by introducing a time constant τ. In the present case, this constant is called the relaxation time constant. R. Debye was the first proposing a model describing the observable relaxation process [81, 82]. His equation reads

$$\epsilon(\omega) = \epsilon_\infty + \frac{\epsilon_s - \epsilon_\infty}{1 + i\omega\tau} = \epsilon_\infty + \frac{\Delta\epsilon}{1 + i\omega\tau} \tag{3.2}$$

where τ is the relaxation time while ϵ_∞ and ϵ_s are the dielectric constants for very high (high frequency dielectric constant) and very low frequencies (static dielectric constant), respectively. More models exist which expand Eq. 3.2 to fit experimental data. These

models are the Cole-Cole model, Cole-Davidson model, Havriliak-Negami model and others. A complete overview of these models is given by K. Asami [83].

Expanding Eq. 3.2 into the real and imaginary part leads to

$$\mathrm{Re}[\epsilon(\omega)] = \epsilon'(\omega) = \epsilon_\infty + \frac{\epsilon_\mathrm{s} - \epsilon_\infty}{1 + \omega^2\tau^2} \tag{3.3}$$

and

$$\mathrm{Im}[\epsilon(\omega)] = \epsilon''(\omega) = \frac{(\epsilon_\mathrm{s} - \epsilon_\infty)\omega\tau}{1 + \omega^2\tau^2} \tag{3.4}$$

which are usually used to plot the dielectric permittivity (Eq. 3.3) and the loss factor (Eq. 3.4).

Dispersion of Pure Water

Pure water is one of the substances which shows one dispersion up to frequencies in the ultraviolet range. At 20°C pure water has an $\Delta\epsilon = 73.97$ and a relaxation time of $\tau = 9.4\,\mathrm{ps}$. In Fig 3.1 both the real and the imaginary part of the permittivity are shown for illustrative purposes as water is the main component of biological matter. An overview of the theory and additional experimental numbers can be found in [83, 84, 85, 86].

Dispersion of Electrolyte Solutions

In the low frequency range, electrolyte solutions in general show a decreased static dielectric constant [87]. The reason for that is that in the presence of ions in solution the water molecules form a hydration shell around the ions due to attractive coulomb forces. As a matter of fact the water molecules experience a local electrical field due to the presence of the ion. In general the magnitude of this field is bigger than the external field and thus the polarization effect due to the external electrical field is decreased. Consequently the static dielectric constant decreases [88]. Measurements of the dielectric dispersion for a NaCl, KCl and CsCl at different concentrations and temperatures for frequencies up to 20 GHz can be found in literature [89, 90].

Dispersion of Cells

In biological cells a number of phenomena play a role which contribute at very different frequencies and thus Eq. 3.2 has to be expanded to

$$\epsilon(\omega) = \epsilon_\infty + \frac{\Delta\epsilon_\alpha}{1 + i\omega\tau_\alpha} + \frac{\Delta\epsilon_\beta}{1 + i\omega\tau_\beta} + \frac{\Delta\epsilon_\gamma}{1 + i\omega\tau_\gamma} + \cdots . \tag{3.5}$$

The three terms describe the three main dispersions that are observed in a lot of biological cells. This behavior was first described by H. Schwan *et al.* and it is caused by a

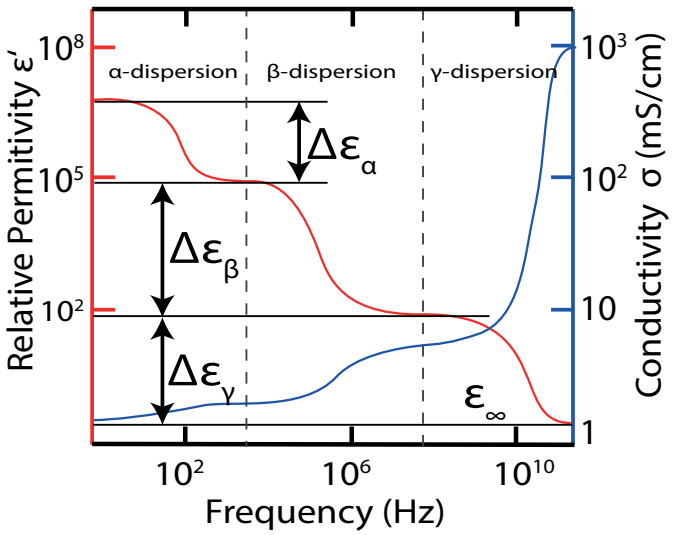

Figure 3.2: Dielectric dispersion in ϵ' and σ of muscle tissue showing the characteristic α-, β- and γ-dispersion of the tissue. Image taken and adapted from [91].

plethora of effects [91, 92]. In Fig. 3.2 the frequency dependent dielectric permittivity and conductivity for muscle tissue is plotted as it was described by H. Schwan. The dispersions are called α- β- and γ-dispersion. An in-depth discussion of several physiological factors causing this dispersion can be found in the literature [93, 94, 95].

Surprisingly, cells show extremely high values for the dielectric permittivity for low frequencies followed by a dispersion in the Hz to low kHz regime, the so called α-dispersion. The reason for this behavior is still not completely understood. One major effect contributing to this low frequency distribution is the cell membrane itself which is typically charged negatively. Therefore, positively charged ions are attracted, thus forming an electrical double layer leading to the formation of a double layer capacity and surface conductivity around the whole cell [91, 96]. This shell of charges in the double layer responds collectively to an external electrical field leading to the α-dispersion. Furthermore, ion channels in the membrane alter the conductance of the membrane which affects the α-dispersion [81, 91].

The β-dispersion is an effect observed at up to tens of MHz frequencies and it is caused by the shell-like structure of the cell. It is analytically described by the Maxwell-Wagner effect [91]. As a simplified approximation, the cell membrane can be modeled as a non-conductive interface with a thickness of 5 nm. Therefore, the capacity of a cell membrane is in the order of $1\,\mu F/cm^2$. This capacity is observed for the majority of cell types [97]. Low frequencies are blocked by the capacitance of the membrane while the capacitance is shorted out at higher frequencies as is expected due to the AC-resistance of a capacitor. This effect is observed for cells and manifests itself in the β-dispersion. Depending on the

membrane structure, i.e. if the cell that is investigated is built from a single shell, or has shells inside, like a nucleus, the β-dispersion can vary [81, 98].

Finally, for very high frequencies the relaxation of the water within the cytoplasm causes the γ-dispersion. Especially molecules within the cell that are dissolved in the cytoplasm can be weakly bond to water molecules and consequently decrease the relaxation frequency of pure water significantly [96].

3.1.2 Theoretical Prospects Regarding the Measurement of Electrical Properties

After discussing theoretically how the dielectric properties of cells can be described, the question remains, how these properties can be measured. A general setup for flow cytometric RF screening is shown in Fig. 3.3 (a). It consists of two parallel facing electrodes and a fluidic channel in between. An AC signal is used to create an alternating electrical field between the electrodes. Particles translocating through this AC field (see Fig. 3.3 (b)) are disturbing the electrical field depending on the electrical properties of the particle itself and on the geometry of the electrodes. What is even more important, is that the expected signal originating from the translocating particle is dependent on the frequency of the AC field.

Measuring the electrical properties of a particle can be generalized when building an equivalent circuit model of the setup as shown in Fig. 3.3 (c). The device electrodes form a parallel plate capacitor and the impedance of this capacitor, which contains a cell within its active volume can be written as

$$Z = \frac{1}{i\omega C} = \frac{1}{i\omega \epsilon_{\mathrm{mix}} G_{\mathrm{f}}} \approx \frac{1}{i\omega \epsilon_{\mathrm{mix}} \frac{A}{d}}. \tag{3.6}$$

The capacity C is associated with the capacitance of the two electrodes (see Fig. 3.3 (a)). Obviously, when a particle enters the sensing volume (i.e. the capacitor) the permittivity of the medium within the volume is temporarily changed and so is the capacitance $C = \epsilon_{\mathrm{mix}} A/d$. Here, ϵ_{mix} is the permittivity of the particle-medium mixture within the sensing volume and A and d are the area and the distance of the measurement electrodes for the case of parallel facing electrodes. G_{f} is a geometric factor. Its expression becomes more complicated when the electric field is not homogeneous and where fringing fields play a crucial role [99, 100].

According to T. Sun *et al.* [99, 100] and L. Batyuk *et al.* [101] the complex permittivity of the mixture is given by Eq. 3.5. Combining Eq. 3.6 and Eq. 3.5 leads to the impedance value of the detector with a cell centered in it. This equation can be compared to the impedance of the equivalent circuit model depicted in Fig. 3.3 (c). The operation is

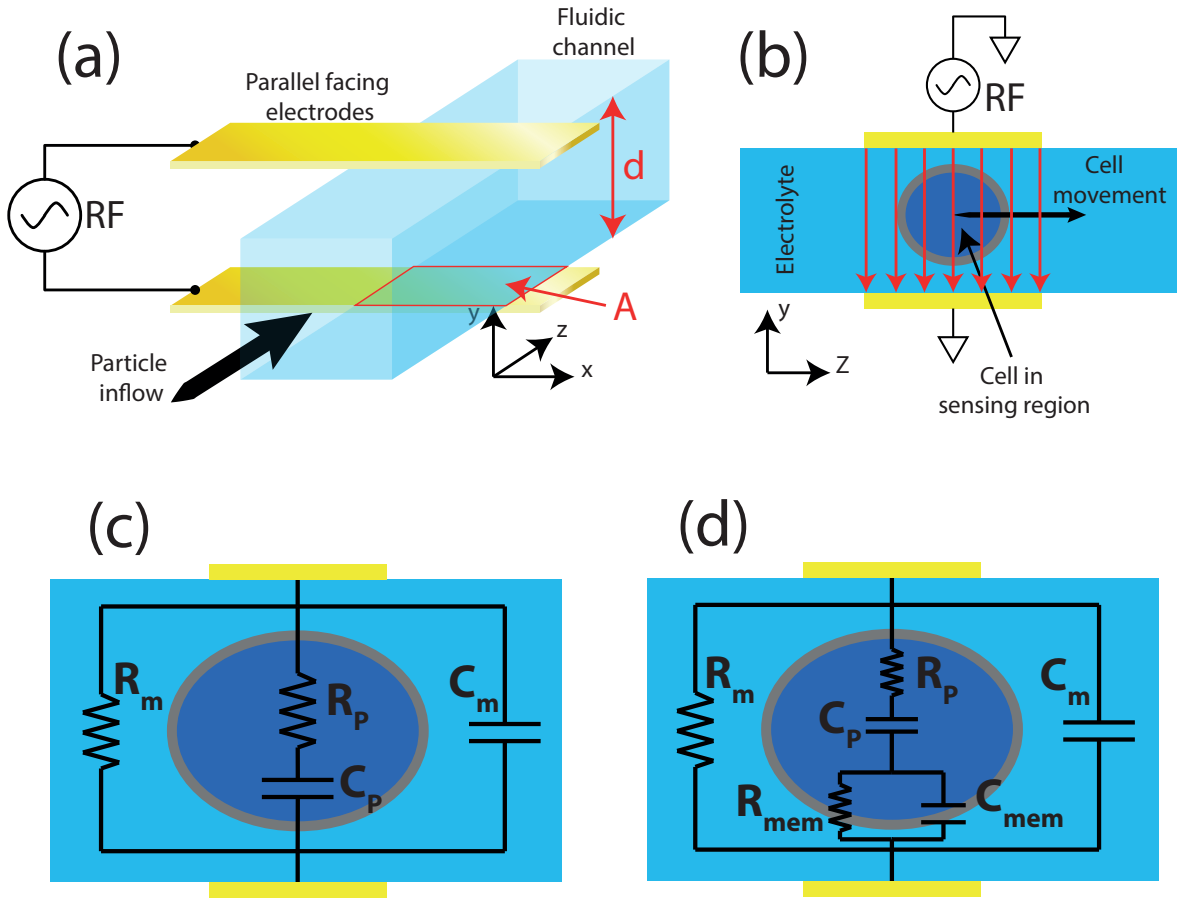

Figure 3.3: (a) Schematic of a general RF detection strategy, comprising of two electrodes encapsulating a fluidic channel. The electrodes are used to produce an alternating electrical field within the sensing region. (b) Cut through the length of the sensing region with cell in the center of the device. In this simplified configuration the two electrodes form a capacitor, and the presence of the cell is altering the dielectric permittivity within the sensing region. Lumped circuit models of biological cells within the detector for a simplified model (c) and a more complete model including the internal capacity of the cytoplasm and the finite resistivity of the cell membrane (d). Images (c) and (d) are taken and adapted from [99]

straight forward and leads to an approximation for the lumped circuit elements. A full discussion can be found in [100] and the results are

$$R_{\mathrm{m}} = \frac{1}{\rho_{\mathrm{m}}(1-\frac{3}{2}f)G_{\mathrm{f}}} \quad \text{and} \quad C_{\mathrm{m}} = \epsilon_{\infty} G_{\mathrm{f}} \tag{3.7}$$

for the resistance and capacitance of the suspension medium. Here ρ_{m} is the conductivity of the bulk medium, ϵ_{∞} is the high frequency limit permittivity of the medium and f is the volume fraction of the particle within the sensing volume. Furthermore, for the cell the coresponding values are

$$R_{\mathrm{p}} = \frac{4\left(\frac{1}{2\rho_{\mathrm{m}}} + \frac{1}{\rho_{\mathrm{i}}}\right)}{9fG_{\mathrm{f}}} \quad \text{and} \quad C_{\mathrm{shell}} = \frac{9fRC_{\mathrm{shell},0}}{4} G_{\mathrm{f}}. \tag{3.8}$$

For a more complex equivalent circuit model as shown in Fig. 3.3 (d) the process of determining the values for the circuit elements is very similar. The corresponding results can be found in [100].

3.2 State of the Art RF Devices for Cell Detection

Dielectric spectroscopy of cells can be divided roughly into two main areas namely one where an overview of a cell sample is obtained and the other one where each cell is measured individually.

The former one is the older approach and here electrodes on the surface of a cell culture or inside a cell suspension are used for the measurement [83, 102]. Cells can adhere to the surface of the electrodes or can be suspended in electrolyte and the frequency-dependent properties of the sample are measured by sweeping the frequency of the applied AC signal and recording the electrical response, picked up by the electrodes. Here, the dielectric properties of the whole or at least a macroscopic portion of the sample are measured thus leading to an inherently averaged signal [103].

The latter approach, which became more popular in recent years uses flow cytometers for the measurement. This method has the advantage that individual cells are measured consecutively and thus the result is reflecting on the potential heterogeneity of the sample as different cells, even of the same cell type might show different AC response depending on their biological state [75, 103]. The method presented in this thesis is aiming at providing a single particle approach, too. To put this method into perspective, a short review on the evolution of these setups is given in the following and the different measurement configurations that will be discussed are shown in Fig. 3.4. More complete reviews concerning flow cytometry operated at different frequencies can be found elsewhere [99, 104, 105].

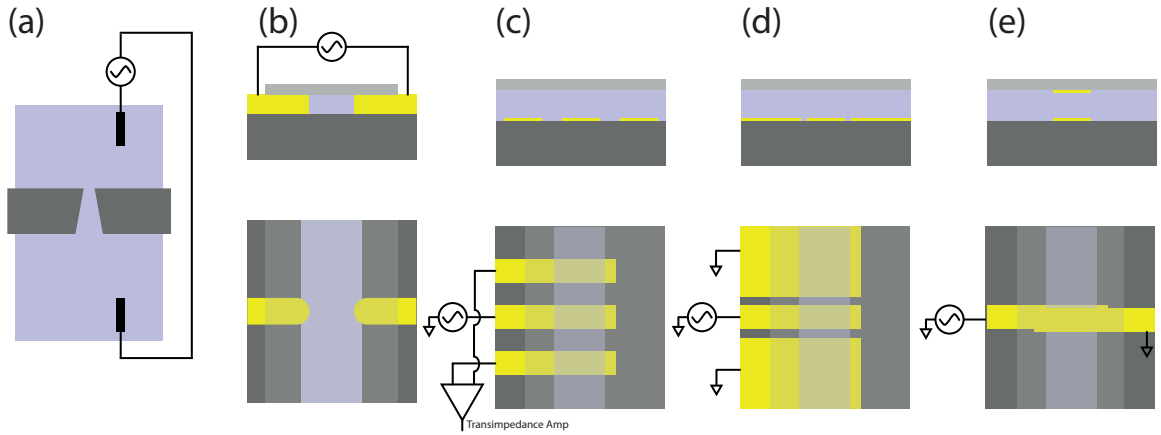

Figure 3.4: Overview of different measurement setups. (a) Coulter device with an applied AC current, (b) In-plane electrodes inside a microfluidic channel with the electrical field being orthogonal to the channel, (c) electrodes on the substrate used for differential measurements with respect to a pair of electrodes, (d) coplanar waveguide design used for high frequency measurements and (e) parallel facing electrodes. The upper row in (b)-(e) shows a cross section of the devices, while the lower row shows a top view.

3.2.1 Flow Cytometric Approaches

In 1978 and 1981 R. Hoffman *et al.* was the first to develop a flow cytometer enabling the measurement of electrical cell properties for DC signals and AC signals at 4.5 MHz, simultaneously [75, 106]. They used a Coulter Counter setup and applied an AC current to the orifice through which the cells translocate. A schematic of this setup is given in Fig. 3.4 (a). As they used a comparatively low frequency they observed a correlation between the AC signal and the corresponding DC signal.

The first cytometer comprising of a fluidic channel with a diameter of 10 µm and a height of 4 µm containing in-plane gold electrodes for local signal readout was demonstrated by H. E. Ayliffe *et al.* in 1999 [107]. In their design the ends of the gold electrodes are facing each other thus creating a electrical field between the tips which are placed within the channel (see Fig. 3.4 (b)). They were able to show that red blood cells and granulocytes show different magnitude and phase signals at frequencies as high as 2 MHz. A similar approach was demonstrated by L. Sohn *et al.* showing that measuring the capacitive change between the electrodes, situated within a polydimethylsiloxane (PDMS) based microfluidic channel, can be used to determine the state of the cell under investigation within the cell cycle [108]. It shall be pointed out that, as their measurements were carried out at 1 kHz the measured quantity most probably reflects the change of cell sizes during the cell cycle [99].

In 2001 S. Gawad *et al.* presented a flow cytometer based on a set of three adjacent

planar electrodes which were used for differential spectroscopy. Their setup is schematically shown in Fig. 3.4 (c). Particles translocating through the channel will interact with the electrical field between the first pair of electrodes while the electrical field between the second pair of electrodes is not altered. In this sense the measurement is differential as it inherently compares the signal of the pair of electrodes with the particle in the sensing volume with the signal of the pair of electrodes without a particle. As a matter of fact, each cell is directly compared to the surrounding electrolyte. Their device is able to differentiate different cell types by measuring the impedance response at two frequencies (1.72 MHz and 15 MHz) [109].

In 2005 D. Wood *et al.* presented a sensitive particle counter operating at 169 MHz and a theoretical bandwidth of 30 MHz [110]. Their design comprises of a flat coplanar waveguide protruding into a fluidic channel and the high measurement sensitivity at high speeds is achieved by a resonance enhanced measurement strategy (see Fig. 3.4 (d)). Two years later the same group demonstrated a similar approach but with a new chip design, schematically illustrated in Fig. 3.4 (d). In the new design the measurement electrodes were not planar but rather one electrode was patterned on the substrate while the counter electrode was placed on top of the fluidic channel [111]. The translocating particles were studied using a reflection measurement at a frequency of about 100 MHz. This geometry has the huge advantage that the signal originating from translocating particle is less dependent on the trajectory of the particle while translocating through the sensing region. A similar approach with rolled up electrodes within a micro tube was proposed and demonstrated experimentally by C. Bausch *et al.* [112].

G. Ferrier *et al.* published a paper in 2009 demonstrating a flow cytometer capable of detecting capacitive changes induces by particles flowing over a planar interdigital transducer (IDT) which is driven at a frequency of 1.6 GHz [113].

More recently, in 2014 Haandbaek and coworkers used a differential measurement strategy with a pair of opposing electrodes (similar to Fig. 3.4 (e)) to measure the cell response in amplitude and phase starting from 0.5 up to 500 MHz. Furthermore, they use the same setup with an additional resonance enhanced measurement which increases their signal-to-noise ratio [114, 115].

3.3 RF-Measurements: Theoretical Considerations

To handle RF signals in an experimental setup, transmission lines are routinely used and therefore they shall be discussed in the following. A brief introduction is given into the theory of transmission lines as well as definitions of typical measurement parameters. Furthermore, it shall be discussed how the parameters that are introduced in the discussion

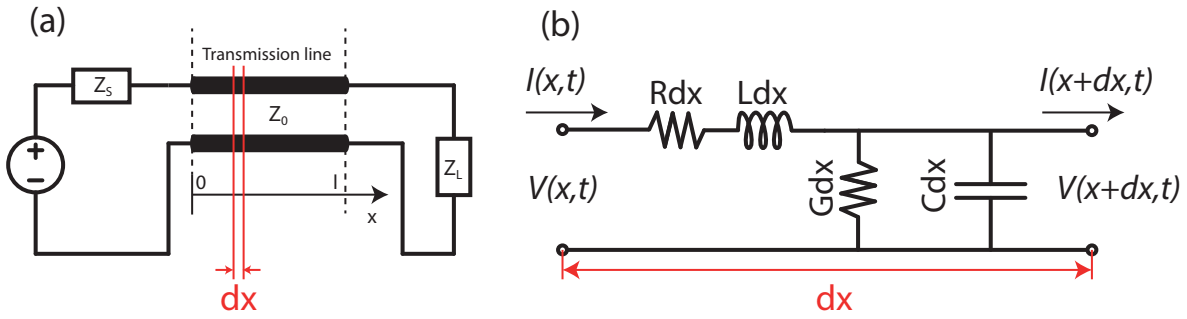

Figure 3.5: (a) Setup of a transmission line with characteristic impedanc Z_0 which is connected to a source with an input impedance of Z_s and is terminated with a load which has an load impedance of Z_L. The transmission line is assumed to have a constant impedance over the entire length l. (b) Lumped element representation of a infinitesimal small fraction of the transmission line.

can be measured using a vector network analyzer (VNA). For further measurements at increased sample rates compared to the VNA measurements, a lock-in amplifier is used. Its functionality is discussed in the last part of this section.

3.3.1 Transmission Line Theory

Transmission lines are structures capable of transmitting AC current with high frequencies. Typically, conventional electrical cables are used to transmit DC currents as well as AC currents like mains power (i.e. 50-60 Hz) and audio signals. Above the audible frequency range (i.e. $\approx$ 20 kHz) the AC current tends to get lost due to the radiation of radio waves. The following discussion follows the one found in Ref. [116, 117]

A schematic of a typical transmission line setup can be seen in Fig. 3.5 (a). It consists of a source with a specified source impedance Z_s, the transmission line that is capable of transmiting RF waves and a load with a specific impedance Z_L. The load is connected after a certain length l of transmission line and the transmission line itself has a so called characteristic impedance Z_0 which does not depend on its length. In physical systems, this characteristic impedance is real with a value of 50 Ω or 100 Ω. Throughout this thesis experiments are done in a 50 Ω environment.

In Fig. 3.5 (b) a representation of a infinitesimal small length element of a transmission line is depicted. Although, typically the line has very little loss due to the resistivity R of the conductor, there are alway some ohmic losses associated. Beside that, dielectric losses can play an important role at higher frequencies. They are included in the conductivity G. The length element shown in the figure can be solved by applying Kirchhoff's laws, leading to the following differential equations

$$\frac{\partial V(x)}{\partial x} = -(R + i\omega L) \cdot I(x) \tag{3.9}$$

and

$$\frac{\partial I(x)}{\partial x} = -(G + i\omega C) \cdot V(x). \tag{3.10}$$

Combining those two equations one gets

$$\frac{\partial^2 V(x)}{\partial x^2} - \gamma^2 \cdot V(x) = 0 \tag{3.11}$$

and

$$\frac{\partial^2 I(x)}{\partial x^2} - \gamma^2 \cdot I(x) = 0. \tag{3.12}$$

The constant γ is called the propagation constant and can be written as:

$$\gamma = \alpha + i\beta = \sqrt{(R + i\omega L)(G + i\omega C)}. \tag{3.13}$$

Eq. 3.11 and Eq. 3.12 are wave equations that can be solved using a simple ansatz

$$V(x) = V^+ e^{-\gamma x} + V^- e^{\gamma x} \tag{3.14}$$

and

$$I(x) = \frac{1}{Z_0}(V^+ e^{-\gamma x} - V^- e^{\gamma x}) = I^+ e^{-\gamma x} - I^- e^{\gamma x}. \tag{3.15}$$

In this equation Z_0 is the characteristic impedance defined by:

$$Z_0 = \sqrt{\frac{R + i\omega L}{G + i\omega C}} \tag{3.16}$$

and $V^\pm$ have to be conducted from boundary conditions. A physical representation of $V^\pm$ is a wave traveling in positive and negative x-direction. The real and imaginary parts of Eq. 3.13 are of technical relevance. The real part α is the attenuation constant and it describes how a wave is attenuated while traveling along the transmission line. Accordingly, β is the phase constant describing the phase change along the line.

3.3.2 Transmission Lines

A plethora of transmission lines exist that are used to transmit RF signals. The typical textbook example of a transmission line is the coaxial cable such as BNC and SMA cables. Coaxial cables consist of a central conductor surrounded by a dielectric material with a certain thickness. The cable is enclosed by an outer conductor. Depending on the size of the dielectric material that is insulting the central signal conductor from the outer

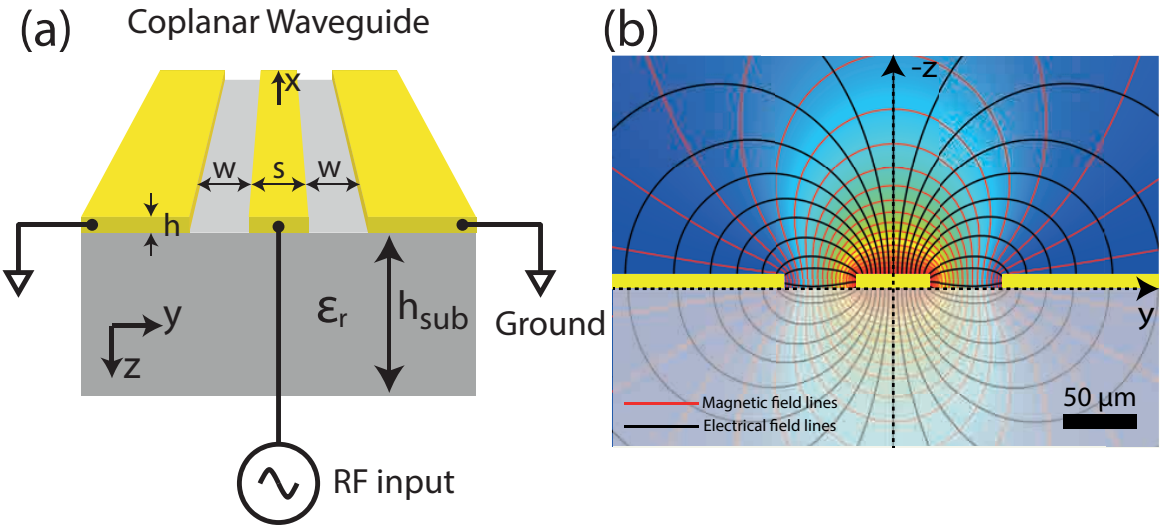

Figure 3.6: (a) Schematic of the coplanar waveguide. The CPW has a metalization with height h on one side of the substrate comprising of one signal line with width s in the center surrounded by the ground planes with a distance of w from the signal line. Both ground planes are connected to the same ground and the signal line is connected to a signal generator. (b) Electric and magnetic field lines in the transverse plane of the CPW.

ground conductor the characteristic impedance can be tuned. Very similar to BNC cables [118] SMA cables [119] are used routinely as they are capable of transmitting higher frequencies at lower insertion losses. As the RF wave propagates exclusively within the dielectric material, the wave propagates in a transverse electrical mode (TE-mode).

Not only cables with a cylindrical geometry can be used; also planar waveguides are extremely common in RF circuits. In the scope of this thesis, an open-ended CPW is used as the particle detector. The following discussion is limited to these planar transmission line structures.

CPWs were first proposed by C.P. Wen in 1969 [120]. A schematic of a CPW is shown in Fig. 3.6 (a). It consists of a dielectric substrate with a thickness h_{sub} and a dielectric constant ϵ_{r}. On top of the substrate there are three metal stripes. The two outer stripes are connected to a common ground and the central stripe, which is called the signal line, with a width s is connected to the alternating RF input. Furthermore, there is a constant gap with size w between the ground metalization and the signal line. In contrast to strip lines which consist of a metal stripe on the top side of the dielectric substrate and a ground metalization on the rear side of the substrate, CPWs have the advantage of a simple production process, as the substrate has to be covered with metal from one side only. Furthermore, the implementation of lumped circuit elements that have to be

connected to the ground plane can be done without the need of via holes in the substrate.

A complete discussion of the theory regarding CPWs and other planar transmission lines can be found elsewhere [121]. Here the basic results are discussed that will give solutions for the characteristic impedance Z_0 of the CPW that follow from a quasi-static approximation.

Because of the interface between the dielectric substrate on which the metal layer is patterned and the air, RF waves propagate as quasi-TEM waves along the line. The electric and magnetic field in the transverse plane of a CPW is shown in Fig. 3.6 (b). In the previous section the characteristic impedance of a general transmission line was already given in Eq. 3.16. For the sake of simplicity the following discussion is limited to the case of a lossless line (i.e. $R = G = 0$) and thus the characteristic impedance can be written as

$$Z_0 = \sqrt{\frac{L}{C}}. \tag{3.17}$$

According to Eq. 3.13 the propagation constant for this case simplifies to $\beta = \omega\sqrt{LC}$. The phase velocity of a propagating TEM wave is $v_{\mathrm{ph}} = \frac{\omega}{\beta} = \frac{c}{\sqrt{\epsilon_{\mathrm{eff}}}}$ and consequently Eq. 3.17 can be rewritten to be

$$Z_0 = \frac{1}{v_{\mathrm{ph}} C}. \tag{3.18}$$

Obviously, the characteristic impedance can be calculated with the capacitance and the phase velocity and the effective dielectric constant ϵ_{eff} associated with the line.

A method to determine the capacitance C of a planar transmission line is to use conformal mapping. To simplify the discussion, it will be assumed that the dielectric substrate has an infinite thickness and a dielectric constant of ϵ_{r}. Additionally, it is assumed that the ground metalization has an infinite width. The discussion follows the one in Ref. [121].

For the conformal mapping one half of the transverse plane surrounding the metalization layer and the dielectric material is translated into the complex numbers via $z = x + iy$ and this coordinate system is transformed using the Schwarz-Christoffel transformation

$$w = \int \frac{dz}{\sqrt{(z-a)(z-b)}} \tag{3.19}$$

where $a = s/2$ and $b = a + w$. This transformation is shown graphically in Fig. 3.7. The w plane simplifies the calculation as in this coordinate system the signal line and the corresponding ground, in one quarter of the transverse plane of the CPW, form a parallel plate capacitor which capacitance can be given easily as

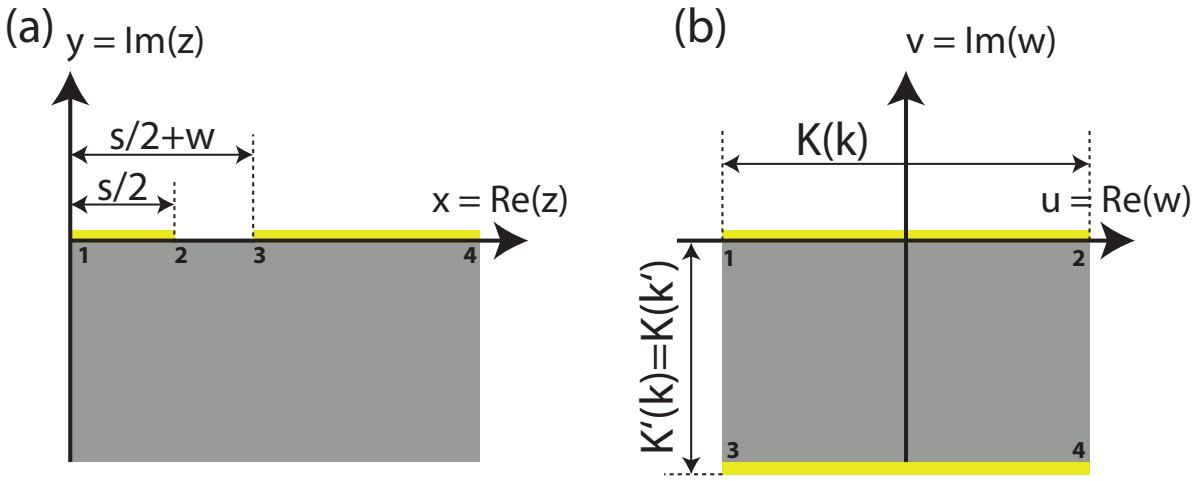

Figure 3.7: (a) One half of the CPW structure in the $z = x+iy$ plane which is used for the conformal mapping technique. (b) Region of the structure shown in (a) after transforming the structure into to $w = u+iv$ plane. The resulting structure is in the form of a parallel plate capacitor.

$$C_2 = 2\epsilon_0\epsilon_\mathrm{r}\frac{K(k)}{K'(k)} \tag{3.20}$$

where ϵ_r is the dielectric constant of the dielectric material and $K(k)$ and $K'(k)$ are complete elliptical integrals of the first kind. Substituting the dielectric constant for air into Eq. 3.20 (i.e. $\epsilon_\mathrm{r} = 1$) the capacitance C_1 for the side filled with air follows accordingly due to symmetry.

The complete capacitance is thus given as

$$C = C_1 + C_2 = 2\epsilon_0(\epsilon_r + 1)\frac{K(k)}{K'(k)}. \tag{3.21}$$

The effective dielectric constant of the system is given as

$$\epsilon_\mathrm{eff} = \frac{\epsilon_\mathrm{r}+1}{2} \tag{3.22}$$

and thus the phase velocity

$$v_\mathrm{ph} = c\sqrt{\frac{2}{\epsilon_\mathrm{r}+1}} \tag{3.23}$$

and finally the characteristic impedance is given as as

$$Z_0 = \frac{30\pi}{\epsilon_\mathrm{eff}}\frac{K(k)}{K'(k)}. \tag{3.24}$$

As a matter of fact, the characteristic impedance depends on the ratio of signal line width and the gap between the signal line and the ground metalization as the argument k and k' of the elliptical integral is given as

$$k = \frac{a}{b} = \frac{s}{s + 2w} \tag{3.25}$$

and

$$k' = \sqrt{1 - k^2}. \tag{3.26}$$

3.3.3 Scattering Parameter

Scattering parameters have been proven to be extremely practical to characterize transmission lines. In the following an introduction into scattering parameters is given because they are used in this chapter for some measurements. The discussion will concentrate on two-port networks. An in-depth introduction into the subject can be found in Ref. [122]

As discussed in the previous section Eq. 3.14 and Eq. 3.15 are wave equations describing a propagating voltage and current wave along the transmission line. These equations can be transformed into the following form:

$$a_\mathrm{i} = \frac{1}{2\sqrt{Z_0}} \cdot (U_\mathrm{i} + I_\mathrm{i} Z_0) \tag{3.27}$$

and

$$b_\mathrm{i} = \frac{1}{2\sqrt{Z_0}} \cdot (U_\mathrm{i} - I_\mathrm{i} Z_0), \tag{3.28}$$

describing waves entering and exiting a specific port i. So far, this is true for am N-port network, where each port has an input impedance of Z_0. For a two port network the relationship between incident waves and exiting waves can be described using a scattering matrix

$$\begin{pmatrix} b_1 \\ b_2 \end{pmatrix} = \begin{pmatrix} S_{11} & S_{12} \\ S_{21} & S_{22} \end{pmatrix} \begin{pmatrix} a_1 \\ a_2 \end{pmatrix}. \tag{3.29}$$

The individual terms can be interpreted physically. If there exists a wave a_1 traveling into port one of the device and if there is no wave a_2 traveling into port two of the device the parameter S_{11} can be interpreted as a reflection coefficient by combining Eq. 3.27 and Eq. 3.28, leading to

$$\Gamma = S_{11} = \frac{b_1}{a_1} = \frac{Z_1 - Z_0}{Z_1 + Z_0} \tag{3.30}$$

which quantizes the amount of reflection at port one when there is no wave transmitted into port two. In the same manner S_{22} is the reflection of a wave a_2 at port two in the

absence of a wave a_1.

Transmission of incident waves can be described by the off-axis elements in Eq 3.29 but as transmission measurements are not conducted in the scope of the thesis they shall not be given here.

If not stated differently the scattering parameter are measured logarithmically in dB. The definition that is used is given as

$$S_{ij1,\mathrm{dB}} = 20 \cdot \log_{10} |S_{ij}| \tag{3.31}$$

with S_{ij} is as described in Eq. 3.29. As a matter of fact, in terms of the reflection parameter S_{11}, $-\infty$ dB represents zero reflection and 0 dB is measured if the port reflects all the power back into the line.

3.3.4 Impedance Matching

According to Eq. 3.30 the reflection of an incident wave is a function of the port impedance Z_1 of the device under test and a function of the characteristic impedance of the transmission line Z_0. An incident wave will be reflected back into the signal source if the impedance of the device is vastly different from the impedance of the transmission line. In general this reflections have to be minimized because the power delivered by the source should always enter the port without reflection so that maximal power transfer between the source and the device is achieved. Minimum reflection is obviously achieved when

$$Z_0 = Z_1 \tag{3.32}$$

The characteristic impedance of the transmission line Z_0 cannot be changed. Its value is fixed and all test equipment used for the experiments have a real characteristic impedance of 50 Ω. To achieve maximal power transfer the device impedance Z_1 will need to be adjusted to match the characteristic impedance. This can be done by introducing passive or active lumped elements like capacitors and inductors into the device circuit which change the overall impedance to a value where its impedance is matching the transmission line impedance. This process is called impedance matching and information on how such impedance matching circuits can be implemented are discussed in standard textbooks [123, 124].

In the scope of this thesis, impedance matching between the transmission line setup and the RF chip is achieved using a tunable varactor diode in series with the signal line. A detailed discussion will be given in Sec. 3.6.3.

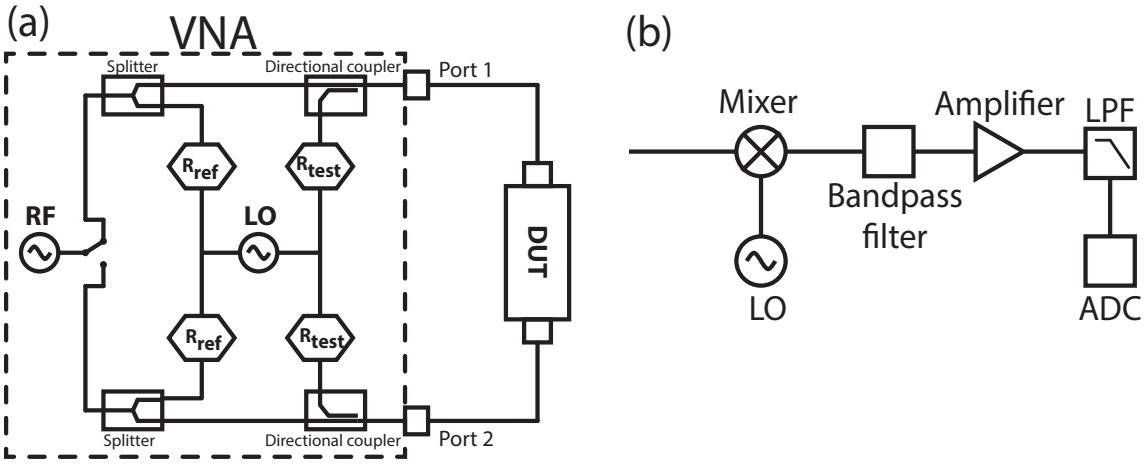

Figure 3.8: (a) Schematic of a vector network analyzer with two ports connected to a two port network. (b) Schematic of the heterodyne receiver design.

3.3.5 VNA-Measurements

The direct way to perform a reflection measurement at frequencies around 1 GHz is to use a vector network analyzer (VNA). A VNA is capable to directly measure the reflection and transmission of a device. As a reflection measurement of the investigated device is critical for the thesis, the working principle of a VNA is discussed in the following. Introductory information can be found in textbooks like [123, 124].

A schematic of a VNA can be seen in Fig. 3.8 (a). The front-end of a typical bench-top VNA has two ports that have a specific characteristic impedance which allows for measuring the frequency dependent reflection and transmission of a device under test (DUT). Internally, an RF source is producing an electromagnetic wave that is coupled into one of the signal paths leading to one of the output ports. The RF source is tunable in frequency. In a first stage, the generated signal is divided by a signal splitter. One of the splitter signals is feed directly into a reference receiver R_{ref} (see Fig. 3.8 (b)). This reference signal is later used to measure the phase of the measured signal. Further down the signal path, the splitted signal is outputted from port 1 or port 2 depending on the position of the initial switch. A DUT is connected via a transmission line and the signals from the VNA are transmitted and reflected by the device. A directional coupler in front of the port 1 couples the reflected wave into the test receiver R_{test} where the reflection coefficient S_{11} is measured. In port 2 the test receiver measures the transmitted wave.

All receivers are connected to a second signal source called the local oscillator (LO) which is mandatory since typically the receivers use a heterodyne detection method for the measurement. A schematic for such a receiver design is shown in Fig. 3.8 (b). Modern VNAs can operate up to frequencies of 100 GHz. Processing signals directly at these

frequencies is impractical. However heterodyne receivers solve this problem by down converting the signal to a frequency range where it can be processed digitally. To down convert the signal a frequency mixer is used. These devices have three ports: a so called RF port where the high frequency input signal is connected, a LO port where the local oscillator signal is connected and an intermediate frequency (IF) output port. The LO is operated at a fixed frequency difference with respect to the RF port and thus the IF frequency is given as

$$f_{\mathrm{IF}} = f_{\mathrm{RF}} \pm f_{\mathrm{LO}}. \tag{3.33}$$

A bandpass filter (BPF) is used to pass the the lower frequency component of Eq. 3.33. As a matter of fact the IF signal is identical to the RF signal but it is down converted in frequency. Similar to the RF source the LO source is tunable in frequency allowing the receiver electronic work at a fixed IF frequency. To simplify the analysis, the IF signal is amplified before a lowpass filter (LPF) rejects all higher harmonics from the IF signal. Finally, the IF is converted into a digital signal which is used by the instrument to calculate all complex reflection and transmission parameters.

The noise in VNA reflection and transmission measurements depend on the so called intermediate frequency bandwidth (IFBW) which is basically the bandwidth of the bandpass filter of the receiver. By using a extremely low IFBW the noise can be reduced dramatically but this happens at the expense of the sampling rate of the instrument.

It will be discussed how this behavior will limit the usability of the VNA for the intended application, as a high temporal resolution is critical for the success of the experiment, which will be discussed in this thesis.

3.3.6 Lock-In Technology

In RF technology it can be difficult to reconstruct a signal at a specific frequency especially if it has a small amplitude. From a frequency dependent perspective a signal is located at a fixed frequency. Additionally, there are noise contributions at the frequencies surrounding the signal which are picked up from the measurement receivers if the noise is within the BW of the measurement device. A straight forward approach to isolate the signal would be to apply a band pass filter (BPF) with the central band at the frequency at which the signal is located. Unfortunately, this is only possible to a certain extend since in the real world a perfect BPF does not exist so that the captured signal is inevitably contaminated by noise originating from the adjacent frequency. The smaller the BW of the filter is the less pronounced is the contamination, but it will never eliminate the problem completely.

Lock-in amplifiers were introduced in the beginning of the century [125, 126] and

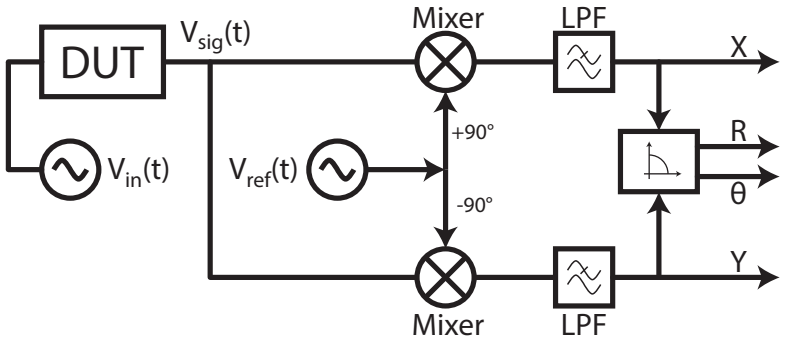

Figure 3.9: Schematic of a lock-in amplifiers circuit. The amplifier comprises of a signal source driving the DUT with a voltage wave $V_{\mathrm{in}}(t)$. The DUT response V_{sig} is first mixed with a in-phase $+90°$ and out of phase $-90°$ reference wave $V_{\mathrm{ref}}(t)$ and is then lowpass filtered. The filtered responses give the in-phase component and the out of phase component that can be back calculated into the amplitude R and phase ϕ of the incoming signal.

they are capable of demodulating a very tiny signal at a known frequency by simultaneously rejecting the background originating from different frequency completely. In this sense lock-in amplifier are ideal BPF. Their working principle is based on comparing a modulated input signal with a reference signal. Thus, only the signal contributions that are modulated on the reference frequency are measured and background contaminations that are not modulated on the reference signal are withdrawn completely. As the lock-in technique is used to perform the high sampling rate and low noise RF measurements its working principle shall be discussed in the following.

A schematic of a general lock-in amplifier can be seen in Fig. 3.9. The lock-in typically consists of a signal input port. Here the modulated signal is interfaced with the amplifier. For the reference signal a reference source is used which is originating from the amplifier itself or an external signal source.

The lock-in principle is based on phase sensitive detection by mixing the input signal $V_{\mathrm{sig}}(t) = V_{\mathrm{s0}} \sin(\omega_{\mathrm{s}} t + \phi)$ with a reference signal $V_{\mathrm{ref}}(t) = \sin(\omega_{\mathrm{r}} t)$. Mixing of two sinusoidal signals is equivalent to multiplying the two signals thus the output of the mixing process leads to

$$X = V_{\mathrm{sig}}(t) \cdot V_{\mathrm{ref}}(t) = \frac{V_{\mathrm{s0}}}{2} \left(\cos((\omega_{\mathrm{s}} - \omega_r)t - \phi) + \cos((\omega_{\mathrm{s}} + \omega_r)t + \phi) \right). \tag{3.34}$$

In the frequency domain it translates to signal components with a low frequency $\omega_{\mathrm{s}} - \omega_r$ and a high frequency $\omega_{\mathrm{s}} + \omega_r$. Lock-in amplifier operate at $\omega_{\mathrm{s}} = \omega_r$ thus leading to a DC

term and a high frequency term after the mixer stage. A lowpass filter is then used to remove the high frequency term. Mathematically, this procedure is related to a time integral over some periods of Eq. 3.34 leading to a output which is not time dependent

$$X = R\cos(\phi). \tag{3.35}$$

Typically the LPF can be tuned, thus allowing to choose different filter orders and filter bandwidths.

It can be seen in Eq. 3.35 that, the so called in phase component, X depends on the relative phase of the input signal to the reference signal. To maximize the output the phase has to be adjusted. Modern lock-in amplifiers not only use the reference signal $V_{\mathrm{ref}}(t)$ but also a reference signal that is phase shifted by 90° (see Fig. 3.9). Accordingly, this leads to a corresponding sinusoidal term

$$Y = V_{\mathrm{sig}}(t) \cdot V_{\mathrm{ref}}(t) = \frac{V_{\mathrm{s0}}}{2}\left(\sin((\omega_{\mathrm{s}} - \omega_r)t - \phi) + \sin((\omega_{\mathrm{s}} + \omega_r)t + \phi)\right) \tag{3.36}$$

and therefore, beside the so called in-phase component X a second, so called out of phase component Y is created which is given as

$$Y = R\sin(\phi). \tag{3.37}$$

Having the two measurements from Eq. 3.35 and Eq. 3.37 it is possible to calculate the signal amplitude

$$R = \sqrt{X^2 + Y^2} \tag{3.38}$$

and the signal phase

$$\phi = \arctan Y/X \tag{3.39}$$

by using simple trigonometry. Both, the amplitude given in Eq. 3.38 and the phase given in Eq. 3.39 are used for cell characterization.

3.4 Device Discussed in the Thesis

The device presented in this thesis varies from most devices discussed in literature as the geometry is different as well as the operation frequency, which is higher than in the majority of applications described so far in literature (see Sec. 3.2). A schematic of the design can be seen in Fig. 3.10 (a).

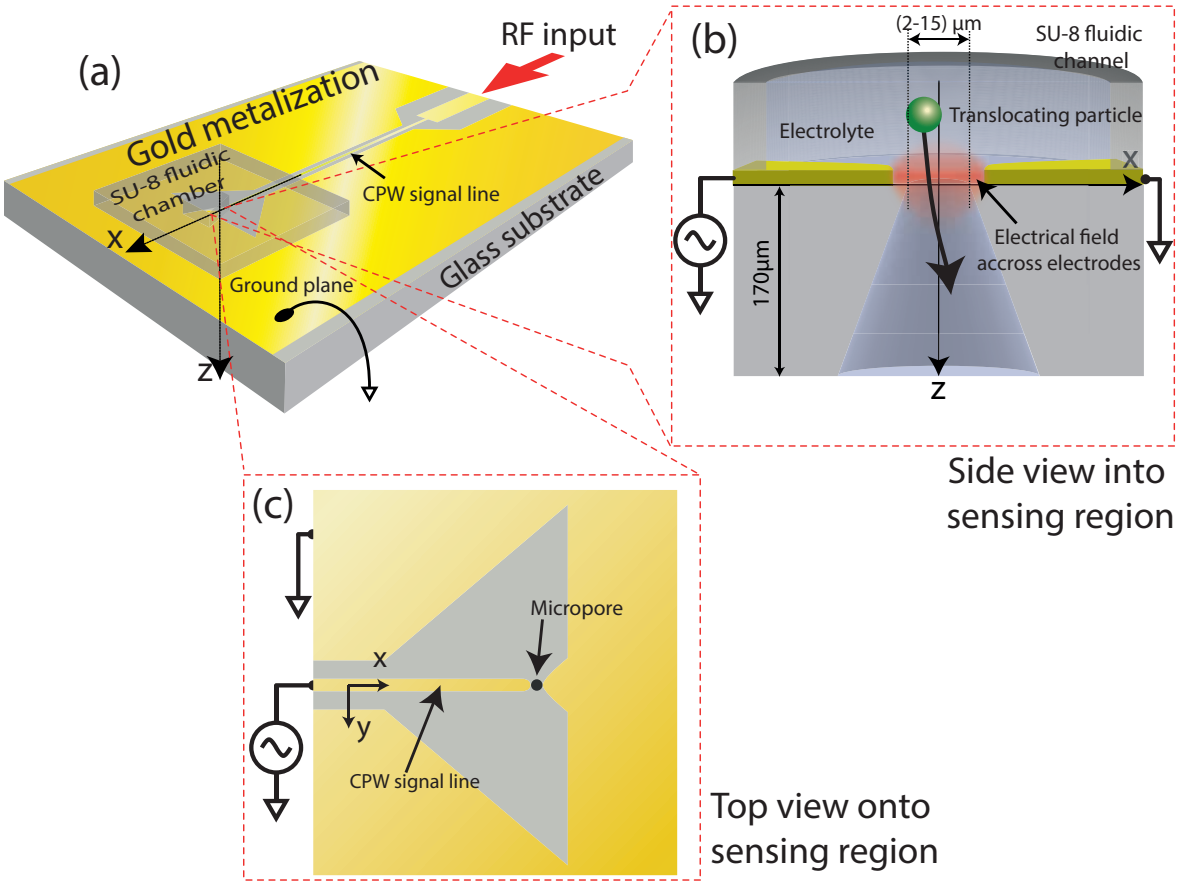

Figure 3.10: (a) Schematic of the RF-chip used throughout the thesis for preforming RF-spectroscopy. It comprises of a CPW on top of a glass slide. The RF wave is fed into the chip via an RF input and the signal line has an open end at which the micropore is located. A fluidic chamber is patterned around the sensing region build from SU-8. (zoomed-in view (b)) Cut through the micropore illustrating the electrode tips that are embedding the pore and illustrating the particle translocating through the strong, localized electrical field. (zoomed-in view (c)) Top view onto the sensing region showing the embedded micropore.

It is based on a MP, similar to those presented in Part I of the thesis, interfaced with a coplanar waveguide (CPW). The CPW is made of gold with a thickness of 110 nm and the signal line is a couple of centimeters long, which determines the point of operation. With the final design the chip will operate at radio frequencies (RF) waves with frequencies above 700 MHz. At the end of the CPWs signal line the MP is embedded, which is built similarly to the pores discussed in Sec. 2.3. Opposing to the open end of the signal line the ground metalization is built adjacent to the MP. This can be seen schematically in the zoomed-in view in Fig. 3.10 (b) and (c).

Particles are introduced onto the device by pipetting the particle-containing solution onto the region where the pore is located and they can translocate through the pore by applying a suction. The device is operated in such a way that a suction will force the particles to translocate the pore in positive z-direction (see coordinate system in Fig. 3.10). To prevent a strong interaction between the RF-field and the fluid, a thick protection layer built from the negative resist SU-8 is patterned around this region preventing the fluid to interact strongly with the electrical filed but simultaneously exposing the sensing region to enable particle translocation.

The principle of operation is, at least in general, the same as discussed in Ch. 3.1.2. An RF wave propagates along the CPW from the RF input along the positive x-axis (see Fig. 3.10 (a) and (c)). Once the wave reaches the end of the signal line it will create a strong electrical field between itself and the opposing ground electrode. A particle which translocates through the pore is acted upon the electrical field, locally changing the dielectric permittivity of the sensing volume and thus changing temporarily the electrical parameters of the device. This modulation can be measured in reflection and the measured quantities will be used for particle characterization.

The device is designed to operate at several hundred MHz, i.e in the RF regime. At frequencies below 100 MHz the metal/liquid interface produces an electrical double layer introducing a parasitic capacitance corrupting the dielectric spectroscopy measurements. Typically the results have to be corrected to account for this effect [127]. As the device is operated way above these frequencies, electrode polarization will play a minor role here [103].

It was shown in Fig. 2.7 that the pore size of laser ablated MPs is tunable which allows the device to investigate colloidal particles in the sub-micrometer range but also biological cells. In the context of this thesis the investigation of biological cells will be discussed mainly. At the operation frequencies in the several hundred MHz regime the device is expected to be sensitive mainly on the γ-dispersion and thus on the cytoplasm of the cell.

3.5 RF-Chip Production

The preparation of the RF chips requires several steps, including standard photolithography for the patterning of the CPW metalization on the glass substrate, a SU-8 processing for the production of a fluidic reservoir on top of the RF sensing region, the pore drilling as discussed in Sec. 2.2.1, a fine adjustment of the sensing region using a focused ion beam milling and metal deposition step by ion beam induced deposition and finally the integration of the RF chip into the RF setup. All these steps are discussed in the following section.

3.5.1 Optical Lithography and SU-8 Processing

The RF chips are prepared on a borosilicate microscope cover slips with a thickness of 170 µm ± 5 µm and dimensions of 2 cm × 5 cm. Prior to the lithography process, they are cleaned in acetone, isopropanol and water, to get rid of eventual dirt and dust. Remaining organic residues are washed off in piranha solution (i.e. $H_2SO_4 : H_2O_2$ in a ratio of 4 : 1) for 1 h. Finally, the glass slides are rinsed in DI-water and then baked for 2 h at 200°C on a hotplate to ensure that the surface is properly dehydrated.

The CPW design comprises of a 75 µm wide signal line that has a length of 3.4 cm with a gap of 50 µm between the signal line and the ground conductor. This high aspect ratio of length to width is necessary as the length of the line determines the frequency at which the chip operates. It should be noted that, this high aspect ratio requires special care in terms of resist profile and adhesion. For good resist adhesion a thin layer of an adhesion promoter[1] is spin coated at 4000 rpm for 1 min and then baked out for 2 min at 200°C on a hotplate. This results in a 15 nm layer of adhesion promoter ensuring a strong adhesion of the following resist layers to the substrate.

The following consecutive steps are schematically shown in Fig. 3.11 (a). A two-layer resist is used for the optical lithography. The first layer is LOR A5 diluted in G-thinner in a ratio 1 : 1. This mixture is spin coated at 4500 rpm for 1min. Subsequently, the positive photoresist S1813 is spin-coated on top at 6000 rpm for 1min. In between the spin coating steps, the resists are baked for 1min at 160°C and 110°C, respectively. After that, the resist is irradiated with UV light through a chromium mask for 13 sec with a power density of 13 mW/cm^2 and finally it is developed in MF 319 for 50 sec. As illustrated in Fig. 3.11 (a) the development of the resist leads to an undercut of the S1813 photoresist thus shadowing a small fraction of the glass chip.

To pattern the metal on the slides, physical vapor deposition (PVD) is used. A 110 nm gold layer is evaporated on top of a 20 nm chromium adhesion layer. To lift off the metal

[1] AR 300-80, Allresist

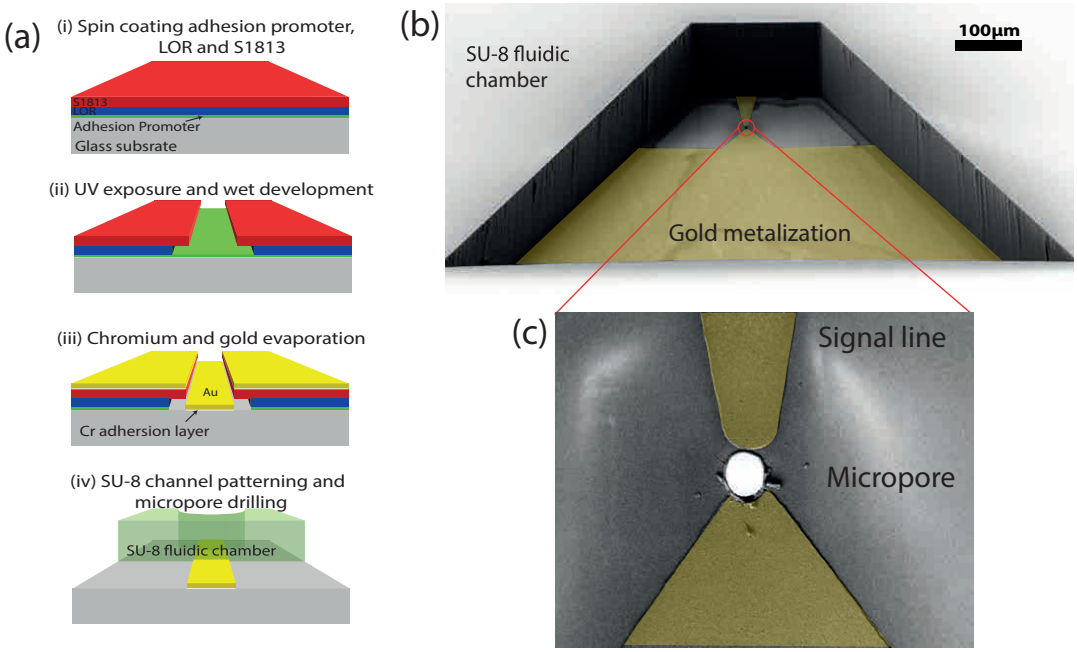

Figure 3.11: (a) Schematic of the relevant cleanroom processing steps necessary for the RF chip preparation. (b) SEM image of the sensing region comprising of the open end of the signal line and ground metalization surrounded by the SU-8 fluidic chamber. (c) Zoomed-in view into the sensing region accommodating the micropore.

the remover 1165 is used. The evaporated glass structures are immersed in the remover over night avoiding strong agitation of the liquid. The excess metal can be removed carefully using a soft disposable swab by gently scraping the gold away in the direction of the length of the signal line.

A fluidic chamber to confine the liquid is patterned using SU-8. For the fluidic chamber the SU-8 photoresist GM1075 is used. This resist allows to pattern fluidic chambers with a thickness of approximately 200 µm. Typically the adhesion of SU-8 to gold is not very strong. Therefore, a cleaning step with acetone, isopropanol and DI-water is performed. After that, the chip is dehydrated for 20 min at 200°C on a hotplate. The best adhesion is observed if the chips are additionally cleaned in an oxygen plasma oven for 5 min. After cleaning, the SU-8 is spin coated on the chip at 950 rpm for 100 sec, resulting in a resist height of 200 µm[2]. To remove the resist edges, the resist is left uncured on a planar surface overnight at room temperature. This step is important because very high resist edges are build up after spin coating because of the high viscosity of the SU-8. When the edges are not removed prior to UV irradiation the the Cr-mask will not have proper contact to the surface of the resist and the structure is not well transferred.

[2] A ramp of +100 rpm/s at the beginning of the spin coating and two consecutive ramps of +400 rpm/s for 1 sec followed by a ramp of −100 rpm/s at the end of the spin coating step is used.

Afterwards, the SU-8 has to be pre backed for 10 min at 120°C. If the pre bake time is too short the SU-8 will still be viscous enough to irreversibly stick to the chromium mask during UV irradiation, potentially destroying the structure. The UV exposure step that follows the pre bake initializes the polymerization of the SU-8, a process which is completed by a final hard bake at 95°C for 1 h.

Finally, the SU-8 is developed in propylene glycol methyl ether acetate (PGMEA). A majority of the non polymerized SU-8 is easily washed away with the developer. But inside the sensing region of the chip, residues of non developed SU-8 will often remain. To get rid of these residues, the PGMEA is manually rinsed in the sensing region with a cannula and a syringe. Under an optical microscope, the cleanness of the sensing region is examined and if residues are remaining, fresh PGMEA is flown with the syringe until the region is clean. This cleaning process is vital as any residues of SU-8 will compromise the final focused ion beam (FIB) induced metal evaporation, which is described in the following. The developed SU-8 channel is shown in Fig. 3.11 (b). From the top the signal line (colored in yellow) can be seen. It is critical that it is covered to a high extend under the SU-8 so that only the tip is exposed to the liquid. Compared to that, the fact that the ground metalization has a lot of contact to the liquid did not influence the performance of the time domain measurement so that the opening of the channel is chosen to be so big that the accessibility for the FIB process is not limited due to the high SU-8 walls.

3.5.2 Pore Drilling and Focused Ion Beam Adjustments

For the production of the MP, the same method is used as described in Sec. 2.2.1. Prior to drilling the MP a screw cap with a mechanically drilled 2 mm hole is glued to the back side of the glass chip. The hole of the screw cap is positioned around the sensing region which is visible without magnification. UV curable glue is used in such a way that an airtight seal is produced between the screw cap and the backside of the RF chip. The cap is later used to interface the chip with the DC amplifier and to allow for pressure control on the MP.

For the RF measurements it is critical that the pore is aligned to the sensing region which is rather difficult with the method at hand because the pore has to be drilled from the back side of the chip because of two main reasons. Firstly, the drilling process produces a lot of debris that should not fall on the sensitive electronics. Secondly, it is not possible with the used laser system to drill a micron sized pore into the front side of the substrate if it has a thickness of 170 µm. This was demonstrated in Fig. 2.7.

The remaining problem is to place the final pore between the open end of the signal line and the ground metalization. This problem was solved in the following manner. The chip is placed on the movable sample stage of the excimer laser with its back side facing

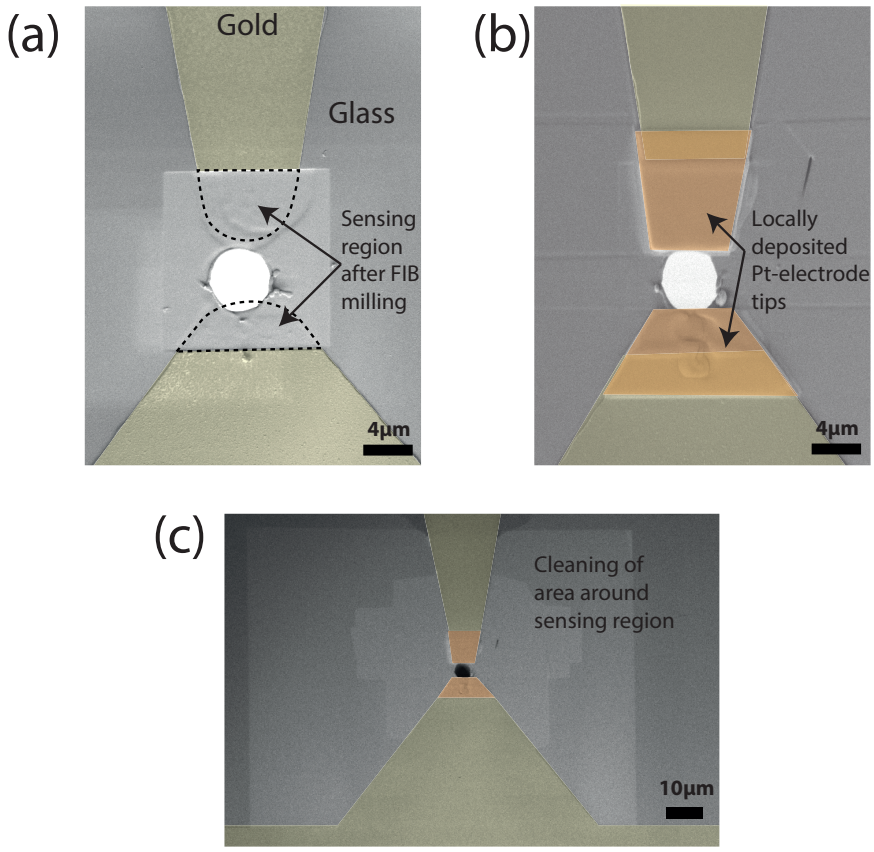

Figure 3.12: SEM images of sensing region. The gold layer, deposited with PVD is colored in yellow while the Pt, deposited with the FIB process is colored in orange. (a) FIB milling of the Au-electrode tips in the vicinity of the micropore to clean up the sensing region. (b) Locally deposition of Pt at the vicinity of the micropore using FIB induced deposition. (c) FIB milling induced cleaning of the sensing region from sputtered Pt to prevent a short circuit between the signal line and the ground metalization.

the laser beam. The laser focus is first adjusted onto the metalization layer and the crosshair of the laser software, which marks the center of the beam, is centered directly in between the end of the signal line and the ground electrode. This position is stored and the laser is then focused onto the backside of the RF chip. With respect to the stored position it was found that, for placing the MP into the sensing region, the stage has to be moved in x and y direction by a certain amount, depending on the desired pore size and the projection mask used for drilling the pore.

A typical example of a pore drilled in the sensing region is shown in Fig. 3.11 (c). With respect to the electrodes, the accuracy of the placement is ± 2 µm which corresponds with the accuracy of sample stage of the laser unit that can move in steps of 1 µm in x- and y-direction.

An optimal signal, originating from translocating particles, is only expected if the

pore is perfectly aligned with the electrodes. Thus, an offset of ±2 µm is in general not acceptable. Furthermore, it shall be pointed out that thicker electrodes in the vicinity of the MP can be advantageous in terms of signal-to-noise. The metal thickness cannot be varied a lot with a PVD process. Both because of economical reasons because of the high consumption of the gold for the production of the chip and for practical reasons as a very high metal thickness is difficult to lift off after the metal evaporation. Therefore, the sensing region is optimized using a focused ion beam (FIB). The FIB allows for locally milling unwanted material as well as for local deposition of metal with highe accuracy.

The process steps are documented in Fig. 3.12. To optimize the sensing region, in a first step the gold deposited by PVD as described before, is removed in the vicinity of the MP. This step cleans up the region around the MP and prepares the region for FIB induced metal deposition. The resulting structure is shown in Fig. 3.12 (a).

In a second step, metal is deposited onto the sensing region by locally injecting a precursor gas which molecules contain a platinum atom. Scanning the ion beam over a predefined region (orange region shown in Fig. 3.12 (b)), ensuring that the region where Pt is deposited has good overlap with the Au electrodes, enables to locally deposit metallic platinum. Ga-ions hitting the precursor gas destroy the complex which results in the local deposition of metallic Pt. This process can be done with high accuracy, thus allowing to vary the film thickness at the tip of the electrodes to a high extend (10 nm − 10 µm) and it allows for placing the electrode tips in the near vicinity of the pore. This further increases the signal strength as it will be discussed in Sec. 3.6.2. For a metal deposition that is flat over the whole scanning area it is important that the Ga-beam has a short dwell time on each position of the scanning area (i.e. 0.1 µsec) and that the beam is moving in multiple passes back and forth over the region.

As a last step, the sensing region around the pore has to be cleaned by locally milling this region with the Ga-beam. It is mandatory as the metal evaporation step is predominantly happening within the predefined scanning area but there is always sputtering happening which leaves a thin layer of Pt metal around the electrode tips. The sputtered metal is sufficient to short-circuit the signal line and the ground metalization. The finished sensing region is shown in Fig. 3.12 (c).

3.5.3 RF Interfacing

Finally, the glass chip has to be interfaced with the measurement setup. The glass chip is soldered onto a two-sided and custom-made printed circuit board (PCB). The top and bottom view of the final device is shown in Fig. 3.13 (a) and (b).

Two SMA connectors are soldered to the PCB enabling to connect the chip to the transmission line (RF-input) and to apply a DC voltage across a varactor diode, which

is used for impedance matching the device (DC-bias input). The central pin of the RF-input SMA connector is soldered to a macroscopic signal line on the PCB and the outer connector is soldered to the corresponding ground metalization (see Fig. 3.13 (a)). Thus, the input wave can propagate as a quasi-TEM wave until it reaches the glass chip that is soldered into the PCB accordingly. The second SMA connector is connected on the bottom of the PCB (see Fig. 3.13 (b)). Two metal connections are soldered to the central pin and the outer conductor thus allowing to apply a bias voltage via a BNC cable, without the need to introduce a second cable between this input and the DC source. For the experiments, the screw cap (see Fig. 3.13 (b)) is used for connecting the chip to the pressure control via a corresponding connector[3]. The connector to the screw cap further accommodates an optional Ag/AgCl electrode thus allowing to measure resistive pulse signals simultaneous to the RF measurements.

The schematic of the impedance matching network is given in Fig. 3.13 (c). It consists of a varactor diode in series to the signal line. Via through holes in the PCB, the DC voltage can be applied across the varactor diode. To prevent any DC to leak into the RF-chip or the RF-input port, two capacitors with a capacitance of 100 µF are soldered in series to the varactor. To further prevent the RF-wave leaking into the DC generator two 1 MΩ resistors are soldered in front of the the two terminals of the DC-bias SMA connector.

3.6 RF Simulations and Measurements

In this section the RF measurements are discussed. The section starts with a FEM simulation on the chip geometry. In this discussion it is shown numerically how a reflection measurement can be used to detect single particles. Furthermore, it is discussed how the geometry has to be designed to achieve a reasonable signal in the scope of this reflection measurement. After introducing the theoretical aspects, an experimental discussion follows. It is shown that the chip is designed in a way that it will act as a tank-circuit with an optimal point of operation at frequencies above 700 MHz. This point of operation is the point where the impedance of the RF chip is matched to the 50 Ω transmission line setup it is attached to. It will be discussed how this impedance matching is conducted and how this influences the measurement performance. The chapter is closed with the discussion of the reflection measurement which will be carried out by sampling the temporal detuning of the chip, due to the translocation of particles through the sensing region, using a VNA directly.

[3]Port-a-Patch Microscope Slide, Nanion

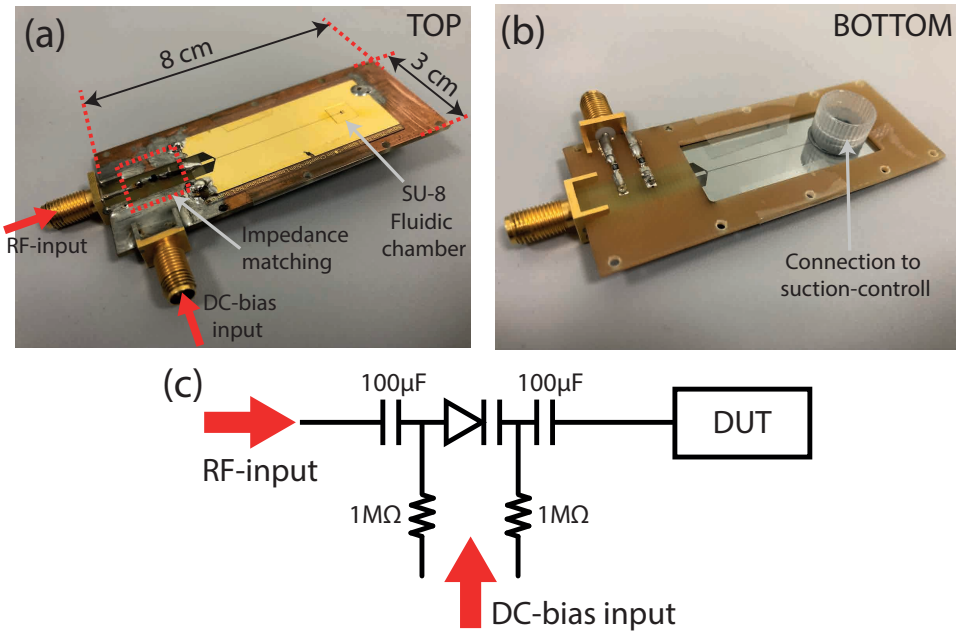

Figure 3.13: Photograph of top (a) and bottom (b) of the final RF device. The glass chip is soldered on a custom printed circuit board which is accommodating the impedance matching circuit. Two SMA connectors are used to interface the RF source to the chip and to tune the impedance matching circuit with an external DC bias. (c) Schematic of the impedance matching circuit soldered onto the PCB, consisting of a tunable varactor diode, two DC blockage capacitors and two resistors preventing the leakage of the RF wave into the DC bias port.

3.6.1 RF Simulations

In the following the simulated response of the RF chip is discussed, which is investigated using a FEM simulation on the sensing region of the RF chip. The simulation is conducted with the software package COMSOL similarly to the simulation discussed in Sec. 2.3.1. The schematic of the simulation geometry is given in Fig. 3.14 (a). The pore and the glass substrate have the same dimensions as those in Sec. 2.3.1. Additionally, the CPW metalization is added to the model. A boundary condition with zero thickness and perfect electrical conductivity (i.e. a perfectly electrical conductor (PEC) boundary condition) is used to model the metal layer. It is a reasonable approximation as in the experiments the metalization thickness of the CPW is three orders of magnitude smaller than the substrate. To decrease the computation time and to avoid a scaling problem between the smallest structure (i.e. the micron sized pore) and the biggest structure (i.e. the $5\,\mathrm{cm} \times 3\,\mathrm{cm}$ glass substrate) only the sensing region is modeled. It comprises of the pore in the glass substrate and the fluidic chamber on top of the sensing region. To study the effect of a finite thickness of the tips of the electrodes, which are facing the MP,

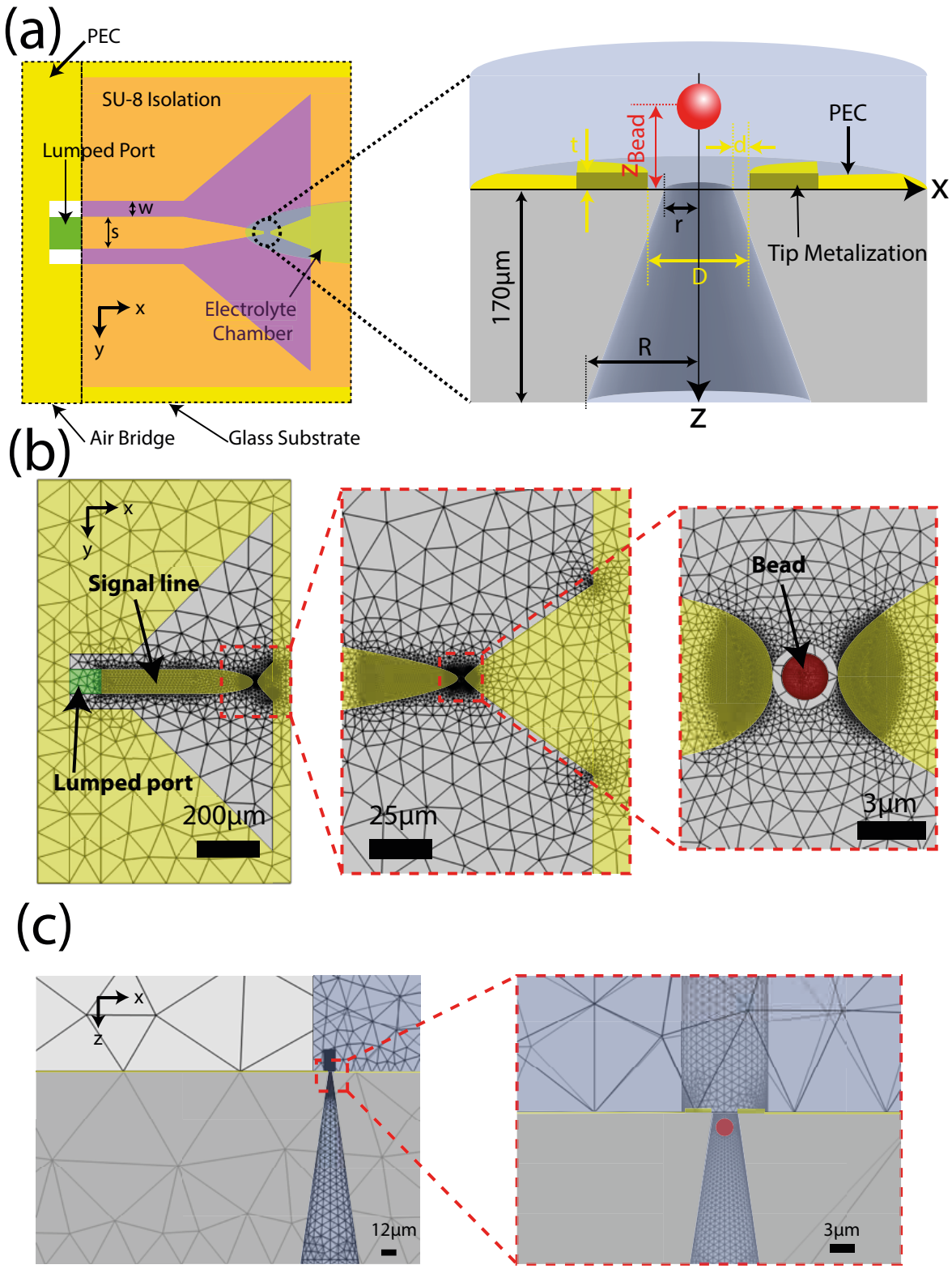

Figure 3.14: (a) Schematic of the simulation geometry used to model the micropore measurements. (zoomed-in) Cut through the sensing region of the RF chip. (b) Mesh of the model shown from the top. The zoomed-in views show more details at areas around the micropore. The bead is colored in red while the metal layer are colored in yellow. (c) Mesh of the model shown from the side. The same mesh is used for the RPS simulation discussed in Sec. 2.3.1

an additional geometry with finite thickness is added in the vicinity of the pore. This geometry is modeling the thick electrodes that are produced by the local metal deposition using the FIB process described in Sec. 3.5.2 and shown in Fig. 3.12 (b) and (c). The surface of this geometry, similarly to the CPW metalization, is set to be a PEC, too.

Compared to the pore region where the particle detection is taking place, the whole simulation geometry is still much larger. To keep the computation time as small as possible, the mesh has to be refined in such a way that the precision of the model is not compromised which is done in multiple refining steps. The mesh on the signal line is refined allowing for a precise simulation of the reflection measurement (see Fig. 3.14 (b)). In the vicinity of the pore (i.e. 10 µm above and below the pore opening) an extremely small mesh size is chosen. The same mesh size is chosen for the bead structure. Finally, the remaining model was meshed coarsely as the behavior far from the pore region does not contribute significantly to the RF response and a coarse mesh helps to decrease simulation time.

The physics that are solved for, is the RF-module that is implemented in the COMSOL software package. This module enables to interface the geometry with an input port through which an electromagnetic wave is introduced. The port is used to evaluate the scattering parameter and port impedance which is characteristic for the overall geometry. Furthermore, the electrical fields due to the presence of the waves traveling on the modeled transmission lines can be evaluated for the whole geometry.

Within the simulation volume, RF excitation is implemented using the so called lumped ports. A lumped port is situated between the signal line and the ground metalization. To realize that the two ground metalization layers are connected, a bridge is introduced in the simulation volume consisting of a PEC (see Fig. 3.14 (a)). The gap between the bridge and the signal line is closed with the lumped port at which the RF signal is fed into the simulation volume and where the S-parameter S_{11} and the port impedance Z_{port} can be measured numerically. Following the discussion in [128] S_{11} is calculated in the following manner: The characteristic impedance in the simulation volume is set to $50\,\Omega$. First, the geometry is simulated without a polystyrene sphere in the simulation volume thus giving the complex measured impedance at the lumped port Z_{ref} which is used as the reference impedance. In a second step, a parametric sweep is conducted during which a particle is translocated through the pore. For every particle position the lumped port impedance Z_{port} is determined. The reflection parameter S_{11} is then calculated via

$$S_{11} = \left| \frac{Z_{\mathrm{ref}} - Z_{\mathrm{port}}}{Z_{\mathrm{ref}} + Z_{\mathrm{port}}} \right|. \tag{3.40}$$

Eq. 3.40 gives a measure for the reflection of the RF device in the presence of a translocating particle. In the simulations discussed, different particle diameters are tested.

These particles will have a spherical geometry with different radii and a constant dielectric constant $\epsilon = 2.3$.

3.6.2 Discussion of the RF Simulations

Fig. 3.15 shows the calculated magnitude of the electric field in the z-y-plane for a bead translocating through the MP. The simulation includes thick electrode tips with a thickness of $t = 1\,\mu m$ which are $d = 1\,\mu m$ away from the MP edge and both electrode tips are $D = 5\,\mu m$ away from one another (see zoomed-in view in Fig. 3.14 (a)). The RF frequency at which the model is simulated is 1 GHz. For every bead position the model is solved, thus showing how the electric field is influenced by the bead with respect to the z-position of the bead.

The magnitude of the electric field is focused at the end of the signal line and at the end of the ground metalization. Therefore, the translocating particles only experience a field gradient when they are located in the vicinity of the metalization layer. As can be seen in Fig. 3.15 (i-iii) the field distribution within the bead is not very different from the field in the water. It is not expected that in this situation, the overall reflection of the chip is altered much. The same is true for the situation when the bead has passed the metalization layer (see Fig. 3.15 (vii-viii)). Significant field gradients are only visible when the bead is located near the metalization layer (see Fig. 3.15 (iv-vi)).

To quantify these observations the reflection coefficient S_{11} is calculated for the model with respect to the position of a particle according to Eq. 3.40. In Fig. 3.16 (a) the reflection coefficient for different bead sizes is plotted for a translocation as discussed in Fig. 3.15. A green vertical bar indicates the position and thickness of the metalization layer. Obviously, bigger particles lead to a bigger RF response. The RF response that is caused by the translocating bead is asymmetric with the highest value when the center of the bead is around 1 µm away from the glass surface. This behavior is very different from the corresponding DC response were the biggest amplitude is reached when the bead is located inside the pore (see Fig. 2.11). When the bead is approaching the pore layer, the reflection increases until it reaches a maximum when the radius intersects with the upper layer of the thick metalization. The response quickly fades off, when the bead is inside the pore, which is in accordance with the field simulations as the field gradient inside the pore is weakened so that the bead does not see the field anymore.

In Fig. 3.16 (b) the results are shown for a model which was adjusted in a way that the thick metalization was put in the near vicinity of the pore so that the tips of the electrodes coincide with the outer edges of the pore (see inset in Fig. 3.16 (b)). Consequently, the amplitude of the RF response is increased for every bead radius. As the tips are closer, the field gradient between the tips is expected to be much bigger and thus the beads

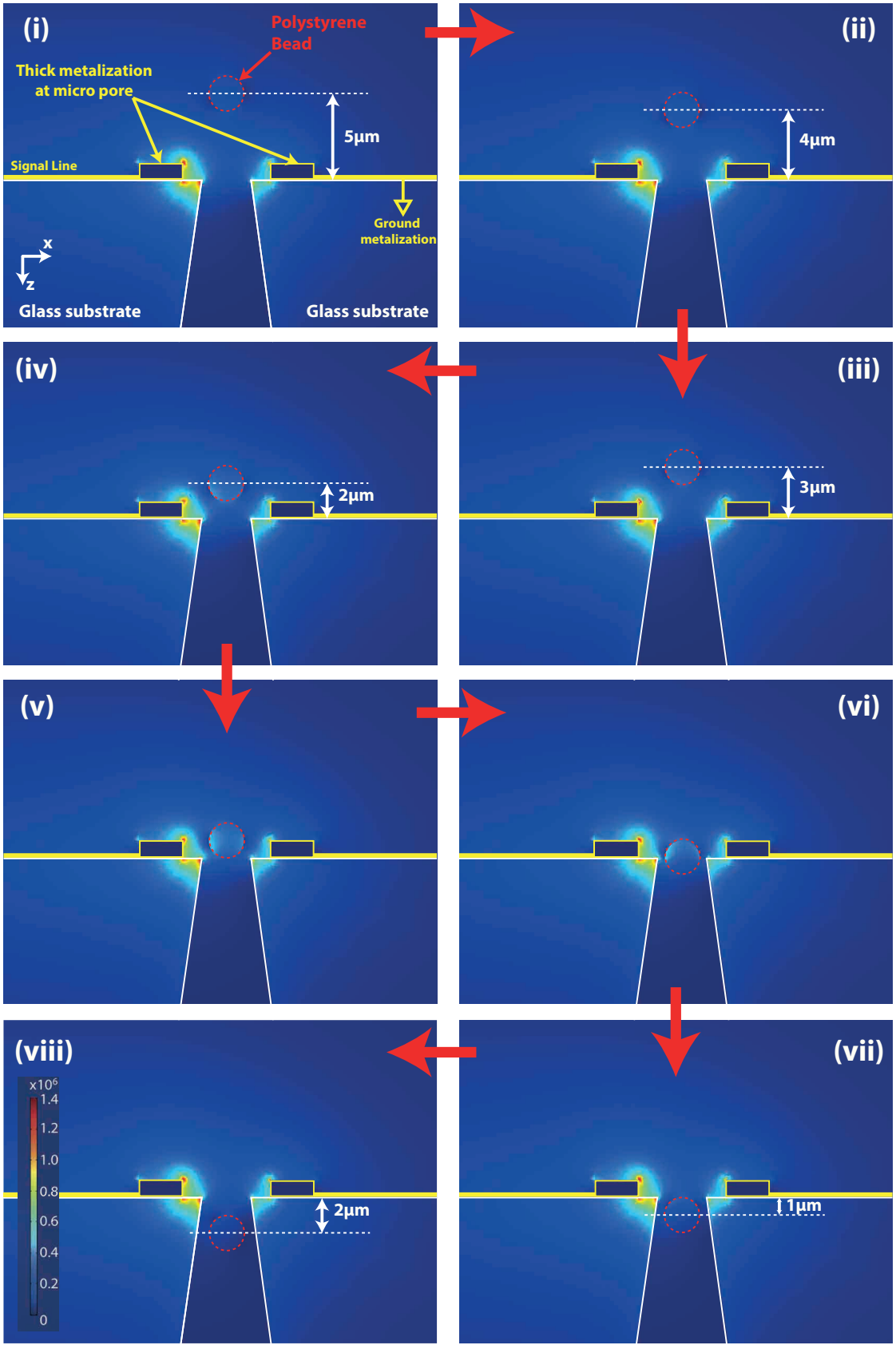

Figure 3.15: Magnitude of the electric field along the pore axis during translocation of a polystyrene bead through the pore. Images (i)-(viii) show the field distribution within the plane through the sensing region for different bead positions. The particle shows polarization effects only if it is located near the metalization layer (iv)-(vi). Above this layer and inside the pore the bead does not interact with the electric field.

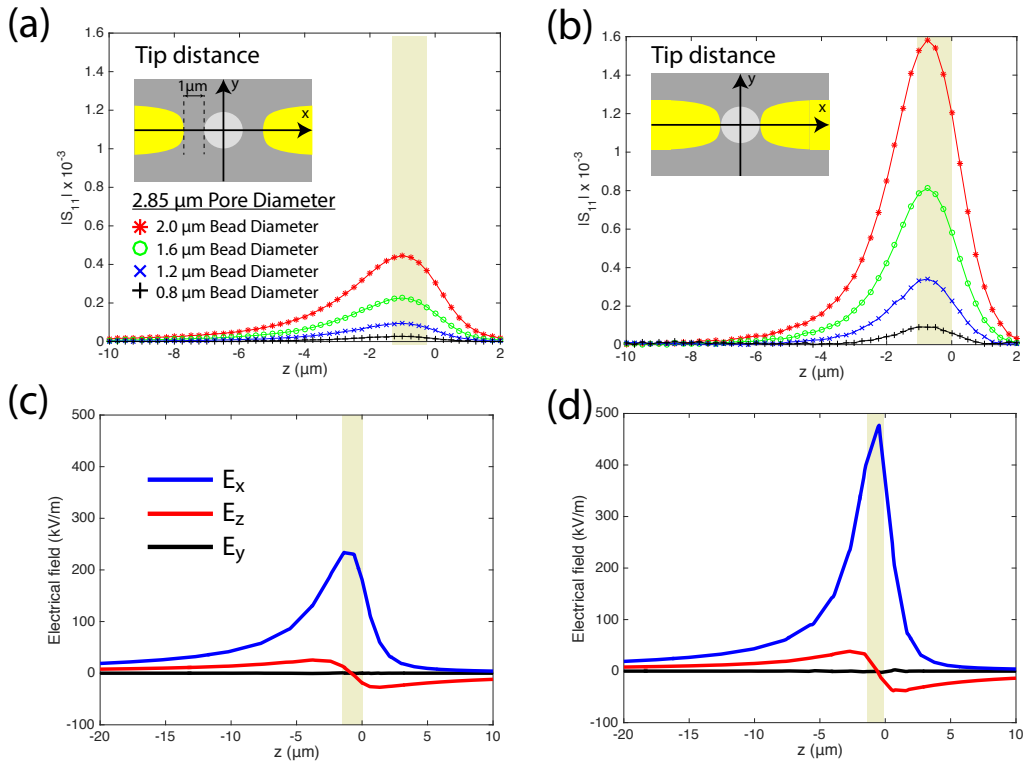

Figure 3.16: (a) and (b) Simulated reflection of the RF chip during the translocation of polystyrene beads through the micropore. Metalization thickness of the electrode tips in the simulation is $t = 1\,\mu m$ and it is marked in the plots as a green band. The diameter of the beads is changed from $2\,\mu m$ (red asterisk), $1.6\,\mu m$ (green circle), $1.2\,\mu m$ (blue cross) to $0.8\,\mu m$ (black cross). The pore opening is located at $z = 0$ and the small pore diameter is $2.85\,\mu m$. Electrode tip distance is $d = 1\,\mu m$ (a) and $t = 0\,\mu m$ (b). In (c) and (d) the components of the electrical field along the x-, y- and z-axis is shown.

experience a much bigger electrical field.

To understand the behavior, the components of the electrical field along the central z-axis are shown in Fig. 3.16 (c) and (d), for both electrode tip positions. The electric field in y-direction is almost zero throughout the axis. A small contribution to the electric field is observed in z-direction. But the biggest field component is the field in x-direction (i.e. E_x) which is the direction of the signal line. As expected the biggest value of E_x is observed in the metalization plane but as the distance D of the electrode tips is increased by $2\,\mu m$ the maximal value of E_x drops by almost a factor of two. As a consequence the signal amplitude decreases.

In Fig. 3.17 the thickness t of the signal and ground metalization is decreased to $200\,nm$. The position of the electrodes is similar to the situation shown in Fig. 3.16 (b) and the reflection caused by the translocating particle is shown. While the overall re-

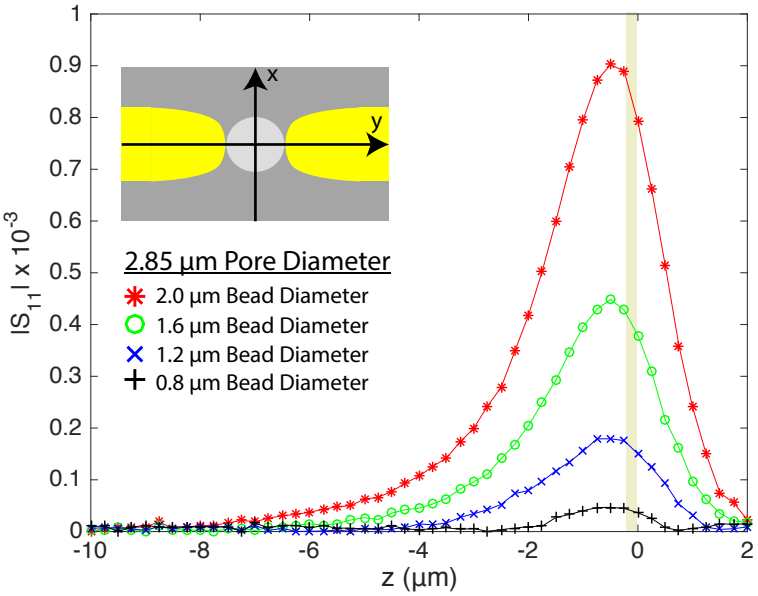

Figure 3.17: Simulated reflection of the RF chip during the translocation of polystyrene beads through micropore. Metalization thickness in this simulation is $t = 200\,\text{nm}$. The diameter of the beads is changed from 2 µm to 0.8 µm with the same color code as in Fig. 3.16 (a) and (b). The pore opening is located at 0 and the small pore diameter is 2.6 µm.

sponse is similar, the amplitude of the reflected signal is smaller than for the electrode tips with a thickness of 1 µm. In terms of the signal amplitude it is probable that the optimal thickness of the electrode tips coincides with the dimensions of the particles that shall be investigated. If the tip thickness would be substantially bigger than the particle dimensions, the event duration will be increased without increasing the event amplitude. Still this parameter remains a matter of speculation but with a more parallel RF chip production, as discussed in the outlook of the thesis, this question can be answered experimentally in future.

In summary, it is advantageous to have thick electrodes in close proximity to the MP. This reflects on the processing strategy presented previously where platinum electrodes are locally introduced by the FIB deposition adjacent to the MP.

3.6.3 Impedance Matching

The following discussion is based on the content of our publication in Physical Review Letters that can be found in Ref. [129].

Precise reflection measurements require a device that is well matched to the source impedance of the measurement equipment. The experiments presented are integrated

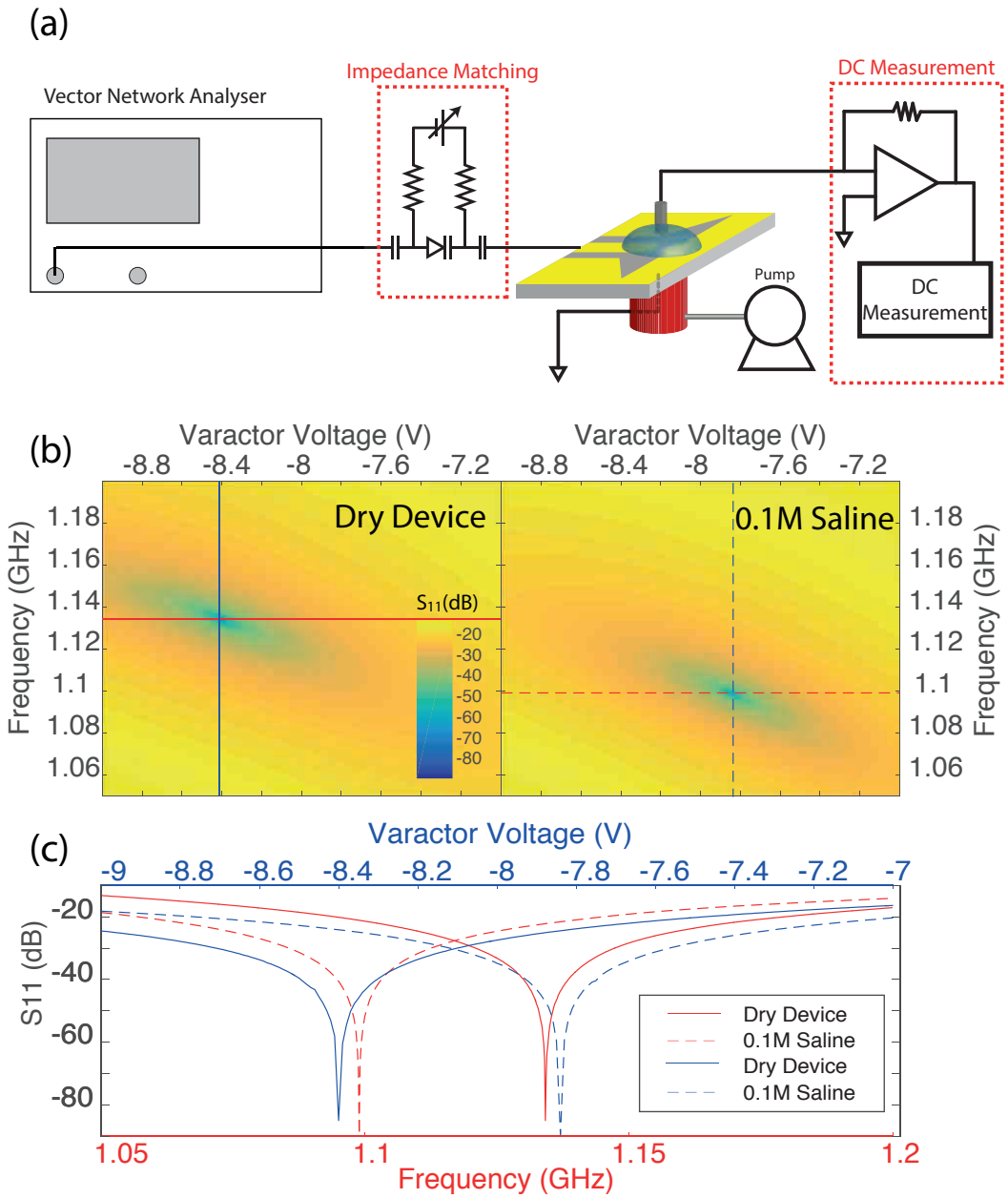

Figure 3.18: (a) Schematic of the VNA based measurement setup including the impedance matching network. (b) Sweep across the tunable varactor voltage and the excitation frequency produced by the VNA. The measurement is done for a dry device and a device filled with electrolyte solution. For one combination of frequency and voltage the device shows zero reflection which is the point of operation. (c) Cut through the point of operation for the dry and wet device. The figure is taken from our first publication regarding this subject [129].

in standard $50\,\Omega$ transmission lines and test equipment. The schematic of the setup is shown in Fig. 3.18 (a). Here the RF-input port of the RF chip is connected to one port of the VNA[4]. As is described in Sec. 3.3.4 a load which is not matched to the source impedance will lead to a reflection of the incident traveling wave. Therefore, for a reflection measurement as presented in the following it is important to minimize any impedance mismatch of the load to the transmission line. Otherwise the receiver will measure the reflected power and if the signal is very weak it will be buried in noise solely due to the impedance mismatch. For validation purposes simultaneous RPS measurements are conducted simultaneously.

To impedance match the device to the transmission line, a varactor-based impedance matching circuit is implemented. A schematic of the circuit is shown in Fig. 3.13 (c). The central part of the circuit is a high frequency varactor diode[5]. It is used as a voltage controlled capacitor with capacitance values ranging from $1 - 10\,\mathrm{pF}$ depending on the applied bias voltage across the the varactor. Changing the capacitance of the varactor will change the overall impedance of the RF chip.

Prior to time domain experiments, a two dimensional scan is done sweeping over the voltage, applied across the varactor diode and the RF frequency driving the RF chip. Eq. 3.30 shows that there is no reflection at a RF port if perfect impedance matching (i.e. $Z_0 = Z_1$) is achieved. Therefore, the scan is looking for reflection minimum at a specific combination of input frequency f and varactor voltage V. The results of the match are depicted in Fig. 3.18 (b). On the x-axis the applied voltage across the varactor and on the y-axis the input frequency is given. The plot is generated by merging the frequency sweeps obtained by the VNA for individual varactor voltages while the reflection (in dB) is given by the color code shown in the legend.

First the impedance matching is obtained for a dry device, i.e. no electrolyte solution was introduced onto the sensing region. The results are depicted in the left plot of Fig. 3.18 (b). For one point, the reflection coefficient reaches a minimum. In practice the actual depth of the impedance match is determined by the number of points within the frequency and voltage sweep but overall reflection coefficients of $-80\,\mathrm{dB}$ and less are routinely obtained for the point of best match. The solid red and blue lines in Fig. 3.18 (b) display the measured reflection through the point of best match versus the voltage across the varactor diode and the input frequency, respectively.

In the right plot in Fig. 3.18 (b) the corresponding result is shown when 100 mM KCl solution is introduced into the chip. Accordingly, the response through the point of best match is shown in Fig. 3.18 (c). For the wet device the point of best match is shifted

[4]PNA Network Analyzer, N5222A, 10 MHz-26.5 GHz, Keysight Technologies
[5]Silicon Tuning Diode: BB 833 SOD323, Extended frequency range up to 2.5 GHz.

towards lower frequencies and higher varactor voltages and thus to a lower capacity. Obviously, the presence of the liquid alters the impedance of the device.

Time domain reflection experiments which are discussed in the following are carried out in the following manner. The RF-chip is flooded with electrolyte solution and is impedance matched to the $50\,\Omega$ transmission line resulting in minimal reflection at the point of best match. At this point, i.e. at a certain varactor voltage V_0 the VNA is set to the corresponding frequency f_0 and the reflection S_{11} is sampled over time. This operation mode is called the constant wave (CW) mode. Changes in the chip impedance, caused by translocating particle will alter the reflection properties temporarily and thus a pulsed increase in S_{11} will be detected every time a particle translocated through the sensing region.

3.6.4 Noise in VNA Measurement

Before discussing the direct time domain reflection measurements with polystyrene beads, the noise in CW measurements at the point of best match shall be discussed. Since a minute change of the overall impedance change due to the translocation of a particle through the detector is expected, a low baseline noise floor is required to perform a successful measurement. As discussed in Sec. 3.3.5 a critical parameter of the VNA measurements is the IFBW. Changing the IFBW to lower values decreases the contamination of high frequency noise but simultaneously decreasing the temporal resolution of the measurement as is discussed in the following.

For the investigation of the noise floor, a RF chip is impedance matched and the CW time trace is recorded for a set number of points in one sweep. The CW data presented is obtained at a frequency of $f_0 = 961\text{MHz}$ at an output power level of $0\,\text{dBm}$. For every sweep, which contains 6402 data points, a different IFBW was selected starting from $1\,\text{kHz}$ to $10\,\text{kHz}$. The resulting time traces are shown in Fig. 3.19 (a). On the x-axis the time is plotted while on the y-axis the measured S_{11} is shown in dB. The plot ranges are chosen to be equal thus it is apparent that with increasing IFBW the noise floor is increasing, too. To further illustrate the change in noise floor a normalized histogram is shown at the right side of the time traces in Fig. 3.19 (a) that contains all reflection measurement data points. A broader noise floor distribution thus translates into lower histogram maxima indicating that the noise floor increases with increasing IFBW.

In Fig 3.19 (b) the measured RMS noise is plotted for IFBWs between $1\,\text{kHz}$ and $10\,\text{kHz}$. Every datapoint in the plot contains a full sweep (i.e. 6402 points). The plot indicates a linear trend between IFBW and noise floor.

Another important aspect of the measurement is clearly visible: At higher IFBWs the time sweeps that can be measured are shortened as a higher IFBW comes with a higher

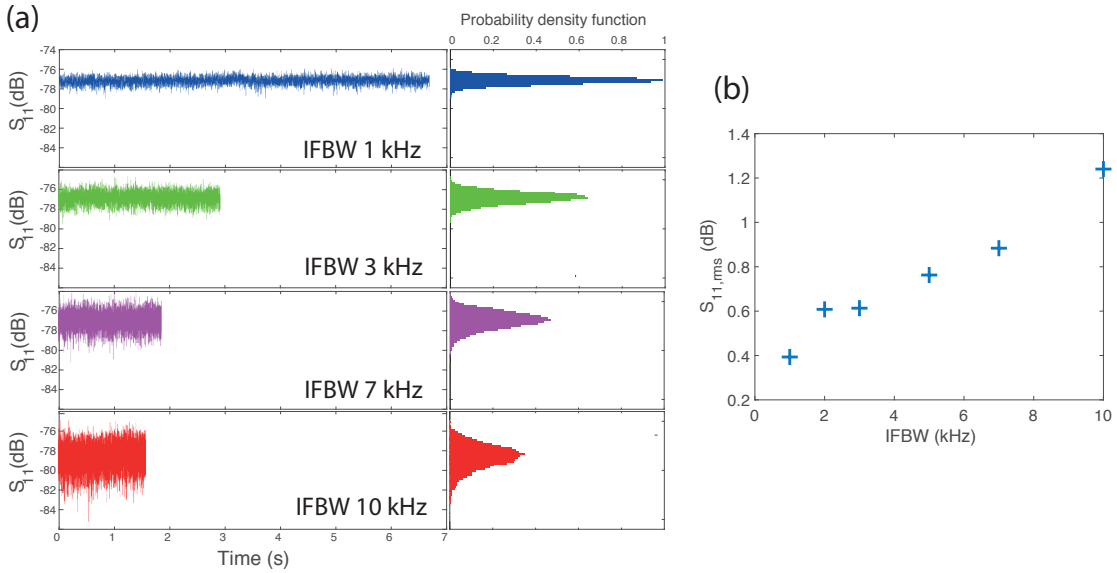

Figure 3.19: Noise measurements of a dry RF chip. In (a) CW measurement of a dry RF chip at the point of best impedance match for different IFBWs are shown. All measurements comprise of a sweep with 6402 data points. For every measurement a normalized histogram which contains the value of the data points is shown. The normalization leads to more narrow distributions for a lower noise floor. (b) RMS noise versus the IFBW setting of the VNA.

sampling rate set by the VNA internally. Data that is acquired, is stored permanently by the machine between sweeps. During this time the machine stops acquisition thus producing dead times between sweeps that might compromise the overall measurement. This is especially true as it is mandatory for constant measurement streams over minutes or even hours. As a IFBW of 1 kHz allows for the longest sweep time with the lowest noise floor it comes with the drawback of a very limited sampling rate. The measurement is extremely slow compared to the higher IFBW measurements. Nevertheless, it will be discussed in the following that a high sampling rate does not help if the noise floor is too high to detect the tiny signal originating from translocating particles.

3.6.5 Time Domain Reflectometry Measurements with Polystyrene Beads

Here, time domain reflection measurements using the VNA are presented and discussed. For a first characterization of the chip design a reflection measurement of a polydispersed suspension of polystyrene beads is performed. The suspension contained beads with diameter of 200 nm and 500 nm diluted within a 100 mM KCl solution. A particle concentration of (10^5-10^6) beads/ml is chosen, which is a typical concentration giving a

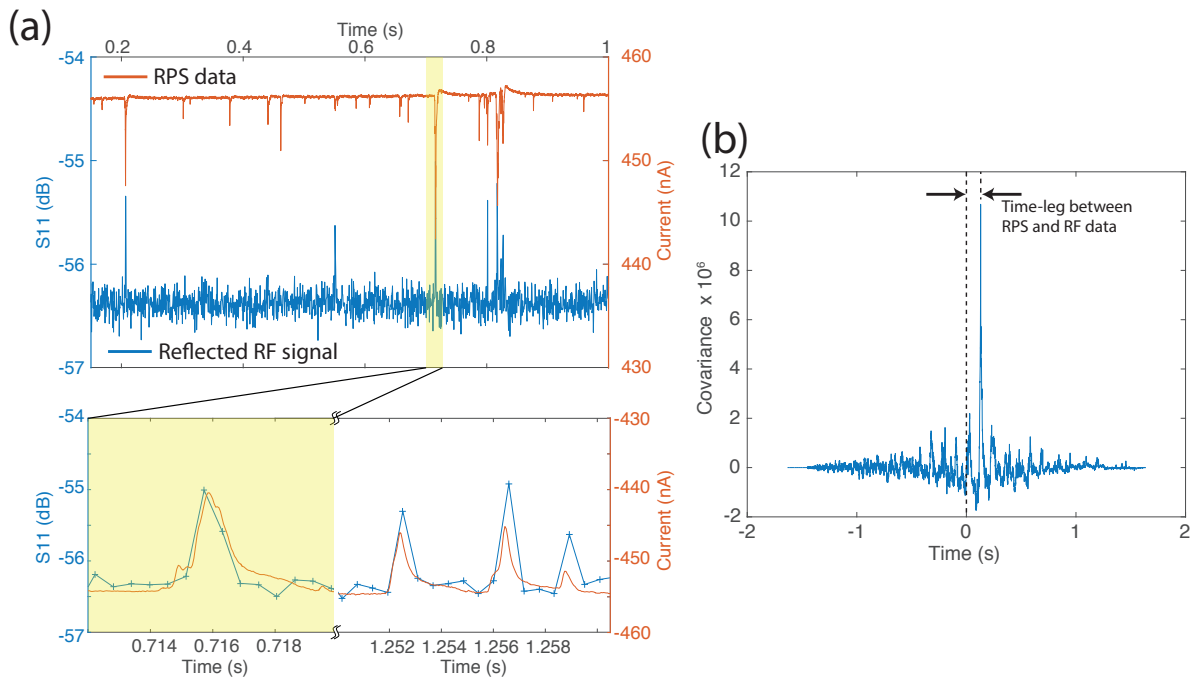

Figure 3.20: (a) Direct reflection measurement of a suspension of 200 nm and 500 nm polystyrene beads. The data is sampled at a IFBW of 1 kHz to reduce the background contamination. The zoomed-in views show examples of individual bead translocations. While the left event is a zoomed-in view into the top figure, the three events shown on the left are part of the same measurement but are not given in the upper overview. The figure is taken from our first publication regarding this subject [129]. (b) Covariance of the RPS method measurement and the corresponding RF reflection measurements.

compromise, based on experimental experience, between event rate and the overall time it is possible to measure without clogging the MP. The MP used for the experiments has a diameter of 4 µm.

Prior to the time-domain measurement the chip is impedance matched to the 50 Ω transmission line setup, according to the discussion in Sec. 3.6.3. When the point of best match is determined as shown in Fig. 3.18 (b) and (c) the operation mode of the VNA is changed from frequency sweep to the CW mode. Results for a CW sweep with an IFBW of 1 kHz and a corresponding maximal sampling rate of 1.650 kHz are shown as the blue trace in Fig. 3.20 (a). S_{11} is measured versus time and simultaneously RPS data is acquired for validation and comparison. The time-synchronized RPS data is shown in the same figure as a red trace.

To prevent particle translocation and thus a non steady reflection measurement during impedance matching, no pressure is applied across the MP during impedance matching. When the CW measurement is started, particle translocations are induced by applying

a suction to the MP and the particle translocation is observed within seconds. But simultaneously the induced flow of electrolyte alters the impedance of the chip and thus S_{11}. It is observed and shown in Fig. 3.20 (a) that the baseline reflection is increased (from $< -70\,\mathrm{dB}$ to $-57.7\,\mathrm{dB}$). Obviously, this shift does not hinder particle detection as this baseline value is still a high degree of impedance matching. It will be discussed in Ch. 5 that slight detuning of the RF chip can even help to increase the signal amplitude (see Sec. 5.2).

Temporal increases in S_{11} due to the translocation of polystyrene beads are clearly visible over the baseline. In the presented configuration the maximum peak height is in the range of 1 dB.

The corresponding RPS measurement is represented in the red trace in Fig. 3.20 (a). These measurements were obtained independently during the experiment without any hardware based synchronization between the RPS and the RF signal. Therefore, it was mandatory to synchronize the signals during post processing of the data. To do that a covariance estimation was performed on the two data sets. In a first step, the sampling rate of the RF-data is artificially increased to match the sampling rate of the resistive pulse trace. Here, it is important to ensure that this process does not distort the overall RF-trace. Once this is done, the algorithm is calculating the covariance between the two datasets for every data-leg, i.e. for every time offset between the two data sets. As the measurements are based on the same physical effect with similar event shapes it is expected, that the datasets are highly correlated when they are time-synchronized. This fact can be seen in Fig. 3.20 (b) where the covariance of the two data sets has one dominant global maximum for a specific time-leg. The time traces shown in Fig. 3.20 (a) are synchronized using this offset time.

A direct comparison between the resistive pulse und the RF-reflectometry measurements are shown for single events in the zoomed-in view of Fig. 3.20 (a). For illustrative purposes the resistive pulse signal is inverted.

The maximum of the two signal peaks match in the time domain. It does not necessarily reflect the physical reality as it is an artifact of the covariance based synchronization. The RPS simulations, shown in Fig. 2.11, and the RF simulations, shown in Fig. 3.16 and Fig. 3.17, even indicate that the maximal amplitudes of the two signals do not occur at the same time. While the particle induces the highest RPS signal when it is fully inside the MP, the corresponding RF signal is maximized before, namely when the particle is entering the metalization layer. Nevertheless, it is observed that every peak in the RF-measurement corresponds to a peak in the resistive pulse measurement, which clearly ensures that the peaks measured with the RF reflection technique are originating from translocating particles and are not measurement artifacts.

Another aspect is the limitation in sampling rate. In the zoomed-in view of Fig. 3.20 (a) the blue crosses indicate the individual sampling points of the VNA measurement. As it was mentioned previously, for the IFBW of 1 kHz the sampling rate was already set to the maximum value available at the VNA. The translocation speed of particles through the glass pores is in the sub-millisecond range and thus very often one translocation event in the reflection measurement is sampled with only one or two sampling points. It was shown in the simulation which are analyzed in Fig. 3.16 and Fig. 3.17 that the RF peaks are expected to have a characteristic shape which is not reproducible at this sampling rate. Furthermore, the low sampling rate leads to the effect that not every translocation event is observed because not every resistive pulse corresponds to an event within the RF reflection measurement.

The measurement strategy that is described in the following will solve for a lot of this ambiguities but it is important to point out that these results already show that the setup works as intended. Translocating particles lead to a measurable amplitude modulation and from the experiments it is save to say that the RF chip with a MP, which had a diameter of 4 µm, is capable of detecting polystyrene beads with diameter of at least 500 nm.

Chapter 4

High-Speed RF-Measurements

As discussed in the previous chapter, the direct sampling capabilities of the VNA are not sufficient to capture the details of the translocating particle through the MP. In the following, it shall be discussed how to address this issue. The section starts with an introduction into the heterodyne mixing measurement setup which is used to down convert the reflected RF signal in the frequency-domain and a lock-in amplifier that demodulates and samples the resulting reflection signal. Subsequently, the impedance matching characteristic and the noise properties of the time domain measurements are discussed in detail.

4.1 Heterodyne Mixing

A heterodyne mixing setup is implemented for low noise and high speed measurements and the schematic of the setup can be seen in Fig. 4.1. The working principle of the setup is similar to the working principle of the lock-in amplifier itself with the difference that for the reflection measurement only one frequency mixer is used for down-converting the frequency of the reflected RF signal. This downconversion is necessary because for the specific chip design the input RF frequency lies between 700 MHz and 1 GHz, which is above the frequency range that commercially available lock-in amplifiers, at reasonable costs, can process. In Fig. 4.1 the signal path is colored in red.

A signal generator[1] drives the RF chip at the frequency f_{RF}. The generated RF wave is first divided by an RF splitter[2] and one half of the signal is fed into the RF-chip via a directional coupler[3]. A directional coupler is a three port RF network. Waves are transmitted through the input-output port without loss. This path is basically a

[1] E8257D 250 kHz-50 GHz, PSG Analog Signal Generator, Agilent Technologies
[2] Splitter: ZFSC-2-372-S+ 10-3700 MHz, Mini-Circuits
[3] Coupler ZHDC-16-63-S+, 50-6000MHz, Mini-Circuits

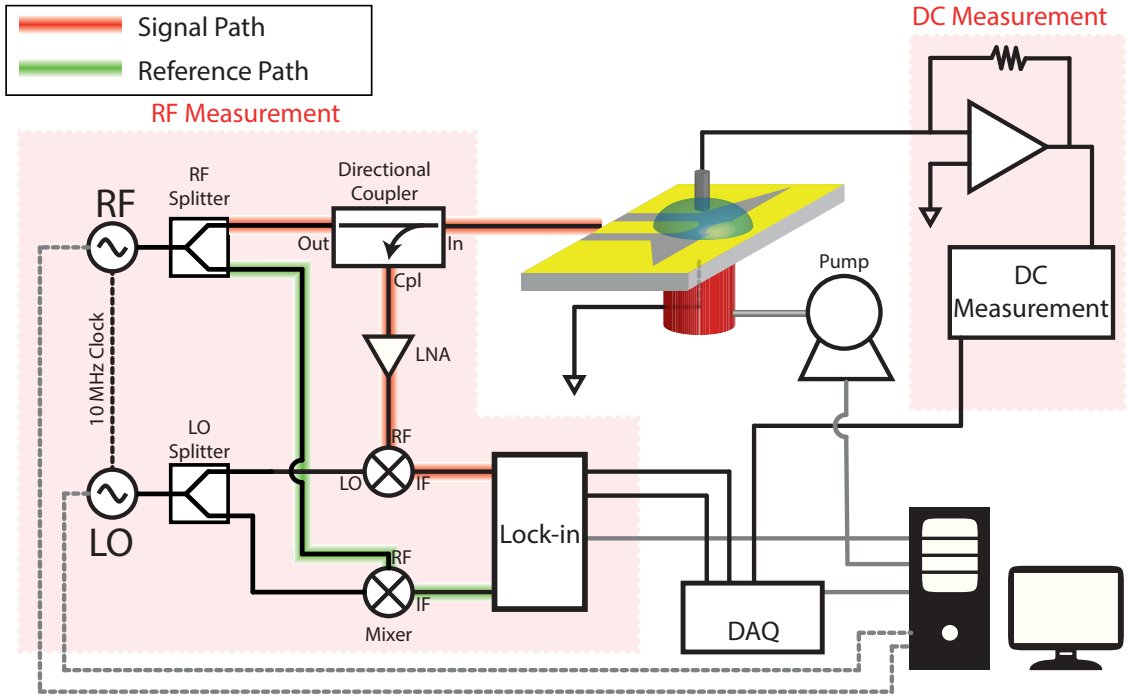

Figure 4.1: Measurement schematic for the low noise heterodyne mixing measurement setup. DC Measurements are conducted by using a conventional amplifier with a feedback resistor. For reflection measurements (signal path - red) the chip is interfaced with a varactor based impedance matching network (not shown here). The RF signal is inputed into the chip using a directional coupler. Reflected signals are coupled out into the RF input of a frequency mixer. Here the RF signal is down converted with a LO signal, which has a fixed frequency difference from the RF signal. The IF signal is fed into a lock-in amplifier that uses an internal reference signal for comparison. For generating an external reference signal (reference path - green) the same RF and LO signals are used and while bypassing the RF chip and using a second frequency mixer a second IF signal is generated that can also be used as a reference signal for the lock-in amplifier. The data from the DC as well as from the RF measurement can be fed into a data acquisition system.

transmission line. A fixed fraction of the wave that transmits into the input port is coupled out into the third so called coupled port. In the experiments, a directional coupler with a coupling coefficient of 20 dB was used, which leads to a coupled signal that is attenuated by −20 dB. An important feature of the coupler is its isolation factor. This measure quantizes the attenuation of the coupled port with respect to waves transmitted into the output port. If a significant fraction would be transmitted from the output to the coupled port the reflected signal, originating from the RF chip, would be contaminated partially by the original driving RF wave. For the coupler which is used the coupling port is isolated by more than 50 dB from the output port. The RF wave which is reflected from the RF chip is attenuated by −20 dB when it exits the coupled port and a low noise

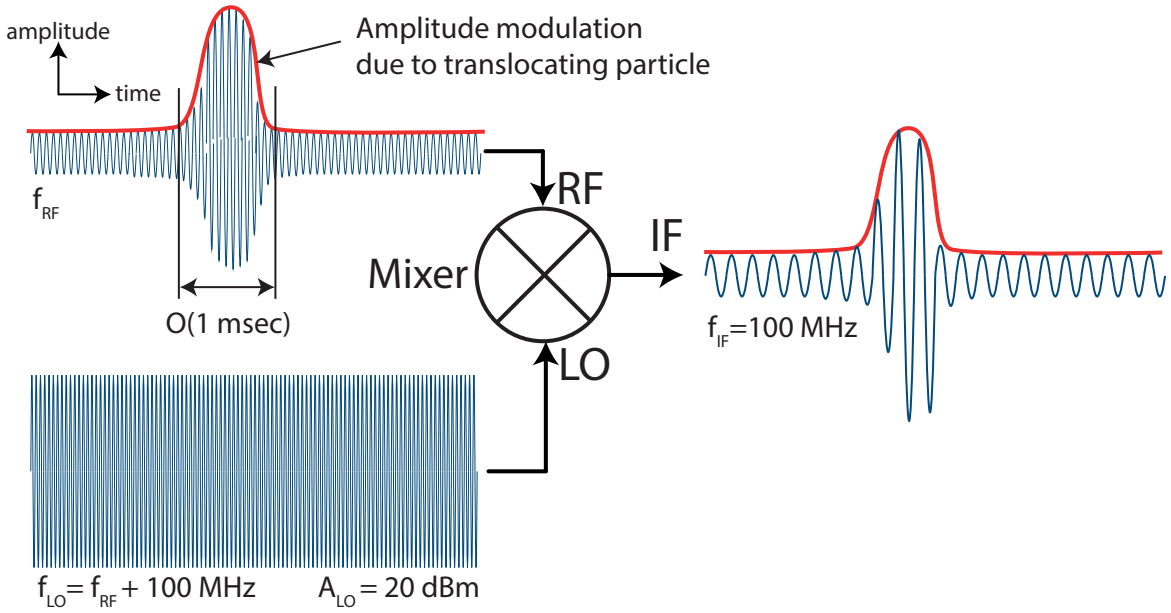

Figure 4.2: Principle of heterodyne mixing as used for the measurement. The RF signal is amplitude modulated due to the translocating particle. This fingerprint is modulated on the RF wave that is reflected from the RF chip. The LO signal is set to have a fixed frequency difference (i.e. 100 MHz for the experiments discussed) with respect to the RF wave. In the mixer the two waves are multiplied, leading to an IF signal showing the same AM as the original RF wave but the frequency of the carrier wave is decreased to 100 MHz which is $f_{\mathrm{RF}} - f_{\mathrm{LO}}$. The $f_{\mathrm{RF}} + f_{\mathrm{LO}}$ component is not illustrated here as it is filtered out due to the limited BW of the lock-in input port.

voltage amplifier[4] is used to increase the signal amplitude back again thus simplifying the further signal processing procedure.

The reflected wave undergoes a heterodyne mixing which is schematically illustrated in Fig. 4.2. The core of the mixing setup is the frequency mixer[5] [130]. As described in Eq. 3.34 the mixer is multiplying two waves that are traveling into the RF and local oscillator (LO) input of the device. Here, the RF wave is an amplitude modulated signal due to the translocating particle. The amplitude modulation (AM) is carried on the RF wave having a frequency f_{RF}. A second signal generator[6], which is operated at a fixed frequency difference with respect to the RF generator, drives the LO of the frequency mixer. Before the LO signal is connected to the mixer it is divided with another RF splitter[7]. One half of the signal is connected to the mixer. Both signal generators are synchronized using their 10 MHz reference clocks, which ensures that there is a stable

[4]Amplifier: ZX60-P33ULN+, 400-3000 MHz, Mini-Circuit
[5]Mixer: ZFM-15-S+, 10-3000 MHz, Mini-Circuits
[6]E8247C 250 kH-20 GHz, PSG CW Signal Generator, Agilent Technologies
[7]Splitter: RFLT2W0002GS 5 MHz-2000 MHz, RF-Lambda

phase relation between these otherwise independent signal sources. After the mixing process, the reflected RF wave is amplitude modulated on the resulting IF wave. This signal can be measured at IF = $f_{RF} - f_{LO}$ and as a matter of fact its carrier frequency is drastically reduced by preserving the AM and the phase of the original signal. In the experiments an IF = 100 MHz was used, if not stated differently. This allows to use signal recovery methods of commercially available lock-in amplifiers working for frequencies in the upper MHz regime[8].

The signal is demodulated and sampled by the lock-in amplifier. To do that, the amplitude modulated signal is fed into the signal input of the lock-in amplifier. Additionally, to the signal, the lock-in needs a reference signal to which the input signal is compared. The amplifier that was used for the experiments uses an external or an internal reference signal to perform this task.

In Fig. 4.1 the green path depicts the transmission line path that was implemented to extract a reference signal. It is basically the same path which is used for the signal but here the RF chip is bypassed. The reference signal has the identical frequency and phase as the reflected wave but it is not amplitude modulated due to the translocating particles. During the first experiments it was observed that the usage of this external reference path is not practical. The reflected signal amplitude is very low because of the impedance matching. Therefore, the lock-in amplifier cannot lock to the external reference signal. If the RF chip is highly detuned and thus if the amplitude of the reflected signal is increased, the lock-in can lock to the reference but this comes at the expense of the detuning the chip and thus potentially compromising the SNR.

The internal signal generator does show a better performance. If the phase of the signal is not measured the lock-in is capable to measure the amplitude of the reflected signal without limitations. It will be discussed in Sec. 5.2 that it is acceptable to slightly detune the chip. This detuning allows for using a phase locked loop (PLL) to phase lock the internal frequency generator to the input signal. With this technique it is possible to measure not only the amplitude of the reflected signal but a change in signal phase, too. As the additional reference path does not interfere with the measurement it was kept in the setup once the functionality of the setup was confirmed.

In principle the setup allows to conduct simultaneous DC measurements which adds a layer of complexity to the experiment and as it was shown in the previous chapter that the RF reflection signals can be synchronized to corresponding RPS signals no further RPS data is acquired and discussed in the following.

[8]UHFLI 600 MHz lock-in amplifier, Zuerich Instruments

4.2 Impedance Matching and Noise Characterization

As it has been mentioned in the previous chapter the RF chip has to be impedance matched to the source to show good sensing capabilities. The VNA results represent a proof of concept measurement that shall be further investigated in the following.

Impedance matching is the most prominent measure affecting the performance of the device. To determine the optimal impedance matching point, the reflectance of the RF chip is measured using the lock-in amplifier according to Eq. 3.35 and Eq. 3.37 for every combination of input RF frequency and voltage across the tuning varactor diode. If not stated differently the sweeping steps in the voltages is $\Delta V = 0.007\,\mathrm{V}$ and for the frequency the steps size is $\Delta f_{\mathrm{RF}} = 0.001\,\mathrm{MHz}$.

The power spectral density is measured for the presented setup, too. As the sampling capabilities of the lock-in amplifier are limited to 400 kHz the time domain signals, which are used to determine the PSD are sampled with an external data acquisition system, which has a sample rate of 2 MHz. This leads to a cutoff frequency of 1 MHz for the highest frequency component that can be measured in the time domain. In the following the PSD is determined by measuring a stream of 4 M points that are processed using a LabVIEW code, which determines the PSD using the Hanning method. To get a clear view on the shape of the PSD, the shown PSD is averaged 50 times using the RMS averaging routine with linear weights.

4.2.1 Influence of IF

Initial experiments are performed to test if the IF has an impact on the best matching point. It is further investigated on what influence the IF has on the noise characteristic of the device. The results can be seen in Fig. 4.3.

In Fig. 4.3 (a)-(c) the reflection characteristic for one device, which does not contain electrolyte solution in the sensing region, is shown for three different IFs starting from 100 MHz to 600 MHz. For the experiments, the RF power is set to 0 dBm. The dashed red and green lines indicate the frequency f_0 and the voltage V_0 where the RF chip is impedance matched, i.e. where the reflected wave amplitude is minimal. The solid red and green lines are the reflection response curves at the corresponding frequency and voltage. Obviously, the point of best match does not change significantly under varying IFs. The varactor voltage V_0 does change by less than 1% in the three experiments while the RF frequency f_0 changes maximally by 0.1%.

It is expected that the point of optimal impedance match should not vary drastically at different IFs. The IF is created by mixing the reflected RF and the LO signal. The reflected RF wave, in turn, is affected by the RF chip but it is unaffected by the mixing

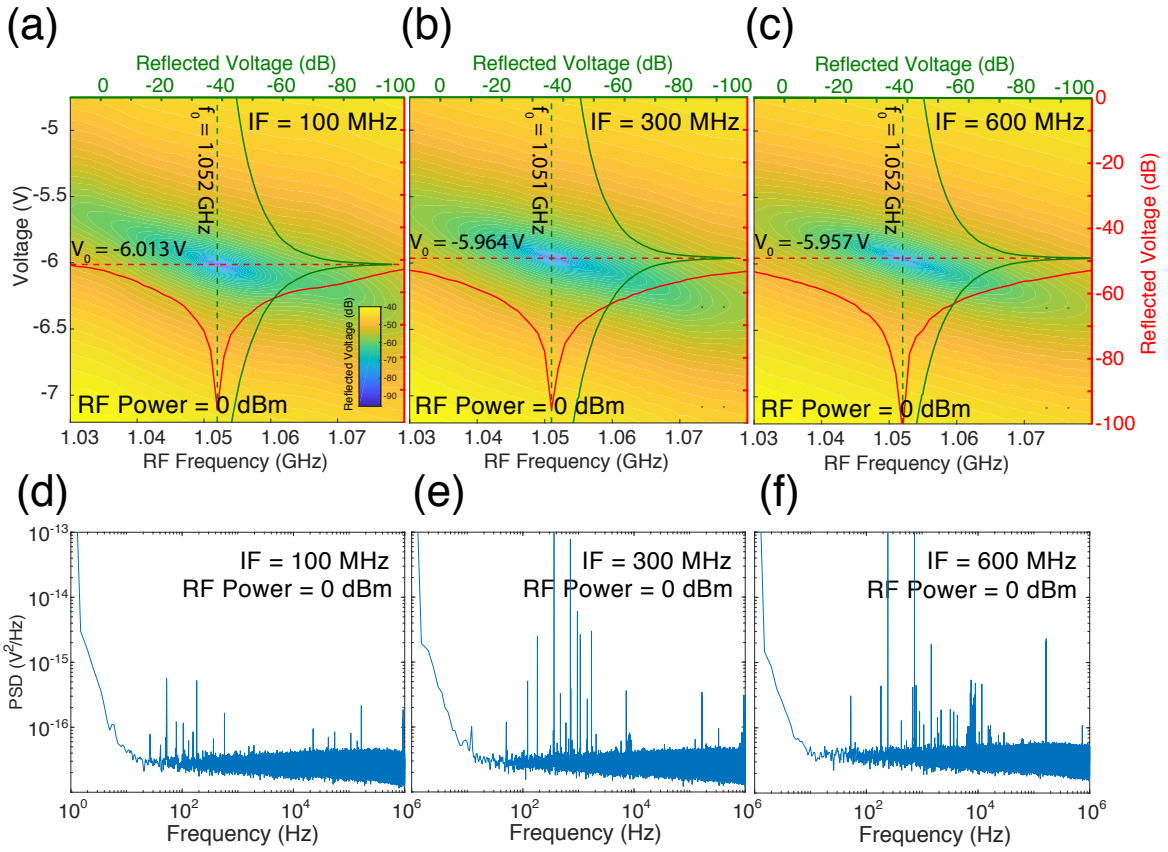

Figure 4.3: (a)-(c) Sweep of the reflected voltage wave around the point of best match for different IFs. The red solid lines show the reflection measurement through the point of best match with respect to the frequency and the green solid line represent the corresponding response with respect to the varactor voltage. Dashed lines indicate the point of best match. The colored axis labels correspond to the corresponding solid lines. (d) -(f) PSD measurements conduced from time domain measurements at the point of best match.

procedure with the exception of the change of the carrier frequency. Consequently, the RF chip should not see a changes in IF as long as there is no leakage of the LO signal into the signal path.

In Fig. 4.3 (d)-(f) the corresponding PSDs at the point of best match are shown. Two main features are obvious that already show the advantage of the RF measurement method over conventional DC measurements that have been discussed in the previous chapter. Firstly, the PSDs do not show any obvious deviation from one another when the IF is changed, which is due to the fact that within this frequency range (i.e. 100 MHz – 600 MHz) the input noise of the lock-in receiver is flat [131].

Secondly, what is even more important, is the fact that the PSD, apart from a low frequency rise below 30 Hz, is flat throughout the whole measurable frequency range. As

was discussed in Sec. 2.2.3 a flat PSD is a characteristic of thermal noise. In contrast to the PSD spectra of the DC measurements shown in Fig. 4.3 there are no high frequency components in the spectrum. Consequently, the RMS noise (see Eq. 2.23) is expected to rise only linearly with frequency. It shall be pointed out that this behavior is in vast contrast to all existing DC measurement strategies demonstrated in literature where the highest measurement BW is in the order of 10 MHz [67, 73]. Although the cited measurements are performed at theses BWs, the corresponding PSD spectra discussed in the cited publications still show a characteristic increase of the PSD due to dielectric and capacitive noise at frequencies above 100 kHz which is absent in the RF measurements presented in Fig. 4.3 (d)-(f).

High frequency noise is still the ultimate limitation of all RPS methods, hindering their usage for measurements with BWs higher than 10 MHz. For the cell measurements, that will be discussed in the next chapter, BWs higher than 10 kHz are not necessary because the translocation time of individual cells are in the millisecond range. Nevertheless, it is worth noticing that due to the flat PSD the experimental setup shows the promise of being used as a platform for high BW measurements in future. A conceptual experiment using this property will be discussed in the outlook of the thesis.

4.2.2 Distance of f_0 and V_0 From Optimal Impedance Match

In Fig. 4.4 it is shown how the noise characteristic is changed when the RF chip is operated at a point beyond the point of best match, i.e. when the chip is intentionally detuned. The PSD spectra are measured for different values for the varactor voltages and input frequencies which do not correspond with the point of best match (see Fig. 4.4 (c) and (d)). Additionally, in Fig. 4.4 (b) the 1-dimensional sweep through the corresponding reflection curves is given.

The reflection map shown in Fig. 4.4 (a) is acquired with the same chip as used for the measurement discussed in Fig. 4.3. The point of best match is found to be at $f_0 = 1.054\,\mathrm{GHz}$ and a varactor voltage of $V_0 = -6.148\,\mathrm{V}$, indicated as solid black lines in the figure. These deviation of the parameters f_0 and V_0 from the results shown in Fig. 4.3 can be explained by the fact that this measurement is conduced a couple of days later. It is observed that slight mechanical changes in the setup can change the reflection measurement. Although the setup is mounted on an optical table movement of SMA cables and the position of the RF chip cannot be controlled with arbitrary precision. Although, one chip shows in general good reproducibility in terms of impedance matching, slight variations are still expected.

As can be seen in the color code of Fig. 4.4 (a), a correlation of the measured reflection of the input frequency and the varactor voltage is observed, in accordance with

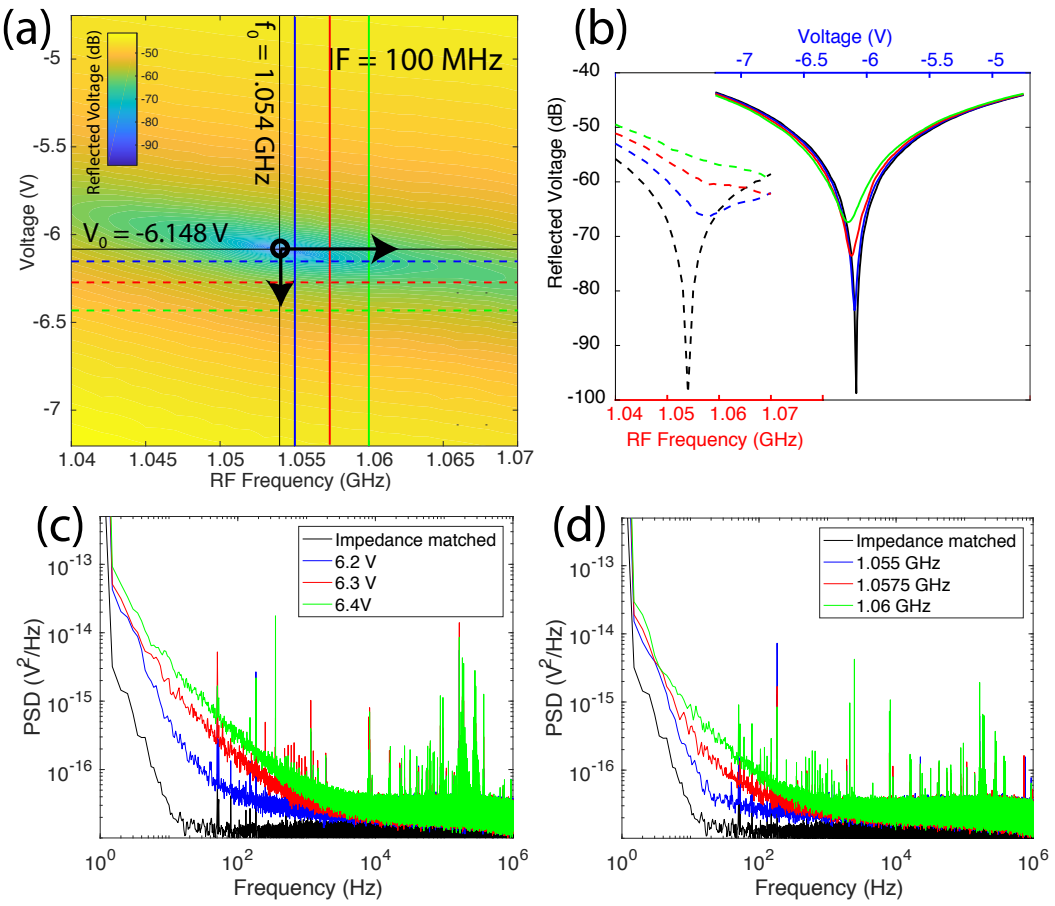

Figure 4.4: (a) Impedance matching of the RF chip at fixed IF frequency and input power. (b) Reflection measurements for different varactor voltages and input frequencies showing that the quality of the match decreases with values different from f_0 and V_0. (c) and (d) PSD for the investigated adjustments of driving frequency f_0 and varactor voltage V_0.

all impedance matching maps shown so far. In Fig. 4.4 (b) the solid and dashed black lines give the frequency and voltage sweeps of the reflection measurement, respectively. It is observed that at the point of best match a minimal reflection of almost $-100\,\mathrm{dB}$ is achieved.

Solid blue, red and green lines shown in Fig. 4.4 (a) and (b) give the reflection curve that are measured at detuned frequencies. The minimal reflection is not higher than $-68\,\mathrm{dB}$.

The dashed lines in the two figures are the corresponding measurements for detuned varactor voltages. In comparison to the detuned frequencies (which deviate maximally by 1% with respect to the point of optimal impedance match) the voltages are chosen to have a maximal deviation of 10% with respect to the point of best match. This strong detuning leads to reflection curves which do not show a characteristic minimum any more.

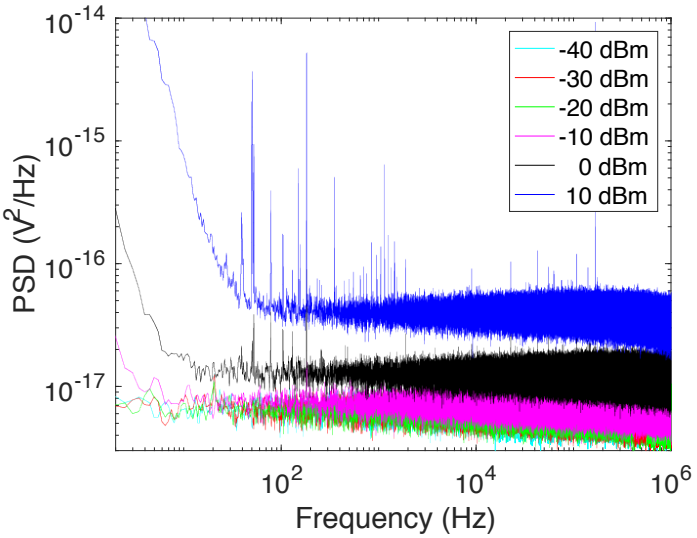

Figure 4.5: PSD of the impedance matched RF chip driven at different RF input power.

The detuning parameters are chosen randomly for illustrative purposes, as the map shown in Fig. 4.4 (a) gives the reflection parameters for every combination of f and V in the measurement range around the point of optimal impedance match.

PSDs for the impedance matched devices as well as PSDs for the the detuned devices are shown in Fig. 4.4 (c) and (d). The color code in the plots corresponds to the color code given in Fig. 4.4 (a) and (b). It can be noted that for a device which is not impedance matched the PSD spectra deviate systematically from the PSD of the impedance matched device. Albeit no high frequency noise is added to the spectra, in the low frequency regime the PSD increases when the chip is operated beyond the point of optimal impedance match. This effect is attributed mainly to an increased baseline signal and it will be shown in Fig. 5.4 that a reasonable time domain signal amplitude, caused by translocating particles through the sensing region, can be acquired even if the device is intentionally detuned from the point of best match.

4.2.3 Influence of RF Power

For the measurements presented so far the input RF power was always set to 0 dBm. In the following, the PSD for different RF input powers at the point of best match are discussed. As it was shown already that the optimal noise characteristic is achieved when the chip is operated at the point of best match, the reflection sweeps in frequency and varactor voltages are not shown.

The results of the experiments are shown in Fig. 4.5. As can be seen for frequencies above 50 kHz all PSD are flat, independent on the input power. For frequencies below

50 kHz the PSD increases only when the input power is larger than −20 dBm. At RF powers below that value the overall PSDs behave equally. Obviously, a critical RF power has to be used to measure an effect on the PSD because at these low input powers the RF chip does not show any response.

Beside the low frequency regime, a collective effect is observed for increasing input powers. A small increase in low frequency noise becomes visible at an input power of −10 dBm. For input powers in excess of −10 dBm not only the low frequency noise increases but the overall spectrum shifts to higher noise values.

While the overall spectrum increases, and thus the RMS noise of the time domain signal, it remains flat throughout the measurement regime. This noise can be attributed to thermal effects. Input signals with amplitudes above 0 dBm lead to heating of the device which causes an increase in noise which is frequency independent as observed in Fig 4.5.

4.2.4 Liquid Sensing Capabilities

A first glance at the sensing capability of the RF chip was already given in Sec. 3.6.3 where the reflection response of a dry chip was compared to a device that is flooded with electrolyte solution (see Fig. 3.18 (b) and (c)). Here, it is further investigated how the salt concentration influences the impedance matching behavior of the RF chip by measuring the reflection response at the presence of different electrolyte concentrations. The electrolyte used in the experiments is KCl at concentrations between 0 and 1 M. Pure deionized water without KCl is considered 0 M.

Fig. 4.6 summarizes the results. The experiments are conducted in the following way: For every electrolyte solution with a specific concentration the response for four different RF input powers from −20 dBm to 10 dBm is measured. After a measurement is acquired with one specific KCl concentration the sensing region of the chip is carefully cleaned and dried before it is filled with the next electrolyte sample. Before starting the experiments a slight negative pressure of −20 mbar across the MP is applied. This pressure induces the flow of electrolyte through the micropore thus wetting the sensing region. To dry the chip, a strong positive pressure is applied (i.e. 300 mbar). The positive pressure is mandatory to empty the MP from the electrolyte from the previous experiment thus preventing cross contamination. To further prevent cross contamination the measurement was started with DI water and consecutively the concentration was increased.

As can be seen in Fig. 4.6 (a) the optimal impedance matching point does change systematically when the concentration of the electrolyte is increased. While the optimal RF frequency f_0 decreases, the optimal varactor voltage increases with increasing KCl concentrations. The overall quality of the impedance match is not altered.

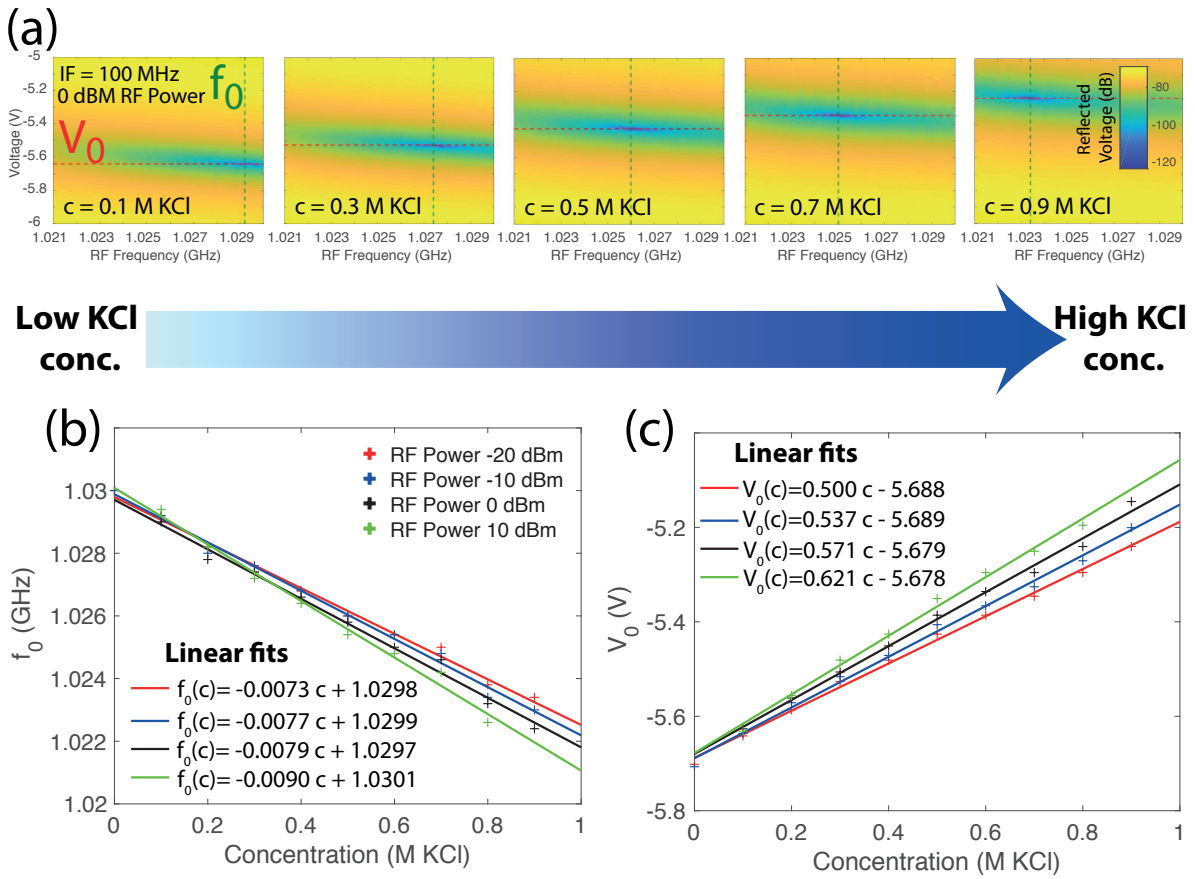

Figure 4.6: (a) Impedance matching for different KCl concentrations measured with a RF power of 0 dBm and a IF of 100 MHz. In (b) and (c) best frequency f_0 and varactor voltage V_0 for the different electrolyte concentrations measured for different RF power.

The point of best match is plotted versus the KCl concentration of the electrolyte for every tested RF power, and the corresponding results can be seen in Fig. 4.6 (b) and (c) for the optimal frequency and voltage, respectively. Both, the input frequency and the varactor voltage show a linear relationship to the electrolyte concentration. These results give a first proof on the sensing capability of the device as the higher the concentration of the electrolyte is, the bigger is the difference in device response.

The linear fit functions for the experiments at the different RF powers are given in Fig. 4.6 (b) and (c), too. Obviously, the measured curves intersect at a concentration of 0 M. This concentration is associated with pure water for which the optimal voltage V_0 and frequency f_0 show very similar values regardless of the RF power. For increasing RF powers the absolute values of the slopes increase. The difference between two salt concentrations in terms of the point of optimal impedance matched is maximal for the highest RF input power. This observation might lead to the assumption that the chip should be operated at maximal RF input power possible, but as it was shown in Fig. 4.5

this comes at the expense of an increased noise contribution.

4.3 Conclusion of the Section

The measurements presented show that there is a certain freedom in choosing the parameter with which the RF chip is operated. It was shown that the chosen IF does neither influence the point of optimal impedance match nor does it influence the noise characteristic drastically. For the time domain measurements which are discussed in the following an IF = 100 MHz is chosen.

Furthermore, it was discussed that the chip, if it is detuned intentionally, does acquire some low frequency PSD components. This contribution leads to a higher baseline signal in terms of the reflected RF wave. It will be discussed in the following chapter how this will be utilized to perform not only measurements of the reflected RF amplitude but to measure the phase of the reflected wave, too.

Finally, the influence of the RF input power in terms of PSD was discussed and it was shown that an increased RF power leads to an overall increase of the PSD spectrum. As these spectra are flat in the frequency domain, the increase is associated with thermal effects. This observation leads to the assumption that although the sensing capabilities in terms of sensing different salt concentrations is maximal at maximal RF input powers, a intermediate RF power should be chosen to prevent unnecessary noise contributions due to thermal noise. Therefore, an input power of 0 dBm is used for all time domain measurements, discussed in the following.

Chapter 5

Time Domain Cell Measurements

In this chapter, the time domain measurements, acquired with the setup shown in Fig. 4.1, are discussed. It is the investigation of human Jurkat T cells which is the main prospect of the chapter. T cells have been under investigation as they are used for the investigation of cell signaling which is an important process in the immune system [132]. The cells are cultured in suspension, they are spherical and easy to transfer from the cell medium into the setup. For the experiments an RF chip with a MP with a diameter of 11 µm is used. It enables the T cells, which have an average diameter of 13.5 µm [128], to translocate through the pore. Small cells will translocate without mechanical interaction with the pore. Bigger cells, due to their deformability, are able to squeeze through the pore. That is by design as it is intended that for the experiments the distance between the signal line and the ground line is minimal to maximize the signal amplitude as was discussed in the RF simulations in Sec. 3.6.2.

5.1 Results of RF Measurements with Jurkat T Cell

In Fig 5.1 a representative measurement of T cells translocating through the MP is shown. Similar to RPS measurements, the translocating cells lead to transient peaks on top of a noisy base-signal for the amplitude of the reflected signal (see Fig. 5.1 (a)). In addition to the amplitude, the phase of the reflected signal is modulated by the translocating cells, too (see Fig. 5.1 (b)). For every transient amplitude peak, a simultaneous phase shift is observed. The analysis of the time domain data is based on the amplitude of the reflected wave, is similar to the analysis of the RPS data discussed in Ch. 2.3.2. The workflow is illustrated in Fig. 5.1 and Fig. 5.2.

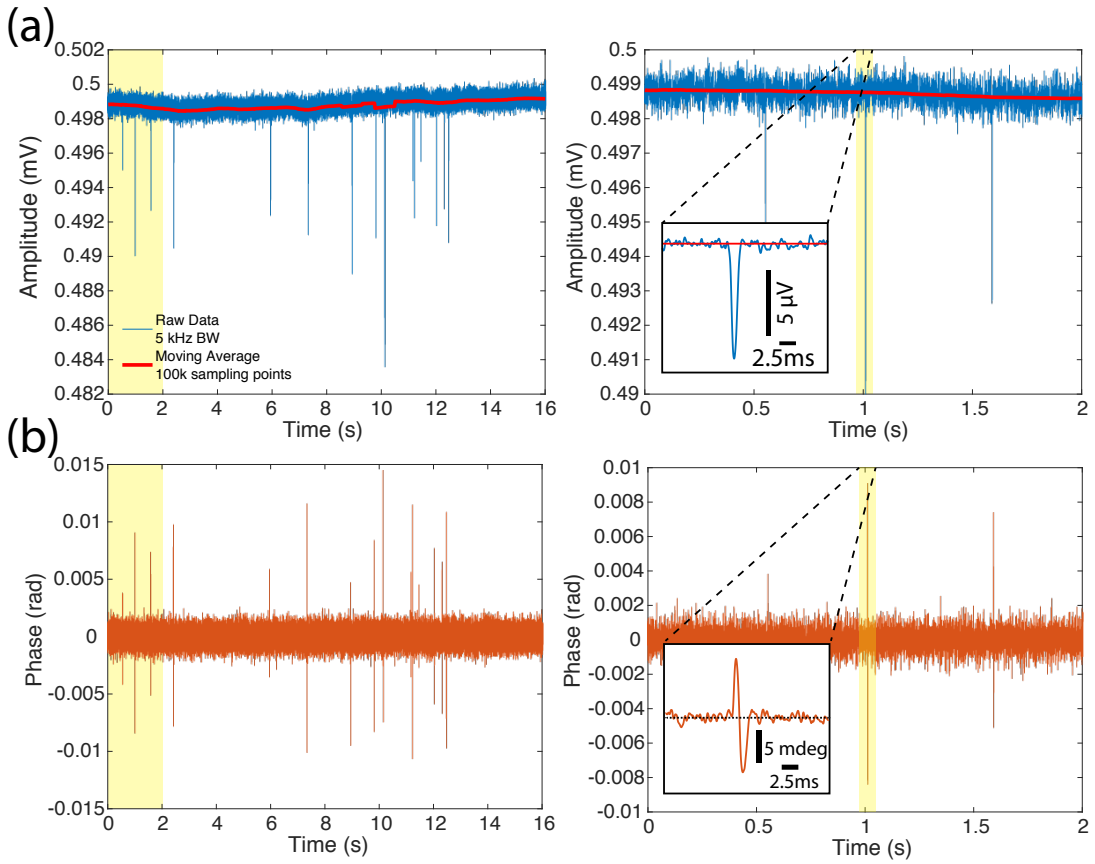

Figure 5.1: (a) Example sweep of a reflected time domain amplitude signal obtained from translocating Jurkat T cells in pipette solution. Individual peaks are originating from a translocating cell. In the right plot a zoomed-in view into the data which is marked in yellow is given. The solid red line gives the moving average which is determined to estimate the baseline signal of the reflected amplitude. (b) Corresponding phase amplitude of the reflected signal. Every peak amplitude is accompanied with a transient phase shift of the data.

5.1.1 Identifying Translocation Amplitude

In the left plot of Fig. 5.1 (a) 16 s of a typical time domain representation of the amplitude of the reflected signal is displayed. Every individual translocating cell leads to a transient peak in the time trace. The data shown here is acquired from translocating Jurkat T cells suspended in a so-called pipette solution. This solution is typically used as the electrolyte in a micropipette for patch clamp experiments [133]. The recipe of the solution as well as the protocol used for transferring the cells from the culture medium into the measurement buffer is given in Ch. A. A cell concentration in the range of 10^6 cells/mL is used for the experiments and in all following experiments, if not stated differently.

The data presented in the figure is acquired at a BW of 5 kHz and a sample rate of 419 kSa/s. As can be seen in the zoomed-in view into the time trace, which is given in

the right plot of Fig. 5.1 (a), the peaks, associated with the translocating particles, have a translocation time in the sub-millisecond to millisecond range. As that is the typical translocation time in all cell experiments discussed here, the 5 kHz BW is sufficient for the measurement. An increase in BW, albeit potentially possible, would only lead to an increased noise floor without delivering any additional information about the dynamic of the process.

Similarly to the RPS method the baseline signal in the RF measurements shows slow variations along the time. A moving average with a window containing 30 kSa is used to give an estimation of the time dependent baseline signal. The moving average is displayed as a solid red curve in Fig. 5.1 (a). Compared to the RPS experiments, which were discussed in the previous chapter, the moving average window contains more sample points because of the drastically increased sample rate of the RF experiment. As can be seen in the figure, this method gives a good approximation of the baseline even at the presence of a transient peak.

The mean baseline amplitude of the measurement is centered around 0.5 mV, which is not the point of optimal impedance match. In fact, the chip is intentionally detuned to enable the measurement of the phase of the reflected signal as was discussed before. The corresponding phase signals are shown in Fig. 5.1 (b). Every transient peak in the reflected amplitude is accompanied by a phase shift of the signal. If no cell is translocating the pore, the phase is centered around zero. A translocating cell temporarily changes the phase of the signal which is observed as a positive rise of the phase signal accompanied by a negative drop before going back to zero phase once the cell has exited the sensing region (see zoomed-in view, shown in the right plot of Fig. 5.1 (b)). Amplitude and phase are originating from the input signal according to Eq. 3.38 and Eq. 3.39 with the same time base. Accordingly, the two quantities are naturally time synchronized.

If the moving average is subtracted from the raw reflected amplitude signal, a flat signal, centered around zero is obtained enabling the use of simple peak finding algorithms similarly to the discussion in Sec. 2.3.2 to obtain individual translocation events from the raw data. The corresponding curve is shown in Fig. 5.2 (a). Having a flat baseline signal allows for a threshold strategy for peak identification. As a first step, the moving standard deviation $\sigma^{\mathrm{std}}_{\mathrm{mov}}$ within a window of 30 kSa is derived. The $1 \times \sigma^{\mathrm{std}}_{\mathrm{mov}}$ and $2 \times \sigma^{\mathrm{std}}_{\mathrm{mov}}$ regions are displayed in the figure as the green and yellow solid lines. The shape of these regions is dependent on the structure of the signal itself. If the event rate or the peak amplitude is high, the local standard deviation of the baseline signal is strongly overestimated. This effect can be exemplarily observed in Fig. 5.2 (a) at about $t = 10\,\mathrm{s}$. To obtain a constant threshold for the dataset, the $3 \times \sigma^{\mathrm{std}}_{\mathrm{mov}}$ region is averaged for the 16 s time sweep. The result is shown as a solid red line in Fig. 5.2 (a).

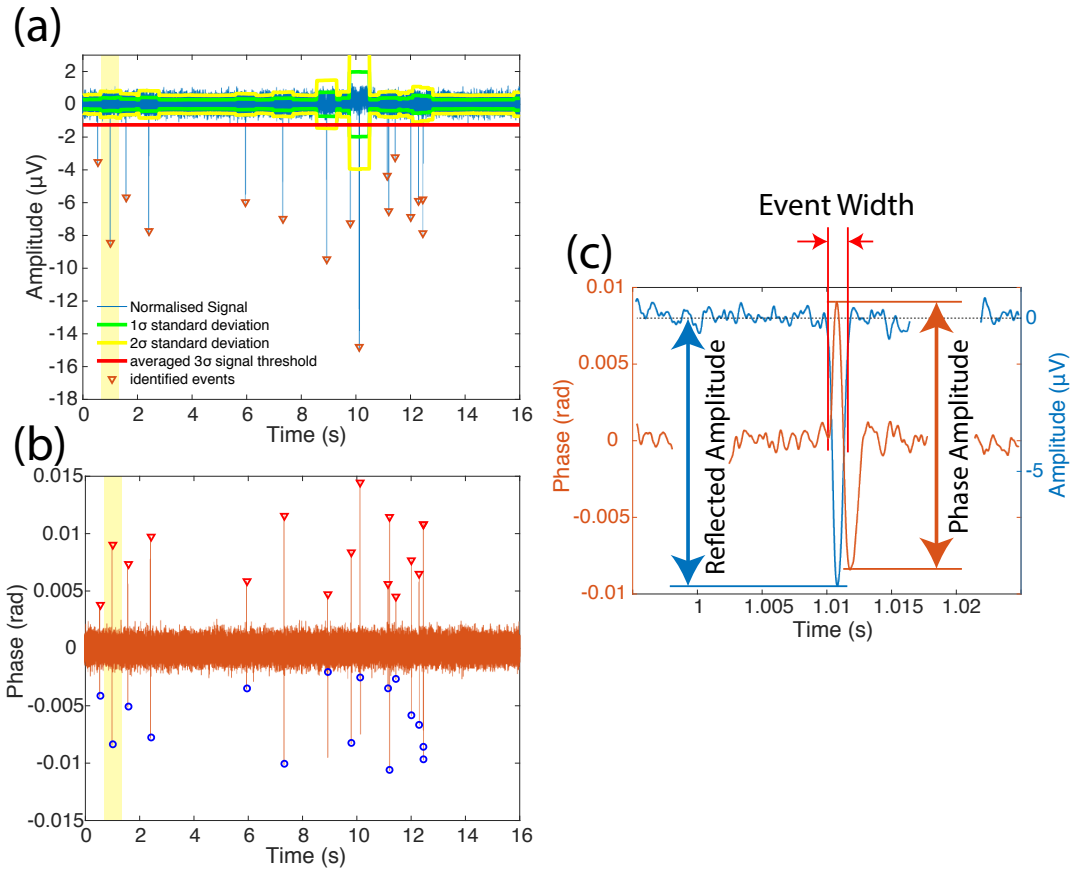

Figure 5.2: (a) Determining a moving standard deviation. The green and yellow lines indicate the $1 \times \sigma^{\mathrm{std}}_{\mathrm{mov}}$ and $2 \times \sigma^{\mathrm{std}}_{\mathrm{mov}}$ standard deviation regions. To obtain a flat threshold for the peak finding algorithm the $3 \times \sigma^{\mathrm{std}}_{\mathrm{mov}}$ standard deviation is averaged over the 16 s window (solid red line). Reflected amplitudes exceeding the threshold are identified as a translocation events (orange triangles). (b) Phase amplitudes obtained by another thresholding procedure which uses the position of the peak found in the reflected amplitude as a reference. (c) Zoomed-in view into a single translocation event, showing how the two events are correlated to one another.

As a last step, a peak finding algorithm is applied which detects deviations from the baseline signal when the reflected amplitude exceeds the averaged $3 \times \sigma^{\mathrm{std}}_{\mathrm{mov}}$ threshold. As the data is acquired at a comparable high sampling rate (i.e. 419 kHz) the peaks can be noisy in themselves. To prevent the algorithm to detect one event multiple times a second criterium is applied. Not only the global threshold has to been exceeded but the peak has to have a certain peak prominence. This criterion prevents the algorithm to detect noise excess as individual peaks over a translocation event. The peaks identified following this protocol are marked with orange triangles in Fig. 5.2 (a).

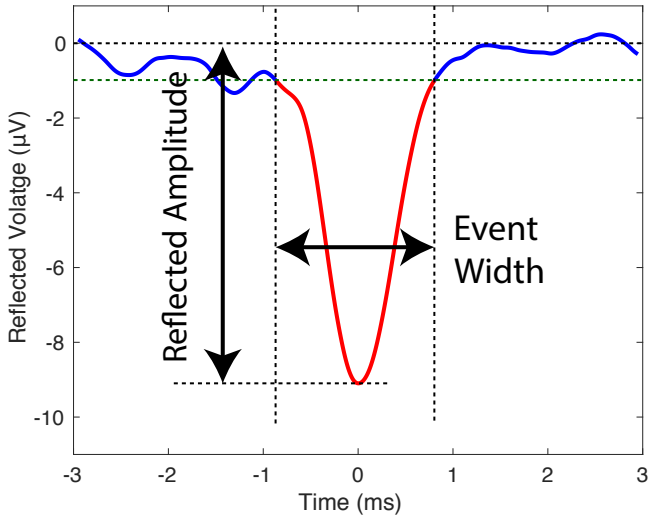

Figure 5.3: Event width determined by a threshold algorithm. Dashed green line indicates the threshold value and the red part of the event is identified as the translocation event while the blue line is the baseline signal.

5.1.2 Identifying Translocation Phase

In Fig. 5.2 (b) the corresponding phase measurement is shown and in Fig. 5.2 (c) a zoomed-in view into one translocation event is given. It can be seen in the zoomed-in view that the two measurement quantities are synchronized in a specific manner. When the reflected amplitude reaches its maximal value, the phase signal reveals a maximum phase shift in positive direction. After that, the phase makes an additional and characteristic decrease before it becomes zero again. This behavior is observed for all translocation events. The phase amplitude is defined as the difference between the most positive value and the most negative value (see Fig. 5.2 (c)). To find these values a peak finding algorithm is used again. The position of the first peak (marked as an orange triangle in Fig. 5.2 (b)) coincides with the position of the peak in the reflected amplitude. Therefore, the search window given to the algorithm is restricted to a small region around this peak position. The negative peak in phase is determined by the algorithm by looking for the next negative peak marked as blue circles in Fig. 5.2 (b).

5.1.3 Identifying Translocation Width

Additionally, to the reflected amplitude and the phase the event duration is of interest for the analysis. This parameter is derived from the individual events by applying a similar threshold method. This procedure was already discussed in Sec. 2.3.2 and shall not be discussed here again since the analysis was transferred to this problem without major

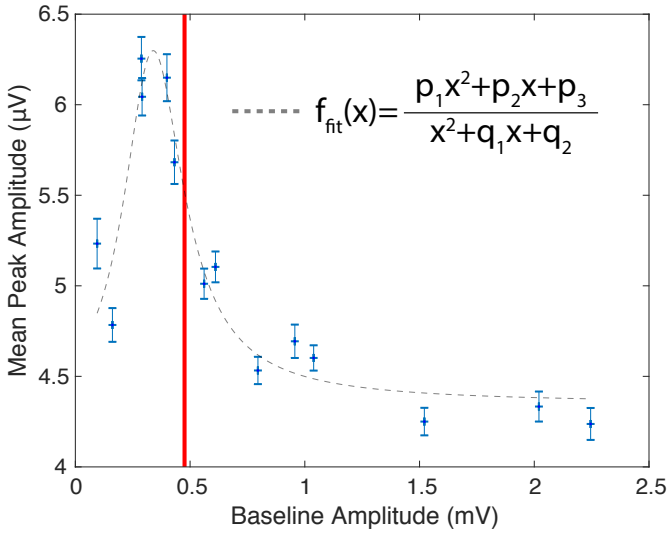

Figure 5.4: Mean peak amplitude of Jurkat T cells versus the baseline amplitude which is adjusted by changing the varactor voltage to higher values with respect to the point of best match. The fit function, which serves as a guide for the eye, is shown as a dashed black line and the solid red line indicates the baseline amplitude that is used for the cell measurements.

modification. The result for one exemplary event is shown in Fig. 5.3.

Having the peaks identified allows for isolating the peaks into a separate file, which is used for further analysis. This is done by storing the time domain data around the detected amplitude and phase shifts within a certain window. Furthermore, for every event the reflected amplitude, the phase amplitude, the width and the global CPU time at which the event is measured is stored, which allows to characterize the measurements quantities with respect to one another as well as to observe whether or not there is a time-dependent evolution of the measurement parameters over the course of the experiments.

5.2 Points of Operation

At the point of optimal impedance match the reflected amplitude of the RF wave would be zero, as the input RF wave is absorbed by the device completely. As was shown in Fig. 5.1 (a), here, the RF chip is not operated at the point of optimal impedance match because it was observed that at this point of operation the baseline amplitude of the reflected signal is too low for the lock-in amplifier to phase lock the reference wave to the input signal. Therefore, the reflected signal is measured at a finite reflection baseline by intentionally detuning the RF chip.

Experimentally, the easiest way to detune the RF chip is to change the varactor voltage

because in this case only one parameter has to be changed. If the RF input frequency would have been changed, the RF frequency and the LO frequency would have needed to be changed simultaneously to maintain the desired IF.

In Fig. 5.4 the mean amplitude of signals obtained from Jurkat T cells suspended in Ca^{2+}-measurement buffer (see Ch. A) is plotted versus the mean baseline signal. The baseline amplitude is adjusted by changing the voltage across the varactor to higher values with respect to the voltage value at the point of best match. At the so adjusted baseline amplitude, translocation events are measured and the mean amplitude is calculated from the set of individual amplitudes. The vertical error bars in Fig. 5.4 reflect on the variation of the individual amplitudes. Horizontal error bars, reflecting on the deviation of the baseline amplitude over time are given, too. These error bars are not visible in the figure indicating that the baseline amplitude is stable during the measurements.

For the sake of orientation, a rational function is plotted to the data and the fit function is shown as a dashed black line in Fig. 5.4. The function does not represent a physical model explaining the shape of the curve. Instead it helps to visualize the overall trend of the data.

As shown in Fig. 5.4 the amplitude of the signal caused by the translocating cells depends strongly on the degree of impedance matching. The highest amplitudes are obtained at baseline currents around 0.34 mV. For lower baseline amplitudes, i.e. a better impedance matching, the mean amplitude indeed decreases. With the data set shown it is hard to conclusively judge whether the point of optimal impedance matching is the best point of operation. Although this is still expected, reaching this point and maintaining there along minutes or even hours is experimentally challenging. It was shown that the point of optimal impedance matching is very narrow and even slight mechanical perturbations change the chip impedance. For example applying the negative pressure is perturbing the setup enough to observe a change in reflected amplitude. As a matter of fact, it is concluded that for the sake of stability of the measurements a detuned RF chip is indeed favorable.

To get a stable phase measurement at a reasonable signal amplitude it was decided to measure signals at a baseline amplitude of 0.5 mV. This value is a compromise between the two aspects: Firstly, it allows for a continuous measurement without interruptions caused by the phase locked loop. If the amplitude is decreased below approximately 0.3-0.4 mV the PLL tends to interrupt temporarily because it is not able to maintain a stable locked loop. Secondly, the amplitude and phase measurement show reflected amplitudes with a decent height above the baseline signal.

5.3 Jurkat T Cell Measurements

In this section experiments are discussed illustrating the potential applications of the method regarding cell characterization. First, it is discussed how electrolytes containing mainly NaCl (140 mM) or KCl (140 mM) change the overall reflected amplitude of translocating polystyrene beads and T cells. It is further shown that the RF chip is capable to distinguish biological cells from polystyrene beads. Finally, it is investigated on how an unphysiological buffer, containing mainly KCl (140 mM and 280 mM) leads to different RF signals that will be attributed to morphological cell changes and to an increased cell membrane conductivity.

A lot of different electrolytes are used for the different experiments. The main difference between them is their concentration of NaCl and KCl. For a better orientation an summery of the electrolytes used is given in Tab. 5.1. The recipes for the electrolytes are given in the appendix.

5.3.1 Comparison Between Jurkat T Cells and 6 µm Polystyrene Beads

For experiments discussed here T cells and polystyrene beads are each suspended in two electrolyte solutions so that four experiments are conducted. In the first set of experiments the beads and the cells are transferred into Ca^{2+} buffer which is used as a standard electrolyte solution for different physiological experiments [134]. It is an isotonic buffer thus the suspended cells are stable for hours. Additionally, the cells and the beads are transferred into the pipette solution which is used as the electrolyte within a micropipette in patch clamp experiments [135, 136]. The main difference between these electrolytes is the concentration of NaCl and KCl. While the Ca^{2+} buffer contains mainly NaCl with a concentration of 140 mM, the pipette solution contains mainly KCl with a 140 mM concentration. The recipes for these electrolytes can be found in Appendix A.2. The concentration of the beads and the cells is in the range of 10^6 /mL.

For all experiments, exemplary sections of 16 s worth of time domain data are shown

Table 5.1: Summary of electrolytes used for the experiments as well as the concentration of their main component.

Extracellular Solution	Main Component	Concentration (mM)	Recipe
Ca^{2+}-buffer	NaCl	140 mM	A.1
Pipette Solution	KCl	140 mM	A.2
High KCl Pipette Solution	KCl	280 mM	A.2
Bath Solution	NaCl	140 mM	A.3

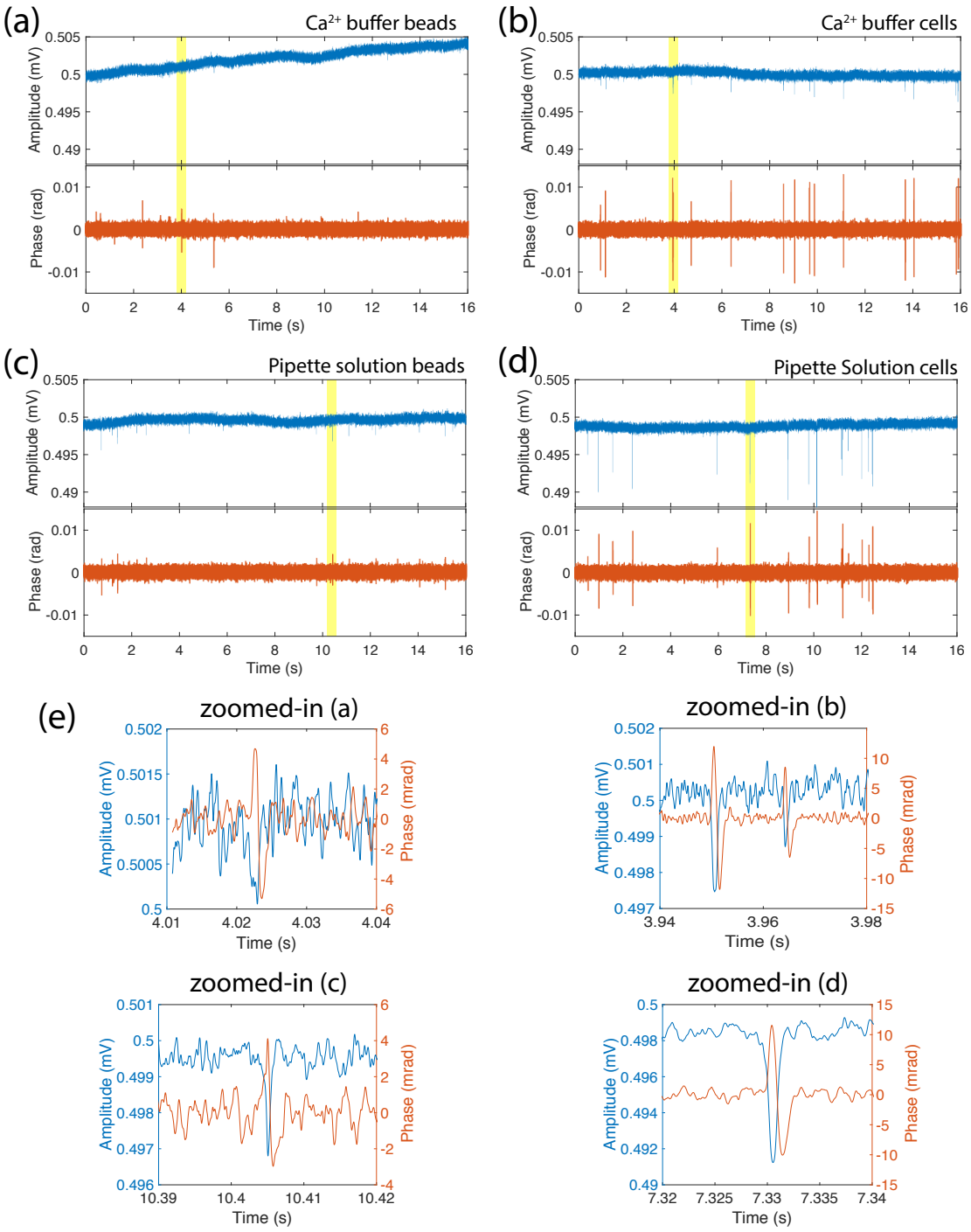

Figure 5.5: Time domain traces for translocating polystyrene beads (6 µm diameter) and Jurkat T cells in Ca^{2+} buffer and pipette solution. Translocation events of beads in Ca^{2+} buffer (a) and T cells in Ca^{2+} buffer (b). Corresponding experiments with beads (c) and T cells (d) in pipette solution. The events that are marked in yellow in (a)-(d) are zoomed-in in (e)

in Fig. 5.5 (a)-(d), which allow for a direct comparison between the bead and the cell measurements suspended in the two electrolytes. The input RF frequency for all experiments is 792.4 MHz after impedance matching with the Ca^{2+}-buffer in the device. The measurements were performed at a baseline amplitude of the reflected signal of 0.5 mV as discussed before.

Fig. 5.5 (a) and (b) show amplitude and phase events from the polystyrene beads and the Jurkat T-cells suspended in Ca^{2+}-buffer. Obviously, the beads do not show a measurable amplitude modulation above the noise floor although some phase shifts are visible. These phase modulations confirm that beads indeed translocated through the MP. In contrast to the beads, with the same measurement parameters, T cells produce a clear measurable amplitude modulation. Simultaneously, every amplitude shift corresponds to a phase shift caused by the translocating cells. It shall be further pointed out that particle translocation during the measurement is additionally monitored with an upright microscope. This optical control is constantly available through all experiments but it is crucial in the present situation where no or very little RF response is observed.

Zoomed-in views into individual events are shown in Fig. 5.5 (e). For the bead measurement the amplitude modulation is hardly noticeable even in the zoomed-in view while the phase modulation shows the characteristic event structure. For the corresponding cell measurements the behavior is much more pronounced. A cell induces a temporal amplitude modulation thus decreasing the reflected signal which manifests itself as a temporal decrease in the measured amplitude. Simultaneously, the phase is increased temporarily. When the cell exits the sensing region the phase shifts downwards one time until reaching the baseline. The behavior is similar for all translocation events observed.

The overall behavior of this experiment can most probably be explained with the geometrical size of the test particles. While the beads have a very narrow size distribution around their nominal diameter of 6 µm (i.e. $\pm 2\%$) the T cells have diameter around 13.5 µm with a bigger size distribution depending on their physiological state. The MP has a oval diameter of 11 µm thus most of the T cells have to squeeze through the pore while being simultaneously deformed. In contrast to that, the beads can easily translocate the MP as they are about a factor of two smaller than the pore. It was numerically shown in Ch. 3.6.2 that the expected impedance variation due to the translocating particle is a function of the particle diameter. As a matter of fact, it is well expected that the comparably small beads will show a smaller signal compared to the cells that are even bigger than the MP.

In Fig. 5.5 (c) and (d) the experiments are shown where the beads and the cells are suspended in pipette solution and thus the main ingredient in the electrolyte is KCl. Even though, the amplitude modulation caused by the polystyrene beads is small, it is now well

above the noise floor compared to the results shown in Fig. 5.5 (a). For every peak in the amplitude caused by a translocating polystyrene bead a corresponding phase shift is observed (see Fig. 5.5 (e)). This effect is indicating that the signals obtained in a buffer, containing mainly KCl, are bigger than in a buffer that contains mostly NaCl.

The difference between the two buffers becomes even more apparent with translocating T cells. These results are shown in Fig. 5.5 (d). Compared to the amplitudes and phases obtained in the Ca^{2+}-buffer the reflected amplitudes in the pipette solution are obviously bigger.

The results of the experiments are summarized in Fig. 5.6. Here, the signal amplitudes, widths and phases are shown as scatterplots in relation to each other. Normalized histograms give the relative frequency of occurrence of the measured values. Data points from the experiments of the polystyrene beads within the Ca^{2+}-buffer are not given as there are no amplitude signals visible over the noise floor.

The scatter plot in Fig. 5.6 (a) shows the measured phase shift compared to the reflected amplitude. These two variables show the highest degree of discrimination between the three experiments. The beads suspended in pipette solution, shown in blue, accumulate at low amplitudes and low phase shifts. A positive correlation between phase and amplitude is observed for the beads. T cells suspended in Ca^{2+} buffer (magenta), albeit having an average amplitude similar to the beads show higher average phase shifts and T cells suspended in pipette solution, shown in red, produce amplitudes around 8-10 µV and thus a significantly higher amplitude than the cells in the other buffer and the beads in the same buffer. For both cell experiments a positive correlation between the two parameters is observed, too.

An interesting feature can be observed for the T cells suspended in pipette solution. In the scatter plot two correlations are visible. Different cells, albeit showing comparable amplitudes, tend to favor either high or low phases which accumulate in two clouds having a high and a low correlation. In the scatterplot (Fig. 5.6 (a)) these clouds are not extremely obvious because the scattering of the phases around these correlations is rather big. Therefore, the measurement is repeated in the next section and the effect is discussed in detail. Furthermore, in the final discussion (see Sec. 5.4) an explanation will be given why the two correlations are not visible very well here.

The normalized histogram in Fig. 5.6 (a) gives the measured amplitudes for the experiments. A fair comparison can only be made between the beads and the cells suspended in the same buffer. The cells showing not only higher amplitudes than the beads, the corresponding distribution is much broader. This effect can be attributed to the size and biological heterogeneity of the cells. While the cells are bigger on average their size strongly depends on their state in the cell cycle and their overall biological fitness. The

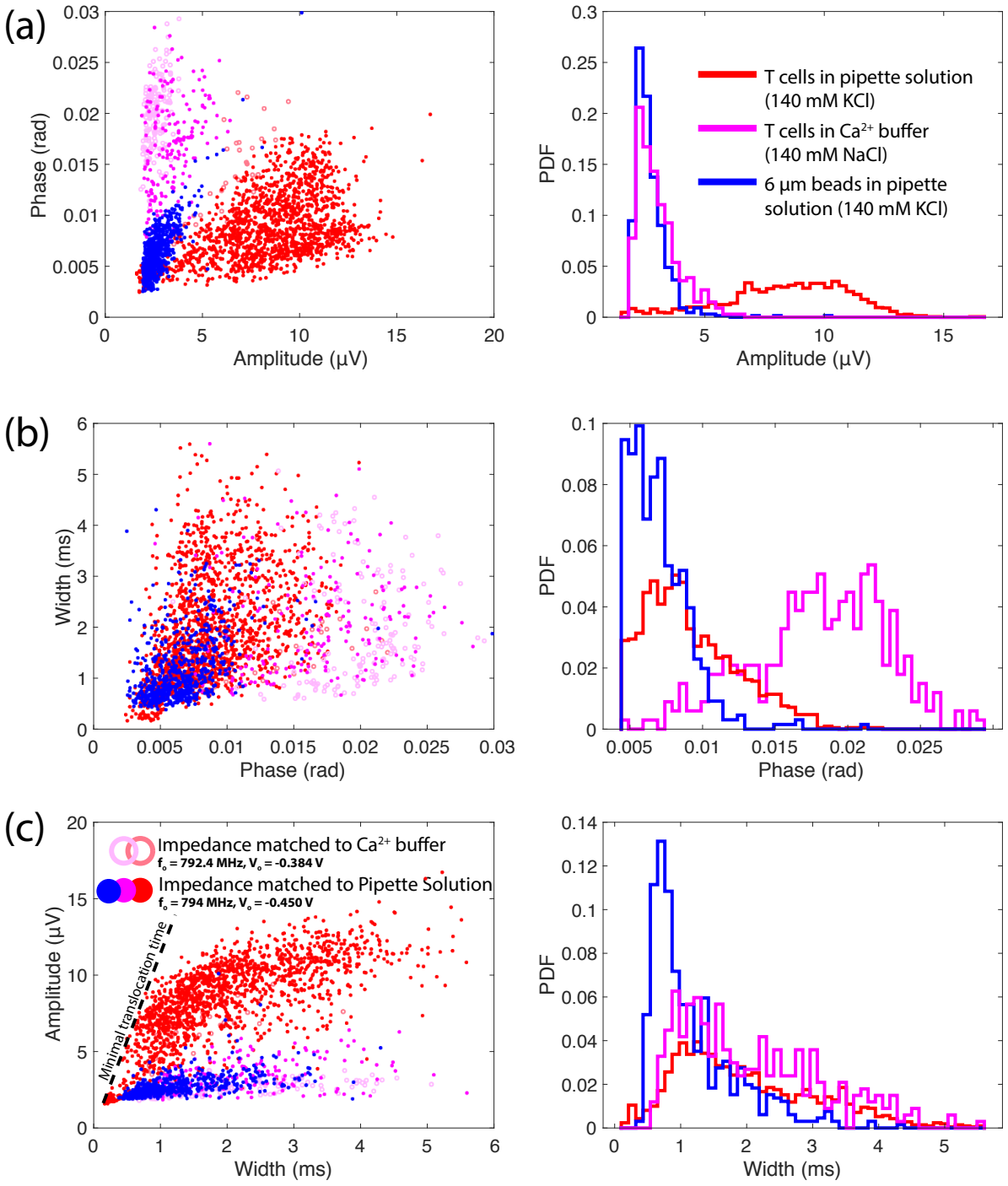

Figure 5.6: Scatter plots and normalized histograms of reflected amplitude, phase shift and event width of 6 µm polystyrene beads and T cells. (a) Amplitude of reflected signal versus phase shift of polystyrene beads (blue) and T cells suspended in Ca^{2+} buffer (magenta) and T cells suspended in pipette solution (red). In (b) and (c) corresponding measurement parameters and histograms are shown for phase shift versus event width and event width versus reflected amplitude, respectively. As the measurements are done in different electrolyte solutions the point of optimal impedance is slightly altered when the liquid is interchanged. Open light red and light magenta circles represent events when the device is impedance matched to the Ca^{2+} buffer and red, blue and magenta solid circles represent measurements taken with a device which is impedance matched to the pipette solution.

histogram in Fig. 5.6 (b) shows the measured phase shifts. It can be seen that the cells in the Ca^{2+}-buffer show the highest phase shift while the beads show the lowest.

The scatter plot in Fig. 5.6 (b) illustrates the correlation between the event width and the induced phase shift. While the observed phase shift for the three experiments is very different the event width is rather similar. As shown in the histogram of the event width (see Fig. 5.6 (c)), the beads tend to move through the MP slightly faster which can be seen by a higher probability for event widths smaller than 1 ms for the beads. The cells have similar distributions in width. Although their electronic response (in terms of amplitude and phase) is very different, their translocation time through the sensing region is similar.

In Fig. 5.6 (c) the amplitude versus the width of the three experiments is shown. Obviously, for the cells in pipette solution there is a minimal translocation time which depends linearly on the amplitude of the reflected signal as long as the amplitude is smaller than $\approx 9\,\mu V$. This minimal width is marked with a dashed black line in the figure. The bigger the amplitude gets the longer the cells translocates through the sensing region. As the amplitude of the reflected signal is, inter alia, a function of the size of the particle, a bigger cell will tend to have more physical interaction with the pore and the pore walls and thus it will be longer in the sensing region. The linearity disappears for amplitudes higher than $\approx 9\,\mu V$ as cells that exceed a certain size will lead to interactions with the pore that do no longer exhibit a linear behavior with respect to the translocation time.

5.3.2 T Cell Signals: Dependence on KCl Concentration

Previously, it was shown how different electrolyte buffer are influencing the signals obtained in the RF-reflection experiments. It was shown that buffer containing mainly KCl lead to a higher amplitudes. Furthermore, a first hint was observed that the phase is modulated uniquely under this conditions. These effects are further investigated here to study whether an even more increased concentration is influencing the signals from translocating T cells.

Buffer with two different concentrations (i.e. pipette solution with 140 mM and 280 mM KCl according to the recipe given in Ch. A.2) are used for the experiments. The results are shown in Fig. 5.7 (a)-(c). The figure is similarly orchestrated as Fig. 5.6. Blue dots and lines indicate the amplitude, phase and width for events measured in a pipette solution containing 140 mM KCl while green dots and lines indicate the same events in a pipette solution containing 280 mM KCl. The two measurements are conducted with the same RF chip as used for the experiments discussed previously.

In the scatter plot shown in Fig. 5.7 (a) the correlation between the phase shift and the amplitude is shown. A strong positive correlation between the amplitude and the

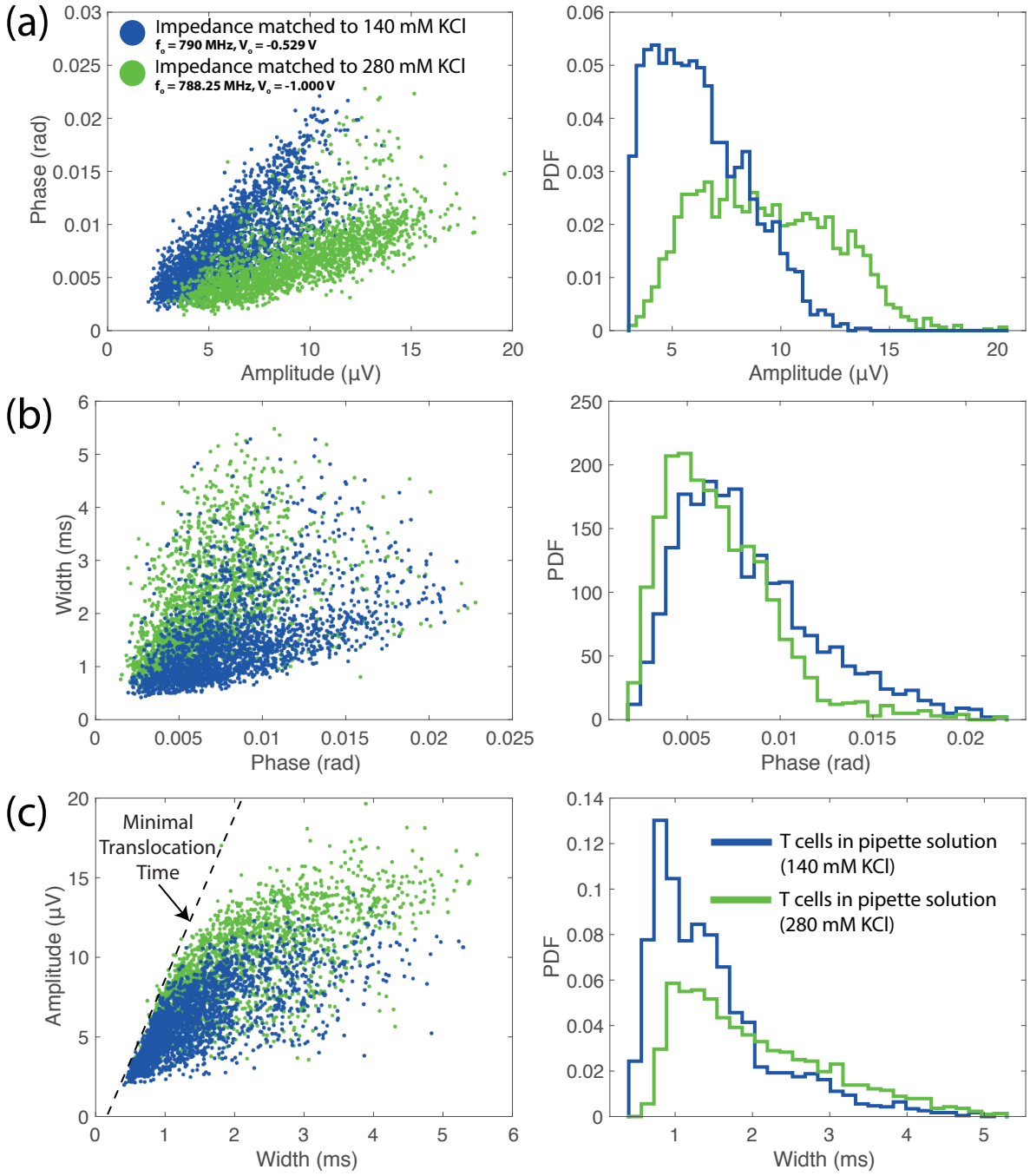

Figure 5.7: Scatter plots and normalize histograms of reflected amplitude, phase shift and event width of T cells in 140 mM (blue) and 280 mM (green) containing pipette solution. (a) Scatter plot of reflected amplitude versus phase shift for T cells in pipette solution of different concentrations. Histogram of reflected amplitude. (b) Phase shift versus event with and histogram of the phase shift. (c) Event width versus reflected amplitude and histogram of the event widths. As the two measurements are conducted in different electrolytes the devices are impedance matched to the corresponding electrolytes.

phase is still observed. Roughly speaking, the events from T cells that give higher amplitudes lead to higher phase shifts. This time, for the cells in the 140 mM KCl buffer there are two correlations visible, in the following referred to as the high and low correlation. Compared to the measurement shown in Fig. 5.6 (a) this effect is much more pronounced here. In Fig. 5.7 (a) the two correlations are obscured by the data obtained with the high concentration KCl buffer. Therefore, the same plot is shown for both concentrations, in Fig. B.1 for the 140 mM KCl buffer and in Fig. B.2 for the 280 mM KCl buffer, independently in the appendix. Interestingly, the cells in the high KCl buffer (green dots) do not show this twofold correlation during the measurement. The reason for this behavior is increased environmental stress of the cells because the KCl buffer is not physiological and changes the cell properties over time as will be discussed in the next section.

If the cells are transferred into the buffer with the increased KCl concentration, the effect disappears or at least it is highly quenched. The phase is decrease while the amplitude is increased in the high salt buffer, which can also be seen in the histograms in Fig. 5.7 (a) and (b), showing the amplitude and the phase, respectively. It shall be pointed out that the histograms, albeit showing the correct trend, are a misrepresentation of the actual effect. As the two variables are highly correlated, the phase seems to change only slightly, if a judgement is made from the corresponding histogram. As a matter of fact, the correlation of the cells in the high salt buffer tends to accumulate in the region where the low phase events occur for the 140 mM KCl buffer. This effect is only visible in the correlation of the two variables.

The scatter plot in Fig. 5.7 (b) shows the correlation between the width and the phase of the translocation events. In general the histograms, shown in Fig. 5.7 (c), indicates a similar distribution in event width between the electrolytes with a slight excess for higher widths in the high salt regime, which already indicates that the overall dynamic of the cells in the sensing region is altered. Cells in the high concentration KCl buffer tend to have longer translocation times indicating that their morphology changes.

In Fig. 5.7 (b) the correlation between the width and the amplitude is given. Similarly to the observations made in the previous section there is a minimal translocation time which strongly depends on the event amplitude. This minimal translocation time is equal for the two experiments. Obviously, for small amplitudes the cells tend to have similar physical interaction with the pore walls and as a matter of fact a similar minimal translocation time.

After the experiments in pipette solution with 140 mM and 280 mM KCl solution were conducted a test was done with T cells which were transferred into a physiological bath solution, typically used for patch clamping experiments. This physiological buffer contains mainly NaCl in a 140 mM concentration. The correlation between phase and amplitude

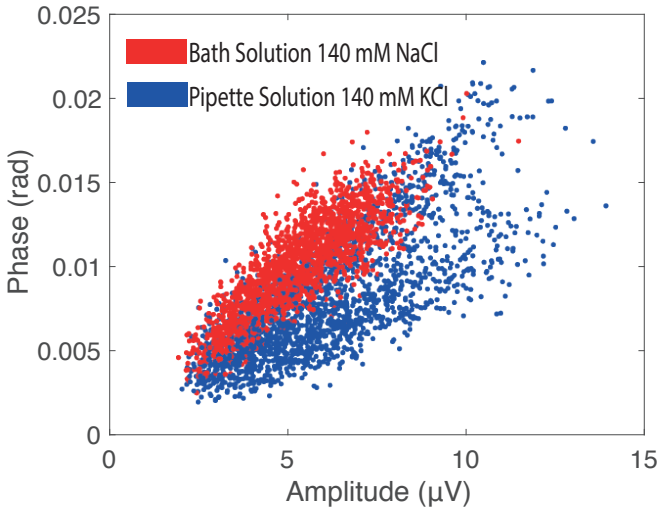

Figure 5.8: Scatterplot between the amplitude and the phase of a reflection measurement with Jurkat T cells in (blue) 140 mM KCl containing pipette solution and (red) 140 mM NaCl containing bath solution. The data shown in blue is equal to the data shown in Fig. 5.7 (a).

in comparison to the discussed data is shown in Fig. 5.8.

Red dots in Fig. 5.8 illustrate the phase and amplitude of the events in the bath solution. In accordance to the results discussed so far the mean amplitude of those events is smaller than the corresponding amplitudes in the pipette solution. This effect is not as pronounced because for these experiments the chip was impedance matched to the bath solution. After impedance matching the baseline signal was adjusted to 0.5 mV as discussed. It shall be mentioned that the statistic and the overall measurement times are similar. Nevertheless, the cells in the physiological buffer accumulate around the high phase correlation obtained from the KCl buffer.

This behavior strengthens the suggestion that the observable overall phases shift is indeed caused by a change of the biological properties of the cell itself. For the bath solution, as it is a physiological buffer, no drastic cell changes are expected over the course of the experiment, which is in vast contrast to the pipette solution where a lot of changes in cell properties are induced, some of which are discussed in the following. The induced cell changes are most like causing the phase changes that are measured.

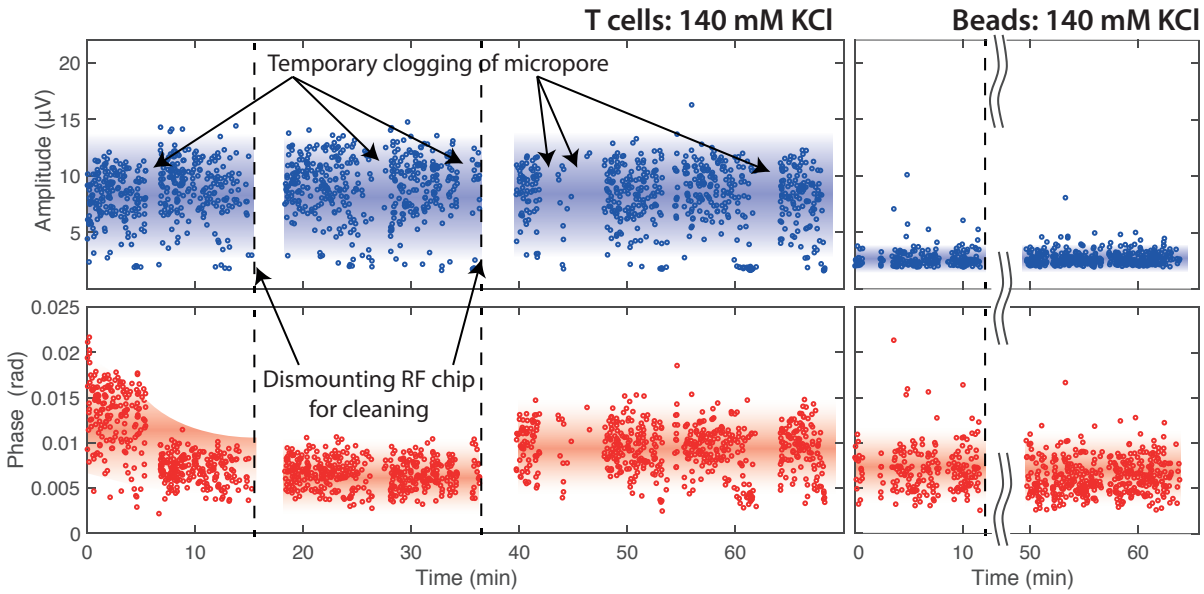

Figure 5.9: (left) Time dependent amplitude heights (blue) and phase shifts (red) of the T cell events, which are suspended in the 140 mM KCl buffer. The data points are plotted versus the time of their occurrence during the experiment which has an overall length of about 70 min. (right) Same plot for the bead signals that were conducted in the same buffer. The events presented here have been shown already Fig. 5.6. The colored blue and red bands are a guide for the eye.

5.4 Discussion of the Results

In the following, the results from the previous section shall be discussed in detail. Further analysis of the data is presented here as well as additional complementary experiments. The analysis and the experiments will pave the way to a better understanding of the findings.

5.4.1 Time Dependent Evolution of the Amplitude and Phase

Fig. 5.9 shows the amplitude and phase shifts for all individual events which were already discussed in Fig. 5.6. Here the measurement values are plotted versus their occurrence during the experiment which was executed over the course of over an hour. The plot is containing the data acquired with the cells which were suspended in 140 mM KCl buffer. Two major gaps at $\approx$ 15 min and at $\approx$ 37 min are visible in the figure. These gaps are caused by the fact that during the experiment the chip was dismounted from the setup, cleaned with DI water in an ultrasonic bath and installed back into the setup again. This procedure is necessary if particles stop translocating the pore due to clogging and if the pore cannot be freed from particles or debris which got stuck in the pore with the help

of an applied positive or negative pressure. In general the chip does show reproducible behavior after cleaning and reintegrating it into the measurement setup. Additionally to these two long gaps which are marked with dashed black lines, in between the constant measurement periods there are time spans where no events are measured. These gaps are caused by temporal clogging of the pore. A temporal clogging can often be eliminated by applying a short but strong negative or positive pressure, so that the particles are pushed or pulled out of the pore so that the time measurement can be continued.

Interestingly, there is a decrease in phase visible during the first 15 min of the cell measurement. Simultaneously, the amplitude of the signal is unchanged and stable during the whole measurement period. At $t \approx 40$ min there is a slight increase in the phase again while the amplitude is still unchanged. Note, this phase value remains now constant over time. It shall be pointed out that the cell sample is renewed after each cleaning step. During the experiment, 5-10 mL of cell suspension are stored in a tube. For every experiment the cells are carefully mixed and 20 µL of the suspension is pipetted into the sensing region before the time domain measurements are continued. The first decrease in phase can be attributed to morphological changes of the cell caused by the biological stress induced when the cells are transferred into the KCl, as will be shown in the following. The second increase is probably caused by a disruption of the setup and thus a changed phase response. This assumption is made as one phase decrease is observed for all cell measurements for which the cells are suspended in KCl solution while a second increase is never observed except for the present case.

It shall be pointed out that the phase change observed at $t \approx 40$ min is causing the fact that the two fold phase correlation, albeit being clearly visible in Fig. 5.7 (a) is blurred out in the measurement shown in Fig. 5.6 (a) although the measurement parameters are the same.

In Fig. 5.9 (right plot) the measurement of the beads, suspended in 140 mM KCl is shown in the same manner. As it was already shown previously, the amplitude and the phase are in general smaller than for the cell measurements. The measurement is interrupted for about 40 min as is indicated in the plot. This interruption is present because in the mean time measurements were done with the chip for the beads suspended in the NaCl buffer, which was discussed in Fig. 5.5 (a). Although, there is this rather huge time gap in the measurement the phase and amplitude of the beads are nicely reproduced even after 40 min and an intermediate experiment. Before the experiment at $t \approx 50$ min was started again, the chip had been cleaned and loaded with the bead sample which had been stored as discussed previously. Although the chip was cleaned twice in the meantime and was even loaded with an other electrolyte it shows excellent reproducibility in terms of measured amplitude and phase shift for the bead sample.

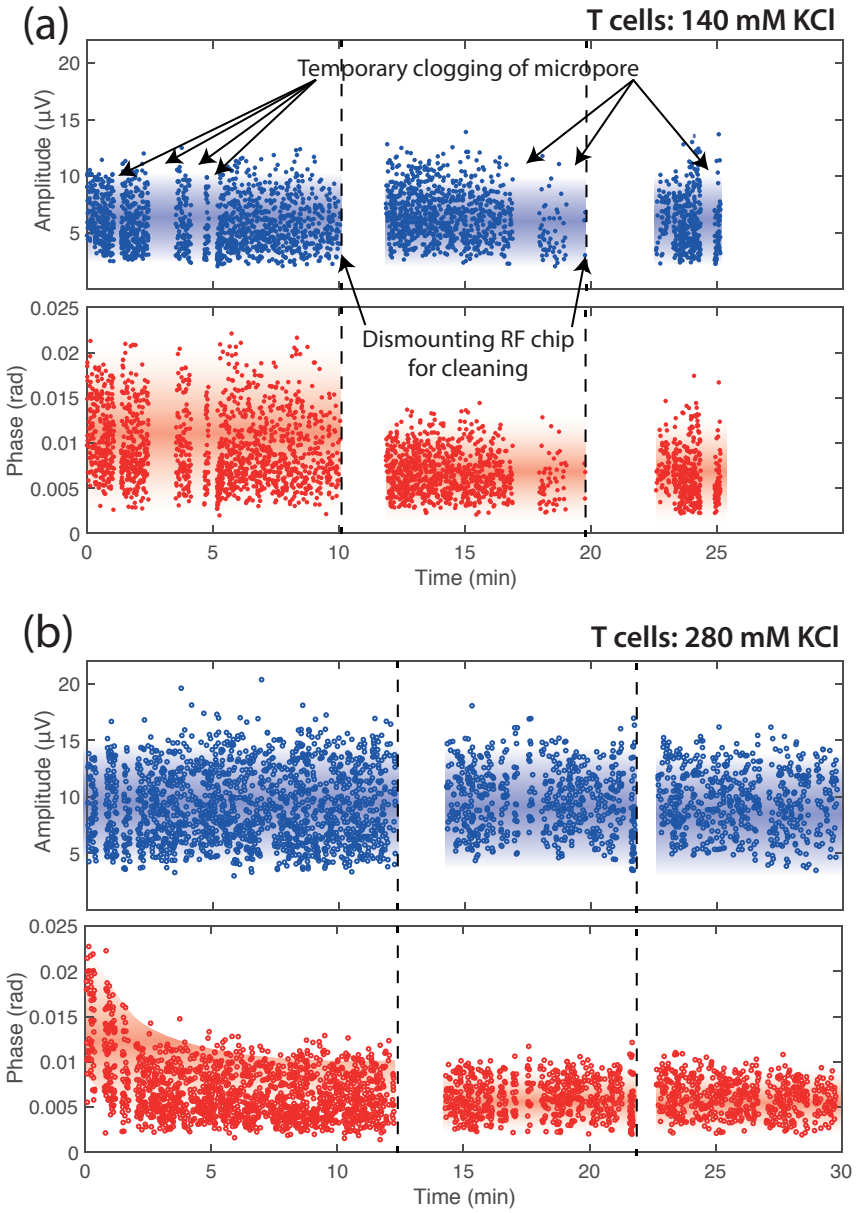

Figure 5.10: Time dependent amplitude heights (blue) and phase shifts (red) of the events shown in Fig. 5.7 for (a) T cells which are suspended in 140 mM KCl buffer and (b) cells which are suspended in 280 mM KCl buffer. The data points are plotted versus the time of their occurrence during the experiment which has an overall length of about 25 min and 30 min, respectively. The colored blue and red bands are a guide for the eye.

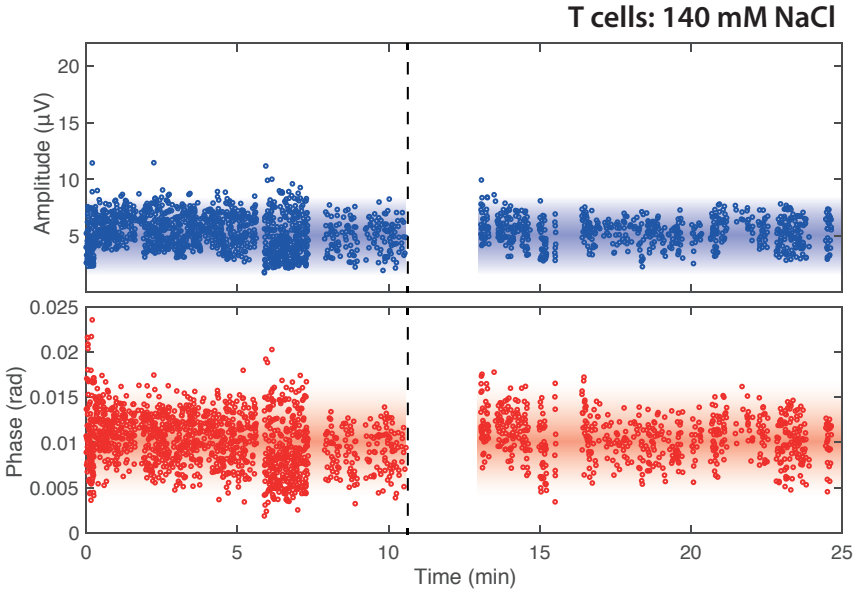

Figure 5.11: Time dependent amplitude heights (blue) and phase shifts (red) of the events shown in Fig. 5.8 for T cells which are suspended in physiological bath solution containing mostly 140 mM NaCl buffer. The data points are plotted versus the time of their occurrence during the experiment, which has an overall length of about 25 min. The colored blue and red bands are a guide for the eye.

The same analysis was done with the data presented in Fig. 5.7 where the influence of the KCl concentration on the signals was investigated. In Fig. 5.10 the time dependent evolution of the amplitude and phase shift of the individual events is shown, accordingly.

Fig. 5.10 (a) shows the data over the course of the experiment which took about 25 min. Before the chip was dismounted and cleaned the first time the amplitude and the phase of the signal are stable. At $t \approx 12$ min when the experiment was started again a clear shift to lower phases is observed while the amplitude is kept constant. The situation does not change for the third run which starts at $t \approx 23$ min.

An interesting observation can be made for the time evolution of the measurement quantities for the experiment which was conducted in the 280 mM KCl buffer. This plot is shown in Fig. 5.10 (b) and the phase measurement shows a clear decrease during the experiment in the first 5 min. After that, the experiment is interrupted two times for cleaning the chip but the phase signal and the amplitude measured for the remaining 25 min of the experiment are unchanged.

The control measurement was shown in Fig. 5.8. Here the signals from cells suspended in a physiological buffer containing mainly NaCl was compared to the buffer containing the same concentration of KCl. The corresponding time domain representation is given in Fig. 5.11. It is apparent that in contrast to the cells, which are suspended in the KCl

containing buffer, the phase does not change in the course of the 25 min of this experiment. As well the amplitude and the phase remain constant.

It shall be pointed out that for the experimental data given in Fig. 5.9, Fig. 5.10 and Fig. 5.11 the point $t = 0\,\text{sec}$ is not well defined. Before the measurement can be started, the cells, which are incubated in RPMS medium in an incubator have to be transferred into the corresponding measurement buffer as discussed in detail in Ch. A. A defined volume of cell suspension is taken from the culture medium and this sample is centrifuged for 5 min to separate the cells from the medium. After that the medium is removed and the cells are resuspended into one of the measurement buffer for washing. It is important to centrifuge the cells a second time to get rid of remaining medium. The second centrifugation step takes again 5 min. Finally, the solution is exchanged again with the measurement buffer and cells are resuspended by resuspending the cell pellet, which is formed during the centrifugation step, with a pipette. The cell sample is then brought to the lab where the RF measurement takes place and the RF chip is impedance matched before the time domain measurement is started. This means that, before the measurement in the RF setup is started, the cells have been in contact with the measurement medium for at least 15 min.

Nevertheless, the observation can be made that cells in physiological buffer as well as beads in KCl buffer do show stable measurements in amplitude and phase for up to 1 h overall measurement time. In contrast to that, cells suspended in buffers containing 140 mM and 280 mM KCl show a characteristic decrease in the phase shift after some minutes while maintaining their amplitude values.

Furthermore, it is observed that the overall amplitudes in the KCl containing buffers are increased and additionally a higher KCl concentration can even further increases the amplitude. For the T cell measurements, this effect can be attributed to an increased conductivity of the cell membrane in the presence of high KCl concentrations as is discussed in the following.

5.4.2 Patch Clamp Experiments

To study this effect, a patch clamp experiment was conduced with T cells in bath solution, which is the typically electrolyte used for patch clamp experiments, and T cells in pipette solution with a 140 mM and 280 mM KCl concentration, respectively. A schematic of the measurement setup is shown in Fig. 5.12 (a).[1]

The measurement is performed in the following way: Cells that are investigated are first immobilized on a 35 mm Petri dish which is coated with the cell adhesive amino acid poly-L-lysine (PLL). The PLL is incubated in the dish for 10 min at room temperature

[1] Jann Haberts has conducted the patch clamp experiments.

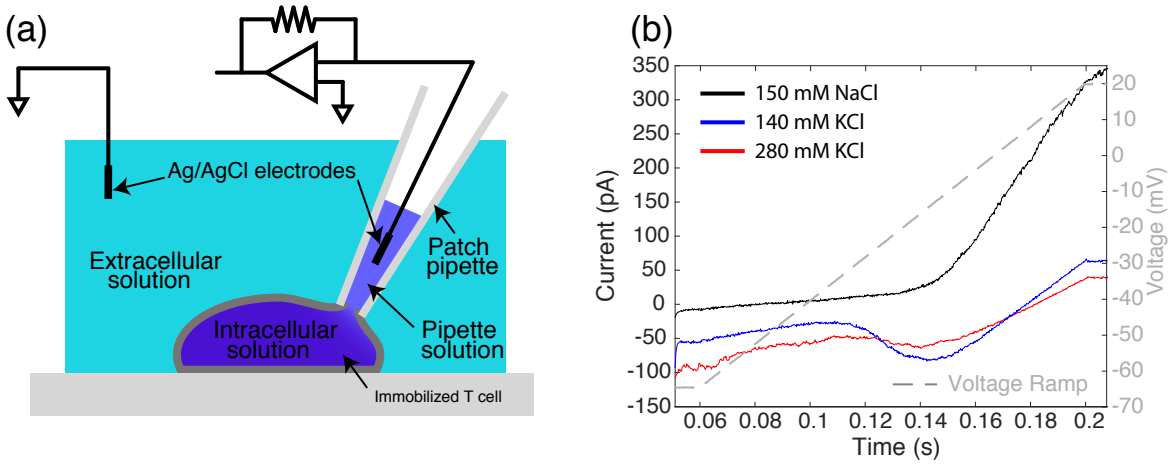

Figure 5.12: (a) Schematic of the patch clamp setup comprising of a moveable patch pipette containing a Ag/AgCl electrode immersed in pipette solution. The pipette can be brought in contact to an immobilized T cell and the membrane patch in the pipette orifice is ruptured, thus opening the inside of the cell and enabling to measure the current through the cell membrane when a voltage is applied (voltage-clamp) or measure the membrane potential when a current is applied (current-clamp). (b) Voltage-clamp measurement of three T cells suspended in different extracellular media. For each measurement the voltage is ramped from −65 mV to 20 mV and the individual measurements give an average over five consecutive voltage-clamp measurements at one cell.

and then rinsed three times with DI water. Before the measurement starts, the cells which are suspended in their growth medium (see Ch. A) are transferred into the Petri dish and are incubated for 20 min so that they can sediment and adhere to the surface of the dish. Depending on the experimental environment which shall be tested, the growth solution is removed by washing the cells three times with bath solution and after the final washing step 1 mL of the desired extracellular buffer is pipetted onto the cells.

Micropipettes[2] are prepared in advanced using a pipette puller[3] producing pipette tips with opening tip diameters of about 1 µm and tip resistances between 3 MΩ and 5 MΩ. For the experiment a pipette is filled with pipette solution (i.e. the regular pipette solution containing KCl in a 140 mM concentration) and the solution is brought in contact with a Ag/AgCl electrode which is connected to the head stage of the identical amplifier that was also used for the RPS experiments. Another Ag/AgCl electrode is immersed into the extracellular solution. The pipette is mounted to a micro manipulator so that it can be brought into contact to a cell by optical control through an upright microscope. Before the pipette is lowered into extracellular solution a slight pressure is applied to the pipette which leads to pipette solution being released constantly into the extracellular solution

[2]GB150T-8P, Scienca Products
[3]P-2000, Sutter Instruments

and consequently the pipette solution is not intermixed with the extracellular solution. When the pipette is brought into the vicinity of a cell, a mild suction at the micropipette is applied, thus the cell membrane is brought into final contact with the pipette in such a way that a high ohmic seal is created between the cell membrane and the micropipette. This seal is called GΩ-seal and having a seal of at least 1 GΩ is vital for the experiment because the currents that are measured via the cell membrane are in the order of pA. If there would be a big contribution to the current originating from leakage currents due to a low seal, these leakage currents would exceed the signals potentially by many orders of magnitude. The membrane patch, which is attached to the micropipette is ruptured with an additional brief suction so that the inside of the cell is directly connected to the inside of the pipette. In this, so called whole-cell configuration, the current across the entire membrane of the cell is measured when a voltage is applied across the two electrodes (voltage-clamp), or the potential across the membrane can be measured if a current is applied across the electrodes (current-clamp).

In Fig. 5.12 (b) the results from voltage-clamp experiments with three different cells in three different buffer solutions are shown. The applied voltage ramp is shown as a gray dashed line in the figure and it is a linear ramp between −60 mV and 20 mV. The solid black, blue and red lines represent the current that is measured across the cell membrane in different buffers.

In black, the response from a cell which is suspended in regular bath solution is shown. The curve shows the characteristic behavior of voltage gated ion channels. For low voltages the current increases only slowly. At a certain threshold value of about 20 mV the current increase, with respect to the voltage increase, becomes strong. This effect is caused by voltage gated ion-channels allowing for ions to flow through the membrane. The higher the membrane potential becomes, the more channels open, resulting in a higher measured current. For low voltages, only small currents can flow because in general the cell membrane is a highly nonconducting entity.

The situation changes when the bath solution is exchanged with pipette solution containing 140 mM KCl. This situation is illustrated in Fig. 5.12 (b) as a blue line. In contrast to the bath solution a current of approximately −50 pA is measured for a membrane potential of −60 mV already indicating that in this environment the membrane has an increased conductivity compared to the physiological environment discussed previously. The current increases with increasing voltage indicating that more current can flow through the membrane in comparison to the cells suspended in bath solution. At voltages around −30 mV the ion channels are open again, as indicated by an increase in the absolute current. Finally, when the potential starts to become positive the overall current decreases. This behavior was always observed when a GΩ seal is achieved for this

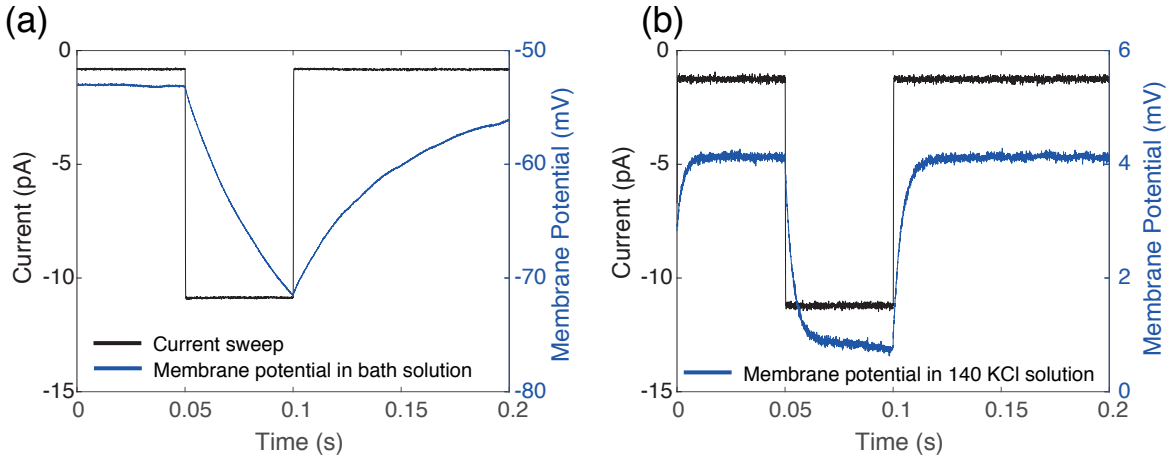

Figure 5.13: Current-clamp measurements of T cells submerged in bath solution (140 mM NaCl) (a) and 140 mM KCl solution (b). The black lines indicate the applied current pulse while in blue the measured membrane potential is shown.

experimental environment.

Finally, cells suspended in 280 mM KCl pipette solution are tested and the result is shown as a red line in Fig. 5.12 (b). At −60 mV, the current across the membrane is further decreased to about 100 pA and the current increase due to opening ion channels is quenched. This is indicating that the overall biological fitness of the cells is decreased, which does not come as a surprise, when the biological stress due to unphysiological environments is even more increased. But the current that can flow through the membrane is even more increased indicating that the conductivity of the membrane is even higher in this experimental environment.

In Fig. 5.13 (a) and (b) the results from current-clamp experiments with cells in bath solution and in 140 mM KCl pipette solution are shown. For both experiments a current step of −10 pA was applied across the electrodes. The bath solution in Fig. 5.12 (a) represents the situation which is expected for a healthy T cell. If no current is applied, a resting membrane potential between −50 mV and −60 mV is expected. When the current pulse is applied, the membrane is further depolarized. As the membrane is conductive to a certain extend and physically it is forming a capacitor the induced change in membrane potential only changes slowly according to the time constant $\tau = R_{\text{mem}} C_{mem}$ where R_{mem} is the resistance and C_{mem} is the capacity of the membrane as illustrated in Fig. 3.3 (d). The membrane capacitance cannot be changed as it is basically a function of the membrane thickness and the cell surface. As a matter of fact, the time constant is mostly governed by the membrane resistance.

If the cells in 140 mM KCl pipette solution are measured in the same manner the

results from the current-clamp experiments change drastically as shown in Fig. 5.13 (b). Even before the current pulse starts the membrane potential is very low (4 mV). The cell is no longer polarized. When the current is applied the membrane potential changes only slightly by about 2.5 mV. Furthermore, the slope of the corresponding change in membrane potential shows a drastically decreased time constant τ directly indicating that the membrane shows an increased conductivity in the KCl buffer.

It shall be pointed out that this experiment was not repeated with the 240 mM KCl containing pipette solution because in this environment the success rate for forming GΩ seals was decreased, already indicating that not only the membrane conductivity changes but that the cell undergoes biological changes, too.

5.4.3 FEM Simulations for Increased Membrane Conductivity

According to the patch clamp measurements it was shown that the membrane does show an increased conductivity in the KCl buffers. This is also supported by experiments presented in the literature [137, 138]. FEM simulations are used to investigate how such an increase can be correlated to the RF signals. To do that the simulation model which was discussed in Sec. 3.6 was expanded in such a way that the particle in the simulation volume is modeled to have a conducting membrane. The membrane is implemented into the simulation as a boundary condition, in COMSOL called a Transition Boundary Condition. A schematic of the simulation volume is shown in Fig. 5.14 (a). The particle in the simulation volume has a diameter of 2 µm and it is filled with a liquid having a conductivity of 1.29 S/m and a dielectric constant of $\epsilon = 80$. For a series of membrane conductivities starting from 100 S/m to 6000 S/m the reflected signal is simulated similar to the simulation discussed previously. The RF frequency is set to 1 GHz and the reflected signal is derived according Eq. 3.40 as discussed before.

The results are summarized in Fig. 5.14 (b). If the membrane conductivity is low (i.e. 100 S/m) the amplitude of the reflected signal is low, too. Increasing the conductivity leads to an increased reflected signal. The simulated increase in the reflected amplitude is not linear but rather it saturates for increasing membrane conductivities. This effect can be explained by the fact that the electrical field which is produced by the electrode tips in the sensing region is shielded from the inside of the particle if its membrane is more conductive. This shielding is more effective the higher the conductivity of the membrane becomes as is shown in the simulation of the magnitude of the electrical field, illustrated in Fig. 5.14 (c).

When the membrane is not conductive to a high extend it acts predominantly as a capacitor as schematically illustrated in Fig. 3.3 (d). In this case the capacitance is shorted out by the 1 GHz RF field and the electrical field can polarize the inside of the

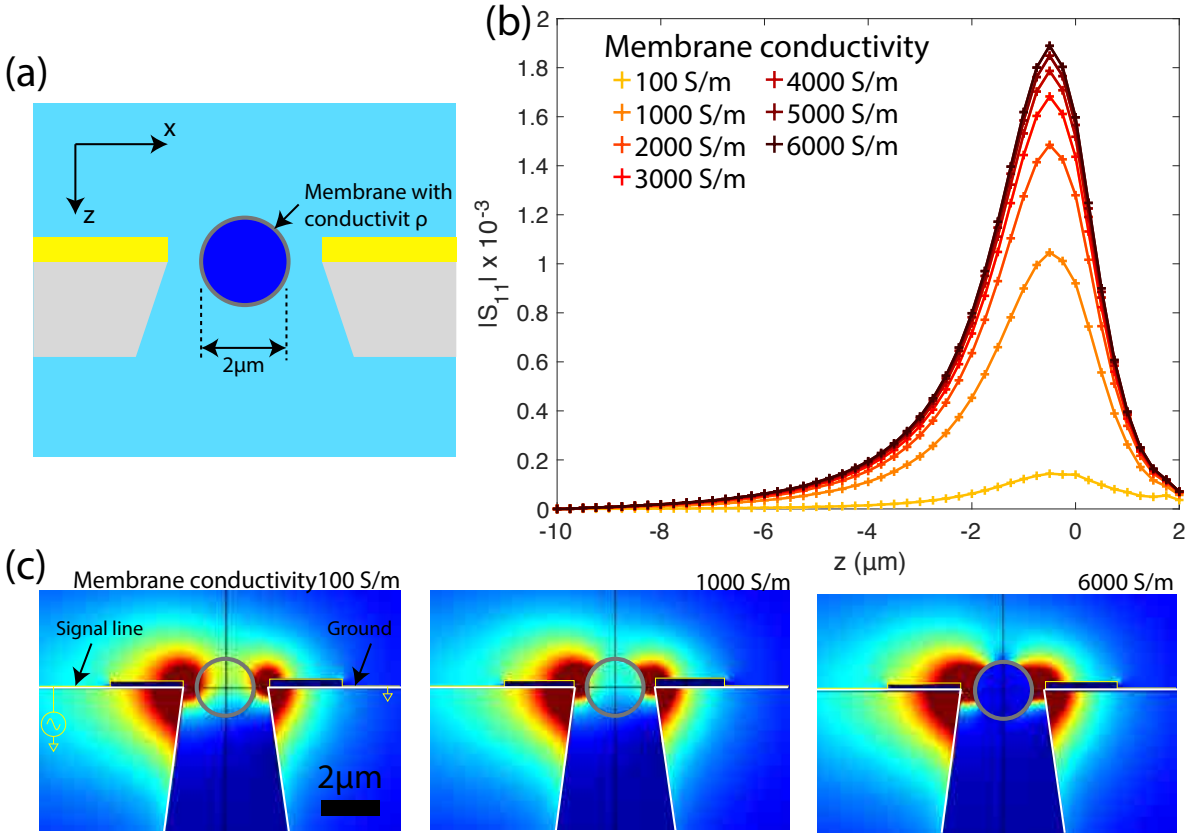

Figure 5.14: (a) Schematic of the simulation volume which is similar to the geometry that is discussed in Sec. 3.6. The test particle, having a diameter of 2 µm, is translocating through the micropore which has electrode tips with a thickness of 1 µm. The particle has a conducting shell that is implemented in the simulation as a boundary condition. Inside the particle there is liquid with an $\epsilon = 80$ and a conductivity of 1.29 S/m. (b) Simulated response of RF reflection for particles with different membrane conductivities translocating through the micropore. The reflected amplitude increases for increasing conductivities. (c) Field simulations in the sensing region with test particles centered in the micropore having three different membrane conductivities. With increasing conductivity the field inside the particles is shielded.

particle. A conducting membrane is shielding the inside more efficiently as is shown in the field simulation for a membrane conductivity of 1000 S/m in Fig. 5.14 (c). For even higher conductivities the electrical field is completely shielded from the inside of the particle and consequently an even higher conductivity does not alter the overall RF response anymore.

The patch clamp measurements and the FEM simulations can now be used to interpret the RF measurements. It was observed that T cells in physiological buffer tend to show lower reflected amplitudes (see Fig. 5.11) compared to the reflected amplitudes in the unphysiological buffer containing mostly KCl (see Fig. 5.9 and Fig. 5.10). Voltage-clamp measurements have shown that in the physiological buffer the cell membrane does show only a small current when the applied voltage is set to −60 mV (see Fig. 5.12 (b)). Additionally, it was argued that the corresponding current-clamp measurements point out that the overall membrane resistance is a lot higher compared to the cells that are suspended in the KCl buffer (see Fig. 5.13). During the patch clamp measurements the increased membrane conductivity was observed right from the first voltage-clamp measurement which was taken only minutes after transferring the cells into the KCl buffer. In accordance with the RF measurements which show stable reflected amplitude for all buffer. The only difference is the overall amplitude that changes when the buffer is changed.

As a matter of fact, this findings together with the presented FEM simulations clearly show that an increased membrane conductivity leads to higher reflected amplitude and that the differences in the measured reflected amplitude can be correlated to the membrane conductivity. A cell with a higher membrane conductivity is shielding its inside from the RF field and thus its interaction with the RF field is increased leading to higher reflected amplitudes.

5.4.4 Microscopy Experiments

The remaining problem is to interpret the phase signal which changes during the RF measurements. These changes are interpreted as cells becoming apoptotic due to the unphysiological environment. Apoptosis is the programmed cell death that cells can go through because of different environmental factors [139]. In contrast to necrosis which is another cell death process, during apoptosis the cell stays intact before it is disposed by the immune system. But typically it is observed that the cell changes its morphology during apoptosis [140].

To see that, the morphological changes of T cells in the 140 mM KCl containing buffer are observed over the period of 1 h in a microscope and the results are shown in Fig. 5.15.[4] Three cells are shown in the figure. In this experiments the first picture was taken directly after the cells are suspended in the KCl buffer. The overall appearance is in accordance

[4]Thanks to Lola Hernandez for taking the pictures.

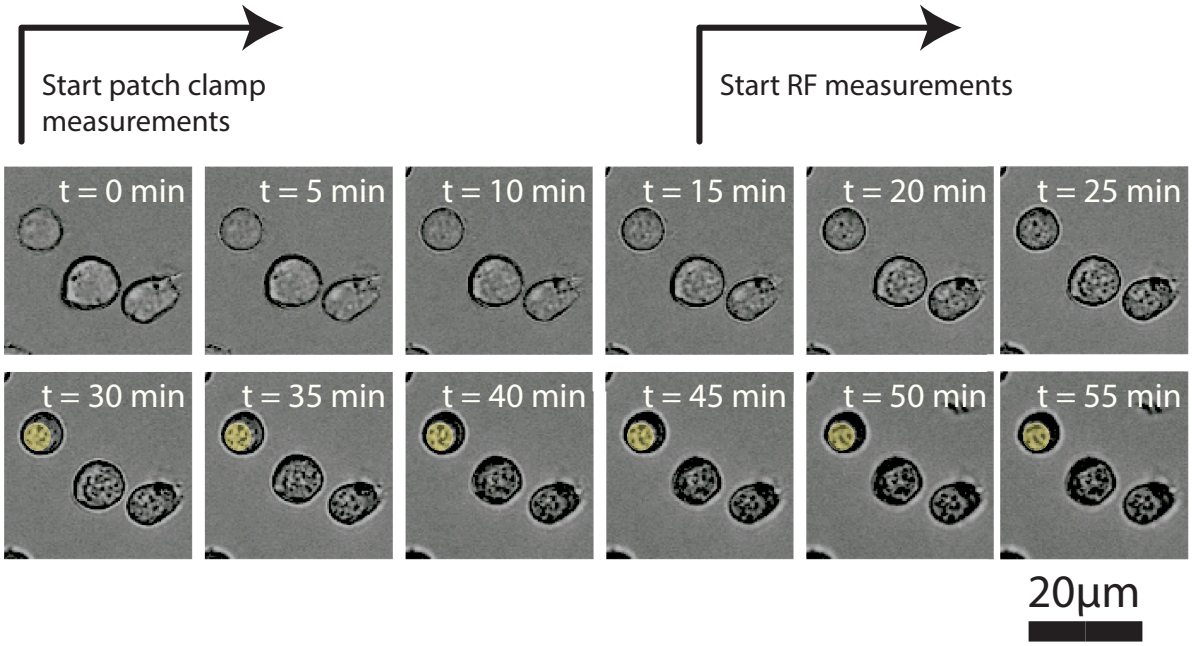

Figure 5.15: Light microscopic time series of Jurkat T cells in pipette solution (140 mM KCl) over the course of 55 min after transferring the cells from the culturing buffer into the pipette solution. During the 55 min observation time the cell membranes becoming wrinkled and they tend to shrink until at $t = 40$ min the cell nucleus becomes clearly visible. For one cell the nucleus is marked in yellow once it becomes visible. The figures are corrected for contrast and brightness and the uncorrected images are shown in Fig. B.3 in the appendix.

with a healthy cell. During the observation time it is seen that the cell membrane starts to become wrinkled and the cells tend to shrink slightly. At about $t = 35$ min after incubation the cell nucleus becomes visible and this visibility is further increased during the rest of the measurement.

This effect can be attributed to the cell loosing its intercellular medium, which a typical process in apoptotic cells [140]. As it was already discussed, a direct synchronization between this effect and a corresponding phase change of the reflected RF signal would be desirable. Unfortunately, in the setup presented this is difficult to realize because before the cells can be measured in the RF setup they have to be transferred into the buffer in which they are measured. Before the measurement can start the cells are in contact with the buffer for at least 15 min as was discussed.

The morphological change of the cell is a process that clearly develops over time, which is in accordance with the observation that the phase of the RF signal is changed during the course of the experiment. The approximate starting point of the RF measurements is marked in the figure to get an impression what the morphological state of the cell is

when the RF measurement is started.

Clearly, more experiments are needed to correlate apoptosis with the RF phase signal, but the presented findings already give an impression that the apoptotic cells in the KCl buffer gradually change over time. This is in accordance with the phase change seen so far.

Chapter 6

Summary

Two electrical and label-free flow cytometric methods used for single particle characterizations were discussed in this thesis. The first one is RPS where a voltage is applied across a glass MP, which is filled with electrolyte solution, to induce an ion current to flow through the MP. Polystyrene beads, suspended in electrolyte solution, are dragged through the pore by an applied suction. Beads translocating the pore temporarily block the ion flow which is observed by measuring the ionic current versus time. The second method is dielectric spectroscopy where an RF wave is brought into the vicinity of such a MP using a CPW. Particles translocating through the pore are exposed to the electrical field originating from the RF wave and their temporal interaction with the field is used to measure different particle properties.

In **Part I** of the thesis the glass MP preparation using laser ablation from an ArF-based excimer laser was discussed. It was shown that the method is capable of directly drilling conically shaped MPs with diameters down to 2.4 µm suitable for RPS experiments. Noise measurements were carried out showing that the ultimate limitation of these measurements is high frequency noise originating from the dielectric glass substrate the MP is embedded in, and from parasitic capacitances. These high frequency noise components can be removed from the measurement using a LPF with a cutoff frequency in the low kilohertz regime. It is enabling the measurement of translocation events with durations in the millisecond range but limiting the overall temporal resolution of the setup. Consequently this is preventing the application from being used for detecting translocation processes that take place at nanosecond timescales.

In the end of Part I commercially available MPs were utilized to show how RPS measurements can be used to observe the pressure induced translocation of polystyrene beads through the MPs. Not only the presence of the beads was detected but the amplitude of the current pulse war directly correlated to the diameter of the individual particles. It was further revealed that the frequency of the RPS current pulses can be correlated to

the particle concentration.

As the RPS method is limited to the measurement of particle sizes and the translocation times, the development of a pore based method using AC signals, for further characterization of particles, is the prospect of **Part II** of the thesis.

It was described how the RF chip, used for the high frequency measurements is manufactured. The glass MP is embedded at the vicinity of the open end of the signal line of a gold CPW and this glass chip is soldered on a custom made PCB accommodating a varactor-diode based impedance matching circuit. When the RF chip is impedance matched to the surrounding transmission lines, it completely absorbs the energy of the input RF wave. A translocating particle temporarily distorts the overall chip impedance which is used for particle characterization. The measurements are carried out by directly tracing the reflection of the impedance matched RF chip using the CW mode of a VNA. Simultaneous RPS measurements were performed to validate the RF measurements. It was proven that translocating polystyrene beads with a diameter of 500 nm can be electronically observed within this RF measurement setup, which is shown by a covariance analysis of the RPS data to the RF data.

In comparison to the RPS data, the VNA reflection measurements revealed very poor performance in terms of sampling the time domain data. As a matter of fact, this method turned out to be not suitable for resolving the dynamic of a translocating particle, which is expected to have a characteristic event shape as proven by FEM simulations.

To improve the sampling capabilities of the setup, a heterodyne mixing scheme was implemented, which allows for down converting the RF signal to a frequency that can be sampled with a lock-in amplifier. This procedure further allows for not only measuring the amplitude of the reflected RF signal but to simultaneously measure the induced phase shift.

A series of studies were performed to measure the characteristic RF reflection signatures originating from polystyrene beads and Jurkat T cells translocating through a MP with a diameter of 11 µm. It was observed that the signal amplitude is increased if the salt in the electrolyte solution is changed from NaCl to KCl. Furthermore, it was observed that an increased KCl concentration is causing slightly higher amplitudes for the measurements with the Jurkat T cells.

Apart from the amplitudes of the reflected RF signal, the phase change of the translocating cells showed a unique behavior within the KCl buffer. When the KCl concentration was set to 140 mM the phase showed two distinct correlations with the event amplitudes as a function of time. Furthermore, it was shown that the effect did not occur for polystyrene beads in the KCl buffer and for cells suspended in a physiological buffer.

These findings were further analyzed by investigating the time-dependent fingerprint

of the measured amplitudes and phases over the course of the flow experiment. While the amplitude of the events remained stable in all experiments, at a certain point during the experiment the phase decreased if the cells were measured within an unphysiological buffer.

While the amplitude of the RF signal was stable over the course of all experiments, the absolute measured value was changed when the buffers were changed. This is especially true when the amplitudes of translocating T cells in NaCl and KCl buffer were compared. T cells suspended in KCl electrolyte did show a higher reflected amplitude with respect to the NaCl buffer control experiments. This effect was correlated to an increased membrane conductivity of the cell if they are exposed to an excess of KCl, which was measured using patch clamp experiments. These measurements did prove directly that the membrane conductivity increases in this environment. The conductivity increase leads to a shielding of the inside of the cell from the RF electromagnetic field. As a matter of fact, electrically the cell looks bigger to the device. FEM simulations did show that an increase in membrane conductivity correlates with an increase in reflected RF amplitudes.

Phase changes can be attributed to morphological changes of the cell. These changes were observed by optical microscopy and it was seen that if the cells are transferred into the KCl solution the membrane starts to become wrinkly within minutes. During the observation over the course of an hour the cells darken, indicating that they gradually lose their intercellular liquid. At a certain point in time the cell nucleus becomes clearly visible. This behavior is in accordance with apoptosis that is induced by the unphysiological environment, which strengthens our claim that the RF chip is capable of sensing the programmed cell death.

Additionally, to this observation the phase change is induced earlier if the KCl concentration is doubled, which is a hint for morphological cell changes that are induced more rapidly due to the increased biological stress of the cells.

Chapter 7

Outlook

In Part I of the thesis the glass MPs have shown to be a suitable RPS platform. Nevertheless, the pore diameter that can be produced with the direct drilling process is limited. Especially for nanoscopic applications, as e.g. for detecting single DNA strands, a nanometer sized pore is necessary and creating such a pore by direct laser ablation is challenging if not impossible. However, these glass pores can be used as a support structure for nanopores and some preliminary experiments have been performed, yet.

A schematic of such a system is shown in Fig. 7.1 (a). It consists of a glass MP which is coated with a thin layer of PDMS. On top of the PDMS a nanomembrane is located that contains nanometer sized pores. The nanomembrane consists of crystalline GaAs with a thickness of about 20 nm. This membrane is grown with molecular beam epitaxy (MBE) on top of an AlAs sacrificial layer which is located on a polished GaAs wafer. During the MBE process, after growing the stack of materials, it is possible to locally etch holes into the GaAs membrane with a process called local droplet etching (LDE). Details of this process can be found elsewhere [141]. The LDE process can be tuned in such a way that the induced holes penetrate the nanomembrane and thus if the nanomembrane can be freely suspended, nanopores are formed.

The process of suspending the membrane by transferring it onto a glass MP is illustrated schematically in Fig. B.4 in the appendix. It basically divides into two steps: First, the MBE grown structures are lithographically patterned into micrometer sized tiles that are glued onto a silicon wafer using a photoresist. Once glued to the silicon wafer the tiles can be freed from the GaAs wafer by selectively under etching the sacrificial layer in hydrofluoric acid [142]. In the second step the membranes are pressed mechanically against the PDMS coated MP and they stick to the PDMS due to the Van der Waals force. The resist with which the membranes were glued to the silicon wafer is washed away in a wet etch step. Consequently, a membrane with a thickness of 20 nm is suspended over the glass MP.

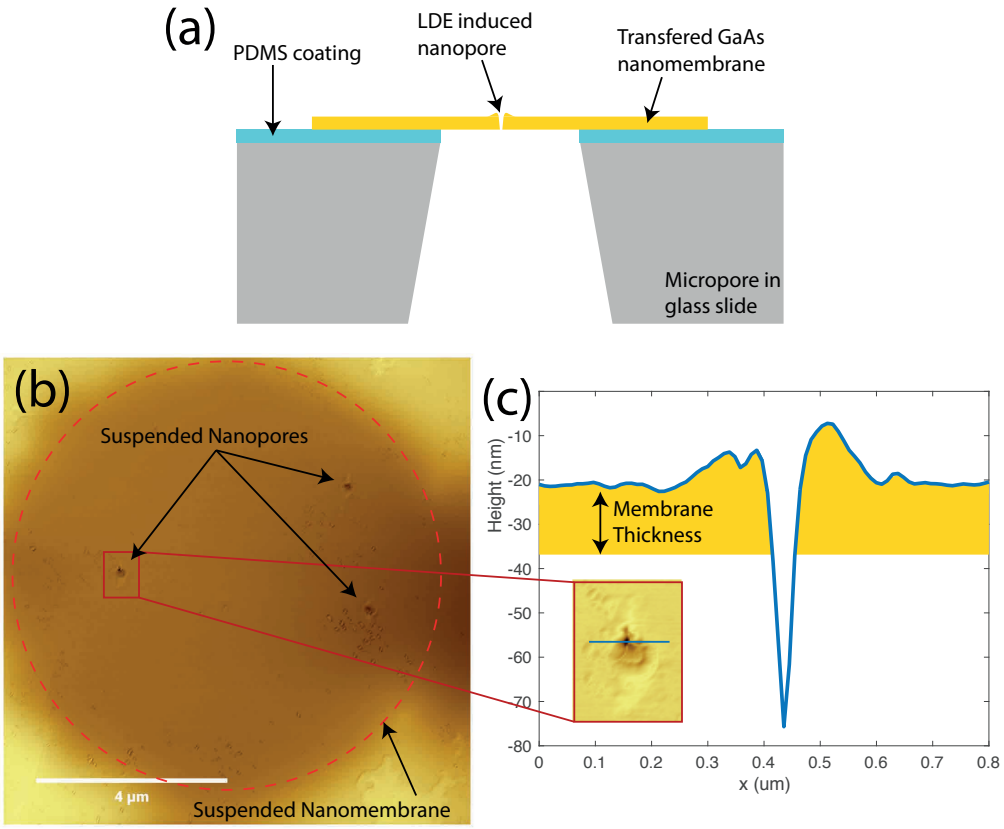

Figure 7.1: (a) Schematic of a transferred GaAs nanomembrane on top of a PDMS coated glass micropore. In the nanomembrane there are nanopores that were produced, using LDE, prior to the transfer process. (b) AFM image of a transferred membrane with three nanopores, which are freely suspended over the micropore. (c) Line scan over one of the suspended nanopores. In yellow the thickness of the membrane is indicated. The line scan shows a deep structure, clearly exceeding the thickness oft the membrane and thus indicating that a nanopore is formed. (inset) Zoomed-in view on one nanopore in the suspended area.

The result of this transfer process is shown in Fig. 7.1 (b). This image is acquired with atomic force microscopy (AFM) and it shows a membrane which is suspended over the MP and three suspended LDE induced nanopores. For a RPS experiment using this system it will be necessary to have only one suspended nanopore. Fortunately, the diameter of the MP can be tuned as shown in the thesis, as well as the density of the LDE induced nanopores is tunable [141, 143]. Therefore, in future the process can be optimized such that the probability of transferring one nanopore onto the MP is maximized. Fig. 7.1 (c) shows a line scan through one of the suspended nanopores. In yellow the thickness of the GaAs membrane is drawn. The measurement indicates that there is a deep hole in the membrane, i.e. the measured thickness clearly exceeds the membrane thickness,

indicating that an open nanometer sized pore is produced.

If the MPE process is optimized in such a way that the LDE holes are optically active, the nanopores might be used for optically detecting DNA molecules translocating the nanopores, as was suggested based on numerical calculations in our paper published in the journal Applied Physics Letters [144]. Additionally, the membrane can be used to accommodate electronic components as e.g. waveguides to interface the suspended nanopores with the RF chip. Beside that the MP can in principle be used as a support structure for common solid state nanopores as e.g. pores in silicon nitride [145], graphene [146, 147] or molybdenum disulfide [148].

In Part II of the thesis the presented RF measurement setup showed that by measuring the time domain amplitude and phase signals from translocating cells in different physiological and non physiological buffers allows to resolve time-dependent cell changes. Furthermore, it was discussed that the setup is in principle capable of detecting polystyrene beads with diameters as small as 500 nm. This detection limit was achieved by having a pore diameter of 4 µm and consequently electrode tips which are placed closer to each other, compared to the cell measurements where a pore diameter of 11 µm was used to enable cell translocations. Still, the setup holds room for improvements, some of which are discussed in the following.

An effect that has to be explained in more detail is the fact that polystyrene beads translocating the sensing region show different amplitudes if suspended in different electrolytes. While suspended in NaCl containing buffer the induced amplitude modulation is barely visible over the noise floor, but translocating beads can be detected if they are suspended in KCl solution. The most obvious difference between these two salts is the size of the Na^+ and K^+ ions. Furthere experiments will be needed to test how the amplitude behaves in RbCl and CsCl. As these ions have a further increased ion radius corresponding experiments will shed light on the influence of the salts on the experimental outcome.

In terms of the RF measurement setup, an improvement can be made in the preparation process of the RF chip. At current state the throughput of chip preparation is vastly limited by the linear and time consuming FIB induced Pt deposition step. For the functionality this step was crucial because it enables to locally thicken the electrode tips by simultaneously aligning the electrode tips with the MP with, in principle, nanometer precision.

As long as the chip is used for the investigation of cells with diameters in the micrometer range the alignment of the CPW structure to the micron sized pore is possible using standard optical microscopy methods as e.g. delivered by a mask aligner. The remaining problem is to locally increase the thickness of the electrodes in the vicinity of the MP

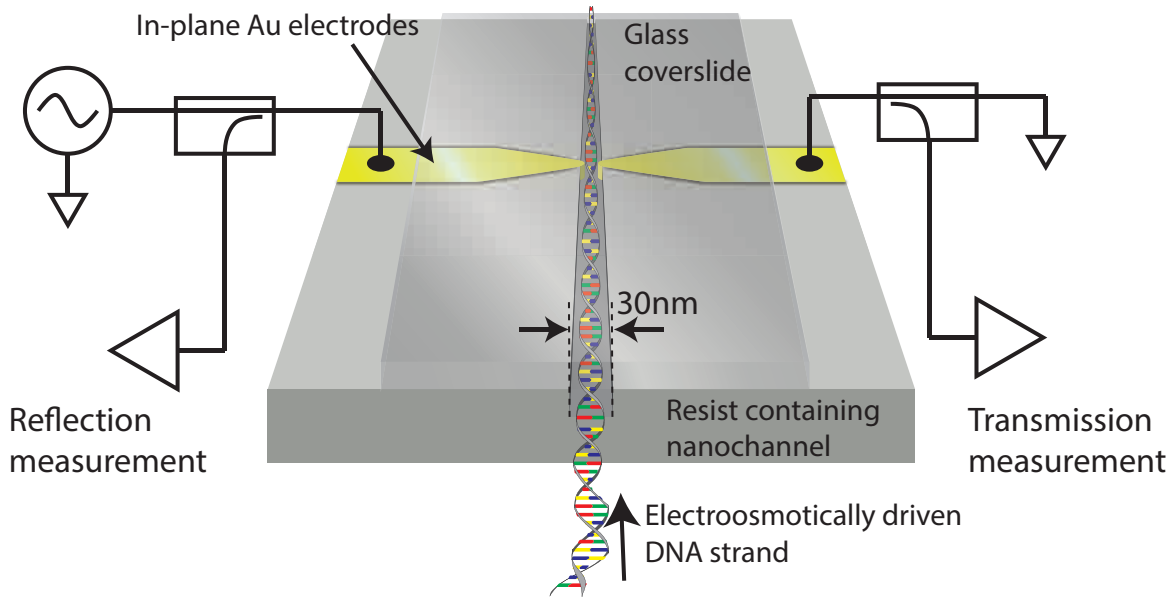

Figure 7.2: Schematic of a nanochannel with integrated in-plane gold electrodes for the investigation of translocating DNA strands. The channels and the electrodes can be patterned using nano imprint lithography and the metalization can be produced using shadow evaporation [151]. For the electronic readout a reflection or transmission readout can be implemented.

to increase the reflected signal as was demonstrated in the numerical analysis shown in Fig. 3.16 (b) and Fig. 3.17. This thickening can in principle be achieved by electrochemical gold deposition through a resist based deposition mask [149, 150]. In this process a conductive seed layer is deposited on the substrate. For the RF chip this seed layer is the CPW metalization layer which is produced by PVD. The electrode tips are exposed using a positive photoresist thus locally exposing the electrode tips while covering the remaining chip. A variety of chemistries exists enabling to electroplate the gold through the mask delivering potentially a high aspect ratio and a smooth Au surface [150]. This method would allow for fabricating multiple RF chips simultaneously and thus decreasing the chip preparation time drastically.

In future, it is aimed to transfer the measurement scheme from micron sized particles like cells to the nanoscale. The vision is to miniaturize the setup to perform these measurement at the nanometer length scale with the goal to ultimately being sensitive to single DNA molecules. A schematic a device that has the potential to achieve that is shown in Fig. 7.2.

The device consists of a nanofluidic channel which can be produced by nano imprinting a stamp into a UV curable resist. This process, called nano imprint lithography (NIL),

is capable to imprint channels as small as 10 nm [152] in a quick, cheep and reproducible manner [151]. Apart from the nano channel fabrication it is possible to selectively metallize the electrode structures which are oriented perpendicular to the nano channel. The method is known as shadow vapor deposition and it was patented by I. Fernandez-Cuesta and S. Cabrini in 2014 [153].

It shall be pointed out that the geometrical scale of this chip will lead to electrodes which have resistances in the kΩ range because of their size. Consequently, the impedance of this chip will be high and as a matter of fact, when connecting this device to a 50 Ω transmission line the RF waves entering the device will be predominantly reflected back because of the impedance mismatch (see Eq. 3.30), which is a common problem in miniaturized RF devices [154]. There are suggestions for experimental setups solving this issue, one of which is an interferometric technique capable to perform an impedance matching even for nanoscopic RF devices with high ohmic resistances. This technique was proposed by H. Happy et al. in 2014 [154]. A schematic of such a system is shown in Fig. B.5 in the appendix. The method uses a tunable reference impedance that is, together with the nano fluidic chip, connected to a RF source via a hybrid coupler. For the measurement the reference impedance is tuned in such a way that the reflected wave from the device and the reference are equal. When reflected back, the signals are phase shifted by 180° by the coupler and thus the two signals interfere destructively. Consequently a slight change in the impedance of the nano fluidic chip is detectable as it is measured in comparison to the reference.

This method comes with some advantages: First of all, it allows for an impedance matching even for nanoscopic devices with a high resistance. Additionally, the method allows for an impedance match within a high frequency range as the reference impedance can be tuned to all supported frequencies, thus the RF chip can be impedance matched at any frequency that is desired. The frequency is not governed by the device geometry but rather by the RF instrumentation that is used (e.g. the frequency range of the hybrid coupler, the attenuators etc.). As a matter of fact, this method can in principle be used with the RF chip discussed in the thesis so that the response of the device at multiple frequencies can be measured sequentially.

In summary it was shown that counting single cells electronically at radio frequencies is possible. Beside that it was demonstrated that the presented method is capable to deliver insight into the physiological state of a T cell. Being a label-free method and operating at frequencies in the low GHz regime the method has the potential of being a versatile tool for nondestructive biological measurements not only at the micrometer range, but due to the flat noise characteristic it has the potential of being used for sensing DNA in future, too.

Appendix A

Test Sample Preparation

A.1 Preparation of the Test Samples

Polystyrene particles are used for testing and calibrating new designs. They have the advantages that they can be purchased with a very wide range of diameters and surface properties. Those particles are commonly used to calibrate resistive pulse measurements. In the scope of the thesis they have been used to test the RF device, too

Jurkat T cells were characterized in the RF setup. The cell culture is discussed. Furthermore, cell preprocessing prior to the RF experiments is described.

A.1.1 Polystyrene Beads

For suspending the polystyrene beads, electrolytes with different salt concentrations were used. The solutions are prepared with purified distilled water. To increase the wetting of the polystyrene 0.01 % (v/v) of Titron-X-100 can be added to the solution. It is important to ensure that the solution is free from impurities that might interfere with the measurement because the impurities can be misinterpreted as signals from translocating polystyrene beads. To purify the solution, it is filtered with a 200 nm sterile filter to get rid of all impurities that are bigger than the filter size. Finally, the polystyrene beads are diluted to the final concentration.

A.1.2 Cell Culturing - Jurkat T Cells

Jurkat T Lymphocytes are cultured in RPMI 1640 medium. The medium is mixed with 7.5 % new-born calf serum (NCS) and 1.2 % penicililin/streptomycin. Incubation is done in an incubator at 37° C with 5 % CO_2. The cells are stored in a cell culture flask and are diluted every second day, except of the weekend (i.e. they are diluted on Monday,

Wednesday and Friday). This keeps the cell concentration at about 10^6 1/mL. Cells extracted form the flask at the day of incubation are used for the experiments.

A.2 Recipes for Cell Buffer

In the following the recipes for preparing the electrolyte solutions which were used for the RF experiments are given. All electrolytes are prepared in DI water and prior to the cell transfer they are filtered with a 200 nm syringe filter.

A.2.1 Ca^{2+} Buffer

Table A.1: Ca^{2+} buffer

Ingredient	Concentration (mM)
KCl	5 mM
NaCl	140 mM
NaH_2PO_4	1 mM
$MgSO_4$	1 mM
$CaCl_2$	1 mM
Glucose	5.5 mM
KOH	adjust until pH = 7.4

A.2.2 Pipette Solution

Table A.2: Regular pipette solution, and high KCl concentration pipette solution when 140 mM KCl is interchanged with 280 mM KCl.

Ingredient	Concentration (mM)
KCl	140 mM, (280 mM)
NaCl	-
$MgCl_2$	2 mM
$CaCl_2$	1 mM
EGTA	2.5 mM
HEPES	10 mM
Glucose	-
KOH	adjust until pH = 7.4

A.2.3 Extracellular Bath Solution

Table A.3: Bath solution

Ingredient	Concentration (mM)
KCl	5 mM
NaCl	140 mM
$MgCl_2$	2 mM
$CaCl_2$	2 mM
EGTA	-
HEPES	10 mM
Glucose	5 mM
KOH	adjust until pH = 7.4

Appendix B

Suplementar Images

In the following, supplementary images are given that were not shown in the main text of the thesis.

B.1 Figures Concerning Chapter 5

In Fig. B.1 and Fig. B.2 the individual scatter plots that were already shown as an overlay in Fig. 5.7 are given. The scatter plot in Fig. B.1 (a) and Fig. B.2 (a) now clearly shows the two correlations that develop over the course of the experiment when the RF response of the T cells in non-physiological buffer is measured.

Fig. B.3 shows the same images that were given in Fig. 5.15. Here the images are not corrected for contrast and brightness and no cell constituents are marked.

B.2 Figures Concerning Chapter 7

In Fig. B.4 the schematic process is illustrated that was used to manufacture the suspended nanomembranes that were discussed in the outlook of the thesis.

A schematic of the interferometric impedance matching strategy which was discussed in the outlook of the thesis is shown in Fig. B.5.

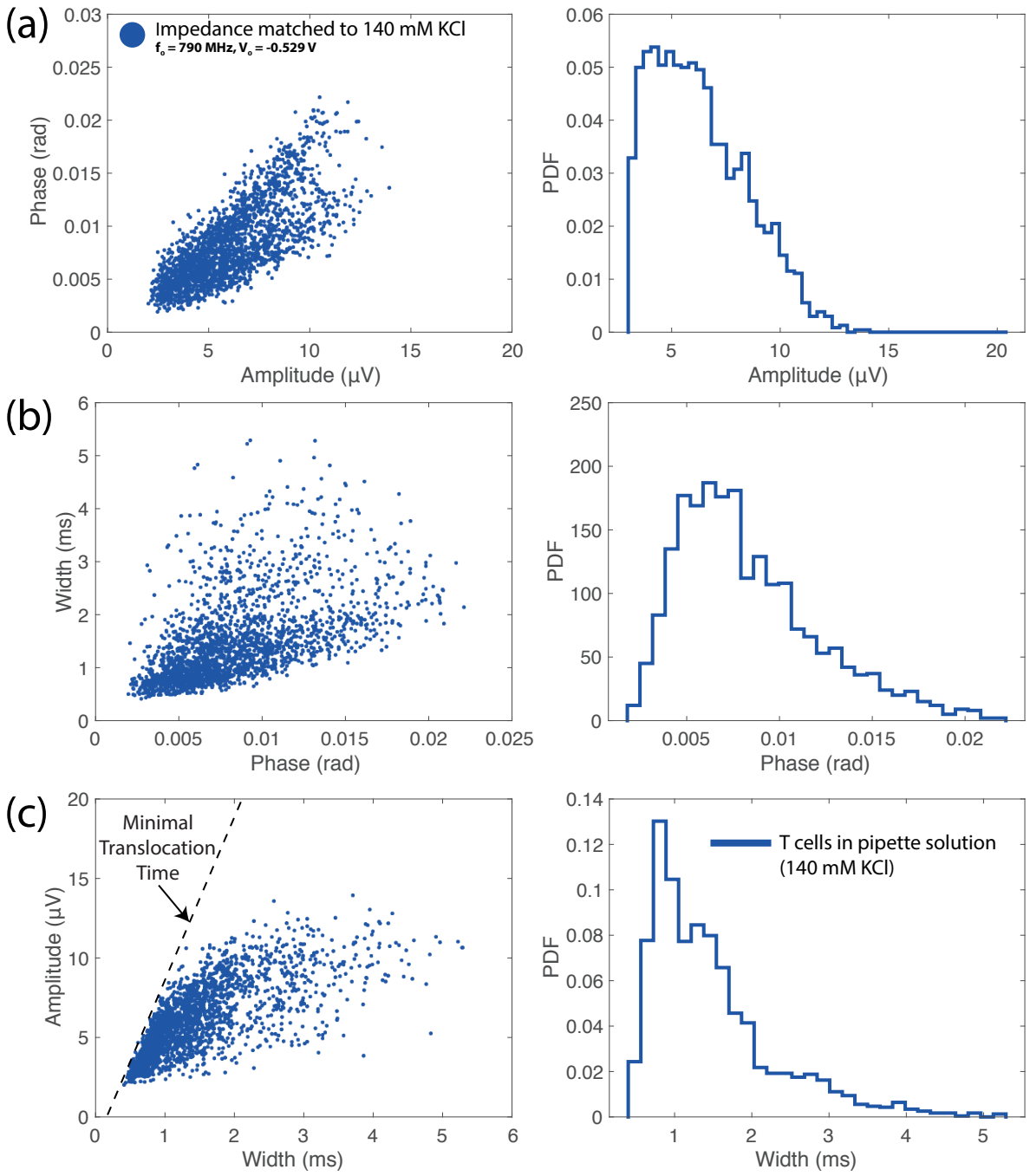

Figure B.1: Scatter plots and normalized histograms of reflected amplitude, phase shift and event width of T cells in 140 mM pipette solution. (a) Scatter plot of reflected amplitude versus phase shift for T cells in pipette solution of different concentrations. Histogram of reflected amplitude. (b) Phase shift versus event with and histogram of the phase shift. (c) Event width versus reflected amplitude and histogram of the event widths.

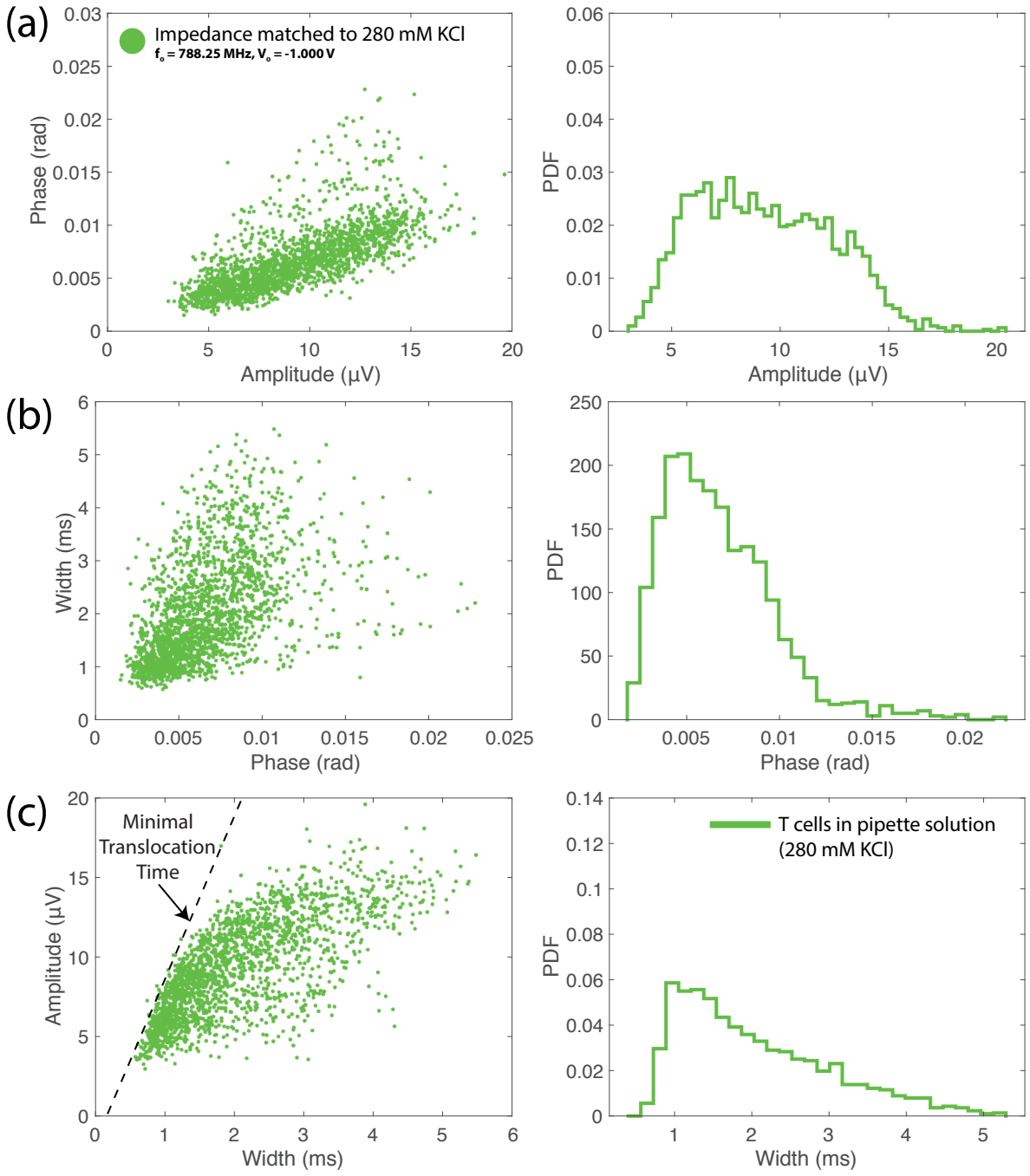

Figure B.2: Scatter plots and normalized histograms of reflected amplitude, phase shift and event width of T cells in 280 mM pipette solution. (a) Scatter plot of reflected amplitude versus phase shift for T cells. Histogram of reflected amplitude. (b) Phase shift versus event with and histogram of the phase shift. (c) Event width versus reflected amplitude and histogram of the event widths. As the two measurements are conducted in different electrolytes the devices are impedance matched to the corresponding electrolytes.

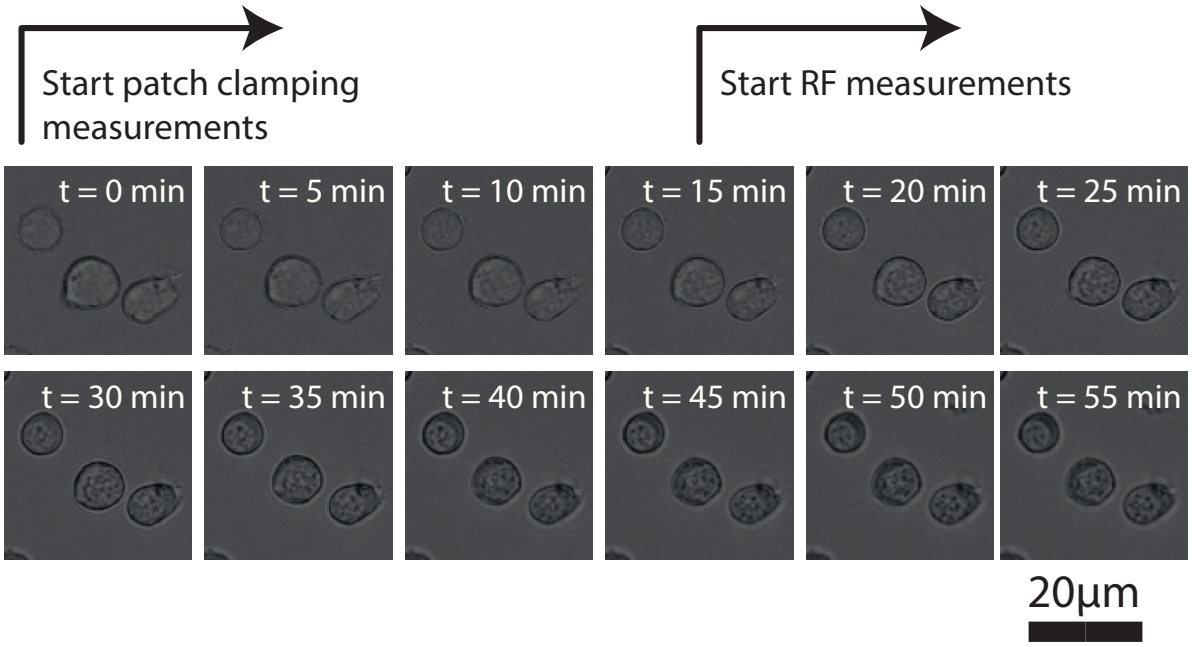

Figure B.3: Light microscopic time series of Jurkat T cells in pipette solution over the course of 55 min after transferring the cells from the culturing buffer into the pipette solution. These figures are not adjusted in contras and brightness.

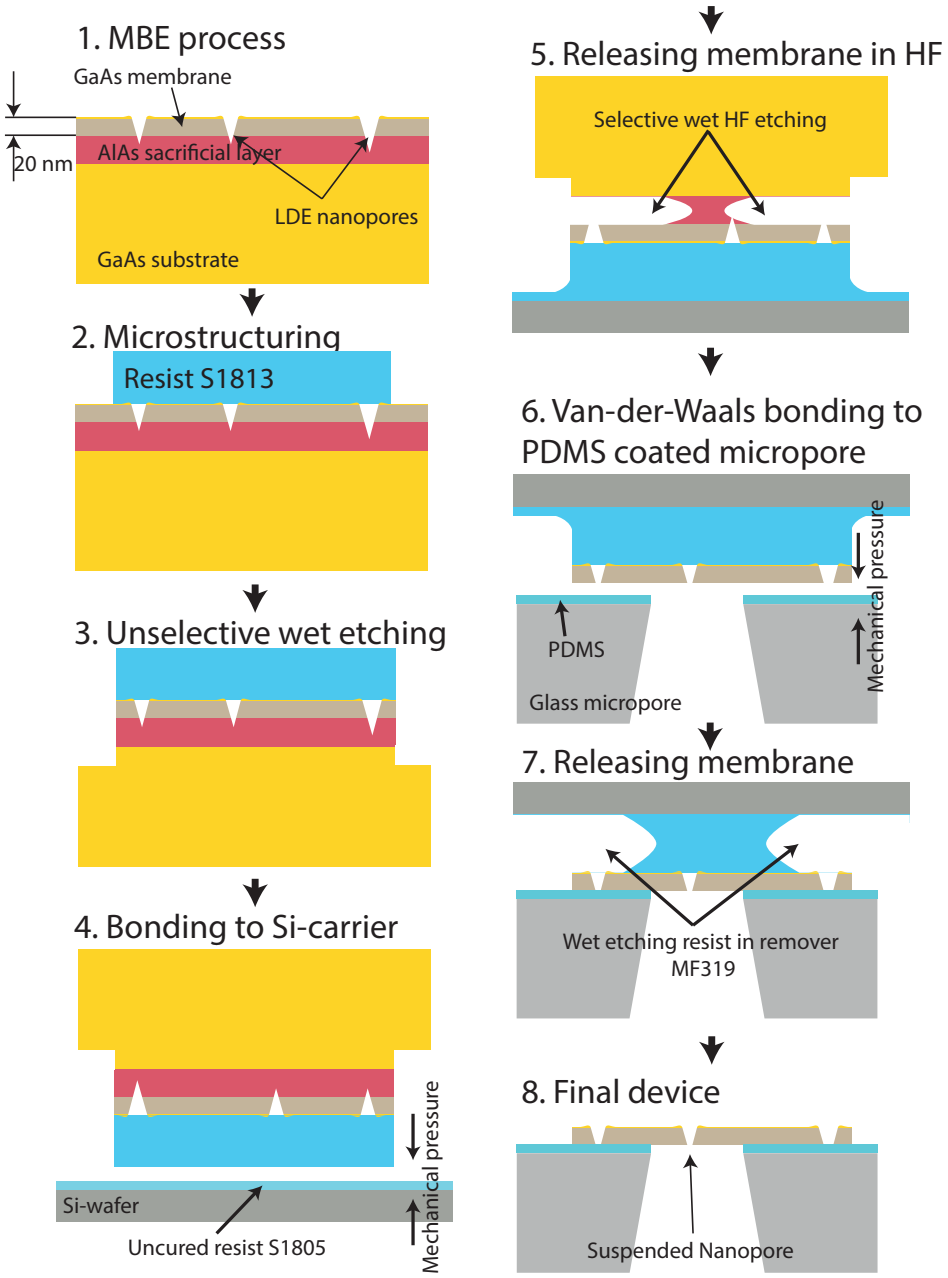

Figure B.4: Transfer process of MBE grown nano-membranes which contain LDE induced nano holes. The membrane has a thickness of 20 nm on top of an AlAs sacrificial layer. (2) The membrane is structured into tiles of 20 µm length. (3) The sample is etched unselectively thus exposing the sacrificial layer and the membrane is bounded onto a Si-waver (4) which is spincoated with a thin resist layer which is not cured when it is brought into contact with the structured resist on the membrane. (5) Membrane are released from the GaAs waver by selectively etching the AlAs in concentrated hydrofluoric acid. (6) Finally the membrane is pressed onto a micropore inside a glass chip, that is covered with a thin layer of PDMS and the resist is dissolved in remover. (7) When the Si carrier falls off the glass chip the membrane is suspended over the micropore containing nanopores.

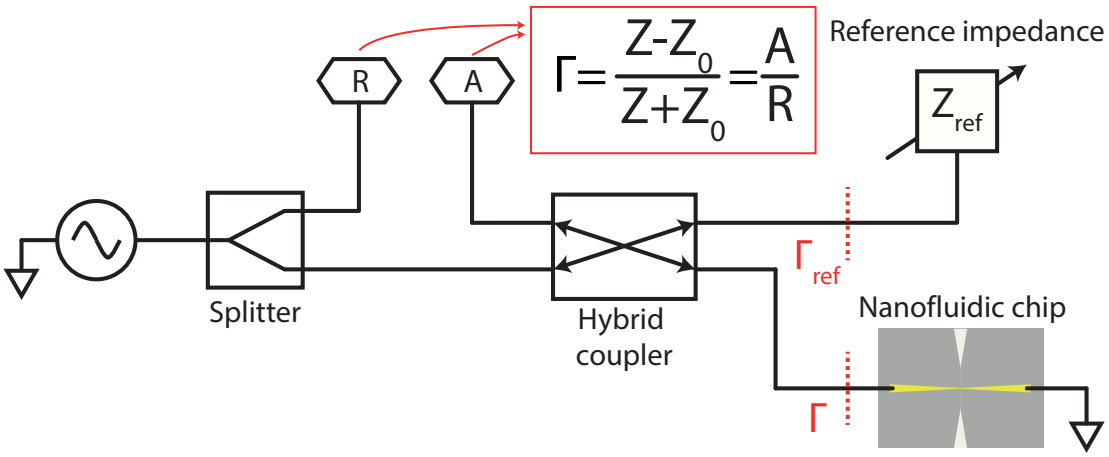

Figure B.5: Interferometric impedance matching circuit as proposed by Happy *et al.* [154]. The circuit consists of a hybrid coupler and a tunable reference impedance. By tuning the reference impedance to have the same impedance as the nanofluidic chip the reflection can be measured precisely because at the receiver A the reflected signal is zero because the signal from the chip and the reference interfere destructively thus the device is naturally impedance matched. The picture is taken and adapted from the corresponding figure shown in shown in Ref. [154].

Bibliography

[1] W. H. Coulter. Means for counting particles suspended in a fluid, October 1953. US Patent 2,656,508.

[2] R. W. DeBlois and C. P. Bean. Counting and Sizing of Submicron Particles by the Resistive Pulse Technique. *Review of Scientific Instruments*, 41(7):909–916, 1970.

[3] C. Dekker. Solid-state nanopores. *Nature Nanotechnology*, 2(4):209–215, 2007.

[4] B. M. Venkatesan and R. Bashir. Nanopore sensors for nucleic acid analysis. *Nature Nanotechnology*, 6(10):615–24, 2011.

[5] J. Clarke, H. Wu, L. Jayasinghe, A. Patel, S. Reid, and H. Bayley. Continuous base identification for single-molecule nanopore DNA sequencing. *Nature Nanotechnology*, 4(4):265–70, 2009.

[6] I. M. Derrington, T. Z. Butler, M. D. Collins, E. Manrao, M. Pavlenok, M. Niederweis, and J. H. Gundlach. Nanopore DNA sequencing with MspA. *Proceedings of the National Academy of Sciences*, 107(37):16060–16065, 2010.

[7] E. A. Manrao, I. M. Derrington, A. H. Laszlo, K. W. Langford, M. K. Hopper, N. Gillgren, M. Pavlenok, M. Niederweis, and J. H. Gundlach. Reading DNA at single-nucleotide resolution with a mutant MspA nanopore and phi29 DNA polymerase. *Nature Biotechnology*, 30(4):349–353, 2012.

[8] A. Adan, G. Alizada, Y. Kiraz, Y. Baran, and A. Nalbant. Flow cytometry: basic principles and applications. *Critical Reviews in Biotechnology*, 37(2):163–176, 2017.

[9] G. Brecher, M. Schneiderman, and G. Z. Williams. Evaluation of electronic red blood cell counter. *American Journal of Clinical Pathology*, 26(12):1439–49, 1956.

[10] C. F. T. Mattern, F. S. Brackett, and B. J. Olson. Determination of Number and Size of Particles by Electrical Gating: Blood Cells. *Journal of Applied Physiology*, 10(1):56–70, 1957.

[11] M. Graham. The Coulter principle: foundation of an industry. *Journal of the Association for Laboratory Automation*, 8(6):72–81, 2003.

[12] M. Sivakumaran and M. Platt. Tunable resistive pulse sensing: potential applications in nanomedicine. *Nanomedicine*, 11(16):2197–2214, 2016.

[13] D. Kozak, W. Anderson, R. Vogel, and M. Trau. Advances in resistive pulse sensors: Devices bridging the void between molecular and microscopic detection. *Nano Today*, 6(5):531–545, 2011.

[14] M. N. Rhyner. The Coulter Principle for Analysis of Subvisible Particles in Protein Formulations. *The AAPS Journal*, 13(1):54–58, 2011.

[15] Y. Song, J. Zhang, and D. Li. Microfluidic and Nanofluidic Resistive Pulse Sensing: A Review. *Micromachines*, 8(7):204, 2017.

[16] L. Yang and T. Yamamoto. Quantification of Virus Particles Using Nanopore-Based Resistive-Pulse Sensing Techniques. *Frontiers in Microbiology*, 7:1500, 2016.

[17] H. E. Kubitschek. Electronic Counting and Sizing of Bacteria. *Nature*, 182(4630):234–235, 1958.

[18] B. J. Berne and R. Pecora. *Dynamic Light Scattering: With Applications to Chemistry, Biology, and Physics*. Dover Books on Physics Series. Dover Publications, 2000.

[19] J. E. Bagness, A. V. Ottaway, and B. W. Young. Centrifugal methods of particle size analysis. Applications of the disc centrifuge in the particle size analysis of pesticide suspension. *Proceedings of the Society for Analytical Chemistry*, 9(4):83, 1972.

[20] H. Vegad. 'Old' technique reborn for nanoparticle size analysis with unparalleled resolution. *Powder Metallurgy*, 50(4):291–293, 2007.

[21] J. C. Maxwell. *A Treatise on Electricity and Magnetism*. Number 1 in A Treatise on Electricity and Magnetism. Clarendon Press, 1873.

[22] E. Weatherall and G. R. Willmott. Conductive and Biphasic Pulses in Tunable Resistive Pulse Sensing. *The Journal of Physical Chemistry B*, 119(16):5328–5335, 2015.

[23] M. Nikolic-Jaric, S. F. Romanuik, G. A. Ferrier, G. E. Bridges, M. Butler, K. Sunley, D. J. Thomson, and M. R. Freeman. Microwave frequency sensor for detection of biological cells in microfluidic channels. *Biomicrofluidics*, 3(3):034103, 2009.

[24] Y. C. Wu, W. F. Koch, and K. W. Pratt. Proposed new electrolytic conductivity primary standards for KCl solutions. *Journal of Research of the National Institute of Standards and Technology*, 96(2):191, 1991.

[25] W. R. Smythe. Flow around a Sphere in a Circular Tube. *Physics of Fluids*, 4(6):756, 1961.

[26] W. R. Smythe. Flow Around a Spheroid in a Circular Tube. *Physics of Fluids*, 7(5):633, 1964.

[27] R. W. DeBlois, C. P. Bean, and R. K.A. Wesley. Electrokinetic measurements with submicron particles and pores by the resistive pulse technique. *Journal of Colloid and Interface Science*, 61(2):323–335, 1977.

[28] Z. Qin, J. Zhe, and G.-X. Wang. Effects of particle's off-axis position, shape, orientation and entry position on resistance changes of micro Coulter counting devices. *Measurement Science and Technology*, 22(4):045804, 2011.

[29] E. C. Gregg and K. D. Steidley. Electrical Counting and Sizing of Mammalian Cells in Suspension. *Biophysical Journal*, 5(4):393–405, 1965.

[30] M.-H. Lee, A. Kumar, K.-B. Park, S.-Y. Cho, H.-M. Kim, M.-C. Lim, Y.-R. Kim, and K.-B. Kim. A Low-Noise Solid-State Nanopore Platform Based on a Highly Insulating Substrate. *Scientific Reports*, 4(1):7448, 2015.

[31] L. Inge Berge, T. Jossang, and J. Feder. Off-axis response for particles passing through long apertures in Coulter-type counters. *Measurement Science and Technology*, 1(6):471–474, 1990.

[32] L. Inge Berge. Particle transit time distributions in single pores by the resistive pulse technique. *Journal of Colloid and Interface Science*, 135(1):283–293, 1990.

[33] O. A. Saleh and L. L. Sohn. Correcting off-axis effects in an on-chip resistive-pulse analyzer. *Review of Scientific Instruments*, 73(12):4396–4398, 2002.

[34] T. M. Squires and S. R. Quake. Microfluidics: Fluid physics at the nanoliter scale. *Reviews of Modern Physics*, 77(3):977–1026, 2005.

[35] Y. Berrouche, Y. Avenas, C. Schaeffer, P. Wang, and H.-C. Chang. Design of a Porous Electroosmotic Pump, Used in Power Electronics Cooling. *2007 IEEE Industry Applications Annual Meeting*, volume 45, pages 1397–1403, 2007.

[36] X. Wang, C. Cheng, S. Wang, and S. Liu. Electroosmotic pumps and their applications in microfluidic systems. *Microfluidics and Nanofluidics*, 6(2):145–162, 2009.

[37] H. Bayley and C. R. Martin. Resistive-Pulse Sensing-From Microbes to Molecules. *Chemical Reviews*, 100(7):2575–2594, 2000.

[38] J. P. Robinson. Wallace H. Coulter: Decades of invention and discovery. *Cytometry Part A*, 83A(5):424–438, 2013.

[39] S. J. Sowerby, M. F. Broom, and G. B. Petersen. Dynamically resizable nanometre-scale apertures for molecular sensing. *Sensors and Actuators B: Chemical*, 123(1):325–330, 2007.

[40] D. Kozak, W. Anderson, and M. Trau. Tuning Particle Velocity and Measurement Sensitivity by Changing Pore Sensor Dimensions. *Chemistry Letters*, 41(10):1134–1136, 2012.

[41] G. R. Willmott, R. Vogel, S. S. C. Yu, L. G. Groenewegen, G. S. Roberts, D. Kozak, W. Anderson, and M. Trau. Use of tunable nanopore blockade rates to investigate colloidal dispersions. *Journal of Physics: Condensed Matter*, 22(45):454116, 2010.

[42] G. Church, D. W. Deamer, D. Branton, R. Baldarelli, and J. Kasianowicz. Characterization of individual polymer molecules based on monomer-interface interactions, 1998. US Patent 5,795,782.

[43] J. J. Kasianowicz, E. Brandin, D. Branton, and D. W. Deamer. Characterization of individual polynucleotide molecules using a membrane channel. *Proceedings of the National Academy of Sciences*, 93(24):13770–13773, 1996.

[44] J. D. Watson and F. H. C. Crick. Molecular Structure of Nucleic Acids: A Structure for Deoxyribose Nucleic Acid. *Nature*, 171(4356):737–738, 1953.

[45] L. Song, M. R. Hobaugh, C. Shustak, S. Cheley, H. Bayley, and J. E. Gouaux. Structure of Staphylococcal alpha-Hemolysin, a Heptameric Transmembrane Pore. *Science*, 274(5294):1859–1865, 1996.

[46] P. Mueller, D. O. Rudin, H. Ti Tien, and W. C. Wescott. Reconstitution of Cell Membrane Structure in vitro and its Transformation into an Excitable System. *Nature*, 194(4832):979–980, 1962.

[47] A. Meller, L. Nivon, E. Brandin, J. Golovchenko, and D. Branton. Rapid nanopore discrimination between single polynucleotide molecules. *Proceedings of the National Academy of Sciences*, 97(3):1079–1084, 2000.

[48] M. Faller, M. Niederweis, and G. E. Schulz. The structure of a mycobacterial outer-membrane channel. *Science*, 303(5661):1189–92, 2004.

[49] T. Z. Butler, M. Pavlenok, I. M. Derrington, M. Niederweis, and J. H. Gundlach. Single-molecule DNA detection with an engineered MspA protein nanopore. *Proceedings of the National Academy of Sciences of the United States of America*, 105(52):20647–52, 2008.

[50] A. H. Laszlo, I. M. Derrington, B. C. Ross, H. Brinkerhoff, A. Adey, I. C. Nova, J. M. Craig, K. W. Langford, J. M. Samson, R. Daza, K. Doering, J. Shendure, and J. H. Gundlach. Decoding long nanopore sequencing reads of natural DNA. *Nature Biotechnology*, 32(8):829–833, 2014.

[51] Y. Feng, Y. Zhang, C. Ying, D. Wang, and C. Du. Nanopore-based Fourth-generation DNA Sequencing Technology. *Genomics, Proteomics & Bioinformatics*, 13(1):4–16, 2015.

[52] D. Branton, D. W. Deamer, A. Marziali, H. Bayley, S. A. Benner, T. Butler, M. Di Ventra, S. Garaj, A. Hibbs, X. Huang, S. B. Jovanovich, P. S Krstic, S. Lindsay, X. Sean Ling, C. H. Mastrangelo, A. Meller, J. S. Oliver, Y. V. Pershin, J. Michael Ramsey, R. Riehn, G. V. Soni, V. Tabard-Cossa, M. Wanunu, M. Wiggin, and J. A Schloss. The potential and challenges of nanopore sequencing. *Nature Biotechnology*, 26(10):1146–1153, 2008.

[53] R. M. Leggett and M. D. Clark. A world of opportunities with nanopore sequencing. *Journal of Experimental Botany*, 68(20):5419–5429, 2017.

[54] N. Fertig, Ch. Meyer, R. Blick, Ch. Trautmann, and J. Behrends. Microstructured glass chip for ion-channel electrophysiology. *Physical Review E*, 64(4):04090, 2001.

[55] A. P. Joglekar, H. Liu, G.J. Spooner, E. Meyhöfer, G. Mourou, and A. J. Hunt. A study of the deterministic character of optical damage by femtosecond laser pulses and applications to nanomachining. *Applied Physics B*, 77(1):25–30, 2003.

[56] R. An, J. D. Uram, E. C. Yusko, K. Ke, M. Mayer, and A. J. Hunt. Ultrafast laser fabrication of submicrometer pores in borosilicate glass. *Optics Letters*, 33(10):1153, 2008.

[57] M. Yu, H.-S. Kim, and R. H. Blick. Laser drilling of nano-pores in sandwiched thin glass membranes. *Optics Express*, 17(12):10044, 2009.

[58] E. Stava, H. C. Shin, M. Yu, A. Bhat, P. Resto, A. Seshadri, J. C. Williams, and R. H. Blick. Ultra-stable glass microcraters for on-chip patch clamping. *RSC Advances*, 4(73):39073–39076, 2014.

[59] E. Stava, M. Yu, H. C. Shin, H. Shin, D. J. Kreft, and R. H Blick. Rapid fabrication and piezoelectric tuning of micro- and nanopores in single crystal quartz. *Lab on a Chip*, 13(1):156–160, 2013.

[60] A.V. Eletskii. Excimer lasers. *Soviet Physics Uspekhi*, 21(6):502, 1978.

[61] J. K. Rosenstein and K. L. Shepard. Temporal resolution of nanopore sensor recordings. *2013 35th Annual International Conference of the IEEE Engineering in Medicine and Biology Society (EMBC)*, 4110–4113, 2013.

[62] R. M. M. Smeets, U. F. Keyser, N. H. Dekker, and C. Dekker. Noise in solid-state nanopores. *Proceedings of the National Academy of Sciences*, 105(2):417–421, 2008.

[63] R. M. M. Smeets, N. H. Dekker, and C. Dekker. Low-frequency noise in solid-state nanopores. *Nanotechnology*, 20(9):095501, 2009.

[64] M. Mayer, J. K. Kriebel, M. T. Tosteson, and G. M. Whitesides. Microfabricated Teflon Membranes for Low-Noise Recordings of Ion Channels in Planar Lipid Bilayers. *Biophysical Journal*, 85(4):2684–2695, 2003.

[65] B. Rudy and L. E. Iverson. *Ion Channels*. Number Bd. 207 in Ion Channels. Academic Press, 1992.

[66] M. Mayer, J. D. Uram, and K. Ke. Noise and bandwidth of current recordings from submicrometer pores and nanopores. *ACS Nano*, 2(5):857–872, 2008.

[67] J. K. Rosenstein, M. Wanunu, C. A. Merchant, M. Drndic, and K. L. Shepard. Integrated nanopore sensing platform with sub-microsecond temporal resolution. *Nature Methods*, 9(5):487–492, 2012.

[68] A. Brüggemann, M. George, M. Klau, M. Beckler, J. Steindl, J. C. Behrends, and N. Fertig. High Quality Ion Channel Analysis on a Chip with the NPC © Technology. *ASSAY and Drug Development Technologies*, 1(5):665–673, 2003.

[69] N. Feliu, X. Sun, R. A. Alvarez Puebla, and W. J. Parak. Quantitative Particle-Cell Interaction: Some Basic Physicochemical Pitfalls. *Langmuir*, 33(27):6639–6646, 2017.

[70] L. Luo, S. R. German, W.-J. Lan, D. A. Holden, T. L. Mega, and H. S. White. Resistive-Pulse Analysis of Nanoparticles. *Annual Review of Analytical Chemistry*, 7(1):513–535, 2014.

[71] V. Tabard-Cossa, D. Trivedi, M. Wiggin, N. N. Jetha, and A. Marziali. Noise analysis and reduction in solid-state nanopores. *Nanotechnology*, 18(30):305505, 2007.

[72] D. W. Deamer and D. Branton. Characterization of Nucleic Acids by Nanopore Analysis. *Accounts of Chemical Research*, 35(10):817–825, 2002.

[73] S. Shekar, D. J. Niedzwiecki, C.-C. Chien, P. Ong, D. A. Fleischer, J. Lin, J. K. Rosenstein, M. Drndic, and K. L. Shepard. Measurement of DNA translocation dynamics in a solid-state nanopore at 100 ns temporal resolution. *Nano Letters*, 16(7):4483–4489, 2016.

[74] E. L. C. J. Blundell, R. Vogel, and M. Platt. Particle-by-Particle Charge Analysis of DNA-Modified Nanoparticles Using Tunable Resistive Pulse Sensing. *Langmuir*, 32(4):1082–1090, 2016.

[75] R. A. Hoffman and W. B. Britt. Flow-system measurement of cell impedance properties. *Journal of Histochemistry & Cytochemistry*, 27(1):234–240, 1979.

[76] H. Morgan, T. Sun, D. Holmes, S. Gawad, and N. G. Green. Single cell dielectric spectroscopy. *Journal of Physics D: Applied Physics*, 40(1):61–70, 2007.

[77] A. P. O'Rourke, M. Lazebnik, J. M. Bertram, M. C. Converse, S. C. Hagness, J. G. Webster, and D. M. Mahvi. Dielectric properties of human normal, malignant and cirrhotic liver tissue: in vivo and ex vivo measurements from 0.5 to 20 GHz using a precision open-ended coaxial probe. *Physics in Medicine and Biology*, 52(15):4707–4719, 2007.

[78] K. S. Zubair, S. A. Alhuwaidi, H. H. Song, Y. G. Shellman, W. A. Robinson, A. J. Applegate, and C. M. Amato. Investigation of dielectric spectroscopy response in normal and cancerous biological tissues using S-parameter measurements. *Journal of Electromagnetic Waves and Applications*, 32(8):956–971, 2018.

[79] N. Nikolova. Microwave Imaging for Breast Cancer. *IEEE Microwave Magazine*, 12(7):78–94, 2011.

[80] G. H. Markx and C. L. Davey. The dielectric properties of biological cells at radiofrequencies: applications in biotechnology. *Enzyme and Microbial Technology*, 25(3-5):161–171, 1999.

[81] W. Kuang and S. O. Nelson. Low-frequency dielectric properties of biological tissues: A review with some new insights. *Transactions of the ASAE*, 41(1):173–184, 1998.

[82] P. Debye. Part I. Dielectric constant. Energy absorption in dielectrics with polar molecules. *Transactions of the Faraday Society*, 30:679-684, 1934.

[83] K. Asami. Characterization of heterogeneous systems by dielectric spectroscopy. *Progress in Polymer Science*, 27(8):1617–1659, 2002.

[84] W. J. Ellison, K. Lamkaouchi, and J.-M. Moreau. Water: a dielectric reference. *Journal of Molecular Liquids*, 68(2-3):171–279, 1996.

[85] W. J. Ellison. Permittivity of Pure Water, at Standard Atmospheric Pressure, over the Frequency Range 0-25THz and the Temperature Range 0-100C. *Journal of Physical and Chemical Reference Data*, 36(1):1–18, 2007.

[86] F. Bordi, C. Cametti, and R. H. Colby. Dielectric spectroscopy and conductivity of polyelectrolyte solutions. *Journal of Physics: Condensed Matter*, 16(49):R1423–R1463, 2004.

[87] J. B. Hasted, D. M. Ritson, and C. H. Collie. Dielectric Properties of Aqueous Ionic Solutions. Parts I and II. *The Journal of Chemical Physics*, 16(1):1–21, 1948.

[88] N. Gavish and K. Promislow. Dependence of the dielectric constant of electrolyte solutions on ionic concentration: A microfield approach. *Physical Review E*, 94(1):012611, 2016.

[89] T. Chen, G. Hefter, and R. Buchner. Dielectric Spectroscopy of Aqueous Solutions of KCl and CsCl. *The Journal of Physical Chemistry A*, 107(20):4025–4031, 2003.

[90] R. Buchner, G. T. Hefter, and P. M. May. Dielectric Relaxation of Aqueous NaCl Solutions. *The Journal of Physical Chemistry A*, 103(1):1–9, 1999.

[91] H. P. Schwan. Electrical properties of tissues and cell suspensions: mechanisms and models. In *Proceedings of 16th Annual International Conference of the IEEE Engineering in Medicine and Biology Society*, pages A70–A71, 1994.

[92] H. P. Schwan. Electrical properties of tissue and cell suspensions. volume 5 of *Advances in Biological and Medical Physics*, pages 147 – 209. Elsevier, 1957.

[93] R. Pethig. Dielectric Properties of Biological Materials: Biophysical and Medical Applications. *IEEE Transactions on Electrical Insulation*, EI-19(5):453–474, 1984.

[94] R. Pethig and D. B. Kell. The passive electrical properties of biological systems: their significance in physiology, biophysics and biotechnology. *Physics in Medicine and Biology*, 32(8):933–70, 1987.

[95] H. P. Schwan and K. R. Foster. RF-field interactions with biological systems: Electrical properties and biophysical mechanisms. *Proceedings of the IEEE*, 68(1):104–113, 1980.

[96] H. P. Schwan. Analysis of Dielectric Data: Experience Gained with Biological Materials. *IEEE Transactions on Electrical Insulation*, EI-20(6):913–922, 1985.

[97] R. H. Adrian. *The Capacity of Cell Membranes: Gating Current Measurements*, pages 49–55. Springer US, Boston, MA, 1980.

[98] K. Asami, T. Yonezawa, H. Wakamatsu, and N. Koyanagi. Dielectric spectroscopy of biological cells. *Bioelectrochemistry and Bioenergetics*, 40(2):141–145, 1996.

[99] T. Sun and H. Morgan. Single-cell microfluidic impedance cytometry: a review. *Microfluidics and Nanofluidics*, 8(4):423–443, 2010.

[100] T. Sun, C. Bernabini, and H. Morgan. Single-Colloidal Particle Impedance Spectroscopy: Complete Equivalent Circuit Analysis of Polyelectrolyte Microcapsules. *Langmuir*, 26(6):3821–3828, 2010.

[101] L. Batyuk and N. Kizilova. Modeling of dielectric permittivity of the erythrocytes membrane as a three-layer model. In *Development trends in medical science and practice: the experience of countries of Eastern Europe and prospects of Ukraine*, pages 18–37. Publishing House Baltija Publishing, 2018.

[102] K. Asami. Characterization of biological cells by dielectric spectroscopy. *Journal of Non-Crystalline Solids*, 305(1-3):268–277, 2002.

[103] K. Heileman, J. Daoud, and M. Tabrizian. Dielectric spectroscopy as a viable biosensing tool for cell and tissue characterization and analysis. *Biosensors and Bioelectronics*, 49:348–359, 2013.

[104] J. Chen, C. Xue, Y. Zhao, D. Chen, M.-H. Wu, and J. Wang. Microfluidic Impedance Flow Cytometry Enabling High-Throughput Single-Cell Electrical Property Characterization. *International Journal of Molecular Sciences*, 16(12):9804–9830, 2015.

[105] F. Artis, T. Chen, T. Chretiennot, J.-J. Fournie, M. Poupot, D. Dubuc, and K. Grenier. Microwaving Biological Cells: Intracellular Analysis with Microwave Dielectric Spectroscopy. *IEEE Microwave Magazine*, 16(4):87–96, 2015.

[106] R. A. Hoffman, T. S. Johnson, and W. B. Britt. Flow cytometric electronic direct current volume and radiofrequency impedance measurements of single cells and particles. *Cytometry*, 1(6):377–384, 1981.

[107] H. E. Ayliffe, A. B. Frazier, and R. D. Rabbitt. Electric impedance spectroscopy using microchannels with integrated metal electrodes. *Journal of Microelectromechanical Systems*, 8(1):50–57, 1999.

[108] L. L. Sohn, O. A. Saleh, G. R. Facer, A. J. Beavis, R. S. Allan, and D. A. Notterman. Capacitance cytometry: Measuring biological cells one by one. *Proceedings of the National Academy of Sciences*, 97(20):10687–10690, 2000.

[109] S. Gawad, L. Schild, and Ph. Renaud. Micromachined impedance spectroscopy flow cytometer for cell analysis and particle sizing. *Lab on a Chip*, 1(1):76, 2001.

[110] D. K. Wood, S.-H. Oh, S.-H. Lee, H. T. Soh, and A. N. Cleland. High-bandwidth radio frequency Coulter counter. *Applied Physics Letters*, 87(18):184106, 2005.

[111] D. K. Wood, M. V. Requa, and A. N. Cleland. Microfabricated high-throughput electronic particle detector. *Review of Scientific Instruments*, 78(10):104301, 2007.

[112] C. S. Bausch, C. Heyn, W. Hansen, I. M. A. Wolf, B.-P. Diercks, A. H. Guse, and R. H. Blick. Ultra-fast cell counters based on microtubular waveguides. *Scientific Reports*, 7:41584, 2017.

[113] G. A. Ferrier, S. F. Romanuik, D. J. Thomson, G. E. Bridges, and M. R. Freeman. A microwave interferometric system for simultaneous actuation and detection of single biological cells. *Lab on a Chip*, 9(23):3406, 2009.

[114] N. Haandbæk, O. With, S. C. Bürgel, F. Heer, and A. Hierlemann. Resonance-enhanced microfluidic impedance cytometer for detection of single bacteria. *Lab on a Chip*, 14(17):3313, 2014.

[115] N. Haandbæk, S. C. Bürgel, F. Heer, and A. Hierlemann. Characterization of subcellular morphology of single yeast cells using high frequency microfluidic impedance cytometer. *Lab on a Chip*, 14(2):369–377, 2014.

[116] M. Steer. *Microwave and RF design, A systems approach.* SciTech Publishing Inc., Raleigh, NC, USA, 2010.

[117] D. M. Pozar. *Microwave engineering.* John Wiley and Sons, Inc., Hoboken, NJ, USA, 2012.

[118] L. Ziyu, L. Yan, H. Wei, and L. Zhibo. Analysis on mismatch loss caused by poor contact of BNC connector components. In *2014 4th IEEE International Conference on Information Science and Technology*, pages 1–4, 2014.

[119] J. Palecek, M. Vestenicky, P. Vestenicky, and J. Spalek. Examination of SMA connector parameters. In *2012 IEEE 16th International Conference on Intelligent Engineering Systems (INES)*, pages 259–263, 2012.

[120] C. P. Wen. Coplanar Waveguide: A Surface Strip Transmission Line Suitable for Nonreciprocal Gyromagnetic Device Applications. *IEEE Transactions on Microwave Theory and Techniques*, 17(12):1087–1090, 1969.

[121] R. N. Simons. *Coplanar Waveguide Circuits, Components, and Systems.* Wiley Series in Microwave and Optical Engineering. John Wiley & Sons, Inc., New York, USA, 2001.

[122] C. Bowick, C. Ajluni, and J. Blyler. *RF Circuit Design, Second Edition.* Newnes, USA, 2nd edition, 2008.

[123] D. M. Pozar. *Microwave Engineering.* Wiley, 2004.

[124] M. Steer. *Microwave and RF Design: A Systems Approach.* SciTech Pub., 2010.

[125] W. C. Michels. A double tube vacuum tube voltmeter. *Review of Scientific Instruments*, 9(1):10–12, 1938.

[126] W. C. Michels and N. L. Curtis. A Pentode Lock-InAmplifier of High Frequency Selectivity. *Review of Scientific Instruments*, 12(9):444–447, 1941.

[127] Y. Feldman, E. Polygalov, I. Ermolina, Y. Polevaya, and B. Tsentsiper. Electrode polarization correction in time domain dielectric spectroscopy. *Measurement Science and Technology*, 12(8):1355–1364, 2001.

[128] C. S. Bausch. *Tubular coplanar waveguides for the use in radio-frequency microfluidic flow cytometers.* Dr. Hut, 2016.

[129] A. Bhat, P. V. Gwozdz, A. Seshadri, M. Hoeft, and R. H. Blick. Tank circuit for ultrafast single-particle detection in micropores. *Physical Review Letters*, 121(7):078102, 2018.

[130] J. L. Hogan. The heterodyne receiving system, and notes on the recent Arlington-Salem tests. *Proceedings of the IEEE*, 87(11):1979–1990, 1999.

[131] Zurich Instruments AG. *UHF User Manual*, revision 58300 edition, 12 2018.

[132] R. T. Abraham and A. Weiss. Jurkat T cells and development of the T-cell receptor signalling paradigm. *Nature Reviews Immunology*, 4(4):301–308, 2004.

[133] E. Neher and B. Sakmann. Single-channel currents recorded from membrane of denervated frog muscle fibres. *Nature*, 260(5554):799–802,1976.

[134] B.-P. Diercks, R. Werner, P. Weidemüller, F. Czarniak, L. Hernandez, C. Lehmann, A. Rosche, A. Krüger, U. Kaufmann, M. Vaeth, A. V. Failla, B. Zobiak, F. I. Kandil, D. Schetelig, A. Ruthenbeck, C. Meier, D. Lodygin, A. Flügel, D. Ren, I. M. A. Wolf, S. Feske, and A. H. Guse. ORAI1, STIM1/2, and RYR1 shape subsecond Ca2+ microdomains upon T cell activation. *Science Signaling*, 11(561), 2018.

[135] B. Sakmann and E. Neher. *Single-Channel Recording*. Springer, 2nd ed. 1995.

[136] J. Cuevas. Electrophysiological recording techniques. *xPharm: The Comprehensive Pharmacology Reference*, pages 1 – 7. Elsevier, New York, 2007.

[137] N. Higinbotham, A. B. Hope, and G. P. Findlay. Electrical Resistance of Cell Membranes of Avena coleoptiles. *Science*, 143(3613):1448–1449, 1964.

[138] E. J. Williams, R. J. Johnston, and J. Dainty. The Electrical Resistance and Capacitance of the Membranes of Nitella translucens. *Journal of Experimental Botany*, 15(1):1–14, 1964.

[139] A. K. Murali, and S. Mehrotra. Apoptosis - an Ubiquitous T cell Immunomodulator. *Journal of Clinical & Cellular Immunology*, 01(S3), 2012.

[140] B. Alberts, A. Johnson, J. Lewis, D. Morgan, M. Raff, K. Roberts, P. Walter, and U. Schäfer. *Molekularbiologie der Zelle*. Wiley, 2017.

[141] A. Stemmann, Ch. Heyn, T. Köppen, T. Kipp, and W. Hansen. Local droplet etching of nanoholes and rings on GaAs and AlGaAs surfaces. *Applied Physics Letters*, 93(12):123108, 2008.

[142] E. Yablonovitch, T. Gmitter, J. P. Harbison, and R. Bhat. Extreme selectivity in the lift-off of epitaxial GaAs films. *Applied Physics Letters*, 51(26):2222–2224, 1987.

[143] M. Zocher, Ch. Heyn, and W. Hansen. Droplet etching with indium - Intermixing and lattice mismatch. *Journal of Crystal Growth*, 512:219–222, 2019.

[144] P. V. Gwozdz, S. Ramachandran, A. Dorn, A. Drews, A. Bhat, and R. H. Blick. Optically active semiconductor nanopores for parallel molecule detection. *Applied Physics Letters*, 109(22):223103, 2016.

[145] M.-Y. Wu, D. Krapf, M. Zandbergen, H. Zandbergen, and P. E. Batson. Formation of nanopores in a SiN/SiO2 membrane with an electron beam. *Applied Physics Letters*, 87(11):113106, 2005.

[146] A. Kumar, K.-B. Park, H.-M. Kim, and K.-B. Kim. Noise and its reduction in graphene based nanopore devices. *Nanotechnology*, 24(49):495503, 2013.

[147] C. A. Merchant, K. Healy, M. Wanunu, V. Ray, N. Peterman, J. Bartel, M. D. Fischbein, K. Venta, Z. Luo, A. T. Charlie Johnson, and M. Drndic. DNA Translocation through Graphene Nanopores. *Nano Letters*, 10(8):2915–2921, 2010.

[148] K. Liu, J. Feng, A. Kis, and A. Radenovic. Atomically Thin Molybdenum Disulfide Nanopores with High Sensitivity for DNA Translocation. *ACS Nano*, 8(3):2504–2511, 2014.

[149] L. T. Romankiw. A path: from electroplating through lithographic masks in electronics to LIGA in MEMS. *Electrochimica Acta*, 42(20-22):2985–3005, 1997.

[150] T. A. Green. Gold electrodeposition for microelectronic, optoelectronic and microsystem applications. *Gold Bulletin*, 40(2):105–114, 2007.

[151] I. Fernandez-Cuesta, A. Laura Palmarelli, X. Liang, J. Zhang, S. Dhuey, D. Olynick, and S. Cabrini. Fabrication of fluidic devices with 30 nm nanochannels by direct imprinting. *Journal of Vacuum Science & Technology B, Nanotechnology and Microelectronics: Materials, Processing, Measurement, and Phenomena*, 29(6):06F801, 2011.

[152] P. Lugli, S. Harrer, S. Strobel, F. Brunetti, G. Scarpa, M. Tornow, and G. Abstreiter. Advances in Nanoimprint Lithography. In *2007 7th IEEE Conference on Nanotechnology (IEEE NANO)*, pages 1179–1184, 2007.

[153] I. Fernandez-Cuesta and S. Cabrini. Optofluidic devices and methods for sensing single particles, 2014. US Patent 9,829,425 B2.

[154] H. Happy, K. Haddadi, D. Theron, T. Lasri, and G. Dambrine. Measurement Techniques for RF Nanoelectronic Devices: New Equipment to Overcome the Problems of Impedance and Scale Mismatch. *IEEE Microwave Magazine*, 15(1):30–39, 2014.

Conference Contributions and Talks

Presenting author:

- Poster: **Paul V. Gwozdz**, Abhishek Bhat, Robert H. Blick, Arjun Seshadri, Eric Stava:

  Radio-Frequency tank circuit for DNA Sequencing,

  Biophysical Sociaty 58$^{\text{th}}$ Annual Meeting, San Francisco, California, USA (2014)

- Poster: **Paul V. Gwozdz**, Andre Drews, Abhishek Bhat, August Dorn, Robert H. Blick:

  Simulation results for an optically active semiconductor nanopore,

  Biophysical Sociaty 59$^{\text{th}}$ Annual Meeting, Baltimore, Maryland, USA (2015)

- Talk: **Paul V. Gwozdz**, Abhishek Bhat, Arjun Seshadri, Robert H. Blick:

  Real time detection of sub-micron particles translocating through micropores,

  19$^{\text{th}}$ International Conference on electron dynamics in semiconductors, optoelectronics and nanostructures, Salamanca, Spain (2015)

- Poster: **Paul V. Gwozdz**, Simon Bittmann, Lars C. Erdmann, Björn-Phillip Diercks, Andreas H. Guse:

  Coulter-based flow cytometer for the measurement of cell stiffness,

  European Workshop Label-Free Particle Sorting (LAPASO), Lund, Sweden (2017)

- Talk: Lola Hernandez and **Paul V. Gwozdz**:

  Electrical spectroscopy of T cells using GHz frequencies

  Infectophysics Progress Report Meeting 2018, Hamburg, Germany (2018)

- Talk: **Paul V. Gwozdz**, Lola Hernandez, Udaj Singh, Andreas Guse, Robert H. Blick:

  Dielectric Spectroscopy on T cells

  12th North German Biophysics Meeting, Research Center Borstel, Germany (2019)

Contributing author:

- Talk: Andreas Schlegel, Aune Koitmäe, **Paul V. Gwozdz**, Jann Haberts, Christian Heusinger, Gabriele Loers, Robert H. Blick:

  Synthetic Neuronal Networks on Glass Using Topological and Chemical Cues,

  Frühjahrstagung der Deutschen Physikalischen Gesellschaft, Berlin (2015).

- Poster: M. Valiki, D. Monteiro, R. Vasireddi, T. Glier, T. Gerling, **Paul V. Gwozdz**, R. Blick, H. N. Chapman and M. Trebin:

  Microfluidics and X-ray scattering for In Situ Time-resolved Studies

  CUI Annual Meeting, Hamburg (2016).

- Talk: Andreas Schlegel, **Paul V. Gwozdz**, Christian Heyn, Wolfgang Hansen, and Robert H. Blick:

  Optically active, self-assembled solid-state nanopores for single particle detection,

  Frühjahrstagung der Deutschen Physikalischen Gesellschaft, Dresden (2017).

- Poster: Andreas Schlegel, **Paul V. Gwozdz**, Christian Heyn, August Dorn, André Drews, Wolfgang Hansen, Robert H. Blick

  Optically Active, Self-Assembled Solid-State Nanopores for Single Particle Detection

  Biophysical Sociaty 62^{th} Annual Meeting, San Francisco, California, USA (2018)

List of Publications

Published articles

- Abhishek Bhat, **Paul V. Gwozdz**[1], Arjun Seshadri, Marcel Hoeft and Robert H. Blick

  Tank Circuit for Ultrafast Single-Particle Detection in Micropores

  Phys. Rev. Lett. **121**, 078102 (2018)

- **Paul V. Gwozdz**, Sujatha Ramachandran, August Dorn, André Drews, Abhishek Bhat, and Robert H. Blick.

  Optically active semiconductor nanopores for parallel molecule detection

  Appl. Phys. Lett. **109**, 223103 (2016)

- Hermann Osterhage, Johannes Gooth, Bacel Hamdou, **Paul Gwozdz**, Robert Zierold, and Kornelius Nielsch.

  Thermoelectric properties of topological insulator Bi_2Te_3, Sb_2Te_3, and Bi_2Se_3 thin film quantum wells

  Appl. Phys. Lett. **105**, 123117 (2014)

Pending articles

- Mohammad Vakili, Stefan Merkens, Yunyun Gao, **Paul V. Gwozdz**, Ramakrishna Vasireddi, Lewis Sharpnack, Andreas Meyer, Robert H. Blick, Martin Trebbin

  3D-Micromachined Polyimide Mixing Devices for in situ X-ray Imaging of Block Copolymer Phase Transitions

  Submitted to Langmuir

[1] Equal contribution with Abhishek Bhat

- Stefan Merkens, Mohammad Vakili, Ana Sánchez-Iglesias, Lucio Litti, Yunyun Gao, **Paul V. Gwozdz**, Lewis Sharpnack, Robert H. Blick, Luis M. Liz-Marzán, Marek Grzelczakh, and Martin Trebbin

  Resolving Dynamics of Assembling Gold Nanoparticles with Real-Time Analytics

  Submitted to ASC Nano

- Andreas Schlegel, **Paul V. Gwozdz**, Christian Hyne, Wolfgang Hansen Robert H. Blick

  Processing Nanopores embedded in a thin GaAs nanomembrane from LDE on stable glass substrates

  To be submitted to APL

- Jonathan Rodriguez, **Paul V. Gwozdz**, Hyun-Cheol Shin, Eric Stava, Minrui Yu, José R. Sánchez-Pérez, Max G. Lagally, and Robert H. Blick

  Confined ignition and burning of micro-plasmas for ablating nanopores in single-crystalline quartz

  To be submitted to Optics Express

Patents

- Robert H. Blick, **Paul V. Gwozdz**, Abhisheka Bhat, Wolfgang Hansen and Christian Heyn

  High-Speed DNA Sequencing with Optically Active Nanopore

  US Pat. US 20170029882 A1 (2017)

- Robert H. Blick, Abhishek Bhat and **Paul V. Gwozdz**

  Radio-Frequency Nanopore Sensor

  US Pat. US 20170023545 A1 (2017)

Acknowledgements

An erster Stelle möchte ich Prof. Dr. Robert H. Blick für die Möglichkeit danken, diese Arbeit in seiner Arbeitsgruppe anzufertigen zu dürfen. Seine wissenschaftliche Unterstützung, seine positive und optimistische Herangehensweise und seine Motivation waren und sind mir nachhaltig eine große Hilfe.

Ich danke Prof. Dr. Wolfgang Parak für die Übernahme des Zweitgutachtens der Dissertation.

Auch möchte ich Prof. Dr. Caren Hagner, Prof. Dr. Alexander Lichtenstein und Dr. Robert Zierold dafür danken, dass sie sich bereit erklärt haben Mitglieder meiner Prüfungskommission zu werden. Prof. Dr. Michael Potthoff danke ich dafür, dass er so spontan den Vorsitz der Prüfungskommission übernommen hat

Ich danke der Gruppe von Prof. Dr. Dr. Andreas H. Guse für die Kollaboration an dem RF Projekt. Besonders bedanke ich mich bei Dr. Björn-Philipp Diercks und Lola Hernandez für die vielen Diskussionen, besonders was die biologischen Fragen angeht.

Der Gruppe von Prof. Dr. Wolfgang Hansen gebührt mein Dank für die Präparation der MBE gewachsenen Nanomembrane. Dr. Christian Heyn danke ich für das Wachsen der Strukturen und für die vielen Diskussionen bzgl. des Projekts.

Der Gruppe von Prof. Dr. Martin Trebbin danke ich für die Möglichkeit Mikroskopie in ihrem Labor zu machen. Besonders möchte ich mich bei Mohammad Vakili bedanken, der mir bei diesem Vorhaben ausgesprochen hilfreich zur Seite stand.

Mein außerordentlicher Dank geht an eine ganze Reihe von Studenten, die ich auf ihrem Weg zur Bachelor und Masterarbeit begleiten durfte. Der Dank geht an Steffen Tietjen, Andreas Schlegel, Charline Becker, Simon Bittmann, Sönke Wengler-Rust, Marcel Höft, Lars Erdmann und Daniel Rode.

Darüber hinaus bedanke ich mich bei Dr. Abhishek Bhat, von dem ich das RF Projekt übernommen habe und der mir eine große Hilfe beim Umzug des Messaufbaus von Madison nach Hamburg war.

Ich möchte mich bedanken bei meinem studentischen Hilfskraft Tom Scharringhausen, der mir nach wie vor viel Arbeit im Reinraum abnimmt.

Mein Dank geht an Dr. Robert Zierold, Dr. Irene Fernandez-Cuesta und Dr. Hoan

Vu, die sich die Zeit genommen haben die Arbeit zu lesen und zu korrigieren. Darüber hinaus bedanke ich mich bei Jann Harberts, Andreas Schlegel, Lucjan Grzegorzewski, Mohammad Vakili und Parisa Bayat, die Ausschnitte der Arbeit gelesen haben. Allen gilt mein Dank für die hilfreichen Kommentare und die aufmunternden Worte.

Diese Arbeit wäre nicht möglich ohne technischen Support. Am Standort Jungiusstrasse gilt mein Dank Andrea Köppen, Christina Lampe und Michael Volkmann, die immer ein offenes Ohr hatten, wenn ich mal Hilfe brauchte. Für den technischen Betrieb und Support am CHyN möchte ich mich bei Thomas Finger, Matthias Hein und Bojan Bosnjak bedanken. Außerdem bedanke ich mich bei Georg Welz, zu dem ich immer kommen konnte, wenn ich mal ein Problem mit der Elektronik hatte.

Außerdem gilt mein Dank denen, mit denen ich das Vergnügen hatte das Büro zu teilen. Besonders möchte ich hier erwähnen Dr. Aune Koitmäe, Dr. Cornelius Bausch, Dr. Jens Ehlermann, Daniel Diedrich, Jann Haberts, Cornelius Fendler, Pai Zhao und Yannig Gicquel.

Natürlich danke ich der ganzen Gruppe HB, ohne euch wäre alles nur halb so schön gewesen.

Ich danke allen meinen Freunden: Denen aus der alten Heimat und denen die Hamburg zur Heimat gemacht haben.

Ich bedanke mich bei Lara, für die Geduld, die sie aufbringen konnte, besonders in den letzten Wochen.

Vielleicht mein größter Dank geht an meine Familie. Ohne euch wäre das hier wohl nicht passiert.

Eidesstattliche Versicherung / Declaration on oath

Hiermit versichere ich an Eides statt, die vorliegende Dissertationsschrift selbst verfasst und keine anderen als die angegebenen Hilfsmittel und Quellen benutzt zu haben.

Die eingereichte schriftliche Fassung entspricht der auf dem elektronischen Speichermedium.

Die Dissertation wurde in der vorgelegten oder einer ähnlichen Form nicht schon einmal in einem früheren Promotionsverfahren angenommen oder als ungenügend beurteilt.

Hamburg, den

_____

Unterschrift des Doktoranden